NASA/TM-2001-209625
AFDD/TR-01-A-003

Devices that Alter the Tip Vortex of a Rotor

Kenneth W. McAlister and Chee Tung
Army/NASA Rotorcraft Division
Aeroflightdynamics Directorate (AMRDEC)
US Army Aviation and Missile Command
Ames Research Center, Moffett Field, CA

James T. Heineck
Experimental Physics Branch
Ames Research Center, Moffett Field, CA

National Aeronautics and
Space Administration

Ames Research Center
Moffett Field, California 94035-1000

February 2001

Available from:

NASA Center for AeroSpace Information
7121 Standard Drive
Hanover, MD 21076-1320
(301) 621-0390

National Technical Information Service
5285 Port Royal Road
Springfield, VA 22161
(703) 487-4650

Devices that Alter the Tip Vortex of a Rotor

Kenneth W. McAlister and Chee Tung
Army/NASA Rotorcraft Division
Aeroflightdynamics Directorate (AMRDEC)
US Army Aviation and Missile Command
Ames Research Center, Moffett Field, CA

James T. Heineck
Experimental Physics Branch
Ames Research Center, Moffett Field, CA

ABSTRACT

Small devices were attached near the tip of a hovering rotor blade in order to alter the structure and trajectory of the trailing vortex. Stereo particle image velocimetry (PIV) images were used to quantify the wake behind the rotor blade during the first revolution. A procedure for analyzing the 3D-velocity field is presented that includes a method for accounting for vortex wander. The results show that a vortex generator can alter the trajectory of the trailing vortex and that a major change in the size and intensity of the trailing vortex can be achieved by introducing a high level of turbulence into the core of the vortex.

NOMENCLATURE

a	speed of sound, ms^{-1}
A	area enclosed by circulation path, m^2
c	chord length, m
C_t	thrust coefficient, thrust/$\rho\pi\Omega^2 R^4$
M	hover tip Mach number, $R\Omega a^{-1}$
N	number of points to be averaged
r	radial distance from vortex center, mm
r_c	vortex core radius, mm
R	radius of rotor tip path, m
R_e	hover tip Reynolds number, $cR\Omega\nu^{-1}$
u, v, w	velocity compontents, ms^{-1}
v_c	vortex convection velocity, ms^{-1}
v_i	vortex interior velocity, ms^{-1}
v_θ	circumferential velocity in x-y plane, ms^{-1}
$v_{r\theta}$	v_θ relative to convection velocity, ms^{-1}
x, y, z	coordinates relative to rotor tip, mm
$\bar{x}, \bar{y}$	mean values of x, y, mm
$\tilde{x}, \tilde{y}$	x, y relative to basic blade vortex, mm
α	angle of position vector, deg
β	angle of $\vec{u} + \vec{v}$ vector, deg
Γ	circulation, $\mathrm{m}^2\mathrm{s}^{-1}$
Γ_*	circulation at particular value of r, $\mathrm{m}^2\mathrm{s}^{-1}$
δ	radial departure from mean location, mm
ν	kinematic viscosity, $\mathrm{m}^2\mathrm{s}^{-1}$
σ	standard deviation of vortex wander, mm
ψ	azimuthal angle measured from blade, deg
ω_z	vorticity normal to x-y plane, s^{-1}
Ω	rotational speed of rotor, RPM

ABBREVIATIONS

BERP	British Experimental Rotor Program
BVI	Blade-vortex interaction
CCD	Charged-coupled device
FFT	Fast Fourier transform
LDV	Laser Doppler velocimetry
PIV	Particle image velocimetry
TG	Turbulence generator
VG	Vortex generator

INTRODUCTION

Although the helicopter performs well in hover and low speed forward flight, it lacks community acceptance in populated areas due to the noise that it produces. A major source of helicopter noise comes from the rotor blade as it cuts through its own wake. This phenomenon is known as blade/vortex interaction (BVI) noise, and it occurs primarily when the helicopter is descending. Applying a mitigating device that reduces rotor noise can be quite challenging since the offending trailing vortices are shed from the tips of the rotor blades where the centripetal acceleration is highest. In addition to the force that such a device must withstand, consideration must be given to rotor performance since any alterations to the tip region, where the dynamic pressure is highest, could degrade the aerodynamic efficiency of the blade. Increasing the chord length and reducing the tip speed of the rotor may seem like an obvious solution for reducing BVI noise, however the added weight and control loads may be offsetting.

Earlier studies have identified two important parameters governing BVI noise generation. The first parameter is the miss distance between the rotor blade and the trailing vortex. The second parameter is the size (or intensity) of the vortex. The miss distance and the vortex core size can be simultaneously increased with a nonplanar tip configuration (refs. 1,2), however, the shape of this blade limits its application to hover and low speed flight. Another approach to lowering BVI noise involves a momentary change in blade pitch at just the right azimuth using higher harmonic control (ref. 3), an active flap (ref. 4), or individual blade control (ref. 5). Reductions in BVI noise have been achieved, but it is not certain whether these improvements are the result of an increase in the miss distance, a decrease in the intensity of the interacting vortex segment, or a combination of both effects. There is also some concern that the inputs needed for noise reduction may promote an increase in vibration (ref. 5).

There have been numerous attempts to simply reduce the intensity of the trailing vortex. An early effort was aimed at reshaping the planform of the blade near the tip such that the local flow swirling around the streamwise edge of the blade would not encounter a surface on the upper side on which to reattach (or stagnate). This design was known as the ogee tip and it did result in a significant reduction in the concentration of vorticity in the wake of a model wing (ref. 6). The same design was applied to the blades of a model rotor and was found to produce a similarly diffused tip vortex, however, there was an unacceptable degregation in performance at the higher thrust levels due to an early onset of stall (ref. 7). Other attempts, such as tapering the planform or the thickness, sweeping the tip, or adopting a major planform change (BERP), have all resulted in only modest increases in the diffusion of the vortex, with the conclusion that more intrusive devices need to be considered (ref. 8).

Adding devices to the tip of the rotor is representative of the more agressive measures taken to reduce BVI noise. The first known attempt originated as a spoiler placed on the upper surface near the wing tip of a full-scale transport (ref. 9). Although the maximum swirl velocity was reduced by a factor of 3, there was little difference in the rolling moment experienced by the aircraft following in the wake of the transport (ref. 10). Nevertheless, the dramatic increase in core size was sufficient to attract its application to a model rotor (ref. 11). The device, which functioned as a spoiler, was placed at the quarter chord, normal to the upper surface, and measured 9% in height and 12% in width relative to the chord of the rotor blade. Tests revealed a substantial reduction in BVI noise, however, a discouragingly high level of power was consumed and there was a significant increase in broadband noise (ref. 11).

One of the less intrusive additions to the tip of the rotor blade was the subwing (ref. 12). This device took the form of a small wing with a chord length about 20% that of the rotor blade. The subwing became an extension of the rotor blade and was intended to force the circulation near the tip of the blade to be shed as two co-rotating vortices, each having less intensity than would occur without the subwing. Results from this test showed a slight reduction in torque at moderate thrust levels and a modest reduction in the swirl velocity of the vortex trailing from the rotor blade. A more recent test revealed that the two vortices initially contract more rapidly than for the blade-alone vortex, but then combine into a single vortex (at around $\psi = 150°$, depending on the lift on the subwing) and follow the same trajectory observed for the blade-along vortex (ref. 13).

Recognizing the effectiveness of a spoiler in diffusing the trailing vortex, various devices have been attached to the tip of a fixed wing at locations both near and beyond the trailing edge (ref. 14). Once again, several designs proved quite capable of diffusing the trailing vortex and each carried a certain measure of drag penalty. Since any device that causes an increase in drag on a wing would be expected to be even more objectionable when applied to the tip of a rotor blade, the less intrusive among these spoilers have been tested on a model rotor (ref. 15). Small angles and wedges were attached to the trailing edge of the rotor blade, and a sizeable reduction in BVI noise was observed. Although the results were encouraging, the seemingly inevitable increase in power led to the suggestion that some means of actively deploying these devices might be the only reasonable solution (refs. 8, 11, 15, 16).

While avoidance, rather than forced diffusion, may be the best approach for fixed-wing aircraft to deal with the hazards of across-trail and in-trail vortex encounters (ref. 10), rotor blades engage relatively young vortices so that methods that even temporarily enlarge the trailing vortex could prove useful. Although the concepts of vortex pairing and turbulent diffusion are not new, the present study examines these ideas on a rotor and with a diagnostic technique that provides a level of detail that was not previously available.

Similar to the wake of a fixed-wing aircraft, the dominant feature of a rotor wake is the trailing vortex that is shed from the tip of the rotor blade. Experiments typically focus on the location, size, and intensity (or magnitude of vorticity) of the trailing vortex at various wake ages. The trajectory of the vortex can be accurately determined from flow visualization based on a triangulation technique using laser light sheets (ref. 17). While this technique is relatively easy to apply, it does not provide any information about the structure of the vortex. Although tedious, the structure of the trailing vortex can be obtained using laser Doppler velocimetry (LDV). It is important to note that small disturbances in the freestream flow will cause the vortex to wander, or meander, over a lateral distance that increases with distance from the blade. A point measurement technique, such as LDV, will therefore require some procedure for conditionally averaging the results (ref. 18), especially as the wake ages or when the freestream turbulence level is high. A planar measurement technique, such as PIV, has the advantage of requiring substantially less time to acquire the 3D velocity field. Nevertheless, this data must also be conditionally averaged when vortex wander is present (ref. 19).

This paper contains a discussion of the test setup and a method for obtaining the 3D velocity field in the wake of the rotor at specific wake ages. The procedure for identifying separately the centers of vorticity and swirl, and how they relate respectively to conditional ensemble averaging and the vortex structure, will be presented. Data will be shown that clearly expose the distinguishing features of the flow and the effectiveness of both vortex pairing (with same and opposite sense) and forced turbulent diffusion on the aging trailing vortex.

TEST DESCRIPTION

Test Chamber and Stand- The experiment was performed in the Hover Test Chamber at the NASA Ames Research Center under the authority of the U.S. Army Aeroflightdynamics Directorate. The chamber has a base of 26 ft x 32 ft and a height of 28 ft. To minimize recirculation in the chamber and to limit the influence of the floor on the flow, the collective pitch of the rotor blade was set to a negative angle so that the wake would be directed upwards. With the rotor acting like a pump, air was drawn into the chamber through filters placed across two opposing rollup doors, then confined by an annular diffuser located above the rotor, and finally exhausted to the exterior through openings near the top of the chamber (fig. 1).

The rotary-wing test stand that was used to drive the rotor was configured with a single, 90-hp electric motor and a 2.5:1 transmission. A flexible coupling between the input shaft and the dummy balance was instrumented to measure torque. An encoder with a resolution of 4096 steps per revolution was attached to the rotor shaft. The encoder signals were passed to a variable delay circuit that enabled the PIV cameras and Nd:YAG laser to be synchronized to any desired rotor azimuth.

Rotor Blade and Hub- The rotor consists of a single counter-weighted aluminum blade having a rectangular planform, zero twist, 7.5 in. chord, and a 45 in. radius (fig. 2). The outer 50 percent of the blade conforms to a NACA 0012 profile (thickness at the tip is 22.9 mm). Over the inner portion of the blade radius the profile linearly thickens to a NACA 0020. The rotor hub consists of two steel sections that are clamped together to hold the blade at a 0° coning angle. The collective pitch angle was fixed at −8°. When mounted on the test stand, the rotor and hub were approximately 7.5 ft above the floor of the test chamber. The solidity of this single-blade configuration is 0.053.

Blade Attachments- One of the mechanical devices under study was designed to function as a vortex generator and the other as a turbulence generator (figs. 2 and 3). The vortex generator has a NACA 0012 profile, rectangular planform with a rounded tip, and measures 0.12c in chord and 0.10c in span (where c refers to the chord length of the main element). The quarter-chord axis of the vortex generator passes through the quarter-chord location of the main element. The turbulence generator consists of a flat rectangular section and measures 0.12c in length (with a fixed alignment with the span of the main element) and 0.10c in height (oriented normal to the surface of the main element). The center of the turbulence generator also passed through the quarter-chord axis of the main element. Both generators were mounted 0.057c inboard from the tip of the main element. If the vortex generator were to be rotated 90°, its projected area would appear to the oncoming flow the same as the turbulence generator. The relative dimensions and placement of the turbulence generator are similar to the spoiler employed in an earlier study (ref. 11).

Test Conditions- The present test was performed at a constant rotor speed of 870 rpm (14.5 Hz), which corresponds to a tip speed of 341.7 ft/sec. Based on an average ambient temperature of 65° F and barometric pressure of 760 mm Hg (14.7 psi), the Reynolds number (based on c) at the tip of the rotor blade was $R_e = 1.33 \times 10^6$ and the Mach number was $M = 0.30$. Based on a collective pitch angle of $-8°$, the equivalent two-blade thrust coefficient was $C_t = 0.005$ (ref. 20). The vortex generator was tested at eight angle-of-attack (relative to the chord of the main element) conditions: $-15°$, $-10°$, $-5°$, $0°$, $5°$, $10°$, $15°$, and unrestrained. The turbulence generator was tested at a fixed orientation normal to the upper surface of the main element and parallel to the leading edge of the blade.

Stereoscopic PIV Concept- The velocity of a fluid is inferred from the motion of discrete particles that are suspended in the flow. A thin sheet of light is used to define the plane of interest. The particle images that are recorded at two different times are then cross correlated to yield displacement vectors (magnitude and direction). The time interval between the two images must be short enough that the particles remain in the light sheet, yet long enough that the particle displacements are perceptible. It is assumed that the particles are small enough to accurately track the flow.

A single camera placed normal to the sheet of light results in a two-dimensional array of velocity vectors. If the flow has a significant third component (directed normal to the plane of the light sheet), an error due to perspective develops in the two-dimensional array that is zero in the center and increases toward the image boundaries. This seemingly undesirable sensitivity to out-of-plane motion was later exploited to derive the third component of velocity (ref. 21). In fact, sensitivity to the out-of-plane component of velocity over the entire image plane can be increased by intentionally placing the camera at an oblique angle to the light sheet. To uniquely determine a three dimensional particle displacement requires two cameras that are oblique to the light sheet, each offering a different perspective of the particle motion between the two exposures (fig. 4). This procedure is known as Stereoscopic PIV or 3D-PIV.

The technique demands both critical focus and maximum brightness of the particle image. Conventional lens mounts create a plane of focus in object space that is parallel with both the image plane and the lens plane. When the lens plane is oblique to the object plane (as is the case for Stereoscopic PIV), particles will be increasingly defocused as their distance from the centerline of the object plane increases. The conventional corrective action would be to increase the depth of field by reducing the aperture of the lens. Unfortunately, reducing the lens aperture drastically reduces both the particle image intensity and the image resolution. The problem is solved with Scheimpflug focusing (refs. 22 and 23). To keep the object plane in focus when the lens plane is rotated to an oblique orientation, the image plane (where the camera sensor is placed) must also be rotated such that all three planes (object, lens, and image) intersect along a common line (fig. 5).

Arrangement of Equipment- The cameras were mounted in a forward-scatter position on a horizontal plane that passed 3 in. above the rotor disc (fig. 6). The bisecting angle between the light sheet and each camera was 36°, and the cameras were rotated so that the image areas were coincident. The centerline dimensions of the image area were 14 in. vertical and 18 in. horizontal. Due to perspective the vertical dimension of the image ranged from 12 in. (near side to the cameras) to 16 in. (far side). The lower, outboard corner of the image area was placed so as to capture the trailing vortex over a maximum range of wake ages (which was less than one revolution for this test).

Camera Specifications- Images were acquired with 8-bit charged-coupled device (CCD), cross-correlation cameras having a sensor array of 1008 (horizontal) × 1018 (vertical) pixels. Each pixel measures 9 μm on a side. The cameras can operate in a double-exposure mode and acquire two non-interlaced, full-frame images in a single frame interval. The time interval between images is variable between 2 μs and 30 ms. These are non standard video cameras that can be externally triggered and driven at any frequency up to 15 Hz in double-exposure mode. A computer interface provides control over gain, contrast, black level, and trigger mode. Both cameras used 55-mm f1.2 lenses. The lenses were remotely translated to focus on the centerline of the image area and the sensor (located inside the camera body) was rotated about its centerline to satisfy the Scheimpflug condition.

Laser and Sheet Optics- A Nd:YAG laser was frequency doubled to provide a beam having a wavelength of 532 nm, a pulse width of 9 ns, and power of 350 mJ. The laser model used has a beam diameter of 9 mm and a divergence of 0.50 mrad. All optical elements have damage thresholds exceeding 1 J/cm^2. A laser-light sheet was formed using lenses that thin the beam in one direction and expand the beam in the orthogonal direction. The thickness (horizontal direction in this test) of the light sheet was controlled by two cylindrical lenses, the focal length of one was f = +200 mm and the other f = -200 mm. By adjusting the distance between these two lenses, the beam waist ($\approx$ 1 mm thick) could be positioned in the region imaged by the cameras. The vertical expansion of the light sheet was controlled by a single f = -75 mm cylindrical lens. The distance between the sheet forming optics and the imaged area was about 25 ft.

System Alignment- The rotor blade was positioned at the 0° reference azimuth and a calibrated laser level (sweeping type) was used to establish the vertical plane passing across the trailing edge of the blade. The laser-light sheet was adjusted to be coincident with the laser level. A calibration target was placed against the trailing edge, then translated to coincide with the area viewed by the cameras, and finally leveled to within ±0.01° with a digital inclinometer. The location of the blade tip relative to a point on the calibration target was measured to within ±1/32 in. The alignment of the target was considered to be satisfactory when the surface of the target was evenly grazed by the light sheet. Using only white light to illuminate both sides of the target, the cameras were focused and calibration images were recorded.

PIV Software- This experiment was performed using the Integrated Design Tools (IDT) WinVu v5.10 software (ref. 24). This software functions as both a data acquisition interface and an image-processing interface. This has the advantage of providing a fully integrated calibration procedure that allows for acquisition, quality assurance and data reduction. The calibration yields all the optical parameters required for accurate reconstruction of three-component velocity-vector fields. A calibration was performed before and after each series of runs.

Images are processed by first covering the region of interest with an interrogation grid. The intersections of the vertical and horizontal grid lines define the centers of each interrogation window. The interrogation window is the smaller region in the reference and delayed images that are cross-correlated using an optimized Fourier transform. When the camera calibrations are applied, the grid in each camera view covers the exact same area in the flow field.

The size of the interrogation window is based on the particle density and the maximum instantaneous displacement of the particles. Typically the window size ranges from 8 to 64 pixels on a side. Each interrogation window yields one vector. The cross-correlation of the interrogation window in the reference image with that of the delayed image yields a correlation map. The location of the correlation peak in space determines the local displacement in both magnitude and direction.

WinVu incorporates quality-assurance tests in the vector calculations. The processing begins with a first-pass correlation between the reference image and delayed image to determine the maximum displacement range. For the second pass the software enlarges the interrogation area in the delayed image. The amount of the enlargement is based on the maximum displacement range determined in the first pass. Since the Fourier transform requires both interrogation areas to be identical, the software "adds zeros" to the interrogation area of the reference image to match the size of the delayed image area. This technique maximizes the probability of correlating all the particles found in the reference image interrogation area to those found in the delayed image, thereby maximizing the statistical accuracy.

The software then counts the number of particle images (each composed of several contiguous pixels) in the interrogation window. Ten particle pairs are required to contribute to a correlation map. The centroid of each particle is calculated, thus yielding sub-pixel accuracy of their position. A second-order curve fit is determined from the ten displacements. This curve fit yields a single vector, at the precise grid point location, whose error is reduced by a factor of 0.3 ($1/\sqrt{N}$, where $N = 10$ particles) over the straight fast Fourier transform (FFT) of the same area (ref. 24).

If there are not enough particles in a given interrogation region, the program will automatically enlarge the interrogation area of the reference image. If there are ten or more particles in this enlarged area, then the correlation proceeds in the same manner described above. The data for this grid point is considered to be a recalculation. If ten particles are not counted, the software will expand the interrogation area incrementally. It will repeat this process until the interrogation area expands to a limit of 64x64 pixels. If the ten-particle threshold is not met for the largest area, then velocity values are interpolated for that grid point using a second-order curve fit based on nearest-neighbor values. This vector is also counted as a recalculation. The software tracks the number of these recalculations and displays that number after each camera view is processed. If the number of recalculations is less than 1% of the total vectors, then the data are considered reliable.

Calibration Procedure- The stereoscopic images recorded by the cameras that are oblique to the object field must subsequently be corrected for both magnification and perspective. One method by which this can be accomplished results from recording the images of a flat rectangular target (with precisely known dimensions) that is placed in the field of view of both cameras. The target used in this test consisted of a double sided print containing three rectangles (the largest measuring about 217 mm on a side) and a background dot pattern that simulated a particle field (fig. 7).

A reliable method for assessing the accuracy of the velocity measurements obtained from test data is to evaluate the displacements recorded for known target translations (ref. 25). Consecutive translations of the target over orthogonal distances of 0.200 in. resulted in an in-plane standard deviation of 0.3% (horizontal) and 0.5% (vertical), and an out-of-plane standard deviation of 1.2%. Since actual particle displacements will normally be substantially smaller, the probable error should be increased by several times. Therefore, in the worst case, the out-of-plane component is estimated to be accurate to within about 3%.

Particle Seeding- Proper seeding of the flow is critical to accurate PIV measurements. The seed particles must be evenly distributed and of sufficient density to define the flow without altering its physical properties. The particles must also be small enough that they accurately follow the flow (especially challenging in accelerating flows), yet large enough that they scatter a sufficient amount of light to be detected. It is usually convenient to have remote control over the delivery of the seed material into the flow. The particle generator used in this test employs an inert gas to atomize a non-toxic, pharmaceutical-grade mineral oil. The mist is vaporized and then condensed before being released into the flow. The particle size is estimated to be less than 0.5 μm. The particle generator was located near the floor of the hover chamber so that the particles would mix with the air entering into the chamber before being drawn into the wake of the rotor.

Data Acquisition- The CCD cameras were connected to separate frame-grabber cards installed in a PC workstation. Using WinVu software, images were acquired and immediately processed in order to evaluate the quality of the raw images and the adequacy of the inter-pulse time delay. Good image correlations depend on such issues as background light contamination, particle image brightness, contrast, focus, beam alignment, and light pulse separation.

Prior to taking data, fine focusing and beam alignment were performed using a seeded jet. Focusing was accomplished by translating the camera lenses while observing the real-time image displays. The gain and black levels were adjusted to maximize the contrast and brightness of the particle images. The two laser sheets were judged to be coplanar when both laser pulses were recorded as a single image and the resulting particle images appeared as doublets.

The correct inter-pulse delay can best be determined under actual test conditions. Images are acquired and correlated to determine the maximum particle displacement. This displacement corresponds to the maximum particle velocity and the pulse separation should be adjusted to produce a ± 3 pixel range, regardless of the window size. Pixel displacements that are too small will limit the dynamic range whereas displacements that are too large will decrease the probability of correlation (ref. 26). Because of the high in-plane particle displacements, caused by the high circumferential velocity of the trailing vortex from the rotor at different wake ages, the optimum pulse separations varied from 30 to 50 μs (Table 1). It should be noted that if the thickness of the light sheet is 1 mm and the minimum delay between laser pulses is 30 μs, the highest out-of-plane velocity (w) that can be detected is 33 m/s. Since the tip of the rotor blade is moving at 104 m/s, portions of the flow in the near wake may be in error. If this condition were to occur at a calculation node, an interpolated value based on values at neighboring nodes would result. Therefore, at any point in the flow where w reaches 33 m/s, it may be assumed that the correct value may actually be much higher. Once image quality was assured, 50 image pairs were acquired per wake age. Data for each wake age required about 200 megabytes of storage.

Table 1: Pulse Delay Times (μs)

	Wake Age							
Config	2°	10°	30°	60°	100°	150°	210°	280°
Basic	30	30	30	30	30	30	30	35
Free VG	30	30	30	30	30	30	30	30
0° VG	30	30	30	30	30	35	35	35
+5° VG	30	30	30	30	30	35	35	35
−5° VG	30	30	30	30	30	35	35	35
+10° VG	30	30	30	30	30	35	35	35
−10° VG	30	30	30	30	30	35	35	35
+15° VG	30	30	30	30	30	30	30	30
−15° VG	30	30	30	30	30	35	35	35
90° TG	30	30	30	30	40	45	50	50

Post-Test Data Processing- After completion of the test, the data was processed on a PC workstation using ProVision software, which is a more advanced release that replaces WinVu. To obtain good resolution of the primary vortex, a calculation mesh having 99 nodes (horizontal) by 91 nodes (vertical) was constructed over the region of significant interest in the flow field (fig. 8). The area covered by the mesh resulted in an average of 8.5 pixels between nodes in both directions. The interrogation window was set at 20 pixels on a side, which gave about a 59% overlap. The total physical area measured about 386 mm (with horizontal increment of 3.9 mm) by 237 mm (with vertical increment of 2.6 mm).

A single file for each wake age includes a flag for every velocity measurement that indicates the nature of that vector (such as valid, invalid, interpolated, recalculated, or not calculated). Reduced data files containing the coordinates of each calculation node and the three components of velocity (in terms of displacement) were stored in ASCII format (about 32 megabytes in size) and then transferred to a mainframe computer for analysis.

The velocity components were first converted from displacement units to velocity units based on the pulse duration for that particular measurement. The physical coordinates were transformed so that $x = y = 0$ would correspond to the tip of the rotor blade (fig. 9). The sequence for extracting the characteristics of the trailing vortex (fig. 10) for each case begins with a calculation of the vorticity field, ω_z, for every image pair. Vorticity can either be calculated by differentiation or integration according to:

$$\omega_z = \frac{\partial v}{\partial x} - \frac{\partial u}{\partial y} \tag{1}$$

or

$$\omega_z = A^{-1}\Gamma = A^{-1} \oint (\vec{u}, \vec{v}) \cdot d(\vec{x}, \vec{y}) \tag{2}$$

where the direction of integration is such that the enclosed area, A, is on the left of the integration path. In this study the vorticity was calculated using the integration (or circulation box) method.

When more than one vorticity center is present in the field of view, a single image pair must be processed to determine where the field should be partitioned so that statistics are built on only one vortex. A simple two-part partition is usually sufficient to separate the two vortices. However, when a vortex generator is installed on the rotor blade, a small (but potentially intense) satellite vortex develops along side of the main vortex. In this case it is necessary to focus the interrogation on a more restricted region of the flow field. In such cases the statement "account for wander: focus" will appear in the figure for this data.

After calculating the vorticity distribution over the entire image, a search was performed to discover the zone of greatest vorticity concentration based on values exceeding 50% of the maximum (fig. 11 shows an example of the search). The center of vorticity for a given image was defined to be at the average of these selected locations. The resulting centers of vorticity (one for each image) formed a set for which the mean value $(\overline{x}, \overline{y})$ and the standard deviation (σ) could be calculated. Any image with a vortex center (x, y) that deviated from the mean $(\overline{x}, \overline{y})$ by more than 1.5σ was purged from the set. The 50% threshold criterion prevents the center of vorticity for an image from being determined by a single, and possibly erroneous, measurement. The standard deviation criterion prevents an atypical departure, albeit a legitimate image, from being factored into the average. The threshold and purging criteria both have the effect of reducing the degree of wander in the data (fig. 12). When the acceptance threshold is 100% (the vorticity center in each image is determined by a single point), 47 points are retained and 3 points are discarded because they exceeded the standard deviation criterion. When the acceptance threshold is 50% (the vorticity center in each image is determined by an aggregate of points), a distinct population of 44 points results (some of which are coincident). The quantity δ that appears in this figure, as well as many others, represents the degree to which the vortex wanders for a given set of images, and is calculated by taking the square root of the sum of the squares of the x and y offsets from the mean.

The images must be averaged to smooth out small irregularities in the flow. However, whenever there are large features in the flow, such as a trailing vortex, and the vortex appears in different positions from image to image (vortex wander), important details of the structure tend to be smeared out if a simple average of the images is performed. The remedy is to perform the average after artificially aligning the images based on a recurring feature of the flow, which in this case is the center of vorticity. This process, in contrast to a simple average, is referred to as conditional ensemble averaging, the condition here being the alignment of all the images in the set based on their centers of vorticity. The image with a vortex center closest to the mean location that was established for the set of images was selected as the "anchor". The indices of each image matrix were then adjusted according to the offset of each vortex center from the vortex center in the anchor image. All data in the anchor image were retained. However, some portion of all other images with adjusted indices that fall outside the boundaries of the anchored image were necessarily discarded. Hence, as a consequence of vortex wander, the population contributing to the conditional average was greatest over the interior of the matrix.

For reasons that will become clear in the following discussion, emphasis will be placed on the swirling nature of a vortex flow. To extract information about the geometry of the vortex, the center of the vortex was assumed to be at the center of swirl (which is not necessarily at the center of vorticity that is accreted from the rotor wake as a spiraling sheet with varying vorticity). Using the center of vorticity as a starting point, the surrounding locations are interrogated to determine the best node for which the sum of the dot products of two unit vectors is a minimum over a neighborhood of locations surrounding the candidate node. One of the unit vectors is defined by the coordinates of the neighboring node relative to the candidate node. The other unit vector is defined by the velocity vector at the neighboring node. Denoting the angles of these two unit vectors by α and β (fig. 13), then the node nearest the center of swirl is found when the following expression is a minimum:

$$\sum_{n=1}^{N} |\cos(\alpha - \beta)| / N \tag{3}$$

where N is the total number of neighboring points considered. Relative to the center of swirl for a pure vortex in a stationary flow, α and β will be orthogonal for all neighboring points and the sum will be exactly zero. For most real flows the sum will not be precisely zero, and the procedure works best when the neighborhood under consideration does not extend beyond about one or two core diameters (which is normally sufficient to cover a majority of the vorticity in a single trailing vortex). After locating the center of swirl, the size of the vortex core can be estimated. This is accomplished by dividing the neighborhood into annular zones and then determining the average swirl (or circumferential) velocity for each zone:

$$\sum_{n=1}^{N} |\vec{v}_\theta| / N \tag{4}$$

where N is the number of nodes within a given annular zone. The mean diameter for the zone having the highest average swirl velocity becomes the estimated diameter for the vortex core. This procedure appears to work well even though the flow is not axisymmetric. The swirl velocity, $\vec{v}_\theta$, is defined by the cross product of the unit position vector (relative to the center of swirl) associated with a node and the inplane velocity vector $\vec{u} + \vec{v}$. This relation can be expressed as:

$$\begin{aligned} \vec{v}_\theta &= \frac{\vec{r}}{|\vec{r}|} \times (\vec{u} + \vec{v}) \\ v_\theta &= |(\vec{u} + \vec{v}) \sin(\alpha - \beta)| \end{aligned} \tag{5}$$

where it is understood that v_θ is orthogonal to $\vec{r}$.

The ultimate method for calculating the size of the vortex core requires that the space surrounding the center of swirl again be divided into annular zones. This time a larger array of bins is constructed that contains the average swirl velocity and the associated mean radius of each annulus. This array is then fit with a least-squares spline subject to the condition that the resulting curve have only one inflection along its inner extent (nominally set to twice the estimated core radius that was previously found). The radius of the vortex core is now defined by the point of inflection since that is where a maximum value for $\vec{v}_\theta$ is reached. This procedure is considered to offer a more rational approach for determining the size of the vortex, especially when the velocity peaks that are characteristic of vortices (and upon which core sizes are traditionally based) are dependent on how the vortex is sliced (vertical, horizontal, or otherwise).

The final processing stage involves the construction of contour plots for v, w, and ω_z together with profiles of these variables along a horizontal cut (y=constant) through the center of swirl. The convection of the vortex does not affect w and ω_z, however it does produce an offset (or distortion if the convection field is not uniform) in the u and v components of velocity. In this study the vortex is assumed to be uniformly convected. Two methods for discovering the convection velocity are considered. One method assumes that the convection velocity at any given wake age is determined by the interior velocity measured at the center of swirl (the y component is defined as v_i). In the other method the convection velocity of the vortex is deduced from the record of swirl center coordinates calculated at each wake age (the y component is defined as v_c). The velocity profile for v relative to the convection velocity as determined by each of these methods (either $v - v_i$ or $v - v_c$) is included in the presentation of results.

RESULTS AND DISCUSSION

Including the basic rotor case, a total of 10 configurations were analyzed at 8 different wake ages (Tables 2 and 3).

Table 2: Configurations

Basic
Free Vortex Generator
0° Vortex Generator
+5° Vortex Generator
−5° Vortex Generator
+10° Vortex Generator
−10° Vortex Generator
+15° Vortex Generator
−15° Vortex Generator
90° Turbulence Generator

Table 3: Wake Ages

2°
10°
30°
60°
100°
150°
210°
280°

The vortex generator is defined to be at a positive angle when the trailing edge swings towards the tip of the rotor blade. For positive angles, the vortex that trails from the tip of the generator will have the same sense as the primary vortex that trails from the tip of the rotor blade. The actual angle of attack of the vortex generator may be quite different from its geometric angle because of the influence of the flow around the tip of the rotor blade on the local flow approaching the generator. All data were obtained with the rotor collective angle fixed at -8°, and all wake data were obtained at a constant rotor speed of 870 RPM.

Torque Summary- The rotor torque was recorded at several intermediate speeds prior to reaching the ultimate test speed of 870 RPM. These measurements are summarized in fig. 14 and indicate that all of the vortex generators that were oriented at fixed angles $(0^\circ, \pm5^\circ, \pm10^\circ, \pm15^\circ)$ resulted in torques that were lower than for the basic blade case. However, the "free" (or unrestrained) vortex generator shows an 8% increase in torque while the turbulence generator shows a 18% increase in torque. Given that these devices are located near the tip of the rotor blade, even small changes in the drag force on these elements should produce a noticeable change in the torque. The sizable increase in torque for the turbulence generator case is therefore in keeping with the expected level of increase in drag for such a blunt configuration, and demonstrates why such a device should be retracted when not required. If properly designed, the free vortex generator would be expected to react to the local flow much like a weather vane, and therefore generate a minimum level of drag. Since this does not appear to be the case, the center of gravity may have been offset from the pitch axis, thereby rendering the element at an angle sustained by a centripetal force that increases with RPM, or the element may be in a state of flutter.

Wake Analysis- For the 50 image pairs that were recorded at each wake age, approximately 12% were discarded due to excessive vortex wander from the mean location. Even when the vortex wanders by no more than one core diameter, a conditional ensemble average is required to obtain an accurate profile of the vortex. In contrast to a preferred conditional average of the data, a simple average results in a lower peak velocity and an increased core radius (fig. 15), although the circulation calculated along a circular path in the outer $1/r$ region appears to be independent of the method of averaging. The same conclusions have been reported using an exponential expression for the circumferential velocity and simulating different amplitudes of vortex displacement (ref. 27). It was shown that a substantial degredation in the velocity profile occurs when the amplitude is greater than one core radius.

Circulation, Γ, carried by the entire image will be presented for each case. This value is obtained by summing all of the individual circulation-box calculations within a given image, which amounts to 8,820 contributions for the grid used in this analysis. The total image circulation is quite sensitive to the convection of vorticity through the scene. In very general terms, the circulation calculated for a scene that contains slices of the vortex from two revolutions would be expected to decrease by about 50% when the second slice is convected out of the scene. The total image circulation is useful when comparing the wakes from different rotors (or with different vortex diffusion devices) and for evaluating the overall accuracy of numerical codes.

For an "ideal" vortex, all of the vorticity is contained within r_c and the circulation remains constant for $r \geq r_c$. However, in the case of a "real" vortex that is isolated and two-dimensional, the circulation within this body of fluid will rapidly increase with r until reaching some point beyond the core radius. For larger values of r the circulation will approach a constant value as long as the integration path remains in the outer "inviscid $1/r$" region. For the present rotor wake case the circulation appears to follow the classical trend and approach an asymptotic value only in the immediate vicinity of the vortex, but then deviates from a constant value at distances greater than about twice the core radius (fig. 16). This deviation is even less satisfactory after taking into account the vortex convection velocity. Since the axis of the trailing vortex from a rotor actually follows a helical path, the flow field around any given segment of the vortex will be affected by the induced flow caused by neighboring segments from previous revolutions of the blade. Another factor to be considered is the continual (although diminishing) accretion of chordwise vorticity that was initially shed into the wake along the span of the blade due to changing circulation. Regarding the variation of v_θ with r, there is less scatter in the relative-velocity data than there is in the absolute-velocity data. This is because in the relative case the flow field is referenced to the convection velocity of the vortex, which renders it more axisymmetric.

Given that any experimental technique is subject to some degree of error, it is useful to compare the present results with earlier measurements obtained under similar conditions. After applying a coordinate offset and accounting for the different tip speeds, previously obtained LV data (ref. 20) can be compared to the present PIV data (fig. 17). The PIV data shows a shortfall in the magnitude of the velocity peaks as well as an overestimate of the core size. Since the data in both cases was taken in the near wake, vortex wander (which was not accounted for in the LV data) is not believed to be a factor (which if anything, would have lowered the peak velocities in the LV data). Assuming that the LV data is more correct, the difference is most likely the result of a PIV inter-pulse delay time that was too long to capture the particles having a higher than anticipated out-of-plane component. When this happens, the reported velocities at the grid points where this may have occurred would have been the result of interpolations using lower values at neighboring grid points. As expected, the outer portion of the profiles are greatly different due to the higher wake velocity through the rotor disk in the 2 blade case.

Consider now a popular algebraic expression used to approximate the vortex profile (ref. 28),

$$v_\theta = \frac{\Gamma_*}{2\pi} \frac{r}{(r_c^{2n} + r^{2n})^{1/n}} \tag{6}$$

where Γ_* denotes the entire circulation for the vortex. To compare the above vortex model with the present data, it is assumed that Γ_* has been reached at twice the core radius (recall fig. 16). Focusing on data for the basic blade at $\psi = 100°$, it appears that the model (assuming $r_* = 2r_c$) is in fairly good agreement when n=2 (fig. 18), which is consistent with conclusions about this model reported in earlier studies (refs. 28 and 29).

Basic Blade Wake- The distribution of vorticity in the wake of the basic blade provides an immediate view of the convection path of the vortex during the first revolution of the blade (fig. 19). The strength of the vorticity carried by counter-clockwise rotating fluid, $\omega_z < 0$, is indicated by the level of blue saturation in the contour plot (with the trailing vortex being dominant), while vorticity of the opposite sense is represented by various levels of red saturation. Also included are markers locating the 5 highest neighboring values of vorticity on both extremes. These markers serve to expose the irregular complexion of the vorticity field as well as the migration of isolated concentrations of vorticity. The pattern shows the spiraling accumulation of vorticity from the blade wake toward the center of the vortex. The appearance of positive values of vorticity, $\omega_z > 0$, initially found along the inboard portion of the wake, are shed from the blade where the lift is increasing with blade radius.

The structure of the flow behind the basic blade at different wake ages is shown in figs. 20 - 27, and the more significant characteristics are summarized in fig. 28. The location of the center of vorticity appears to be quite random from blade revolution to revolution, with the extent of the wander increasing with wake age. The center of vorticity (based on the centroid of high values) is generally at a slightly different location than the center of swirl. The midpoint between the velocity peaks, based on either v vs. x or u vs. y profiles across the vortex, is generally not located at the center of swirl. As the vortex ages, the maximum values of vorticity and swirl velocity decrease while the core radius increases. Tracking the location of the trailing vortex based on the centers of swirl at each wake age, the rate of movement toward the rotor axis of rotation, u, decreases toward an asymptotic value while the rate of movement in the direction of the flow through the rotor disk, v, increases toward an asymptotic value.

More traditional displays of the vortex structure are fashioned in figs. 29 - 36 for the quantities v, w, and ω_z in terms of contour plots and cross sections through the center of the vortex. The dominant level of vorticity is clearly contained in the trailing vortex, however the peak value of ω_z is oftentimes not reached monotonically. The out-of-plane component of velocity, w, readily exposes the wake deficit, especially during the early wake ages ($\psi \leq 100°$). Maximum excursions in w appear to coincide with the peak circumferential velocity (as suggested by the profile for v) and are directed back toward the rotor blade (in keeping with the remainder of the wake deficit). Based on the above algebraic model for v_θ, it has been shown (ref. 28) that for $n = 2$ (which best fits the data) that w reaches peak values at about $0.76r_c$. A distinctive zone near the center of the vortex exists where w comes close to matching the velocity in the outer $1/r$ region.

In certain cases ($\psi = 10°$ and $30°$) contour plots show that w actually points in the opposite direction, coinciding with the direction of ω_z. It also appears that during the early stages of wake development ($\psi < 100°$) that the location of this region of "excess" w is offset from the centers of swirl and vorticity. Accompanying the display of the v profile are portrayals of the velocity relative to the movement of the vortex in the wake. If the objective is to obtain a more symmetric profile in the outer $1/r$ region (thereby rendering a Lagrangian-like appearance), then the construction based on the convection velocity ($v - v_c$, solid line, calculated using actual vortex locations) is much more satisfactory than the construction based on the velocity measured at the interior of the vortex ($v - v_i$, dashed line).

0° **Vortex Generator-** In contrast to the wake for the basic blade, a map of the vorticity field with the vortex generator attached and fixed at 0° reveals the presence of an additional zone of vorticity with the same sense as the primary vortex (fig. 37). In relation to the primary vortex, this smaller vortex persists as a distinct body of fluid for $\psi \leq 30°$ and appears to orbit the primary vortex at an angular rate of about 6° for every degree of wake age. Prior to the merging of these two vortices, features relating to the primary vortex are less certain due to distortions of the flow field caused by the proximity of the smaller vortex (figs. 38 - 45). This is supported by a theoretical study of two synthetic vortices which shows that the resulting swirling flow becomes very different as the vortices begin to overlap (ref. 30). A portion of the chordwise vorticity that normally would have gone immediately into the primary vortex may actually have been shed with that from the vortex generator. Later wake ages have the appearance of a single vortex, however they are more intense (magnitude of ω_z has increased and the core size has decreased) than those measured for the basic blade alone (fig. 46). Furthermore, this configuration yields an ultimate trailing vortex that has traveled a shorter distance (in both x and y) from the tip path traced by the basic blade alone, thereby increasing its interaction with the rotor blade during the next revolution. Contour plots and cross sections through the center of swirl for the quantities v, w, and ω_z are shown in figs. 47 - 54. When compared with the basic blade case, the ω_z profile shows that the primary vortex is initially weaker during the early stages of its development ($\psi \leq 30°$), but quickly increases in strength after the two vortices have merged (figs. 47 - 54). The w component of velocity appears to be generally weaker than for the basic blade, however, the shape of the profile is similar.

+5°,+10°,+15° **Vortex Generator-** The wake effects that result from swinging the trailing edge of the vortex generator toward the tip of the rotor blade are shown in figs. 55 - 108. These angles tend to produce tip vortices that have the same sign as that trailing from the tip of the rotor blade. As the lift on the vortex generator is increased, the tip vortex that it produces appears to orbit the primary trailing vortex more rapidly than in the 0° case and finally merge with the primary vortex at an earlier wake age (figs. 55, 73, 91). In each case, distortions in the v component of velocity occur during the early wake ages through $\psi = 30°$ (figs. 56 - 58, 74 - 76, 92 - 94). A noticeable jump in the peak magnitude of the ω_z profiles occurs at $\psi = 60°$, which coincides with the merging of these two vortices (both rotating in the same direction). Once the wake has reached $\psi = 60°$, all three configurations yield a single vortex with a higher peak ω_z and a smaller r_c than occurred for the basic blade alone (figs. 64, 82, 100). Placing the vortex generator at +5° and +10° causes the ultimate trailing vortex to travel farther away from the tip path plane (increased y) and with less contraction (decreased x) than for the basic blade case. The advantage at +5° and +10° of an increased separation distance from the rotor plane is not achieved at +15° possibly due to excessive flow separation from the generator at this high angle.

−5°,−10°,−15° **Vortex Generator-** The wake effects that result from swinging the trailing edge of the vortex generator away from the tip of the rotor blade are shown in figs. 109 - 160. These angles tend to produce tip vortices that have the opposite sign as that trailing from the tip of the rotor blade. Vorticity contours indicate that a secondary vortex does not clearly appear until the vortex generator is rotated to −15° (figs. 109, 127, 145). This would suggest that the local angle of incidence is different from the geometric angle of the generator, which is to be expected in light of the skewed direction of the approaching flow moving around the tip of the rotor blade. Although not obvious in the contour plots, there is a gradually increasing influence on the primary vortex as the generator angle is increased. This influence is evident in the comparatively flat appearance (which increases with the generator angle) on the left side of the v profiles from $\psi = 2°$ to $\psi = 30°$ (figs. 110 - 112, 128 - 130, 146 - 148). Although the sense of the secondary vortex is opposite that of the primary trailing vortex, it orbits the primary vortex in the same direction as in the positive vortex generator cases, but at half the angular rate. The wake eventually adjusts to the presence of the secondary vortex by forming a single vortex with a higher peak ω_z and a smaller r_c than occurred for the basic blade alone (figs. 118, 136, 153). Placing the vortex generator at −5° causes the ultimate trailing vortex to travel farther away from the tip path plane (increased y) and with less contraction (decreased x) than for the basic blade case. The vortex in the −15° case also travels farther away from the tip path plane, but now the contraction is increased as well. This combination of movements places the vortex even farther away from the trace of the rotor tip.

Free Vortex Generator- Assuming that the center of gravity is located on the pitch axis, the angle of this element is free to respond only to local flow conditions. Recalling the previous results with and without a vortex generator, a review of the contour maps and cross sectional plots suggests that this case is unique (figs. 161 - 178). There is no evidence of a secondary vortex present in the contour maps (fig. 161), nor are there any distortions in the v profiles during the early stages of wake development (figs. 162 - 164) comparable to those observed when the generator was placed at fixed angles. However, the initial vorticity field defining the trailing vortex does have an annular appearance similar to the negative generator cases, but remains less focused for a longer period of time (fig. 161). This may explain why the magnitude of the peak vorticity and the maximum swirl velocity are noticeably reduced during the early wake ages (fig. 170). The trailing vortex in this case has moved a shorter distance from the tip path of the rotor as compared to the basic blade case.

Turbulence Generator- Although this element was oriented normal to the blade surface and intended to function much like a spoiler, the local flow may have recognized it as being more like a flat plate at high incidence (and therefore a source of lift). Reference to the preceding vortex generator cases will help to understand the unusual results for this configuration (figs. 179 - 196). The contour maps of vorticity (fig. 179) show that after the trailing vortex has been initially distorted by the turbulence generator, it remains distributed over a much larger spatial region than was observed for all other cases. There does appear to be a neighboring zone of positive vorticity at $\psi = 2°$ and $\psi = 10°$ (similar to that observed in the $-15°$ generator case), and is undoubtedly the result of lift on this element. In keeping with the broadened footprint of the resulting trailing vortex, the corresponding peak velocity and vorticity excursions are substantially reduced (fig. 188). The wake contraction and its convection away from the rotor plane are both less than observed for the blade alone case.

Overview- The merits of each configuration are summarized in terms of vortex strength and location. Tables 4 (near field) and 5 (far field) indicate how these quantities have changed relative to the basic blade. The value of the near-field results may become more important as the spacing between the rotor blades is reduced.

△	quantity increases compared to basic blade
▽	quantity decreases compared to basic blade
○	no significance difference

Table 4: Near Field ($\psi = 30°$)

Config	$Max\ -\omega_z$	$Max\ v_\theta$	r_c	x	y
Free VG	▽	▽	△	○	○
−15° VG	△	△	○	○	○
−10° VG	△	△	▽	○	○
−5° VG	○	○	○	○	○
0° VG	△	○	▽	○	○
+5° VG	○	▽	○	○	○
+10° VG	○	▽	○	○	▽
+15° VG	▽	▽	○	○	▽
90° TG	▽	▽	△	○	▽

Table 5: Far Field ($\psi = 280°$)

Config	$Max\ -\omega_z$	$Max\ v_\theta$	r_c	x	y
Free VG	△	▽	▽	○	▽
−15° VG	△	▽	▽	△	△
−10° VG	△	△	▽	△	○
−5° VG	△	△	▽	▽	△
0° VG	△	△	▽	○	▽
+5° VG	△	△	▽	▽	△
+10° VG	△	△	▽	▽	△
+15° VG	△	△	▽	▽	▽
90° TG	▽	▽	△	▽	▽

In terms of reducing the strength of the trailing vortex in the near field ($\psi = 30°$), the free vortex generator and the turbulence generator are clearly superior to the other configurations. However, in the far field ($\psi = 280°$), only the turbulence generator provides a sustained reduction in vortex strength. In terms of increasing the displacement of the trailing vortex from the path of the rotor tip, none of the configurations studied satisfies this requirement in the near field. On the other hand, a few cases suggest some benefit in the far field, either in terms of a greater contraction or a greater convection away from the rotor plane. The convection velocity, along with the size and location of the trailing vortex, are summarized for all cases at $\psi = 280°$ in figure 197. Relative to the location of the trailing vortex from the basic blade, vortices from all other configurations remain somewhat clustered nearby and with a maximum separation of about one core diameter (or about one blade thickness).

CONCLUSIONS

1. A robust procedure was developed for analyzing a vortex dominated flow field, extracting its principal features, and performing a conditional ensemble average that accounts for vortex wander. Conditional averaging is necessary in order to preserve the intensity and size of the vortex.

2. In vortex flows, the highest out-of-plane velocities often occur where the circumferential velocity is highest. When the delay time between PIV pulses is too long, interpolations will render in-plane peak velocities that are too low. As a result, the vortex will appear weaker due to a reduced circumferential velocity and an enlarged core size.

3. The torque produced at 870 RPM in all of the vortex generator cases where the angle was fixed was lower (up to 6%) than for the basic blade alone. However, there was an 8% increase in torque in the free (unrestrained) vortex generator case and an 18% increase in the turbulence generator case.

4. The peak value of vorticity generally occurs close to the center of swirl. For the basic blade, the

component of velocity that is aligned with the axis of the vortex (the out-of-plane component, w, in this study) has a somewhat annular shape, but is offset from the center of swirl. Peak values of w are directed back toward the rotor blade and are roughly associated with the core diameter defined by the peak circumferential velocity, v_θ. In some cases, the flow in the center of this annular region may be pointed in the opposite direction (away from the rotor). During the initial 280° of azimuth the diameter of the vortex core increases from about 1.2 to 1.5 times the thickness of the rotor blade.

5. A vortex trailing from a vortex generator with a fixed angle will orbit the primary tip vortex at an angular rate of about 6° for every degree of wake age when the two vortices have the same sense. When the subordinate vortex has the opposite sense, the direction of the orbit remains the same, but the angular rate is greatly reduced. In both cases the subordinate vortex cannot be distinguished from the primary vortex after $\psi = 60°$, and eventually, a more intense primary vortex is produced. As the angle of the vortex generator becomes more negative (producing a stronger counter-rotating vortex), the annular shape of the w component of velocity becomes more pronounced as the magnitude of the flow in the interior increases in the direction of the rotor.

6. When the vortex generator is unrestrained, the strength of the primary vortex during the initial wake ages is significantly reduced. Unlike most of the vortex generator cases at fixed angles, this case shows no evidence of a subordinate trailing vortex. Although the advantages in terms of maximum vorticity and core radius are diminished after reaching $\psi = 280°$, the maximum swirl velocity remains lower for all wake ages.

7. The most dramatic changes occurred in the turbulence generator case. The absence of an annular shape and the significant reduction in vortex intensity suggest the effectiveness of the turbulent action toward homogenizing the flow inside the trailing vortex and contributing to its rapid diffusion. Although the torque increased by 18%, the maximum vorticity was reduced by 65%, the maximum swirl velocity was reduced by 57%, and the core size almost doubled after reaching $\psi = 280°$.

8. All of the configurations had some effect on the final position of the trailing vortex, with the greatest departure from the basic blade case being about one blade thickness farther away from the trace of the rotor tip.

REFERENCES

[1] Beesten, B. M. J.: Influence of Non-Planar Blade Tips on Rotor Performance. 18th European Rotorcraft Forum, Paper No. 73, Avignon, France, 1992.

[2] Müller, R. H. G.: Special Vortices at a Helicopter Rotor Blade. Journal of the American Helicopter Society, Vol. 35, (4), 1990.

[3] Splettstößer, W. R.; Kube, R.; Seelhorst, U.; Wagner, W.; Boutier, A.; Michali, F.; Mercker, E.; and Pengel, K.: Key Results from a Higher Harmonic Control Aeroacoustic Rotor Test (HART) in the German-Dutch Wind Tunnel. Presented at the 21st European Rotorcraft Forum, St. Petersburg, Russia, 1995.

[4] Dawson, S.; Straub, F.; Hassan, A.; Tadghighi, H.; Marcolini, M.; Booth, E.; and Kelly, H.: Wind Tunnel Test of an Active Flap Rotor: BVI Noise and Vibration Reduction. Presented at American Helicopter Society 51st National Florum, Fort Worth, TX, 1995.

[5] Jacklin, S. A.; and Nguyen, K.: Full Scale Wind Tunnel Test of a Helicopter Individual Blade Control System. Presented at American Helicopter Society 50th National Forum, Washington D.C., 1994.

[6] Rorke, J. B.; and Moffitt, R. C.: Wind Tunnel Simulation of Full Scale Vortices. 28th Annual National Forum of the American Helicopter Society, Washington, D. C., 1972.

[7] Landgrebe, A. J.; and Bellinger, E. D.: Experimental Investigation of Model Variable-Geometry and Ogee Tip Rotors. 29th Annual National Forum of the American Helicopter Society, Washington, D. C., 1973.

[8] Smith, D.: Helicopter Rotor Tip Shapes for Reduced Blade Vortex Interaction an Experimental Investigation. 33rd Aerospace Sciences Meeting and Exhibit, AIAA 95-0192, Reno, NV, 1995.

[9] Corsiglia, V. R.; Jacobsen, R. A.; and Chigier, N.: An Experimental Investigation of Trailing Vortices Behind a Wing with a Vortex Dissipator. Aircraft Wake Turbulence and Its Detection. Plenum Press, 1971.

[10] Rossow, V. J.: Lift-Generated Vortex Wakes of Subsonic Transport Aircraft. Progress in Aerospace Sciences, Vol. 35, (6), 1999.

[11] Tangler, J. L.: The Design and Testing of a Tip to Reduce Blade Slap. Presented at American Helicopter Society 31st National Forum, Washington D.C., 1975.

[12] Tangler, J. L.: Experimental Investigation of the Subwing Tip and Its Vortex Structure. NASA CR-3058, 1978.

[13] Lau, B. H.; Wadcock, A. J.; and Heineck, J. T.: Wake Visualization of a Full-Scale Tilt Rotor in Hover. American Helicopter Society Techni-

cal Specialists' Meeting for Rotorcraft Acoustics and Aerodynamics, Williamsburg, VA, 1997.

[14] Carlin, G.; Dadone, L.; and Spencer, R.: Results of an Experimental Investigation of Blade Tip Vortex Modification Devices. NASA CR-181853, 1989.

[15] Carlin, G.; Dadone, L.; Sternfeld, H.; Ziegenbein, P.: Results of a Powered Model Wind Tunnel Test of Helicopter Rotor Blade Vortex Alleviation Devices. NASA CR-181969, 1990.

[16] Meadowcroft, T.; Dadone, L.; and Sternfeld, H.: Advanced Concepts for Rotorcraft Noise Reduction due to Blade-Vortex Interaction by Vortex Alleviation Devices. NASA CR-189626, 1992.

[17] McAlister, K. W.; Tung, C.; Sharpe, D. L.; Huang, S.; and Hendley, E. M.: Preliminary Study of a Model Rotor in Descent. NASA TM-2000-208785, 2000.

[18] McAlister, K. W.; Takahashi, R. K.: NACA 0015 Wing Pressure and Trailing Vortex Measurements. NASA TP-3151, 1991.

[19] Heineck, J. T.; Yamauchi, G. K.; Wadcock, A. J.; Lourenco, L.; and Abrego, A. I.: Application of Three-Component PIV to a Hovering Rotor Wake. Presented at the American Helicopter Society 56th Annual Forum, Virginia Beach, VA, 2000.

[20] McAlister, K. W.: Measurements in the Near Wake of a Hovering Rotor. Presented at 27th AIAA Fluid Dynamics Conference, New Orleans, LA, 1996.

[21] Lourenco, L. M.: Particle Image Velocimetry. von Karman Institute for Fluid Dynamics, Lecture Series on Particle Image Velocimetry, 1996.

[22] Arroyo, M. P.; and Greated, C. A.: Stereoscopic Particle Image Velocimetry. Measurement Science and Technology, 2, 1991.

[23] Prassad, A. K.; and Jensen, K.: Scheimpflug Stereocamera for Particle Image Velocimetry in Liquid Flows. Applied Optics, 34:7092-9, 1995.

[24] Lourenco, L.: Mesh-Free Second-Order Accurate Algorithm for PIV Processing. Proceedings of VSJ-SPIE98, Paper AB079, Yokohama, Japan, 1998.

[25] Raffel, M.; Willert, C.; and Kompenhans, J.: Particle Image Velocimetry, Springer-Verlag, 1998.

[26] Westerweel, J.: Theoretical Analysis of the Measurement Precision and Reliability in PIV. Proceedings of the Third International Workshop on PIV'99, 1999.

[27] Leishman, J. G.: Measurements of the Aperiodic Wake of a Hovering Rotor. Experiments in Fluids, Vol. 25, (4), 1998.

[28] Vatistas, G. H.; Kozel, V.; and Mih, W. C.: A Simpler Model for Concentrated Vortices. Technical Notes, Experiments in Fluids, Vol. 11, No. 1, 1991.

[29] Bhagwat, M. J.; and Leishman, J. G.: On the Relationship Between Blade Circulation and Tip Vortex Characteristics. Presented at the 54th Annual Forum of the AHS, Washington DC, 1998.

[30] Strawn, R. C.; Kenwright, D. N.; and Ahmad, J.: Computer Visualization of Vortex Wake Systems. Presented at the 56th Annual Forum of the AHS, Alexandria, VA, 1998.

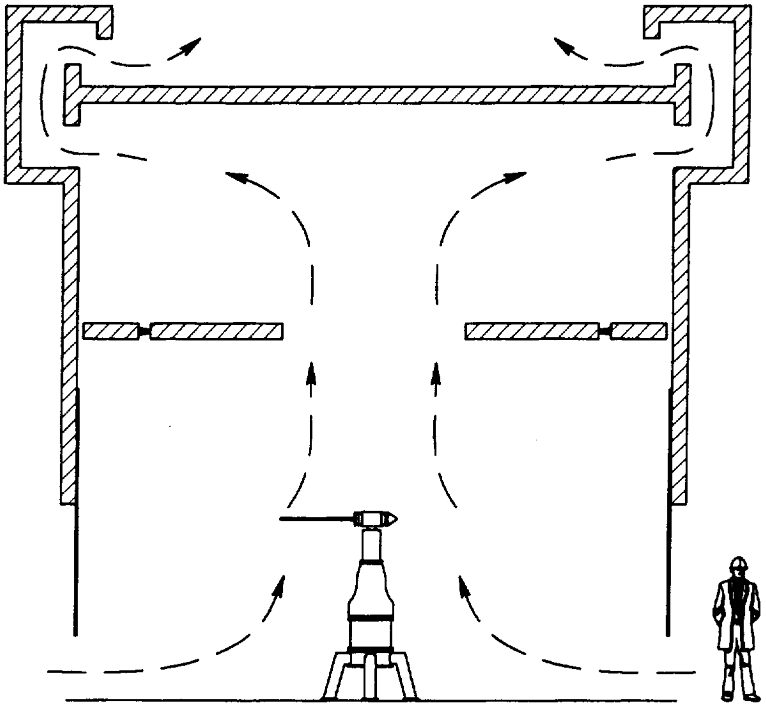

Figure 1: Hover Test Chamber with single-bladed rotor at Ames Research Center.

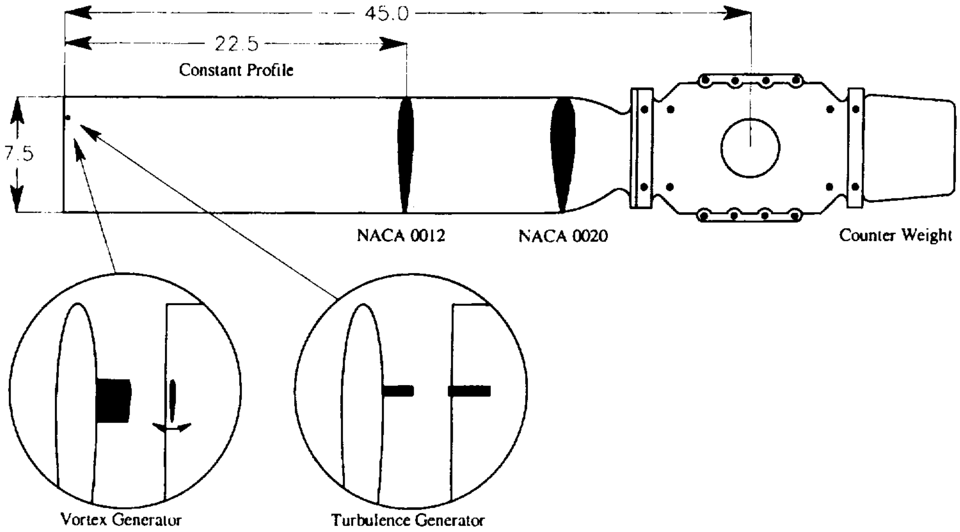

Figure 2: Single-bladed rotor configuration showing location of tip mounted devices.

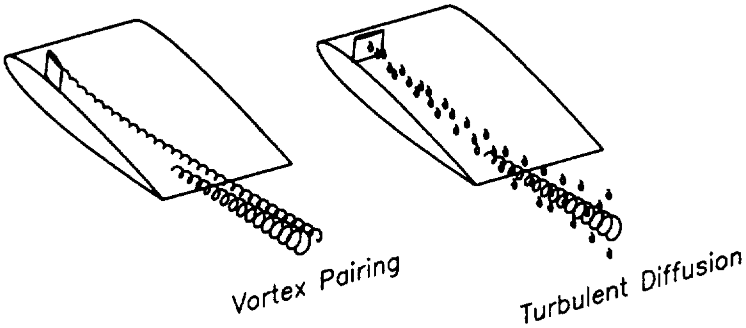

Figure 3: Concepts studied for altering the trailing vortex.

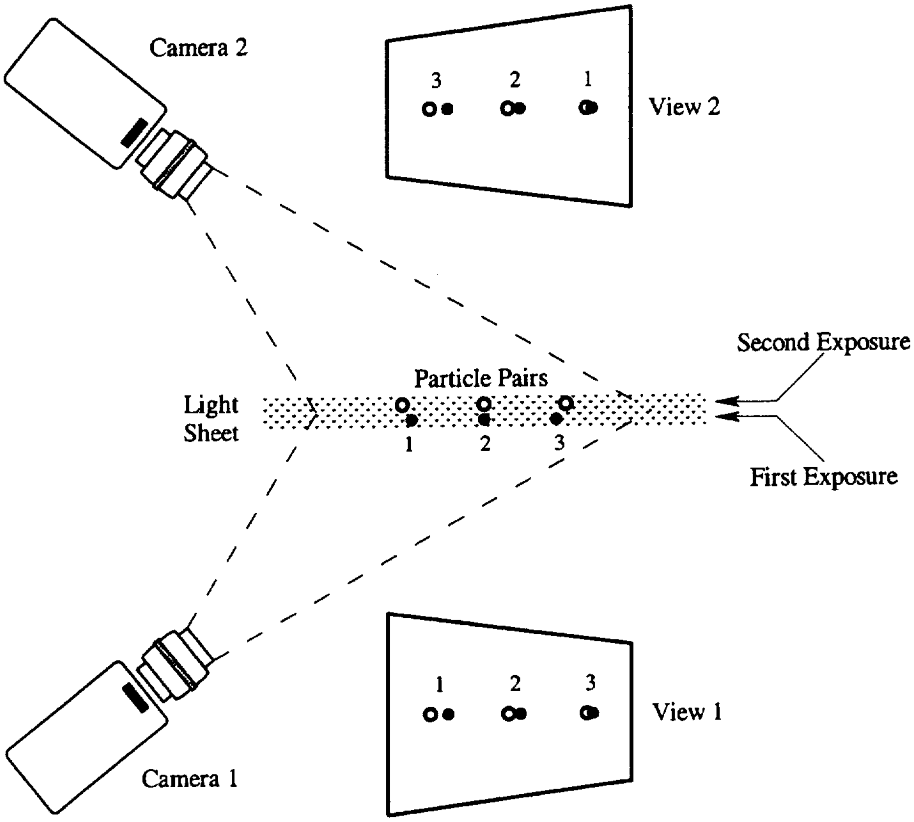

Figure 4: Perspective effect of particle displacement with Stereoscopic PIV.

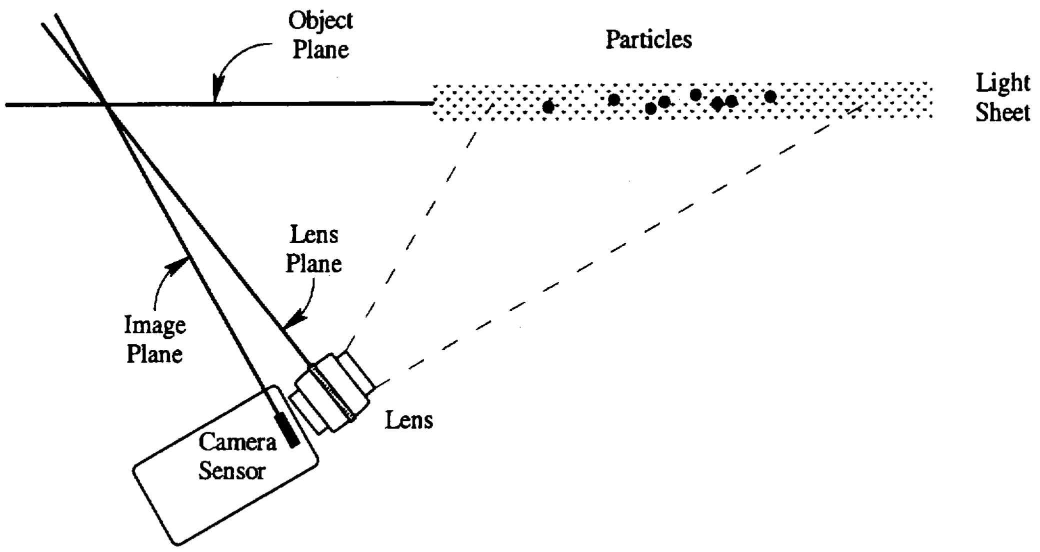

Figure 5: Scheimpflug condition for maintaining image focus.

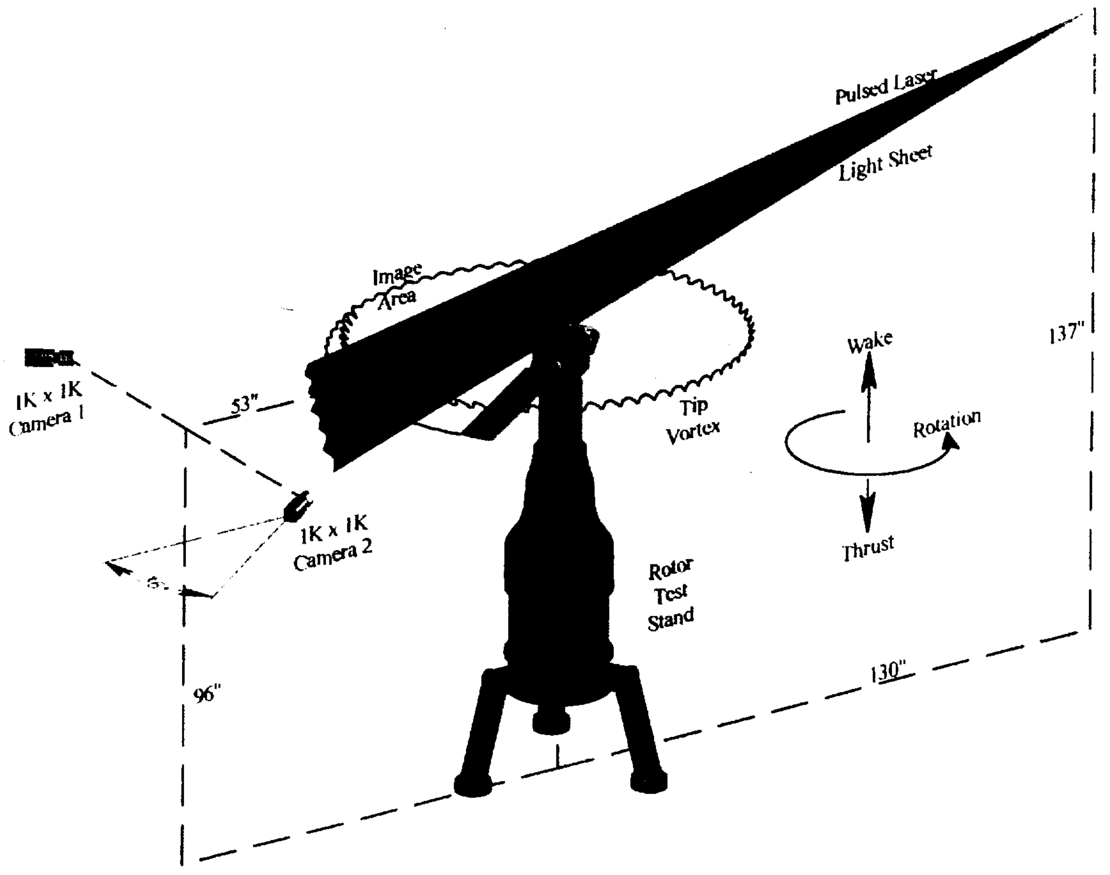

Figure 6: Setup of light sheet and cameras relative to rotor.

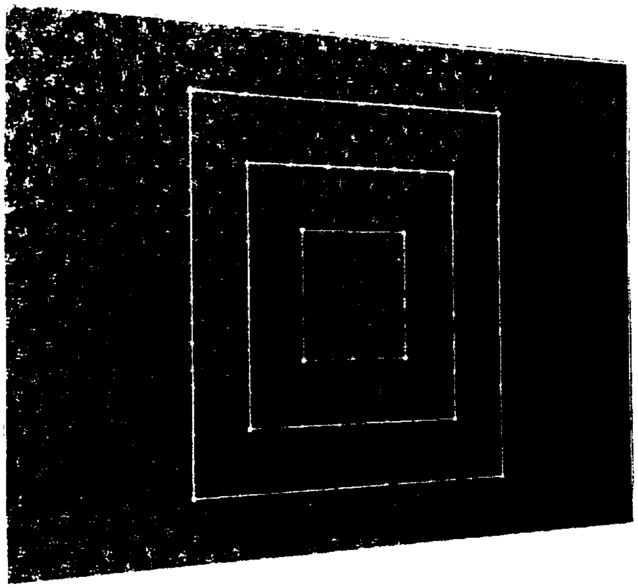

Figure 7: In-situ calibration target as viewed by camera 2.

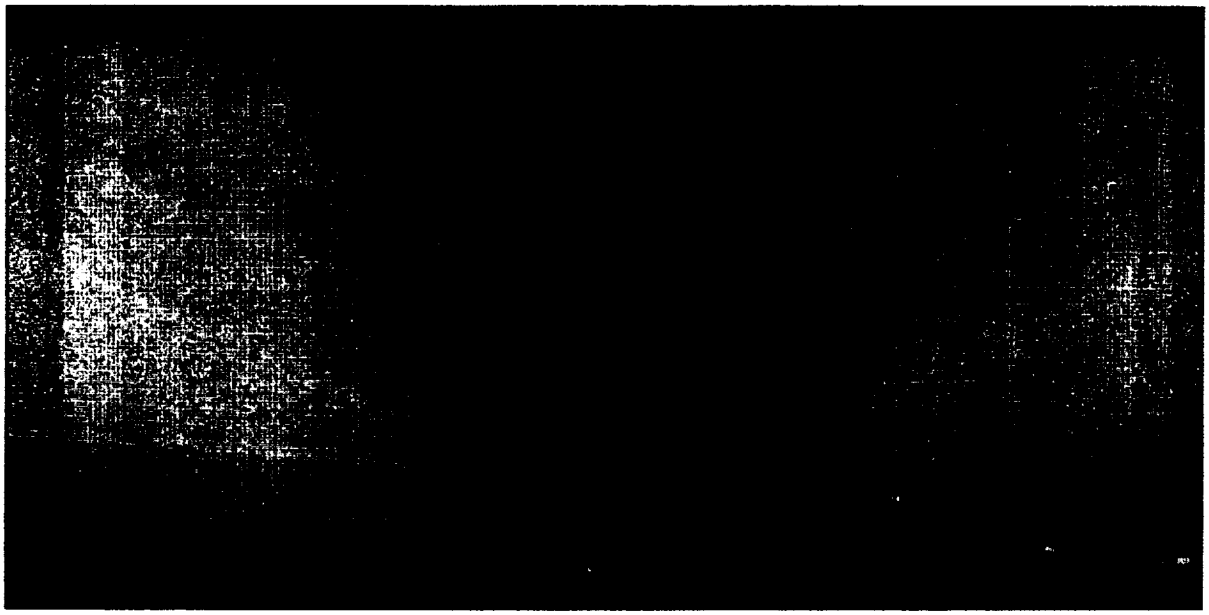

Figure 8: Example of image pair with calculation grid.

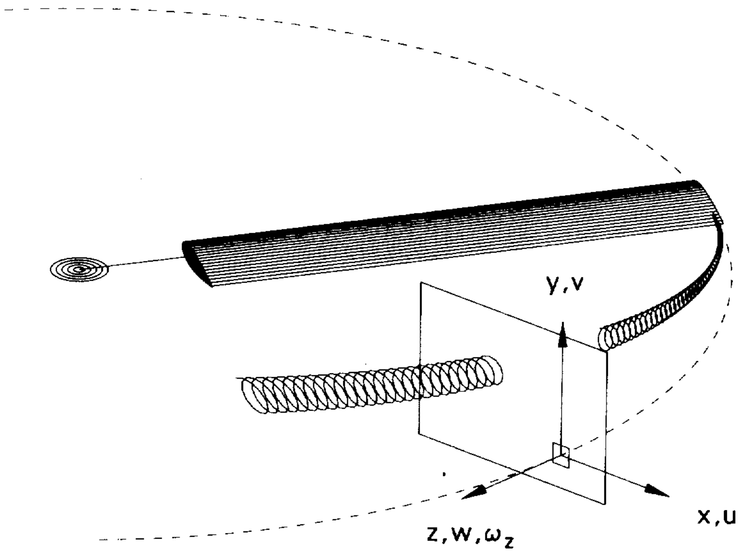

Figure 9: Definition of coordinate system showing origin on rotor-tip path.

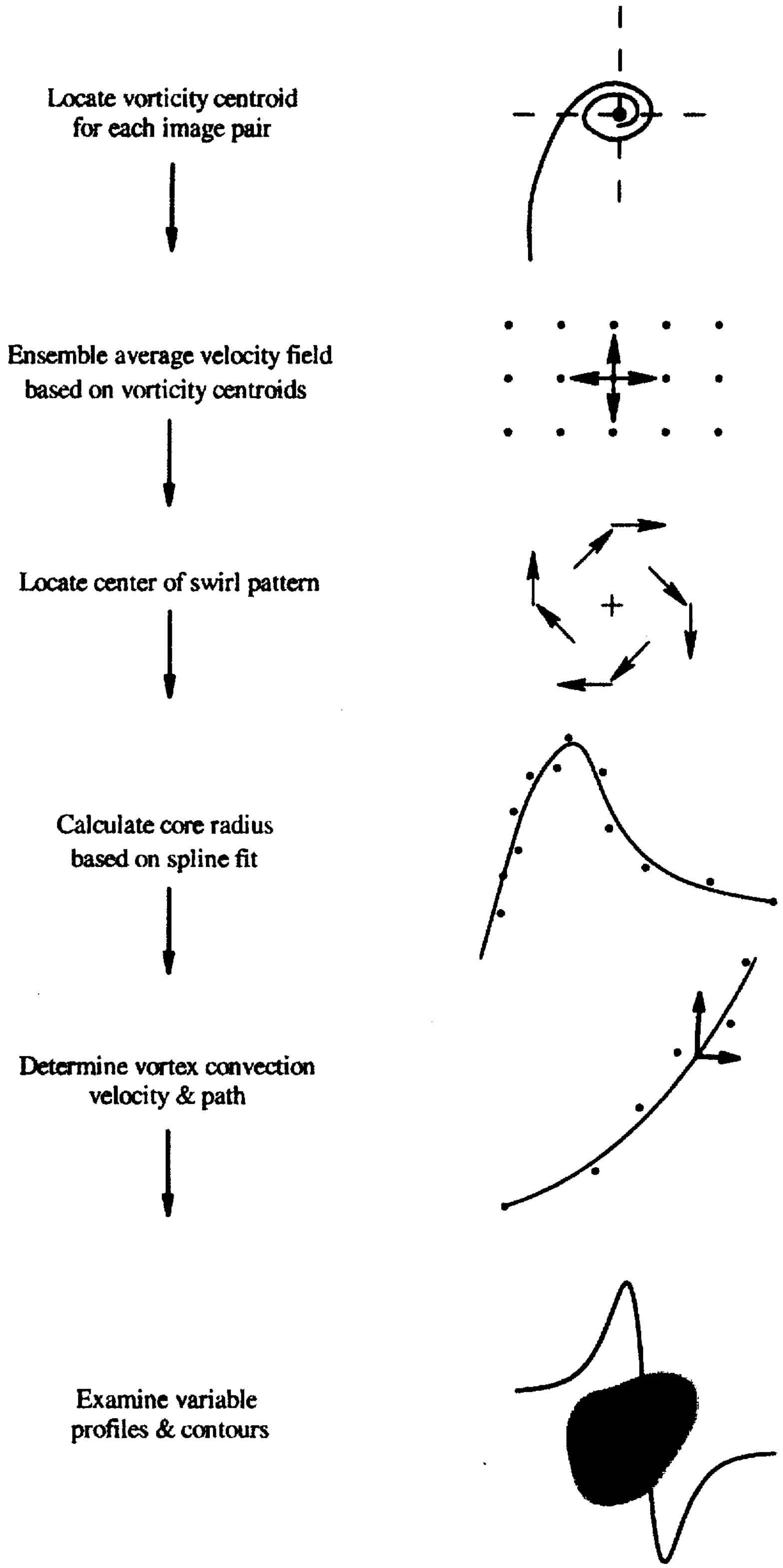

Figure 10: Analysis sequence for extracting trailing vortex characteristics.

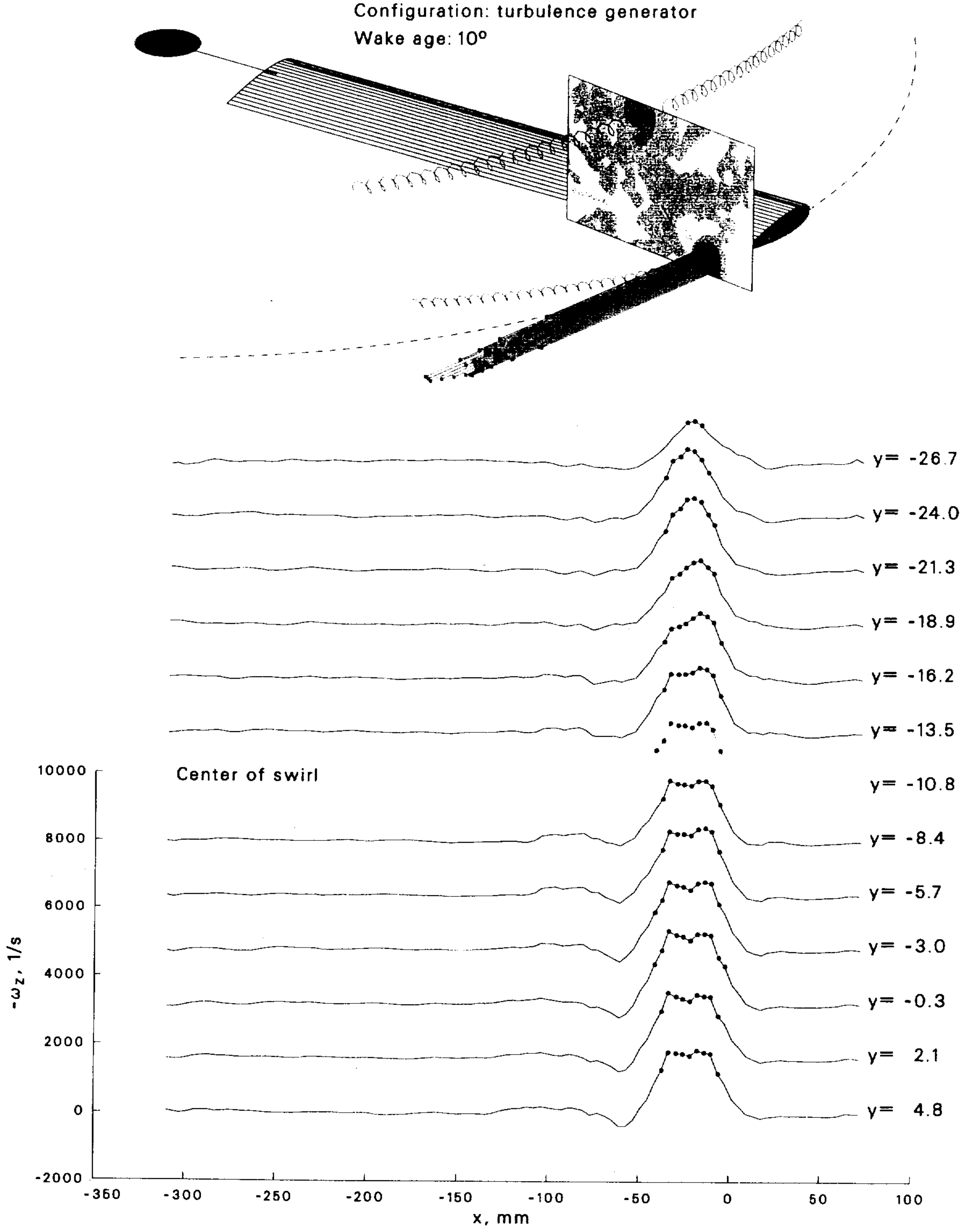

Figure 11: Example search for vorticity exceeding 50% of the maximum value.

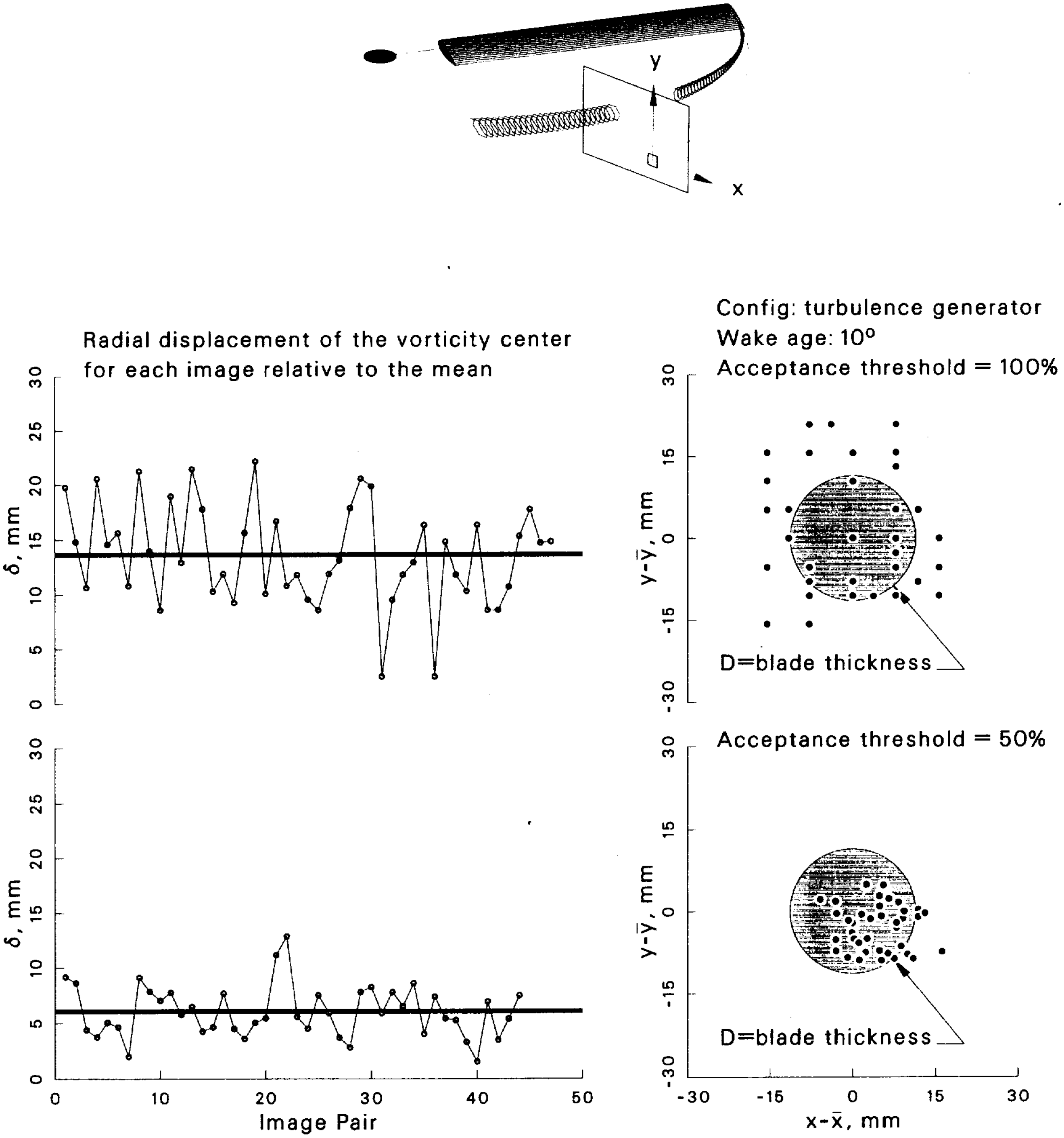

Figure 12: Effect of vorticity acceptance threshold on apparent vortex wander.

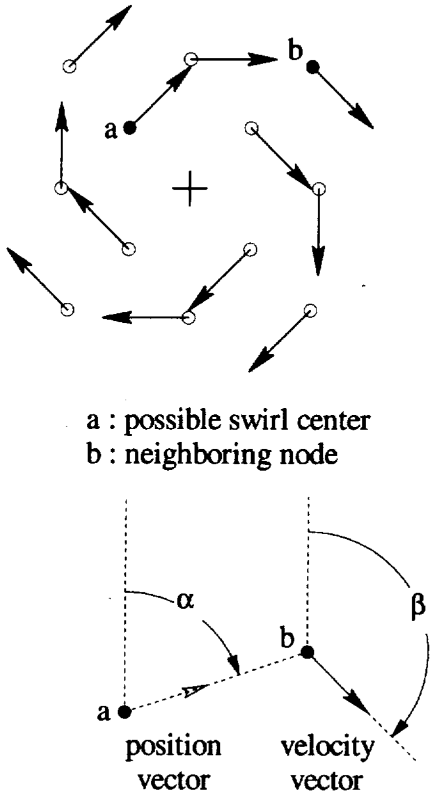

Figure 13: Angles used in the search for the center of swirl.

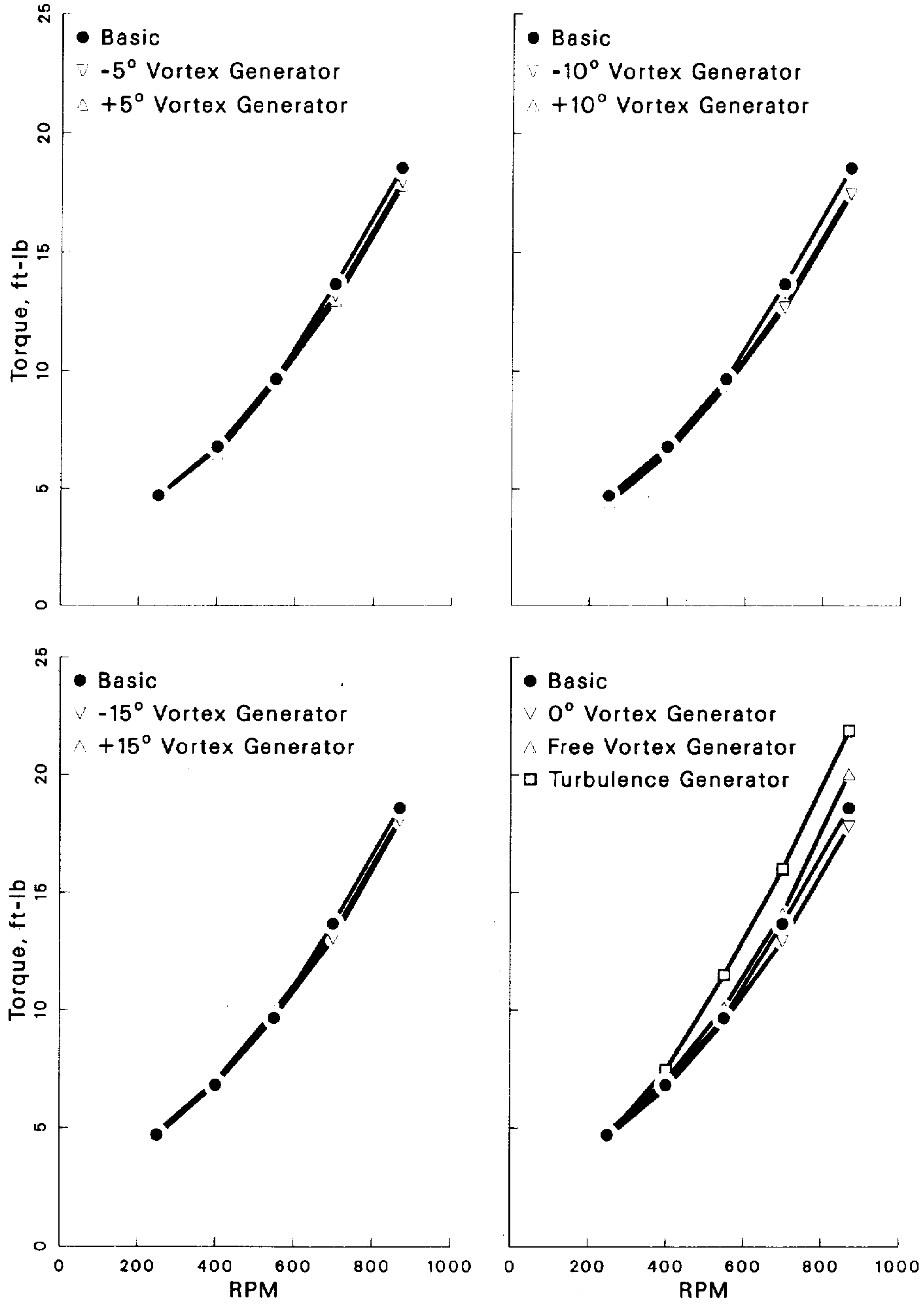

Figure 14: Rotor torque resulting from vortex generator and turbulence generator.

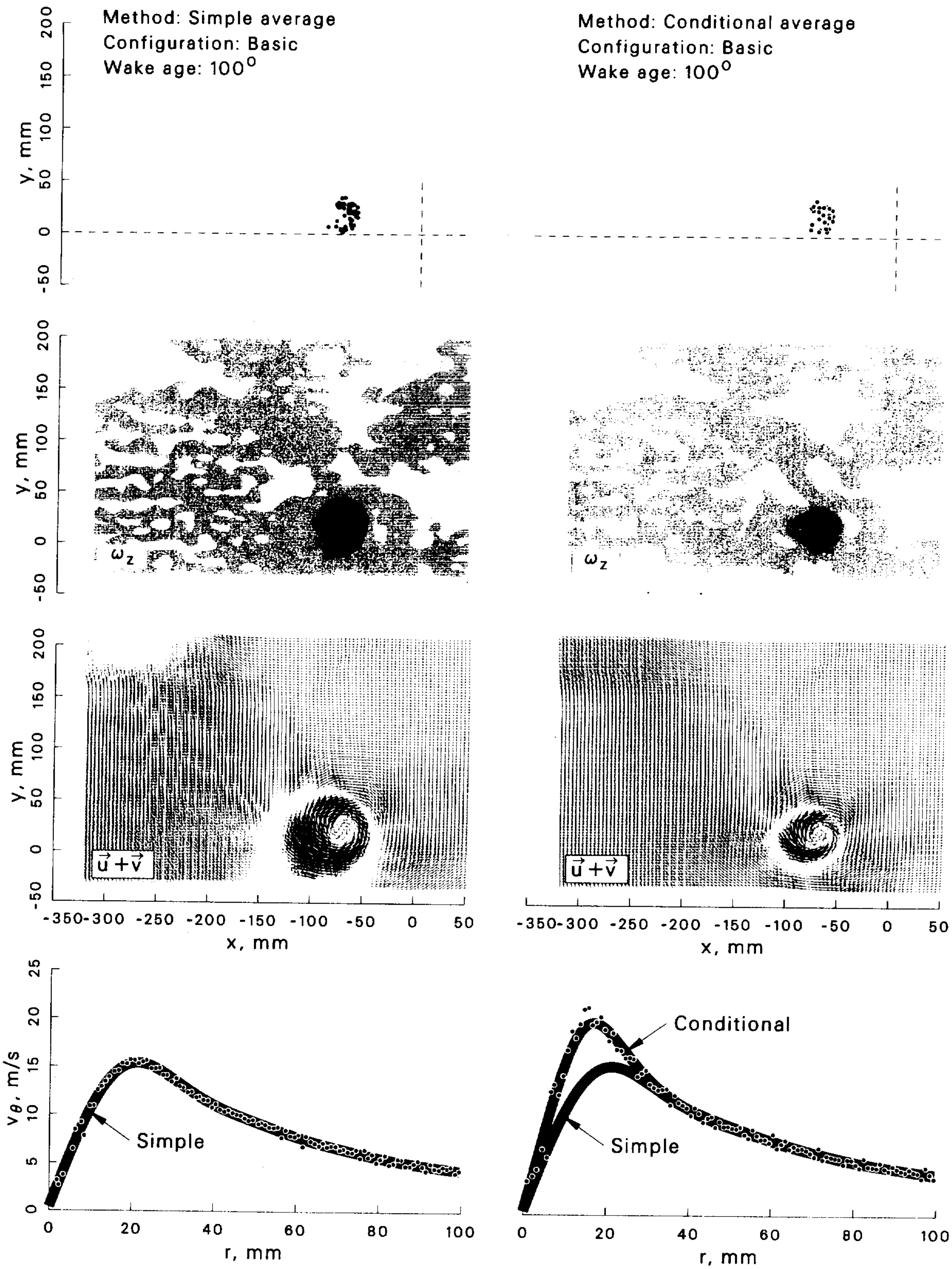

Figure 15: Conditional ensemble average compared to simple average.

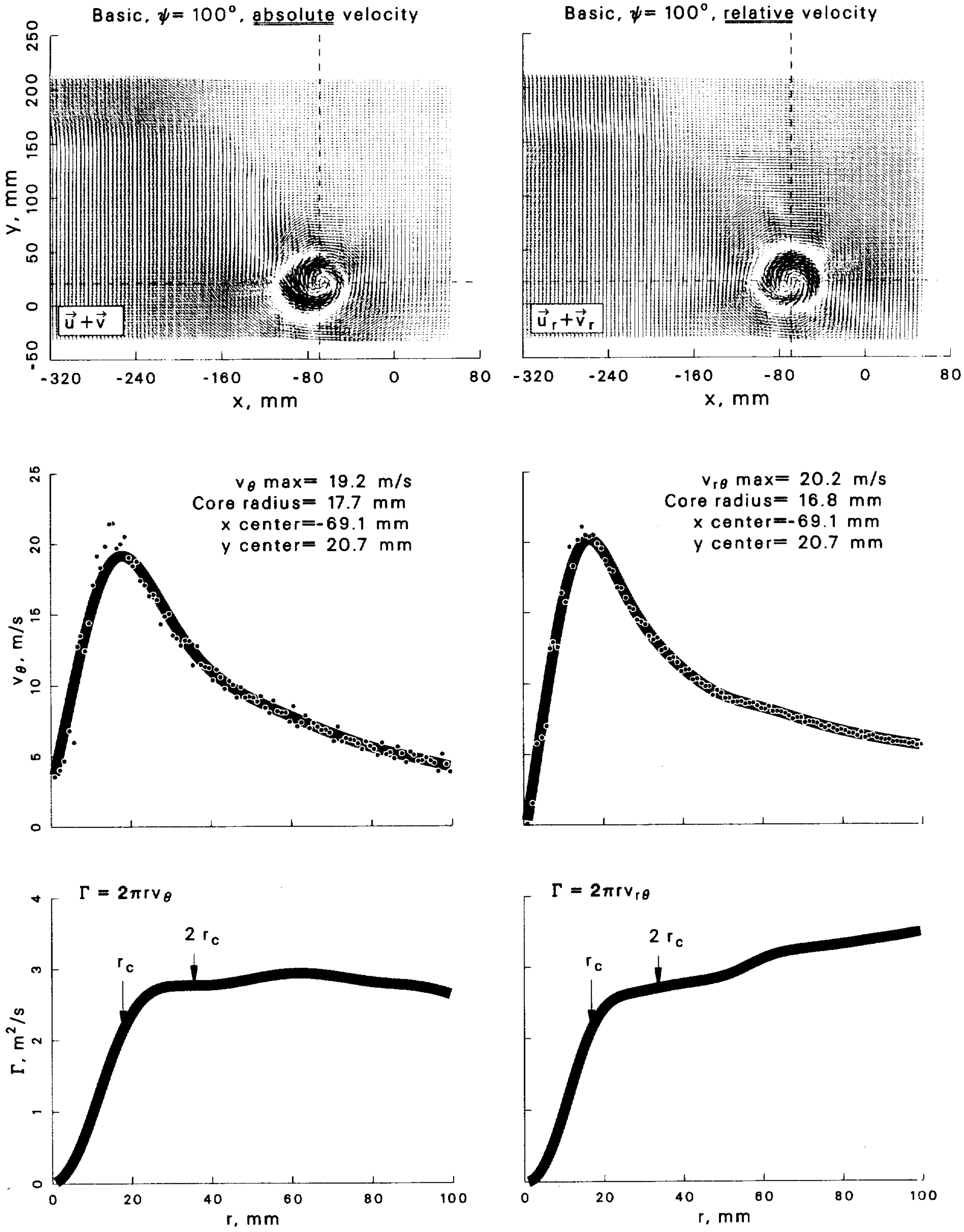

Figure 16: Effect of vortex convection on local circulation.

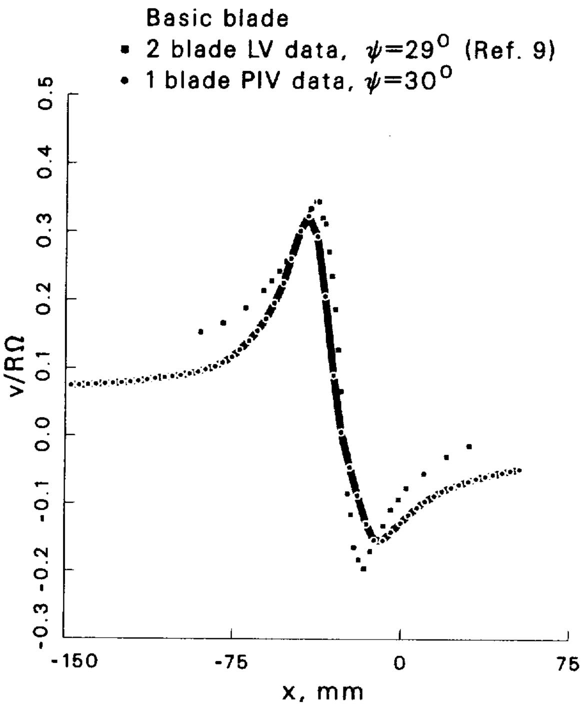

Figure 17: Comparison with LV data obtained in an earlier experiment (ref. 9).

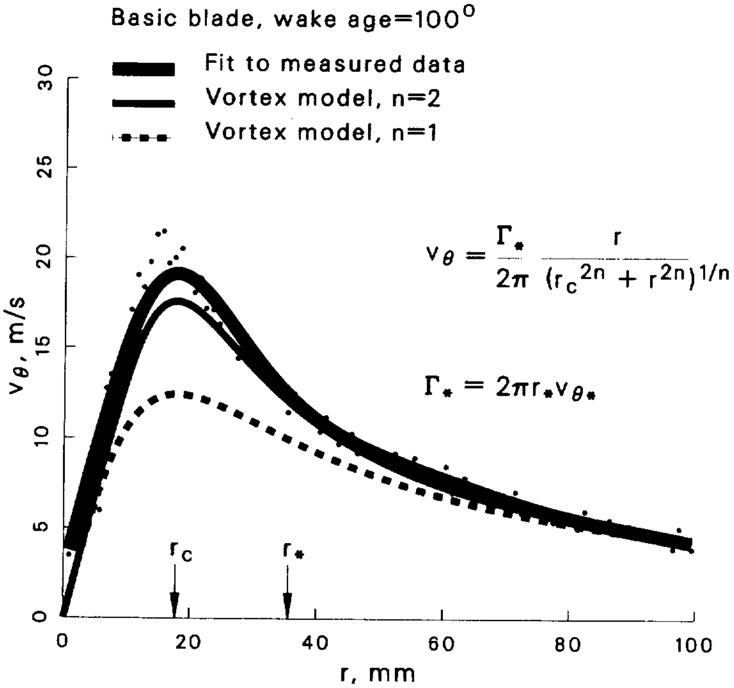

Figure 18: Comparison with algebraic models of vortex.

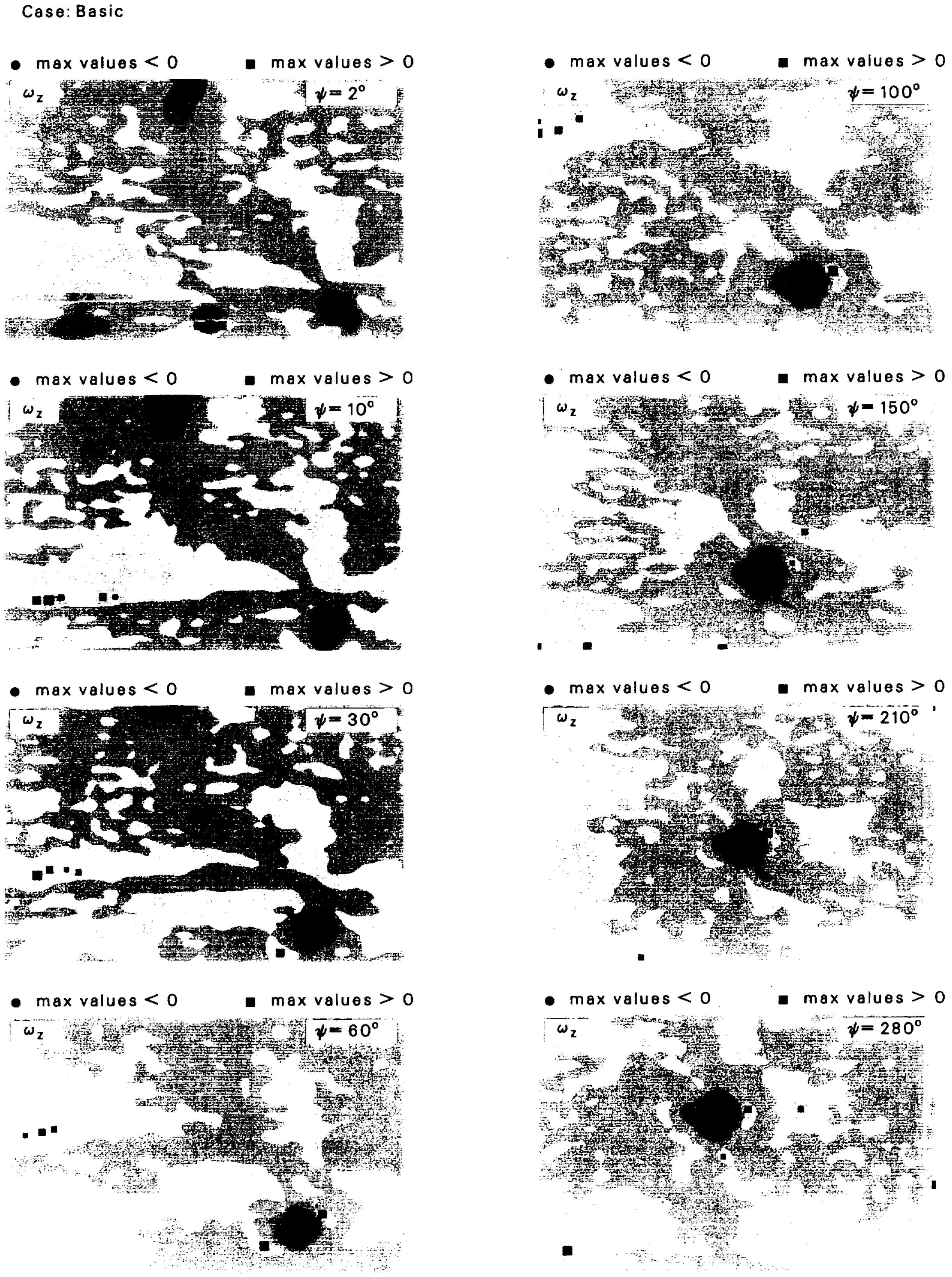

Figure 19: Locations of ω_z extrema at $\psi = 2^\circ \rightarrow 280^\circ$ for the basic blade case.

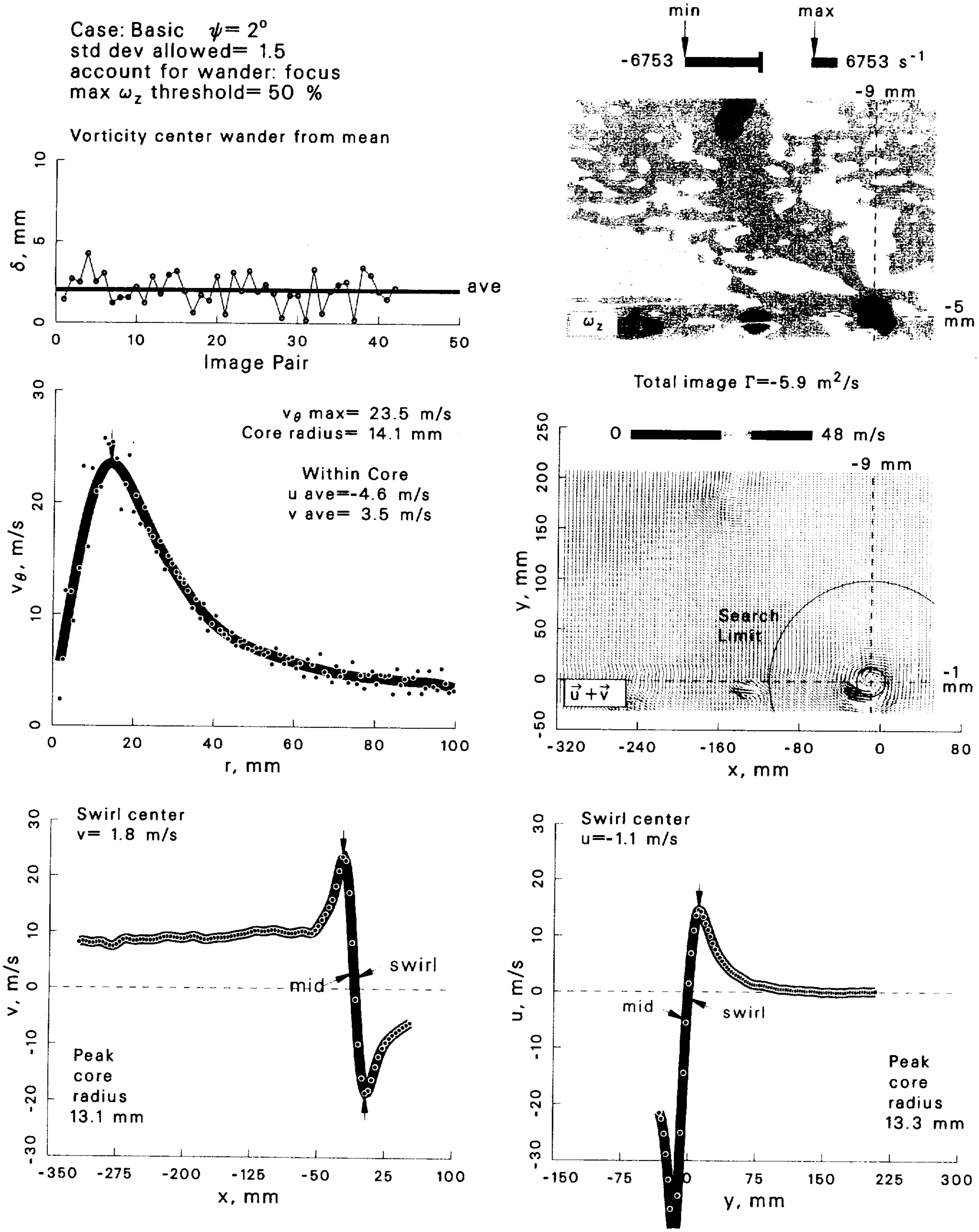

Figure 20: Vortex statistics at $\psi = 2°$ for the basic blade case.

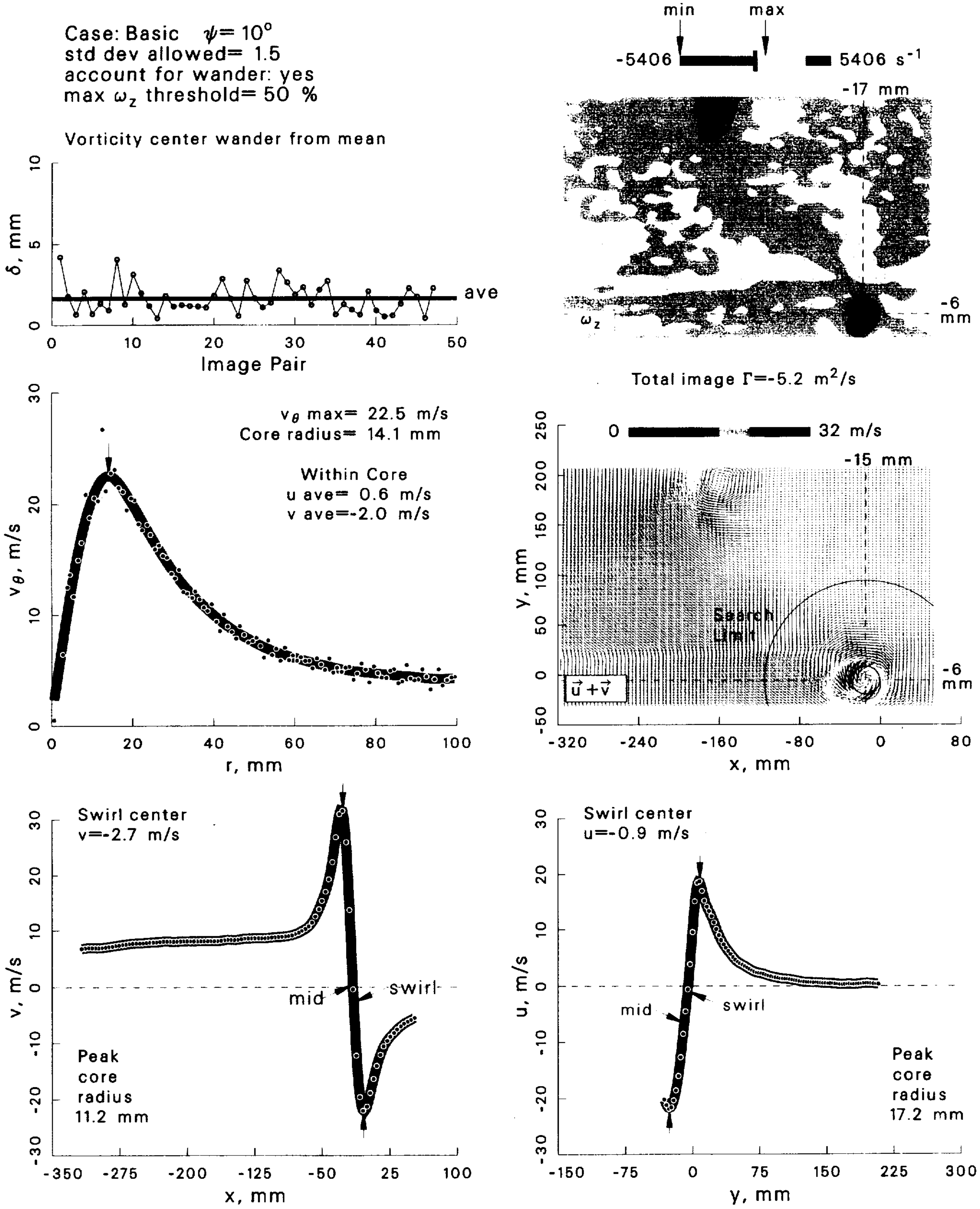

Figure 21: Vortex statistics at $\psi = 10°$ for the basic blade case.

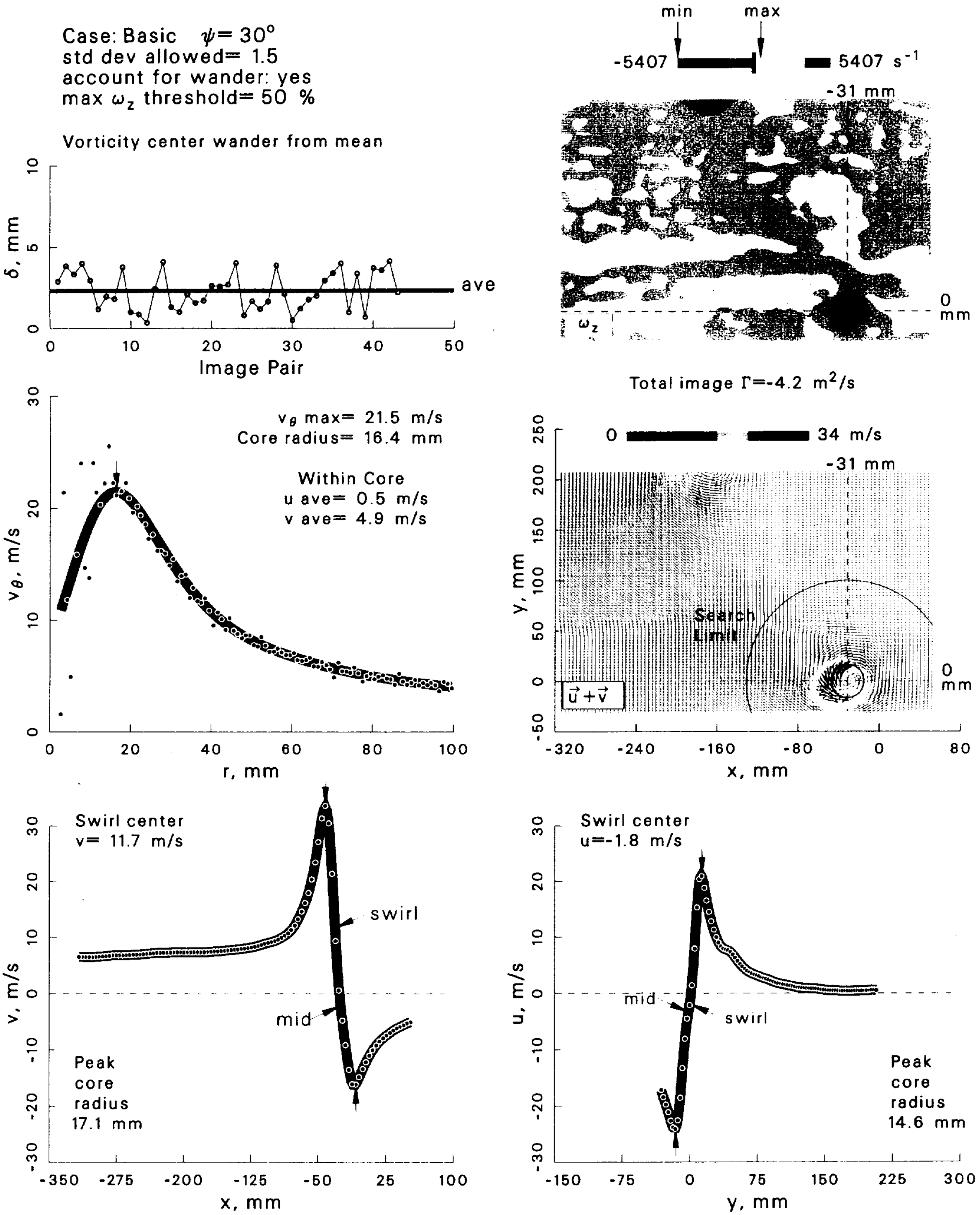

Figure 22: Vortex statistics at $\psi = 30°$ for the basic blade case.

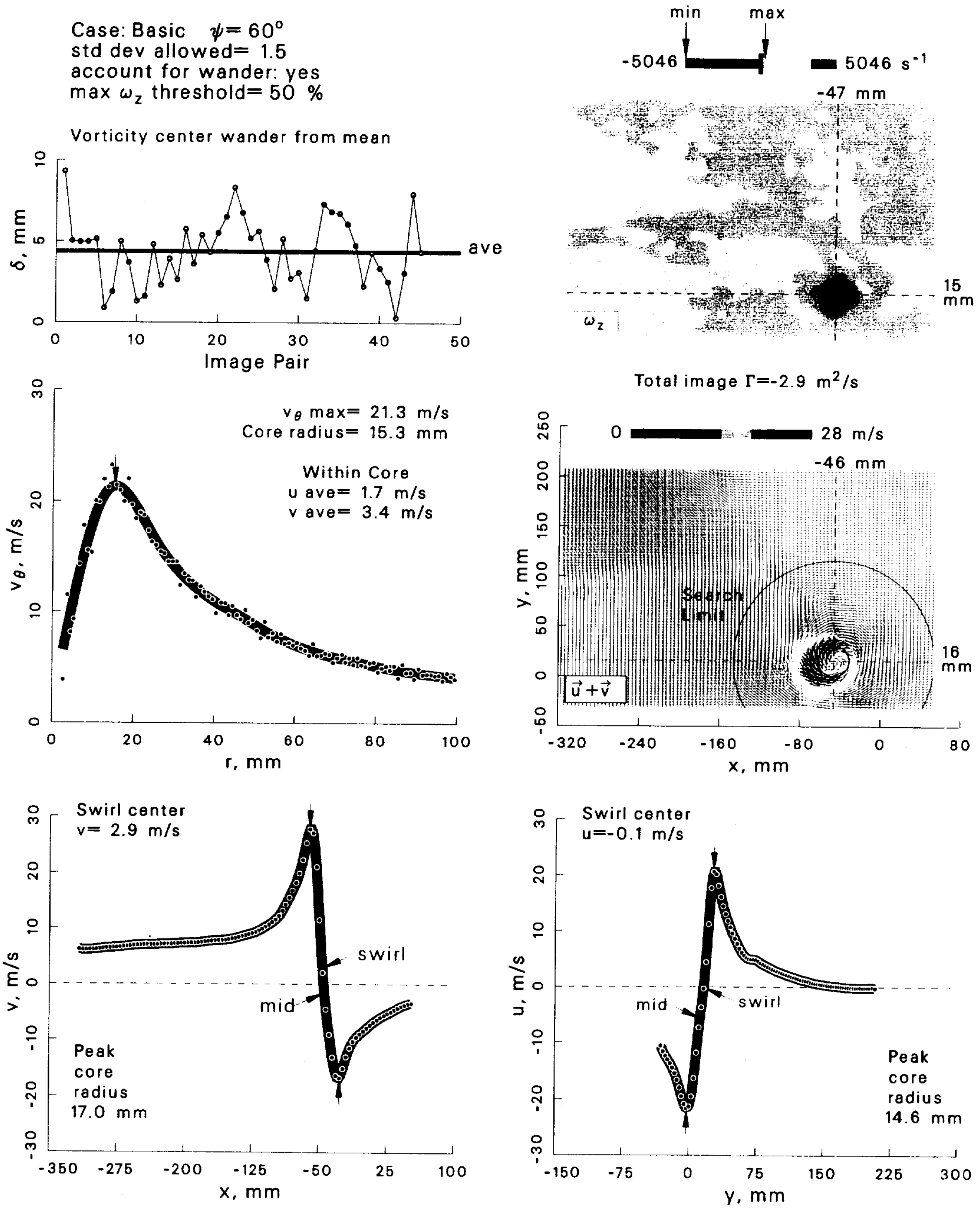

Figure 23: Vortex statistics at $\psi = 60°$ for the basic blade case.

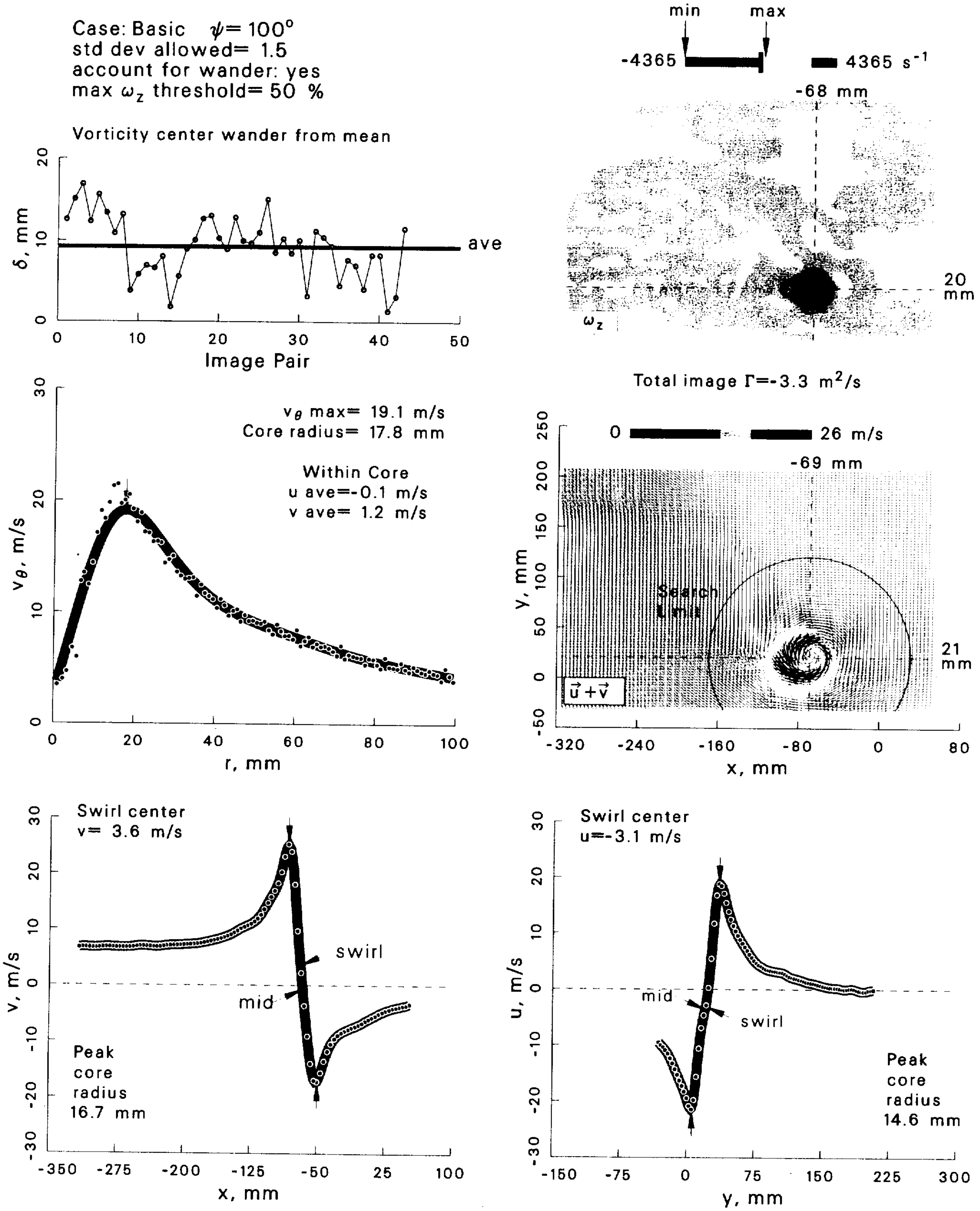

Figure 24: Vortex statistics at $\psi = 100°$ for the basic blade case.

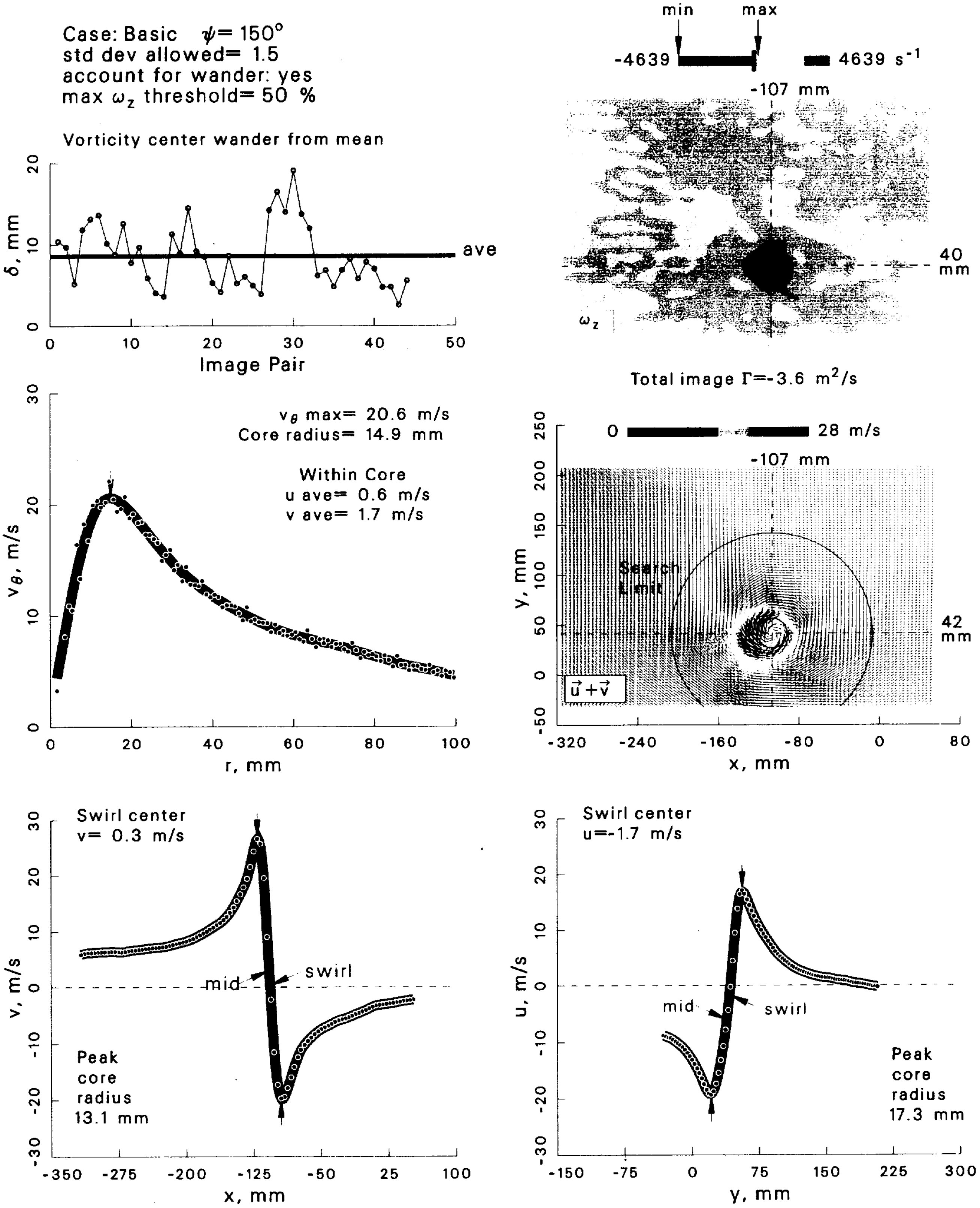

Figure 25: Vortex statistics at $\psi = 150°$ for the basic blade case.

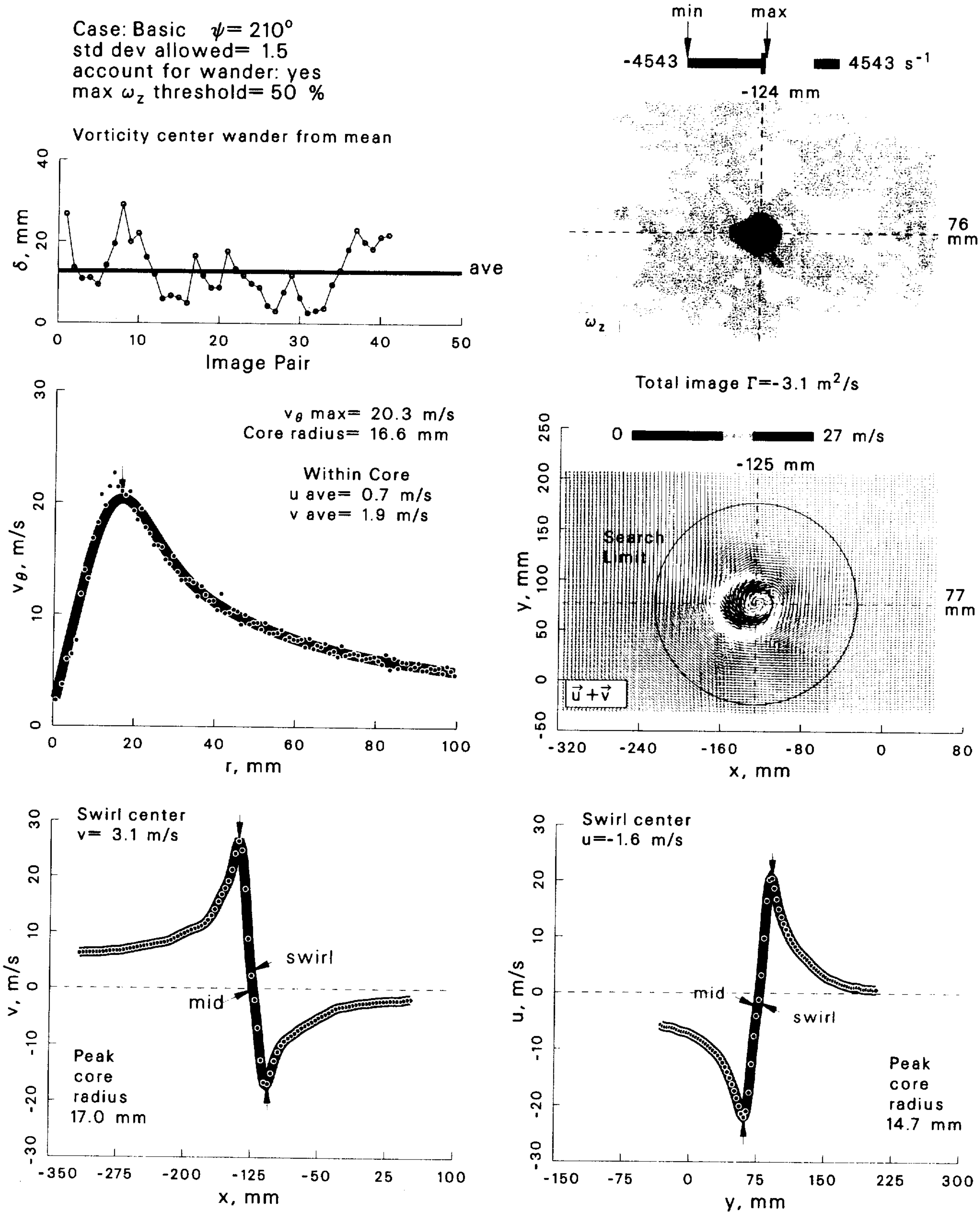

Figure 26: Vortex statistics at $\psi = 210°$ for the basic blade case.

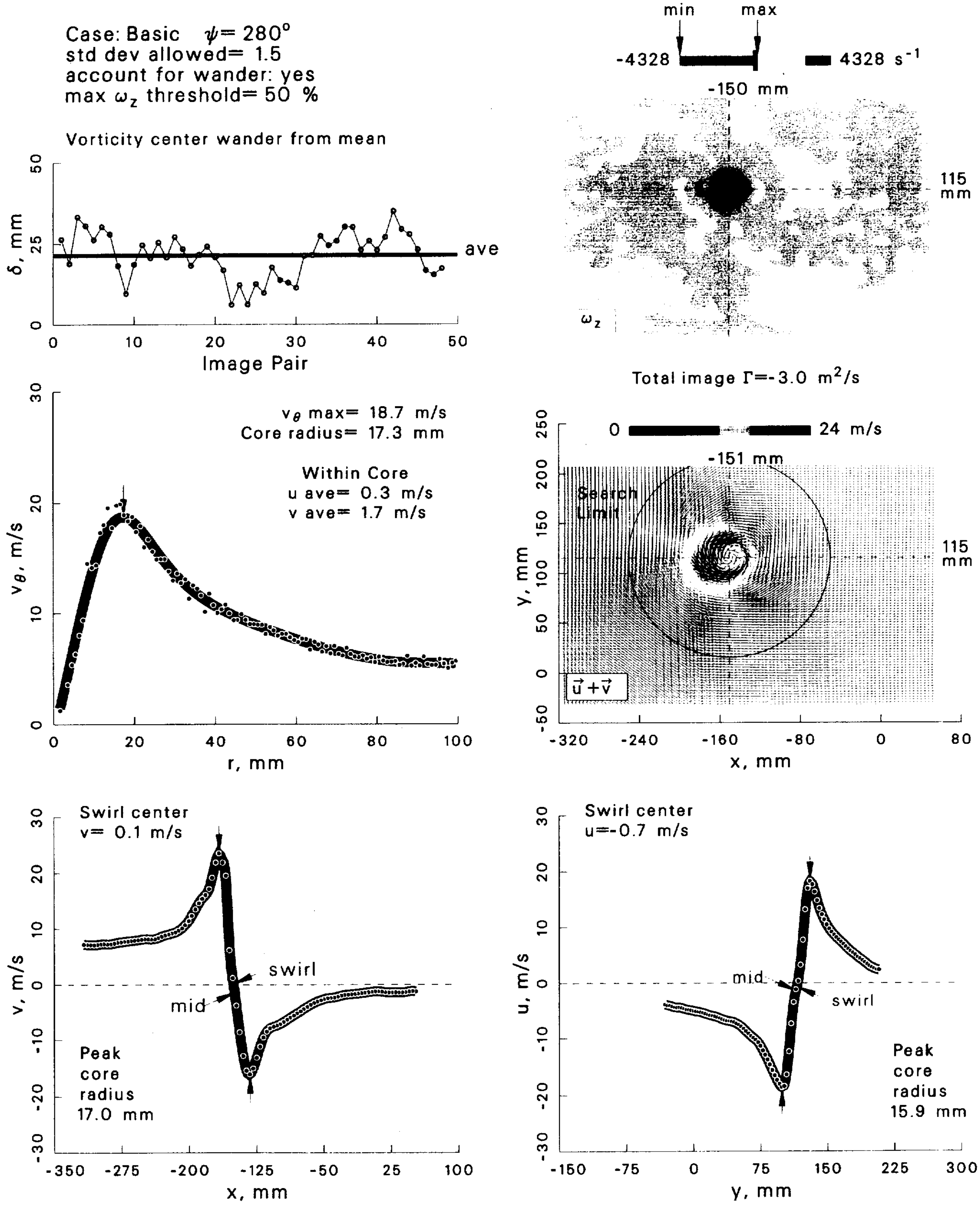

Figure 27: Vortex statistics at $\psi = 280°$ for the basic blade case.

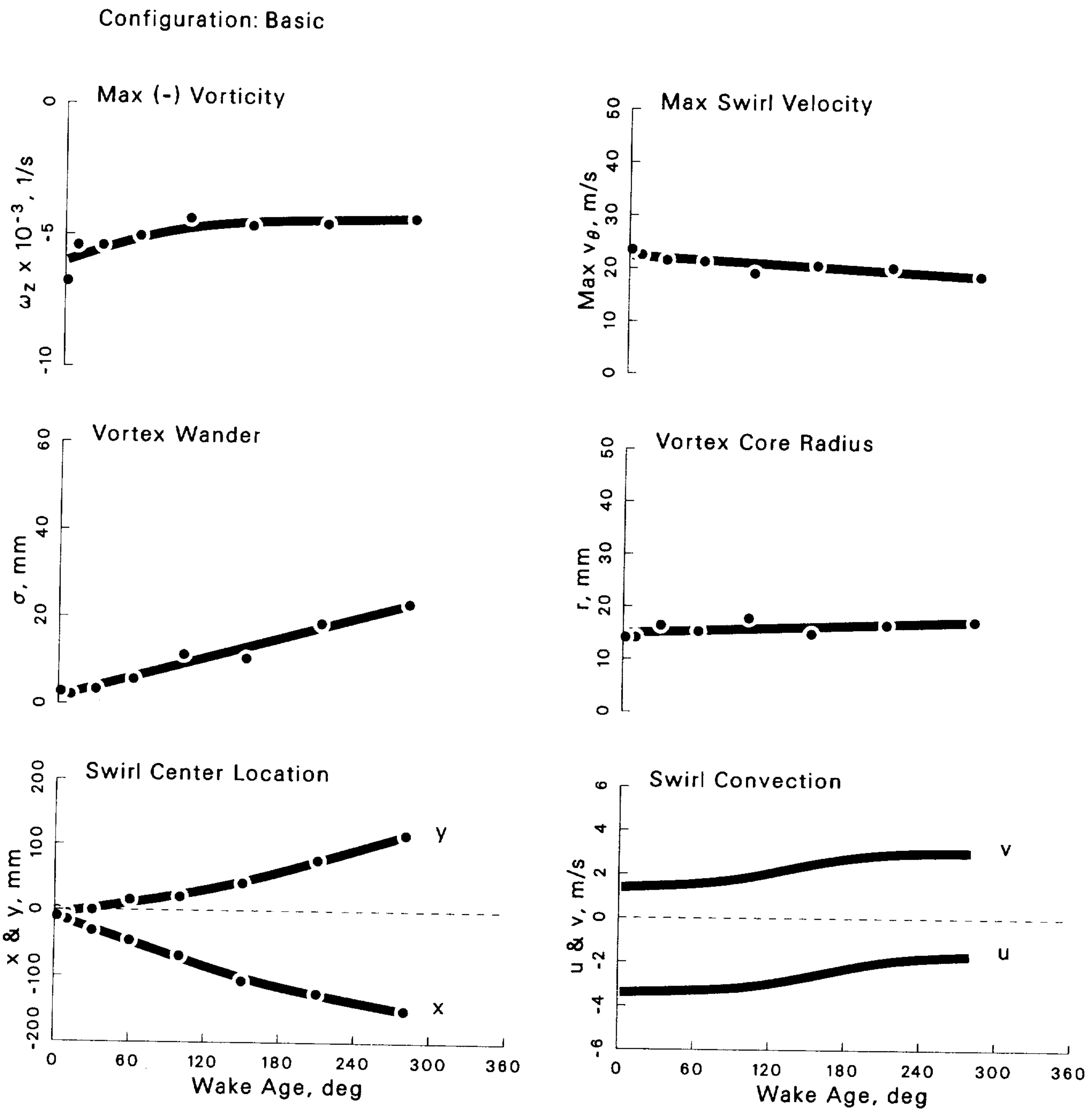

Figure 28: Summary of vortex development from $\psi = 2^\circ \rightarrow 280^\circ$ for the basic blade case.

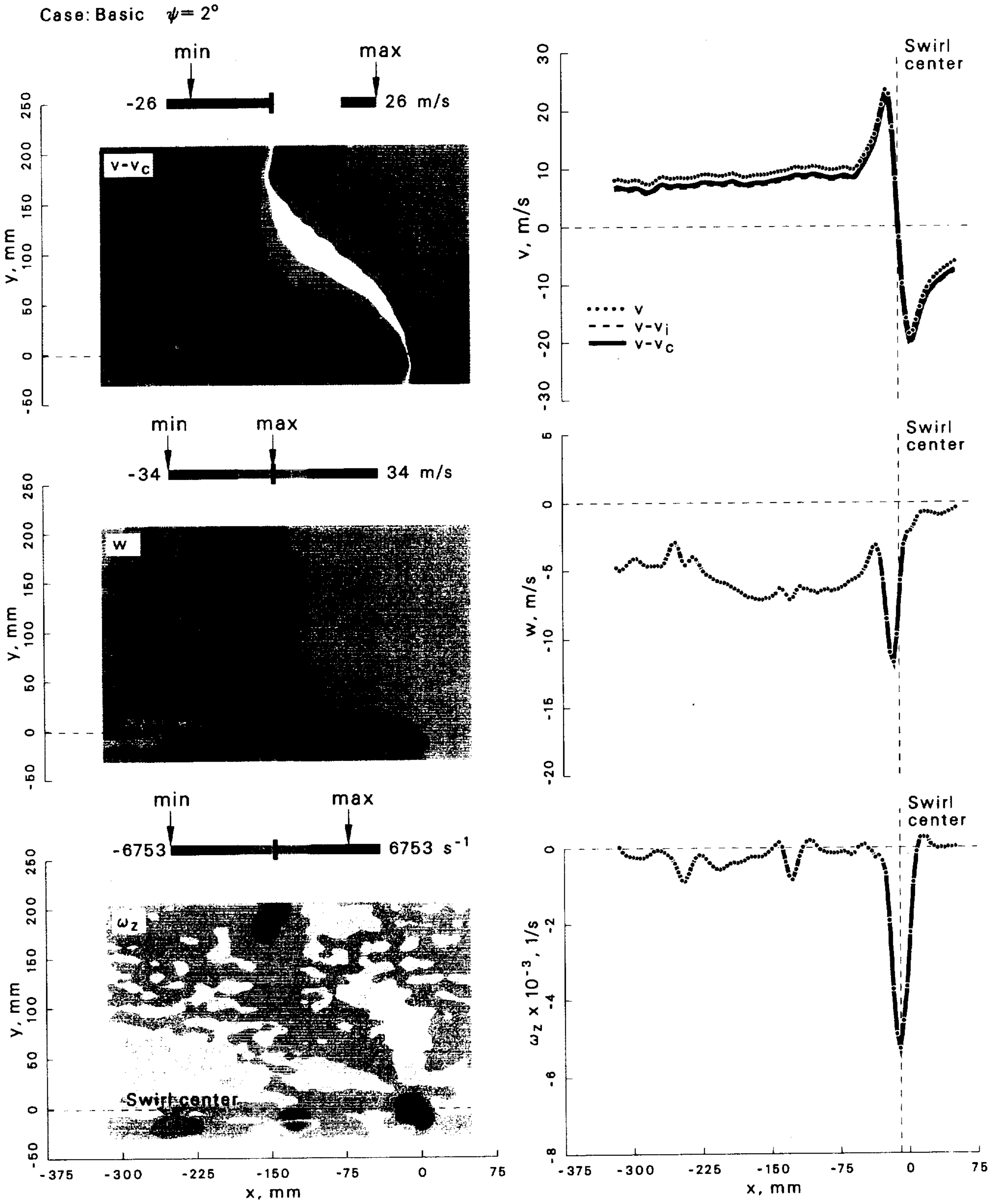

Figure 29: Velocity and vorticity components at $\psi = 2°$ for the basic blade case.

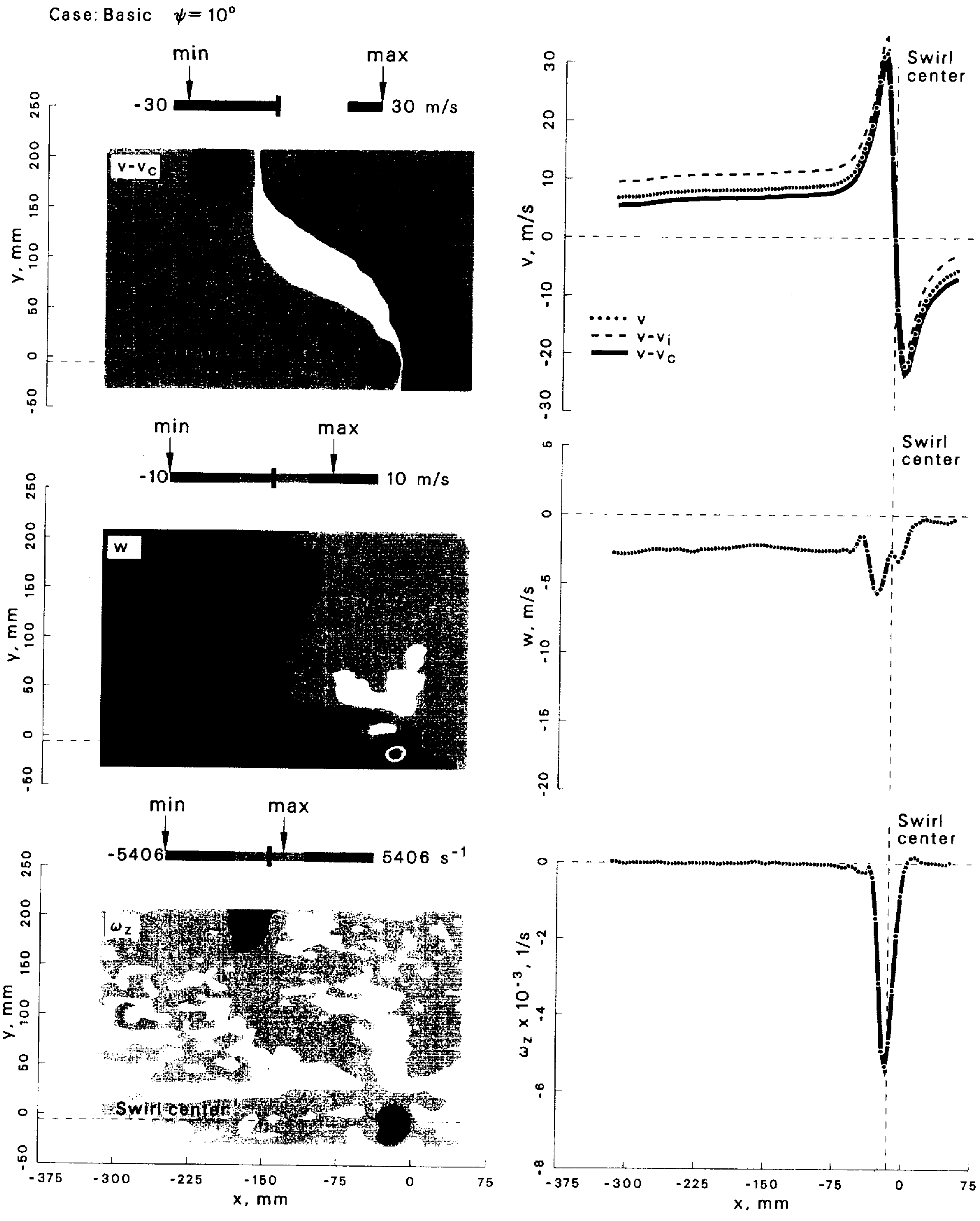

Figure 30: Velocity and vorticity components at $\psi = 10°$ for the basic blade case.

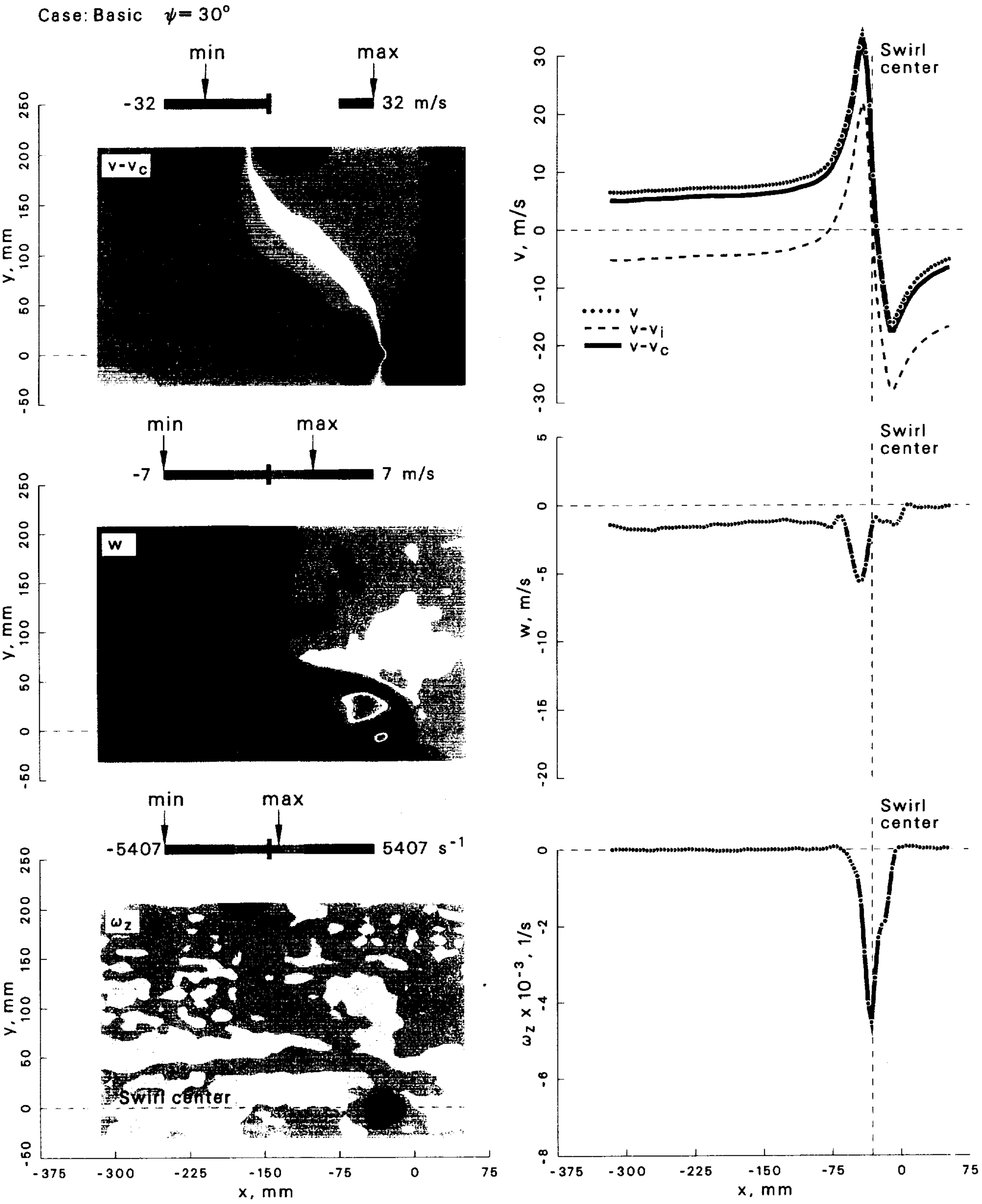

Figure 31: Velocity and vorticity components at $\psi = 30°$ for the basic blade case.

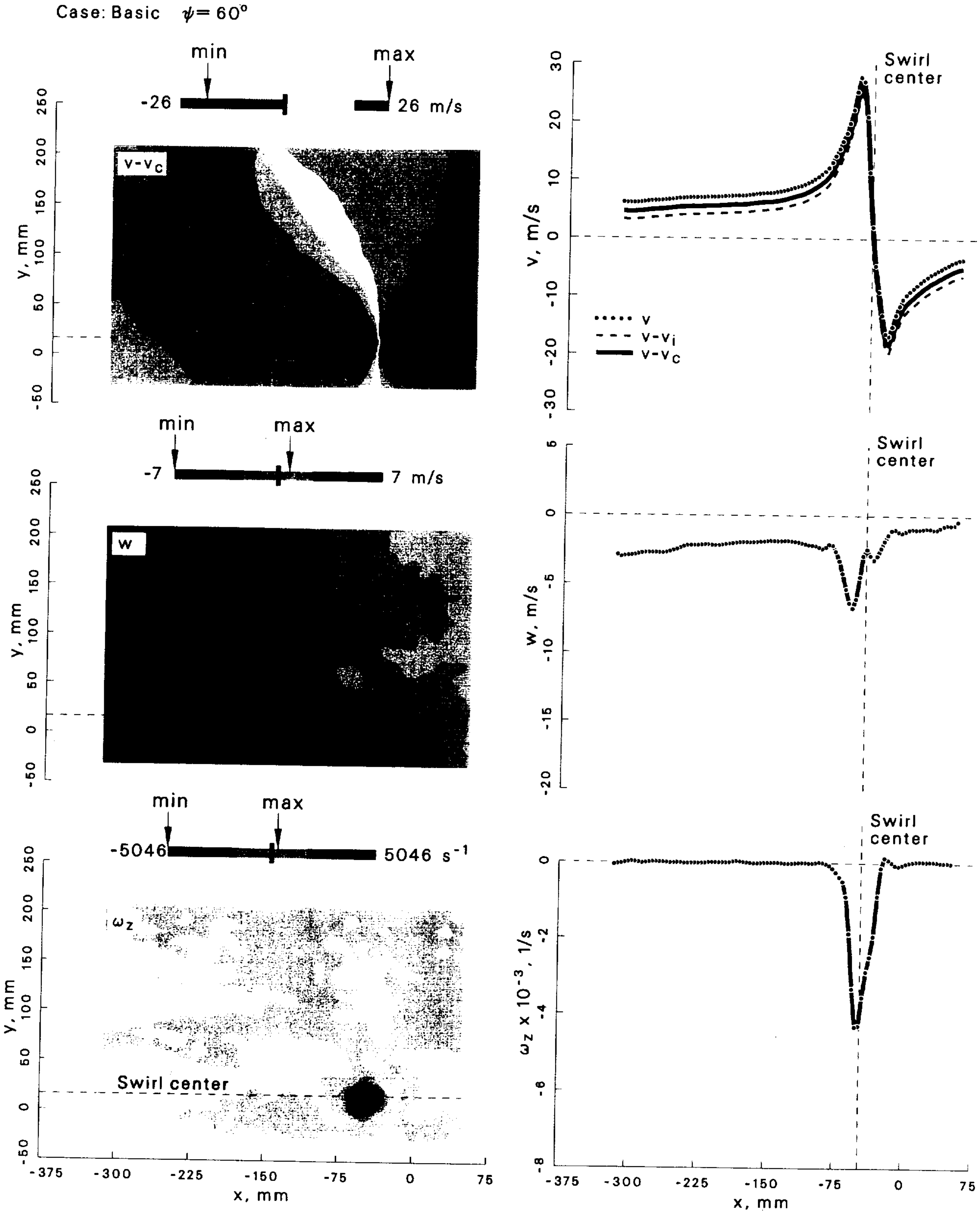

Figure 32: Velocity and vorticity components at $\psi = 60^\circ$ for the basic blade case.

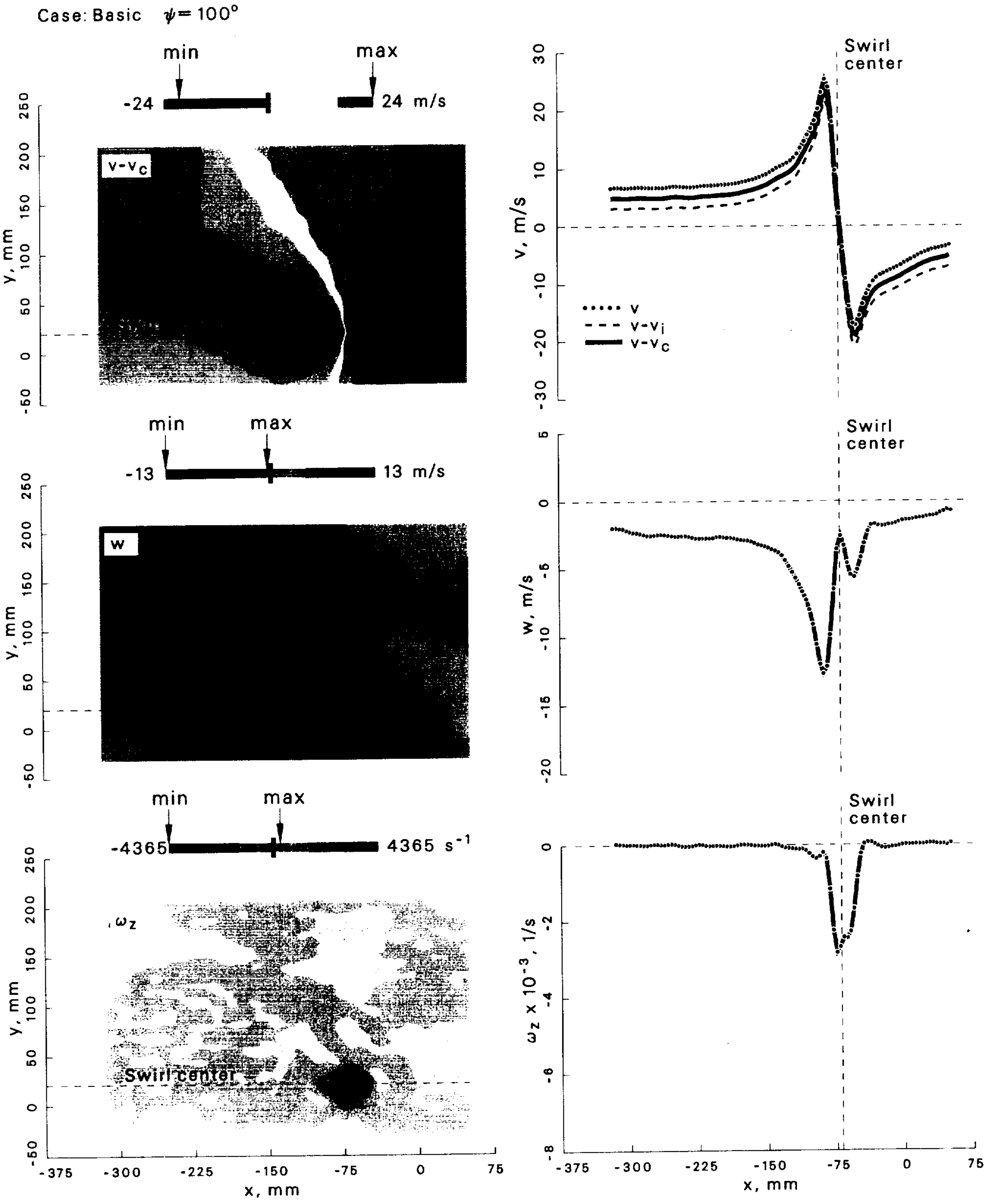

Figure 33: Velocity and vorticity components at $\psi = 100°$ for the basic blade case.

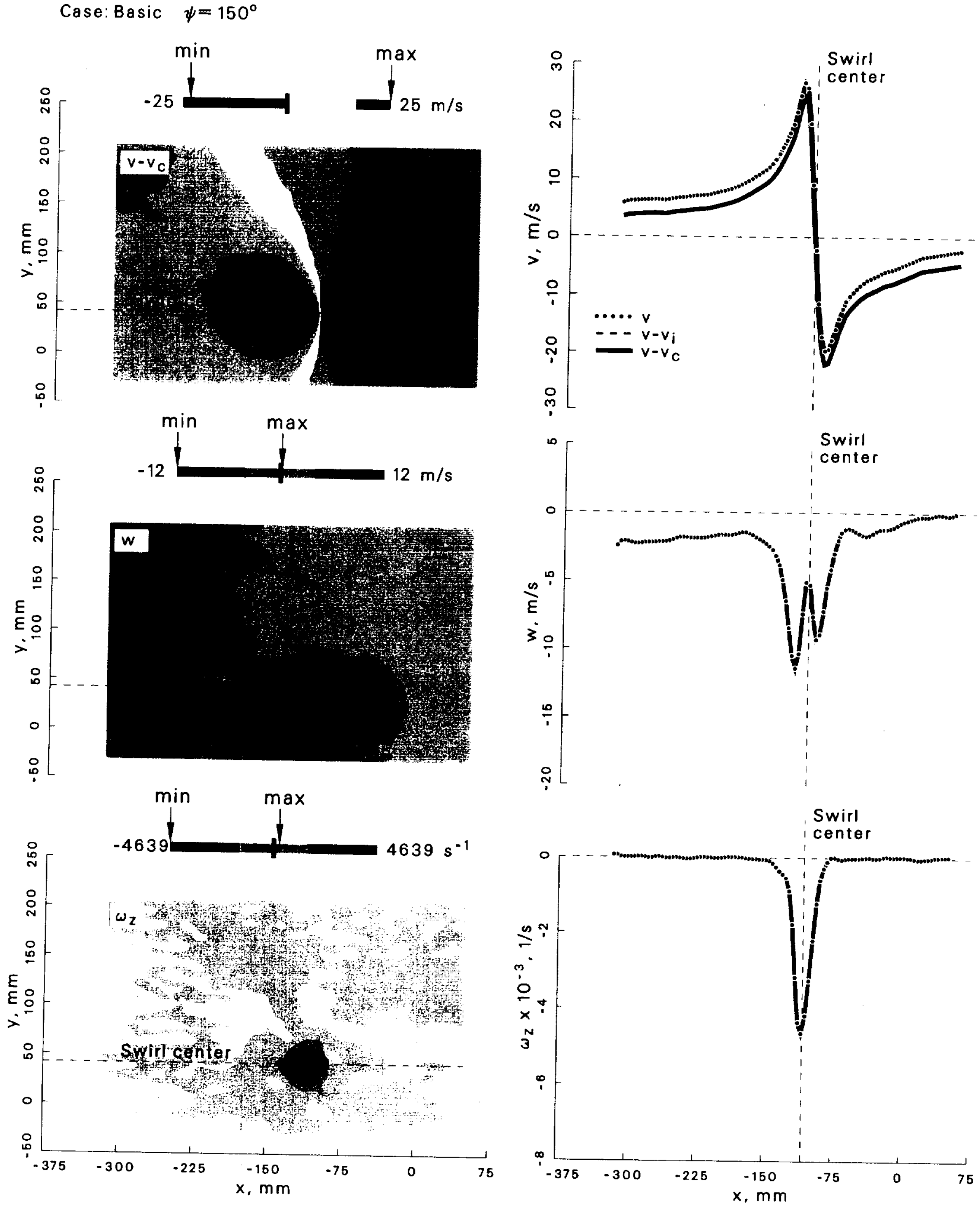

Figure 34: Velocity and vorticity components at $\psi = 150°$ for the basic blade case.

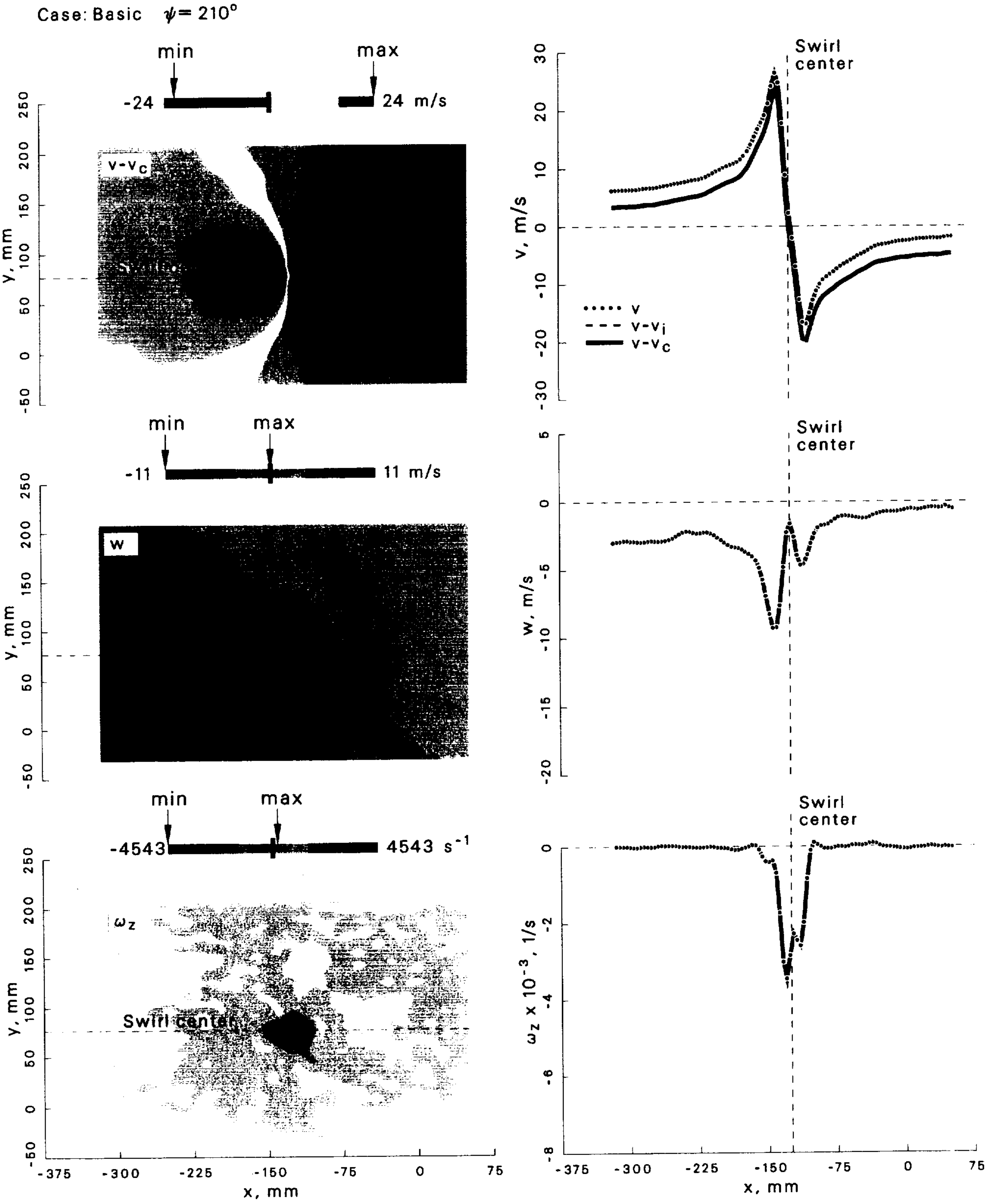

Figure 35: Velocity and vorticity components at $\psi = 210°$ for the basic blade case.

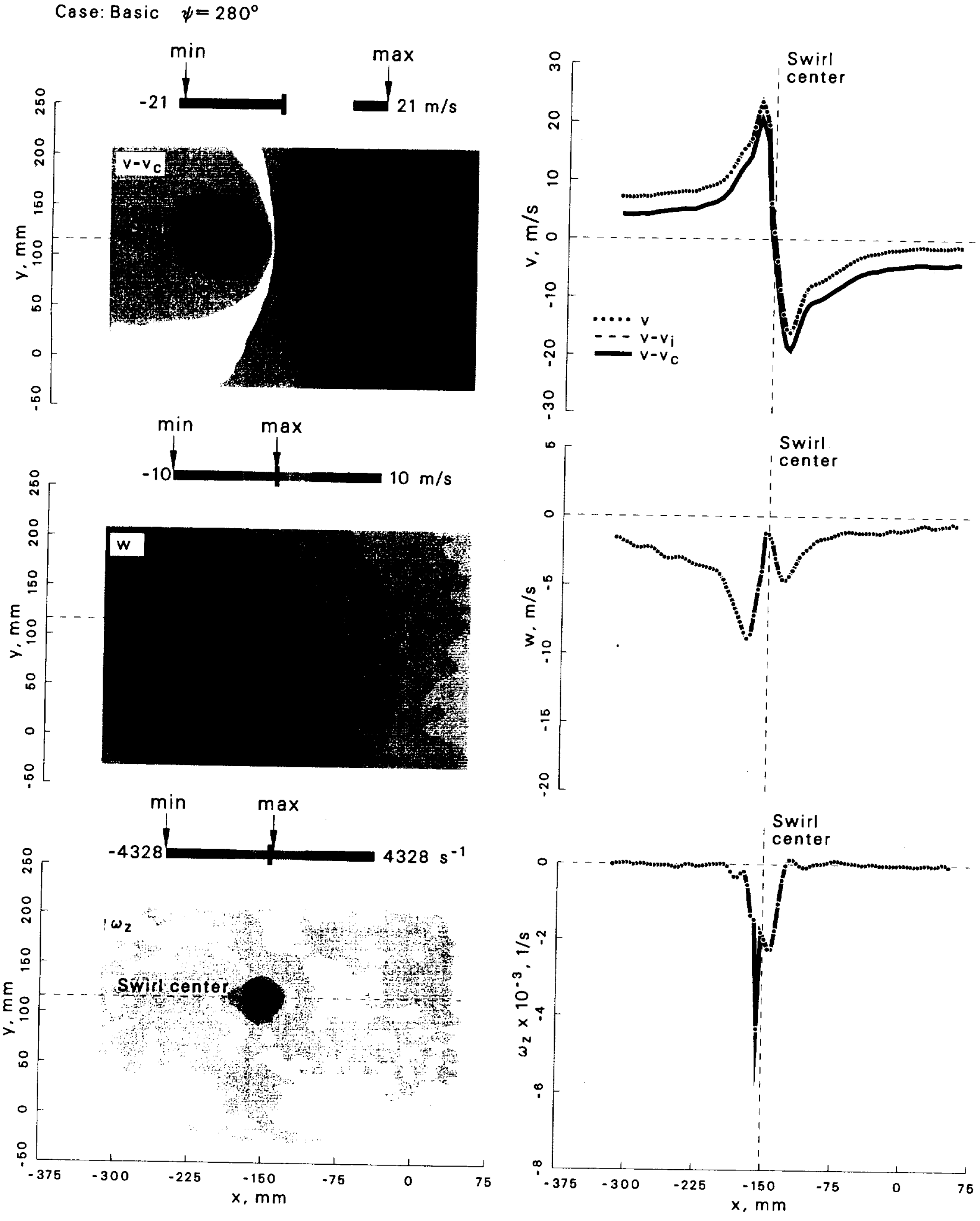

Figure 36: Velocity and vorticity components at $\psi = 280°$ for the basic blade case.

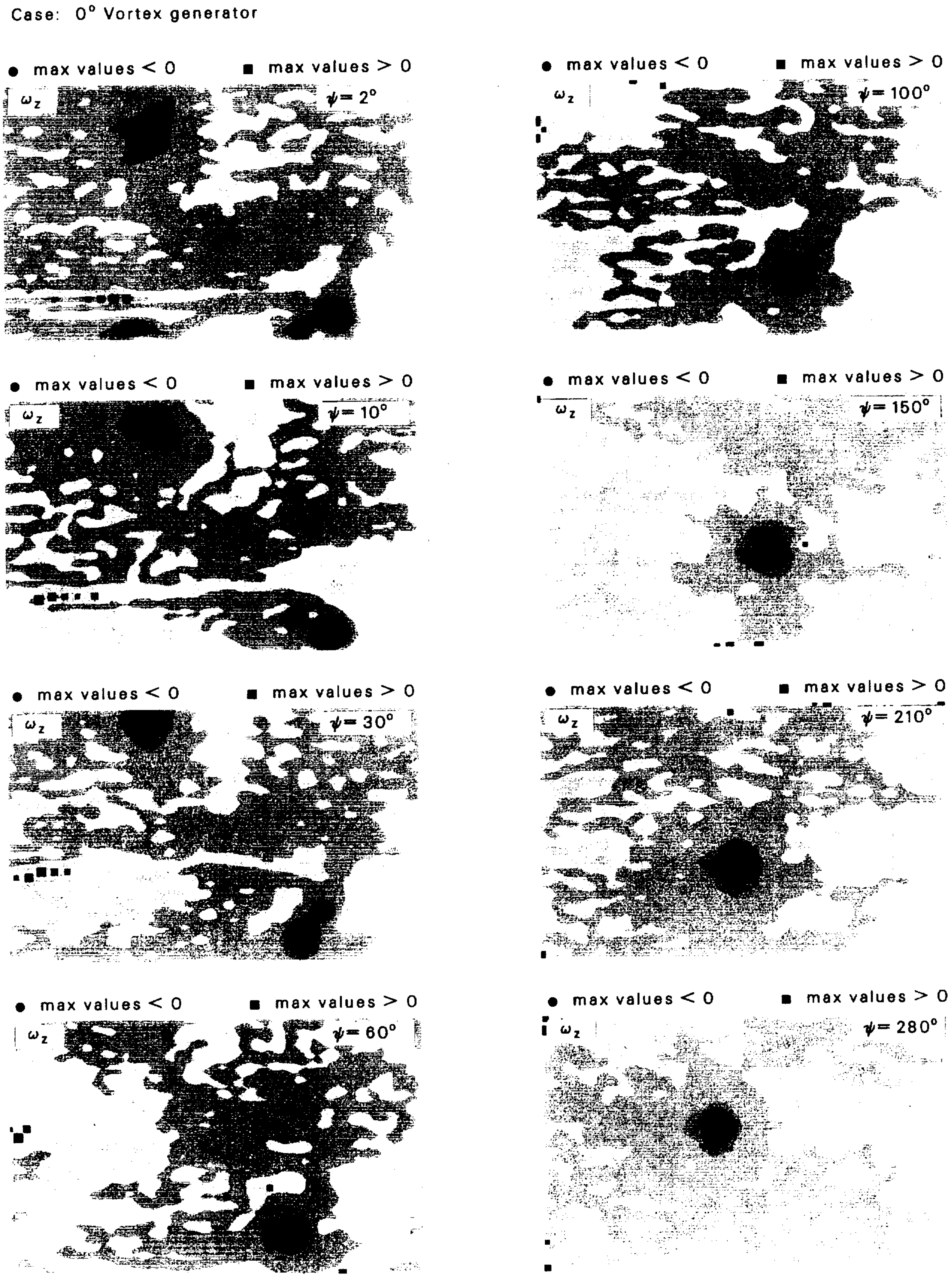

Figure 37: Locations of ω_z extrema at $\psi = 2° \rightarrow 280°$ for the 0° vortex generator case.

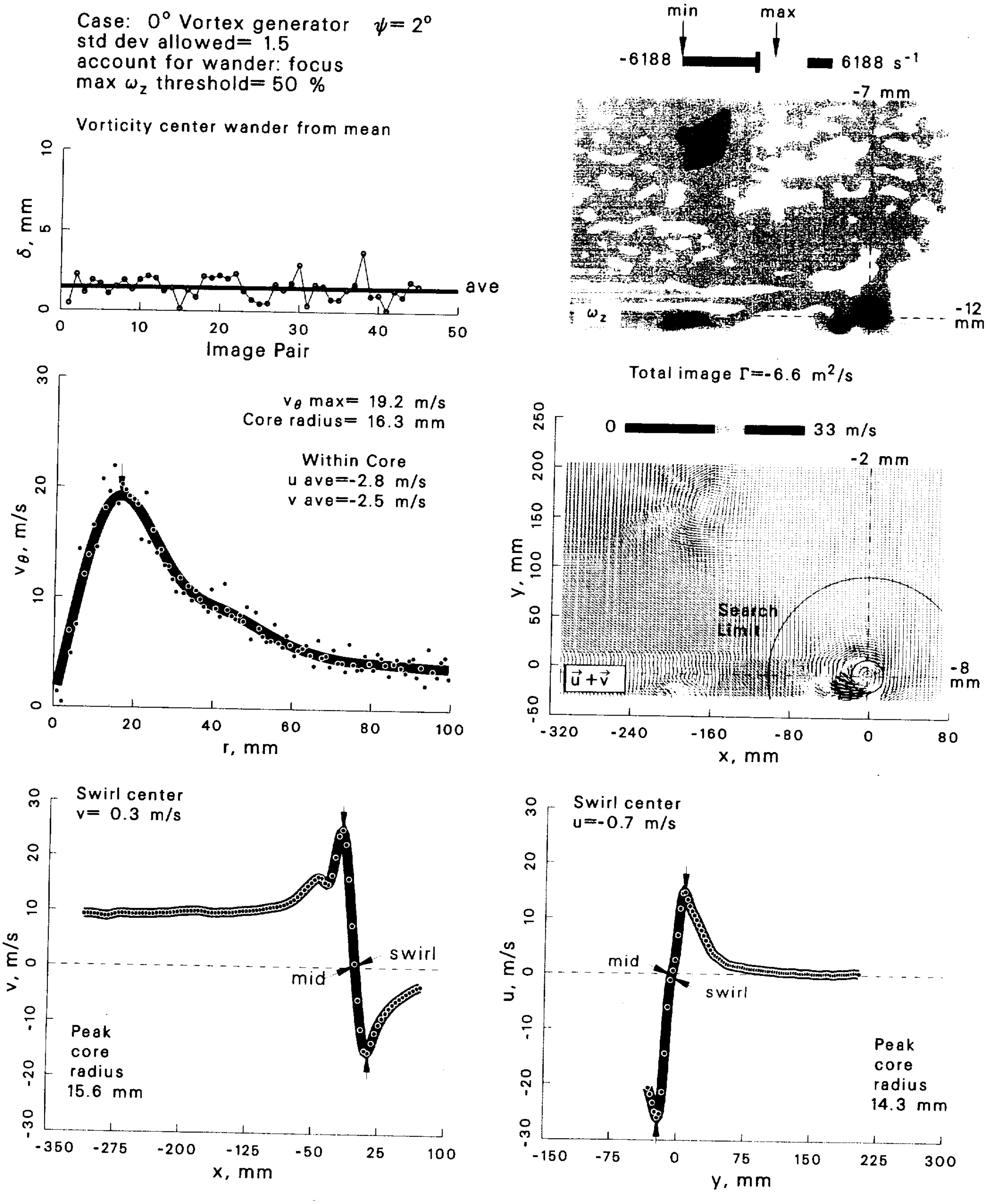

Figure 38: Vortex statistics at $\psi = 2^\circ$ for the 0° vortex generator case.

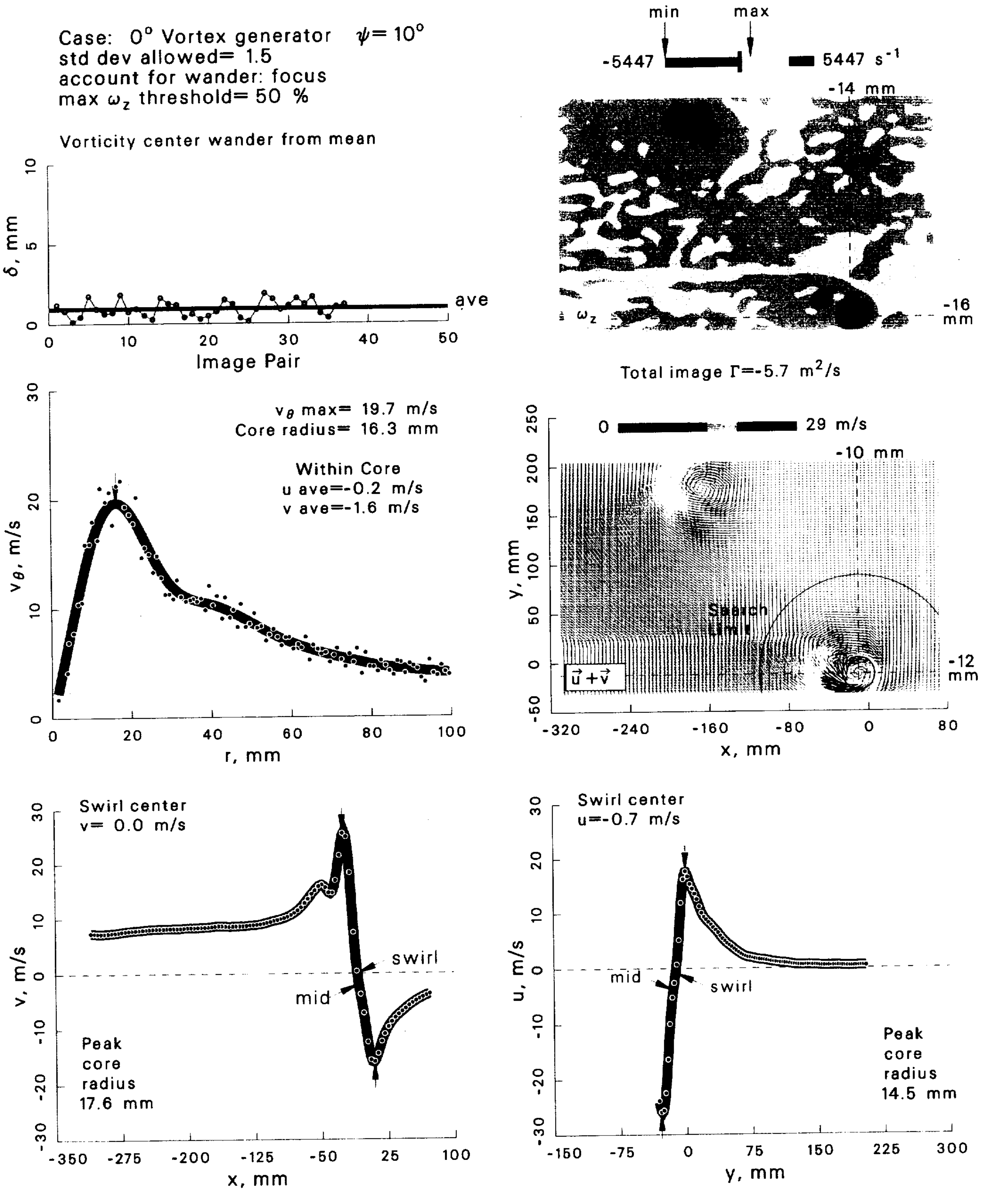

Figure 39: Vortex statistics at $\psi = 10^\circ$ for the 0° vortex generator case.

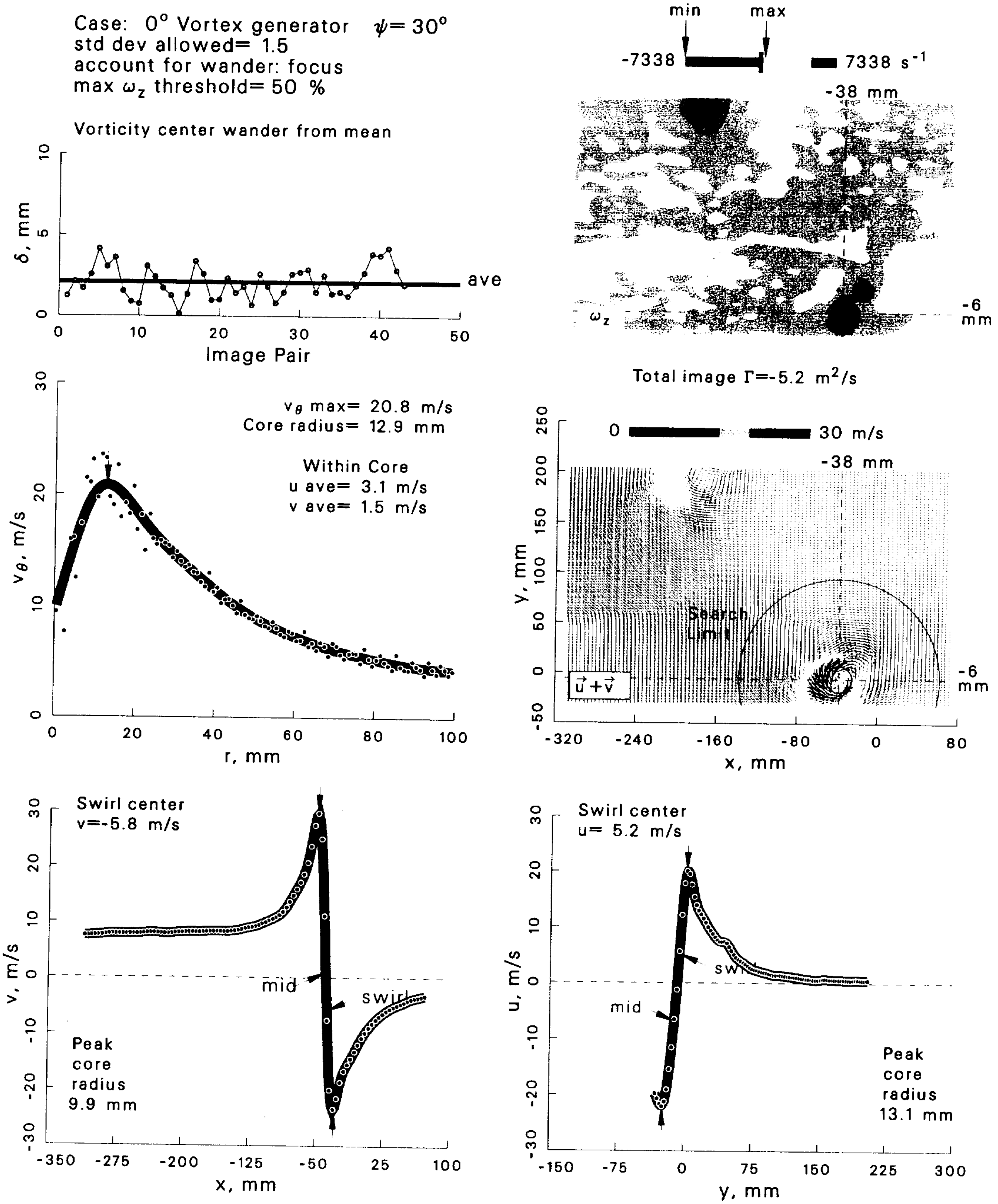

Figure 40: Vortex statistics at $\psi = 30°$ for the 0° vortex generator case.

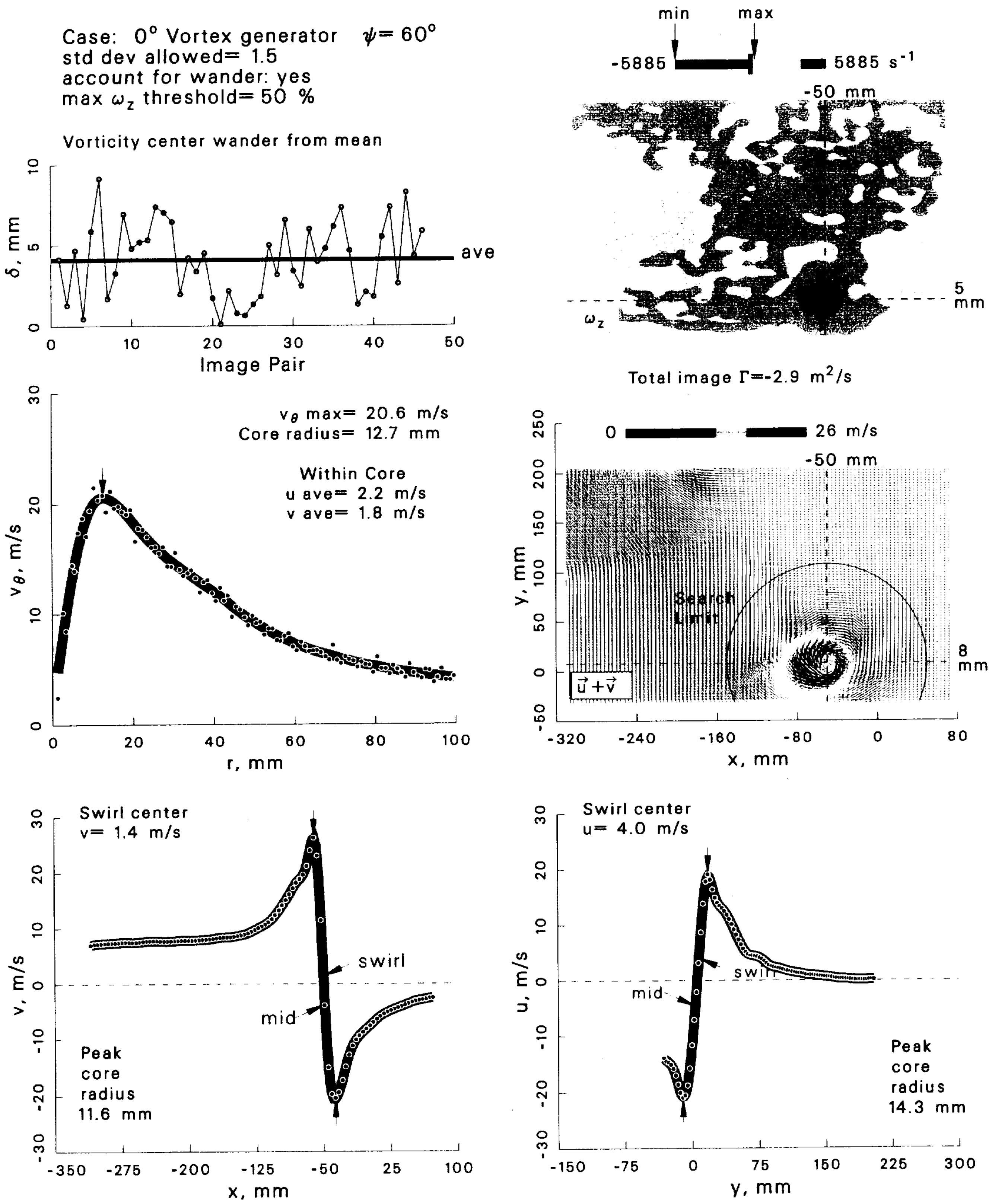

Figure 41: Vortex statistics at $\psi = 60°$ for the 0° vortex generator case.

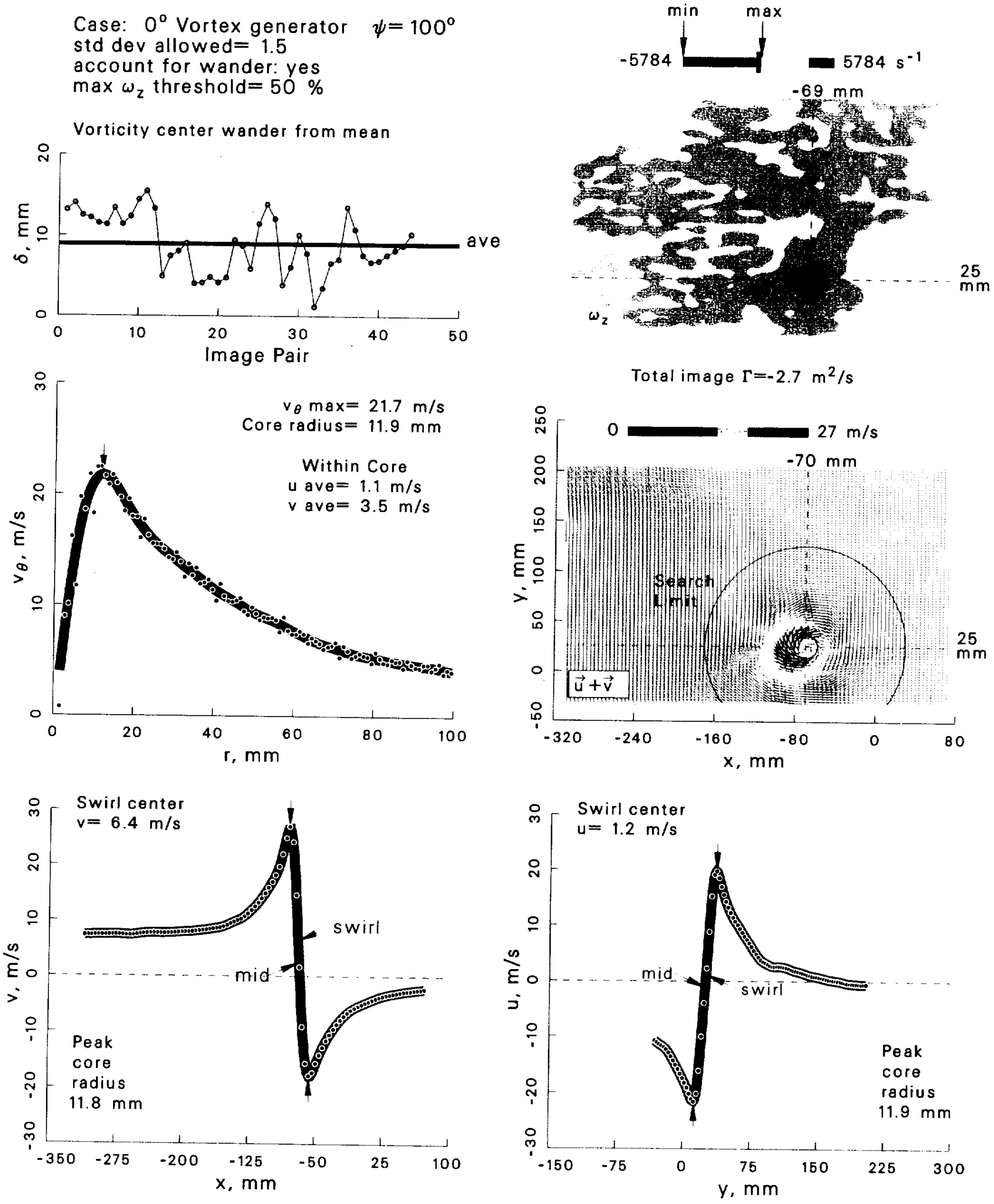

Figure 42: Vortex statistics at $\psi = 100°$ for the 0° vortex generator case.

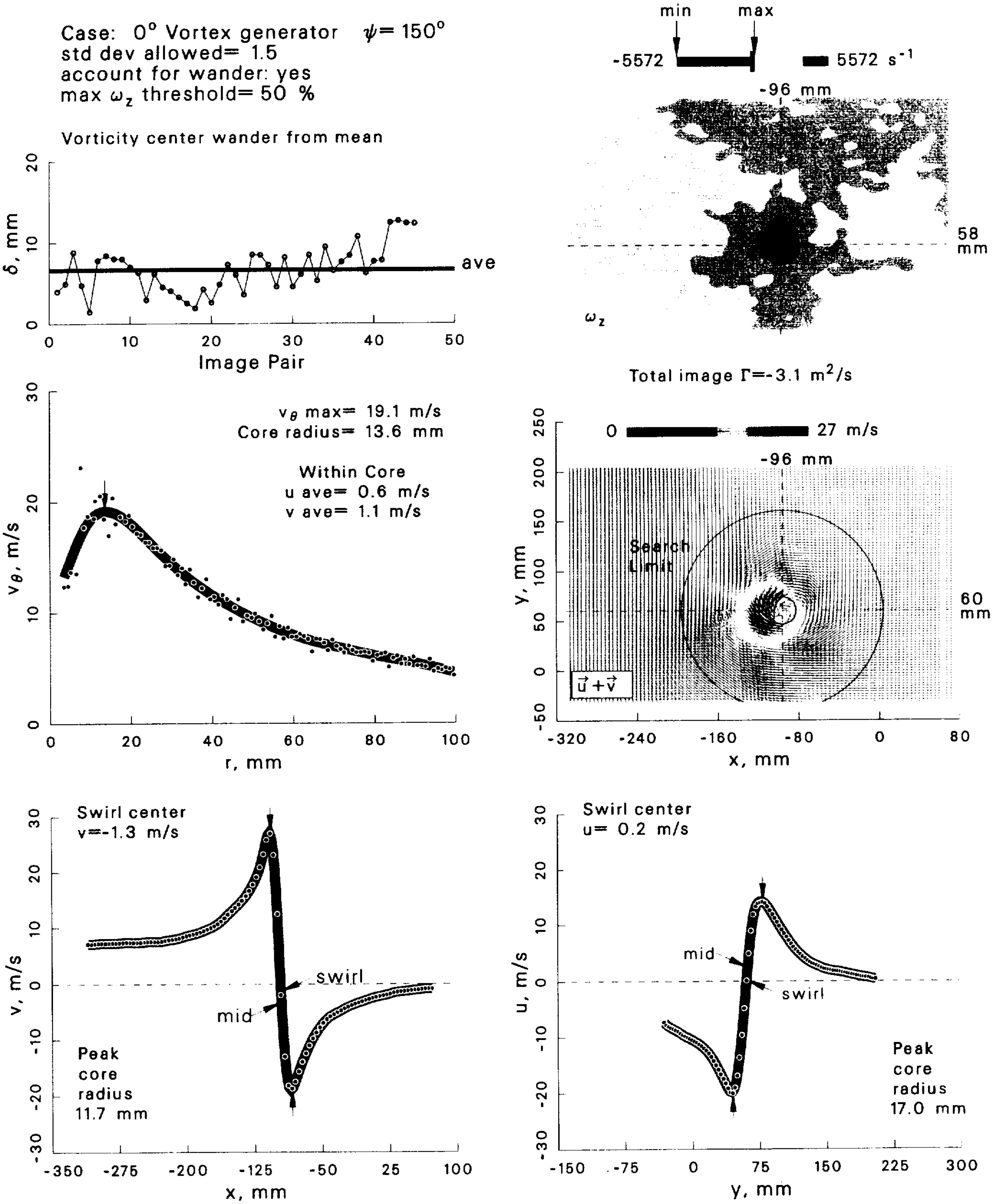

Figure 43: Vortex statistics at $\psi = 150°$ for the 0° vortex generator case.

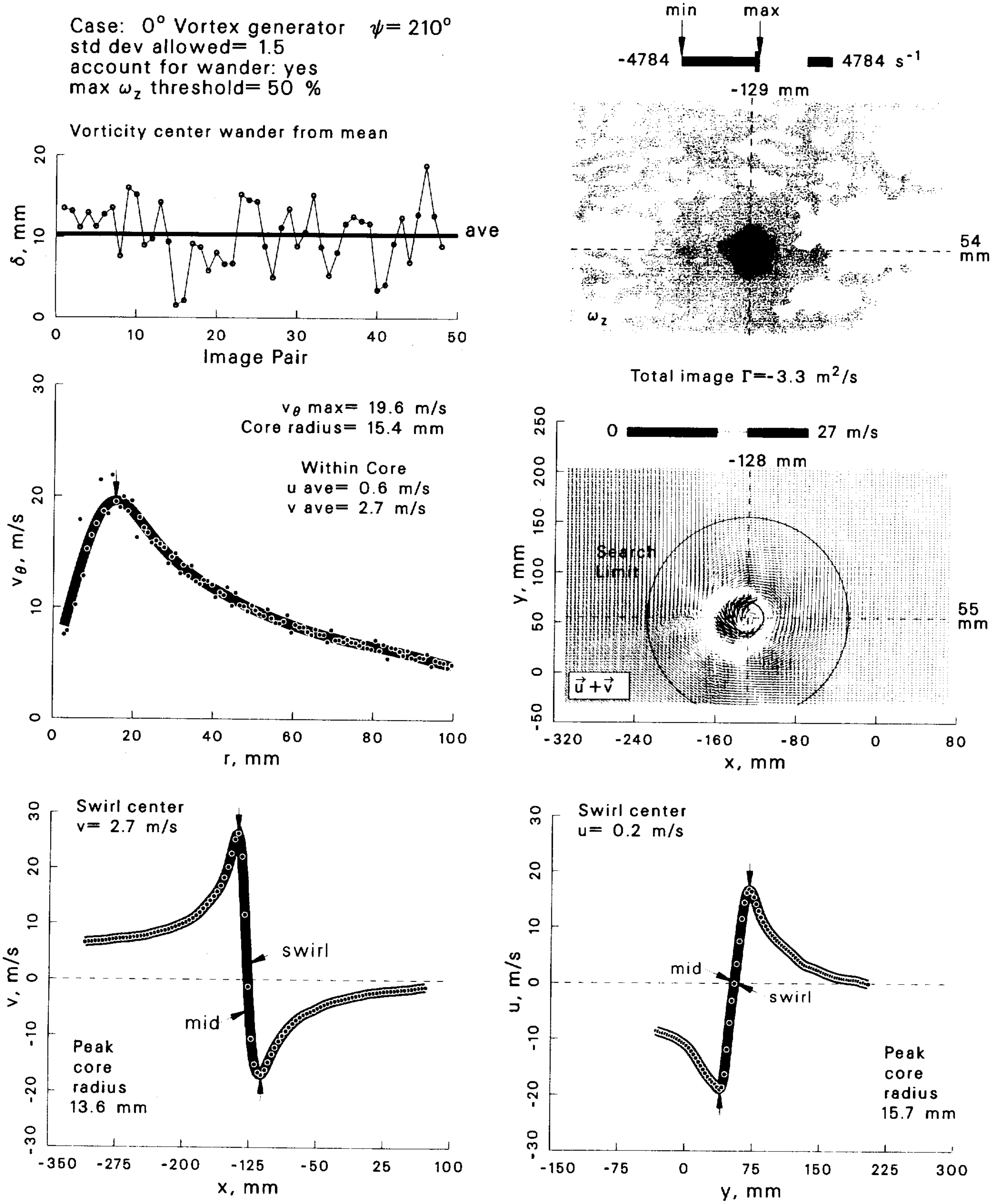

Figure 44: Vortex statistics at $\psi = 210°$ for the 0° vortex generator case.

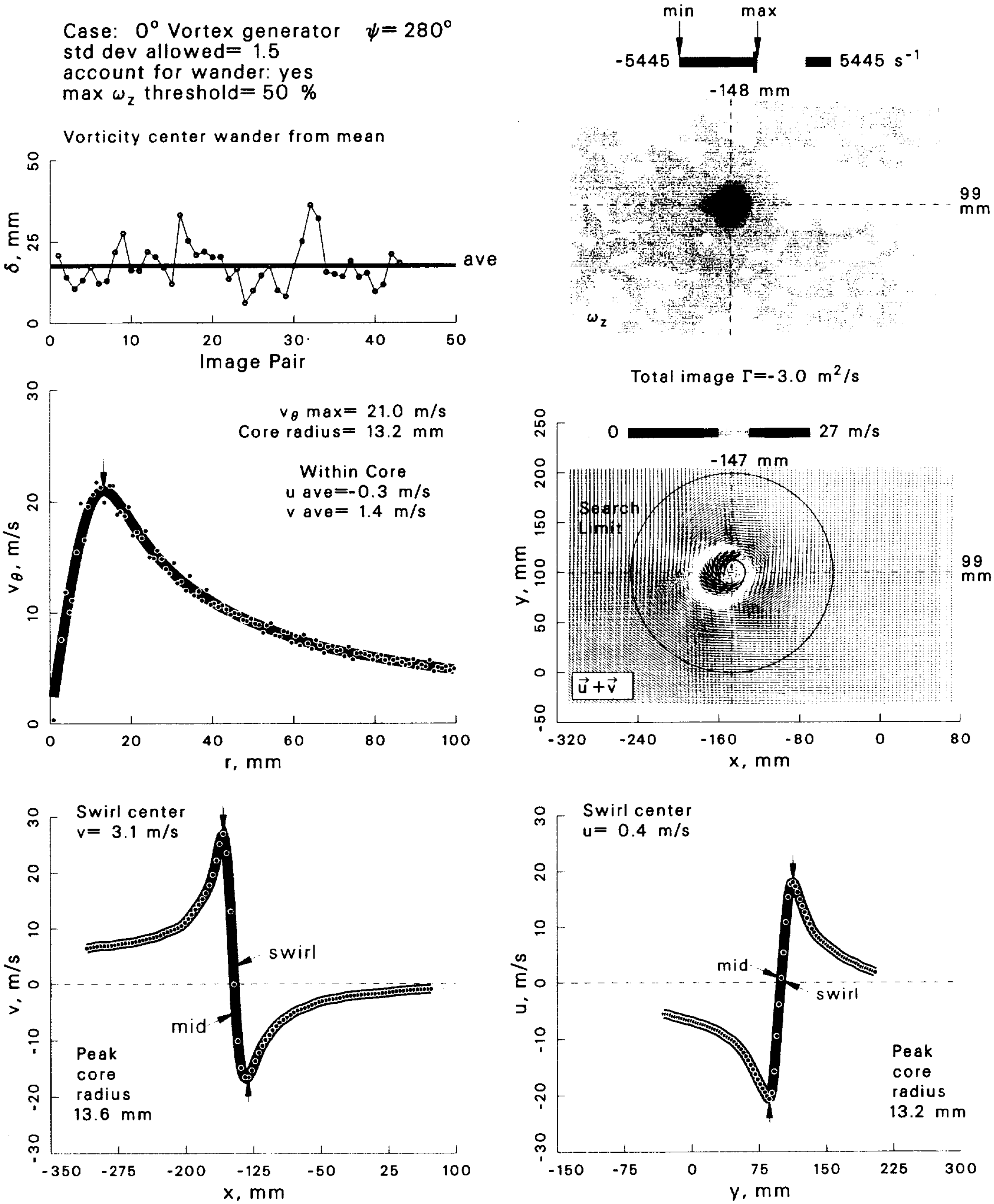

Figure 45: Vortex statistics at $\psi = 280°$ for the 0° vortex generator case.

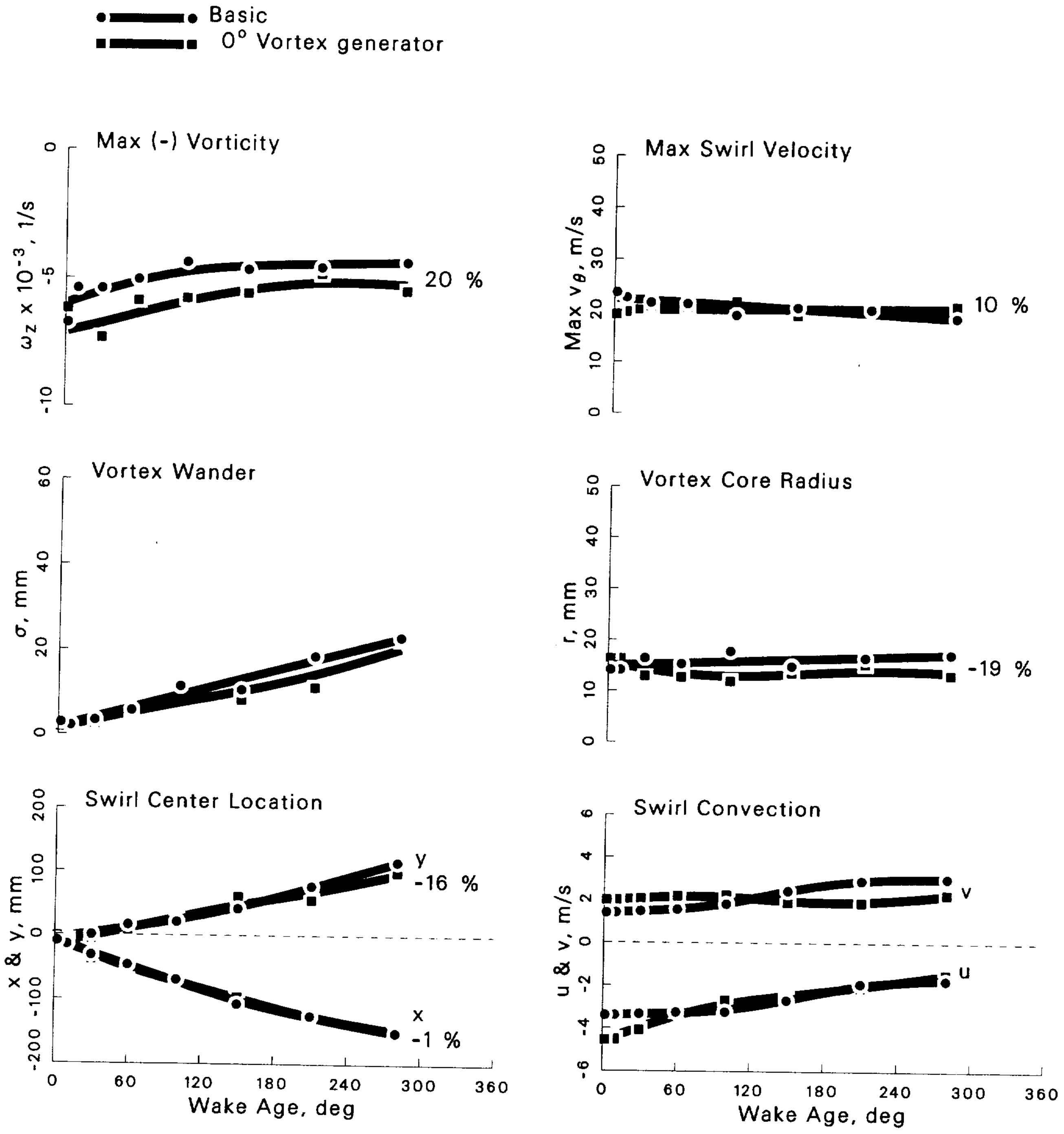

Figure 46: Summary of vortex development from $\psi = 2° \rightarrow 280°$ for the 0° vortex generator case.

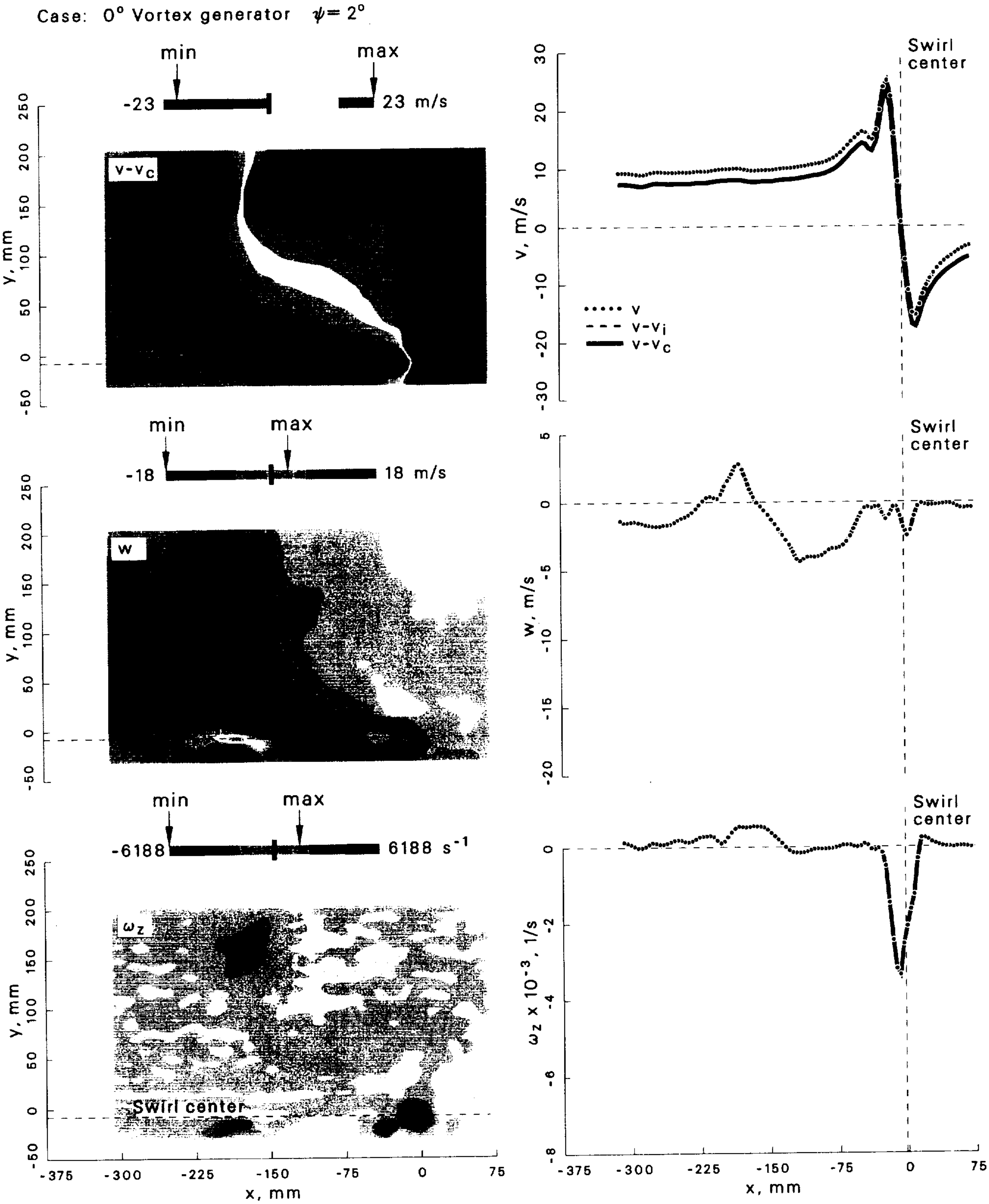

Figure 47: Velocity and vorticity components at $\psi = 2°$ for the 0° vortex generator case.

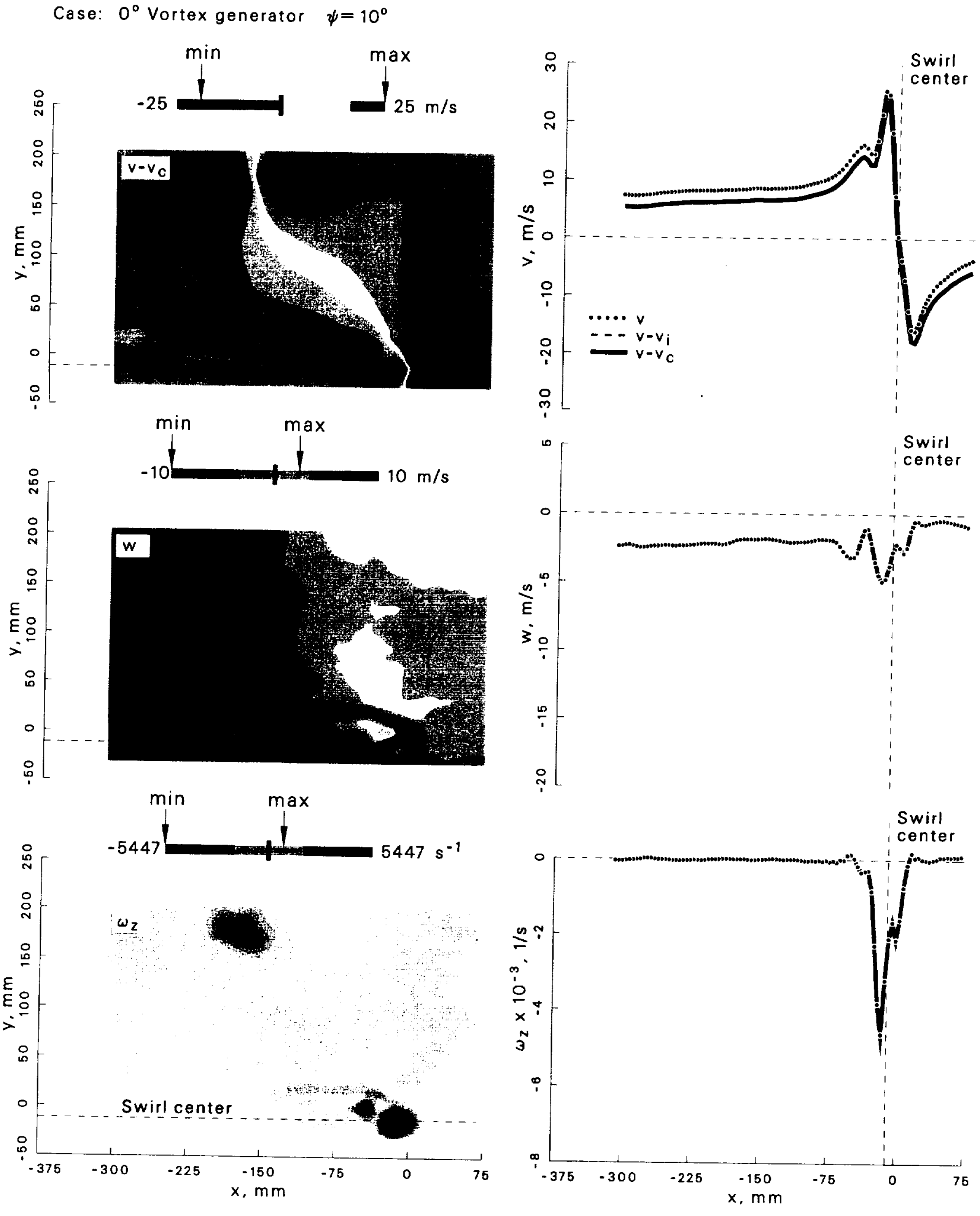

Figure 48: Velocity and vorticity components at $\psi = 10°$ for the 0° vortex generator case.

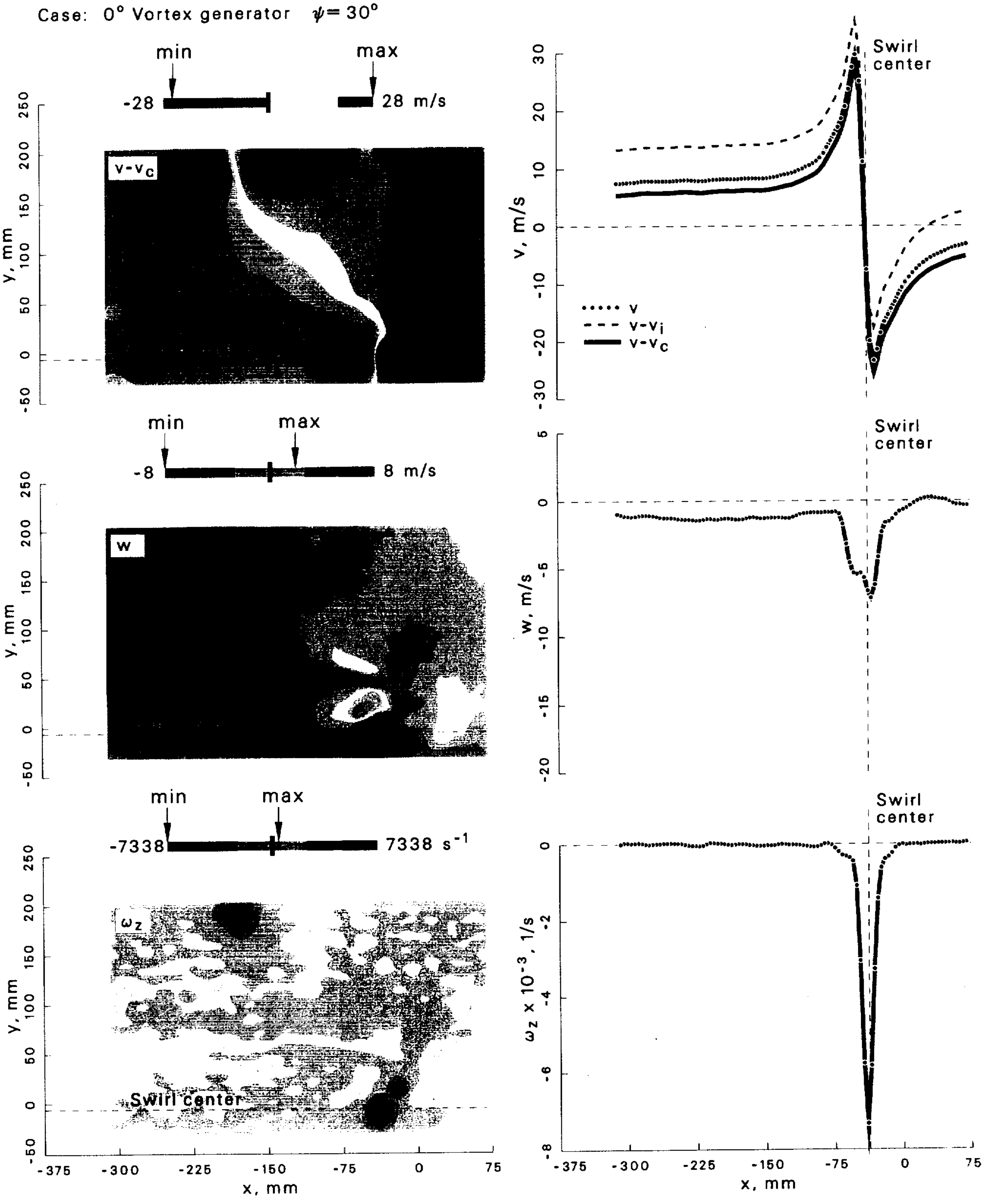

Figure 49: Velocity and vorticity components at $\psi = 30°$ for the 0° vortex generator case.

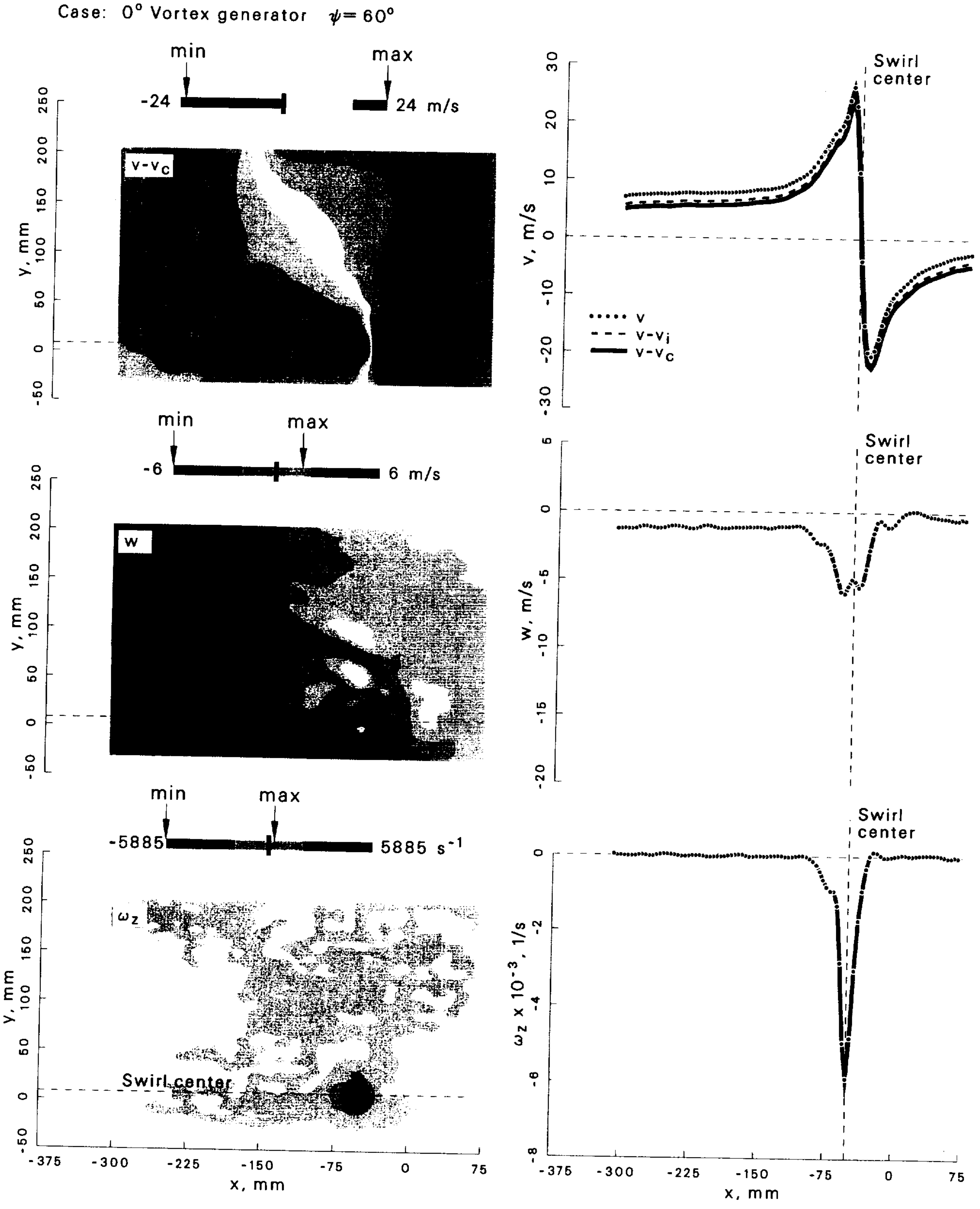

Figure 50: Velocity and vorticity components at $\psi = 60°$ for the 0° vortex generator case.

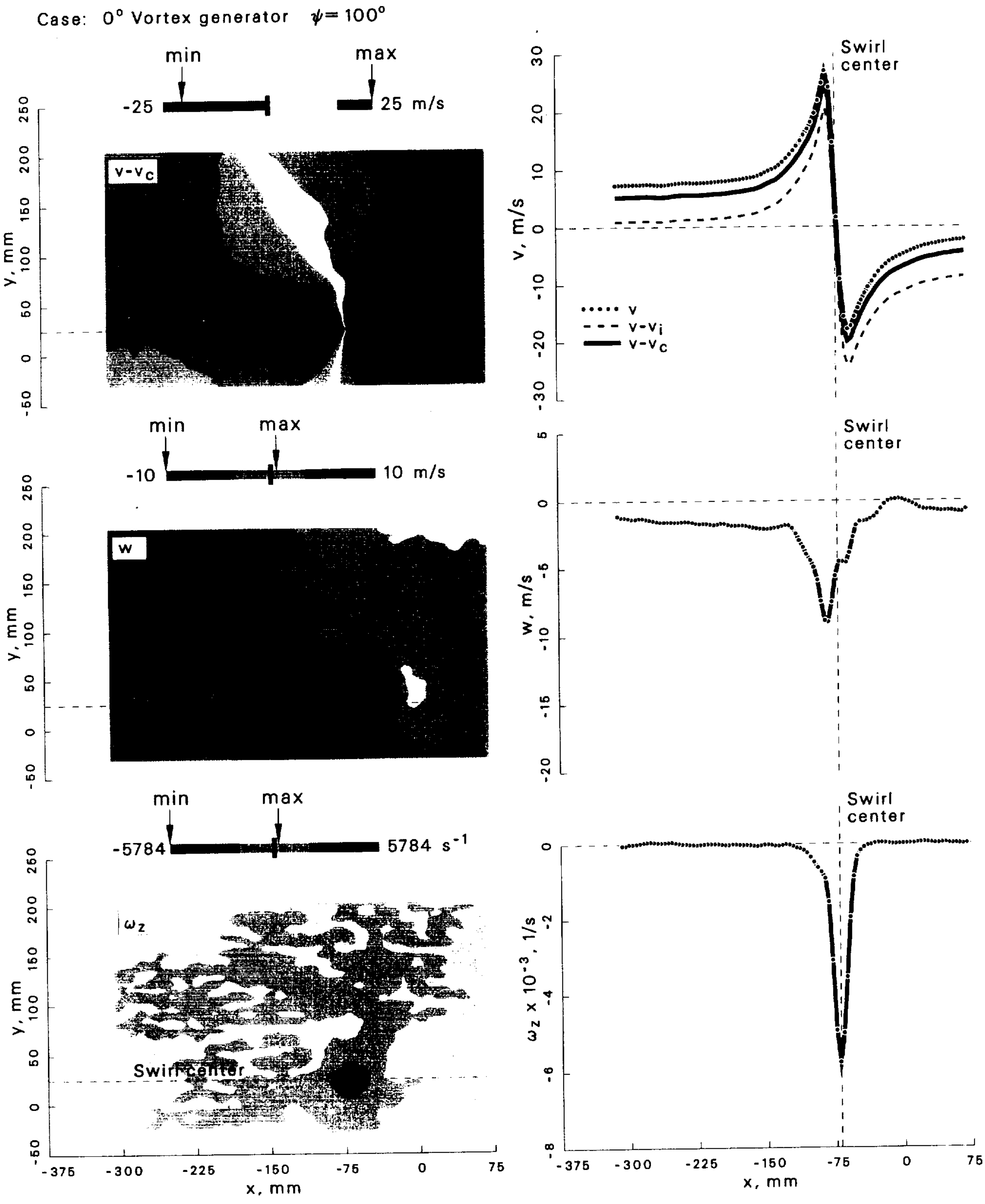

Figure 51: Velocity and vorticity components at $\psi = 100°$ for the 0° vortex generator case.

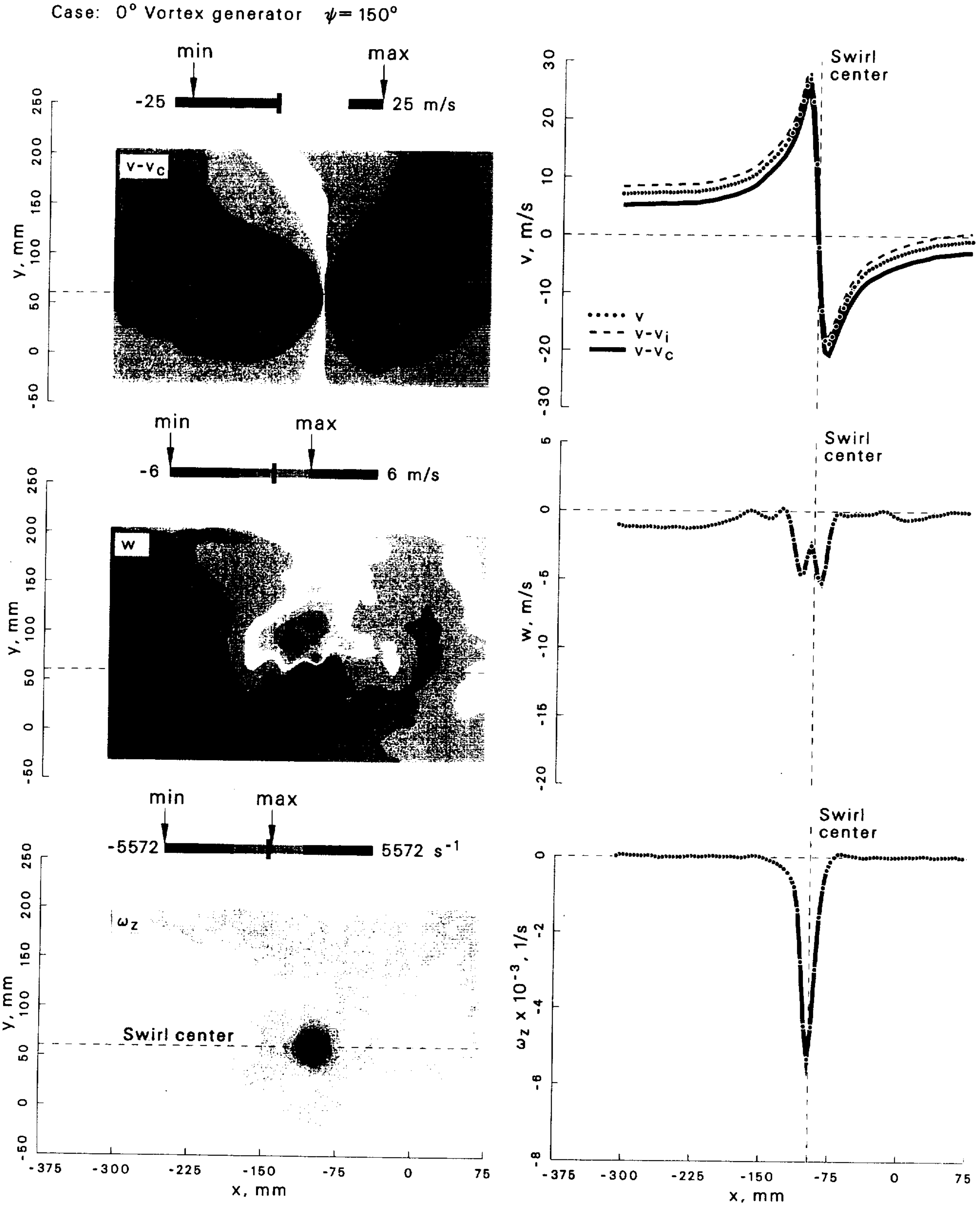

Figure 52: Velocity and vorticity components at $\psi = 150°$ for the 0° vortex generator case.

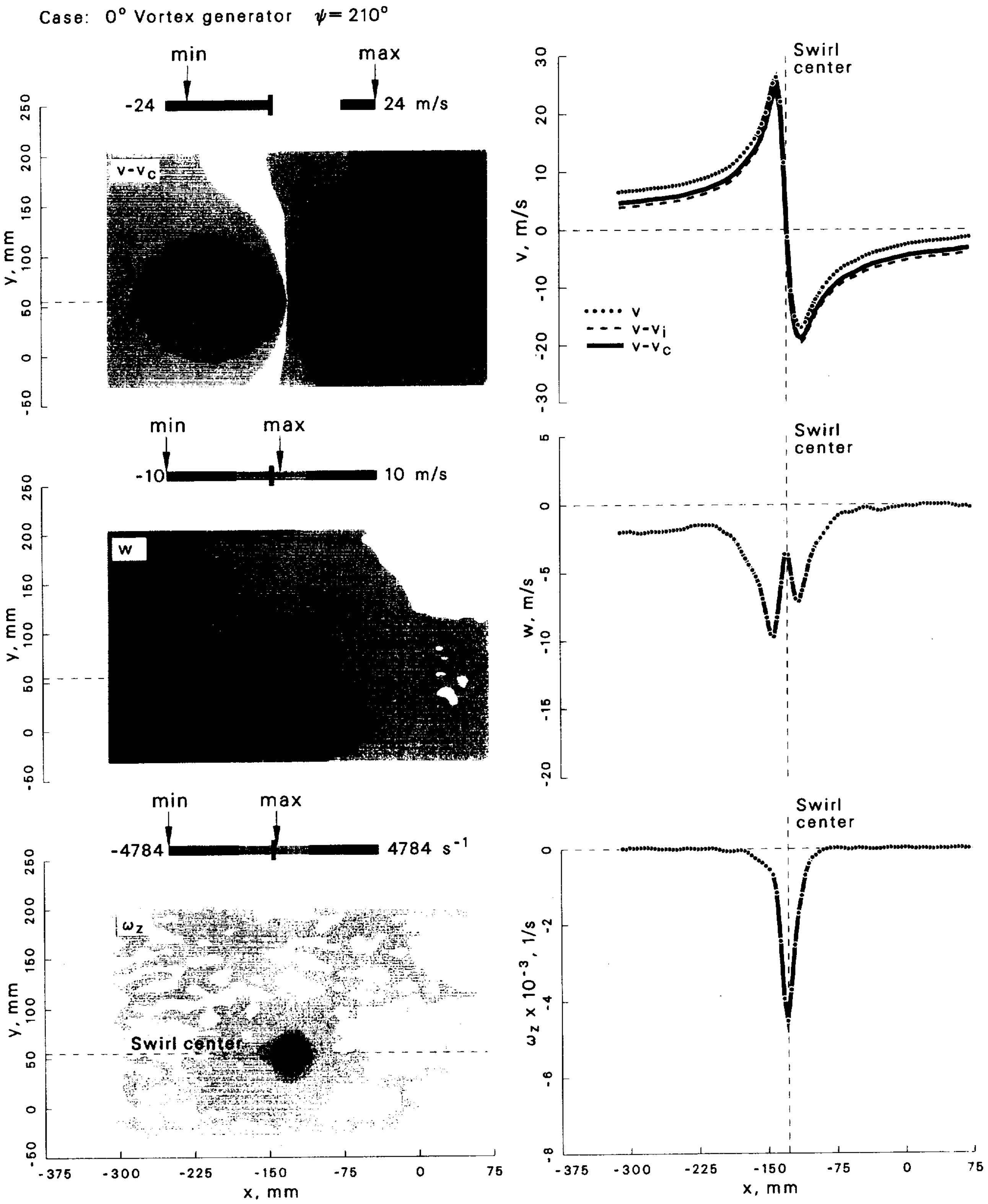

Figure 53: Velocity and vorticity components at $\psi = 210°$ for the 0° vortex generator case.

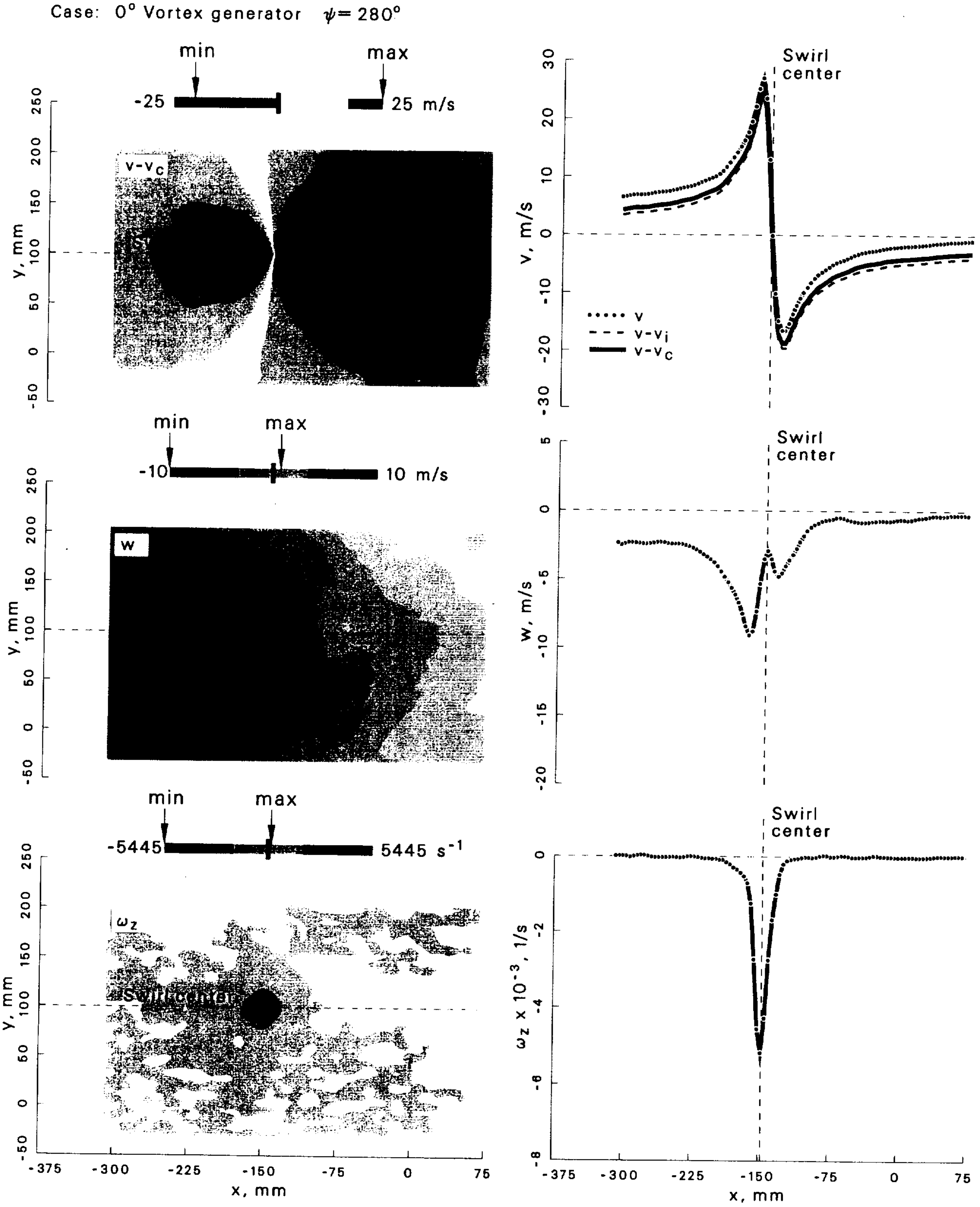

Figure 54: Velocity and vorticity components at $\psi = 280°$ for the 0° vortex generator case.

Case: +5° Vortex generator

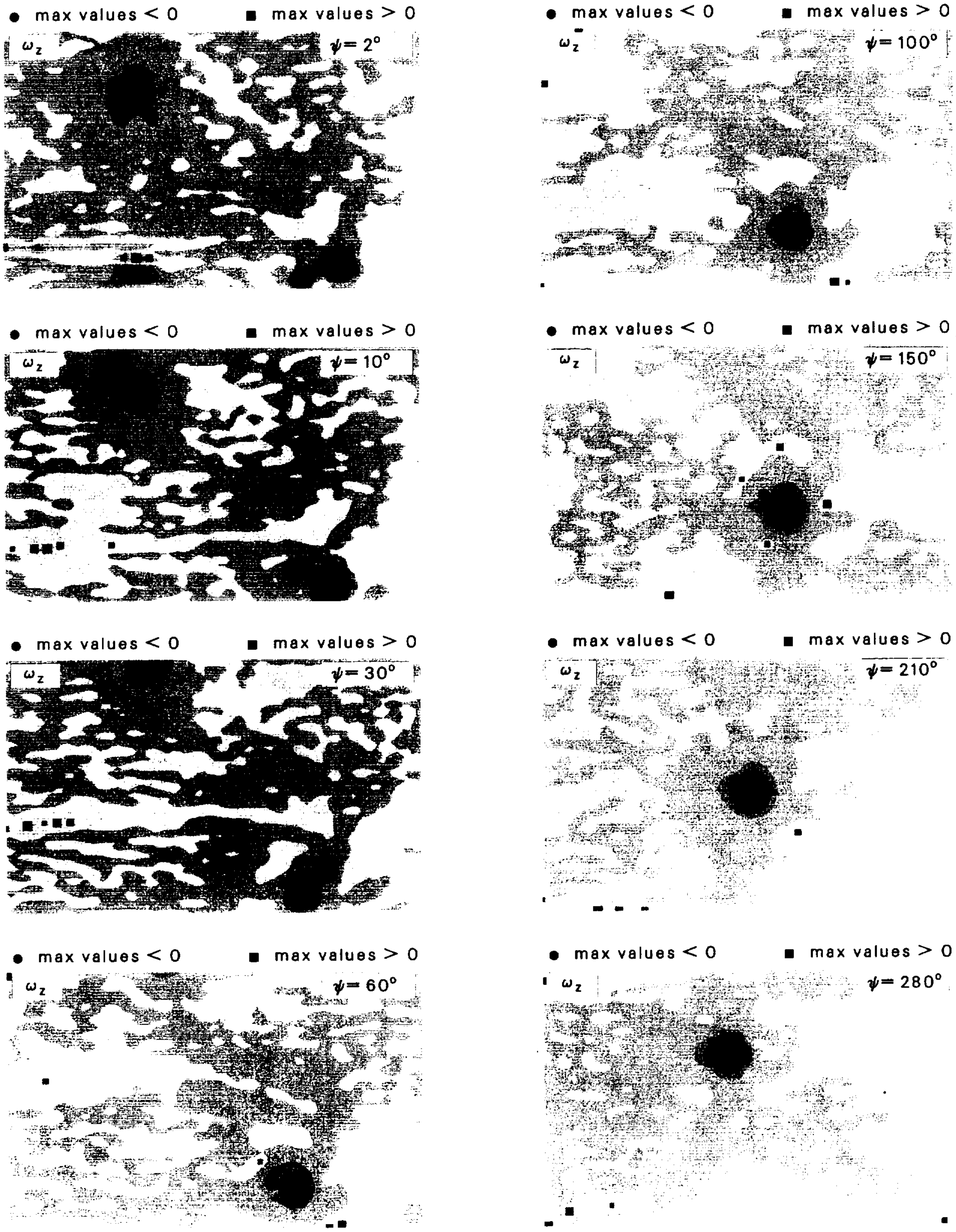

Figure 55: Locations of ω_z extrema at $\psi = 2° \rightarrow 280°$ for the +5° vortex generator case.

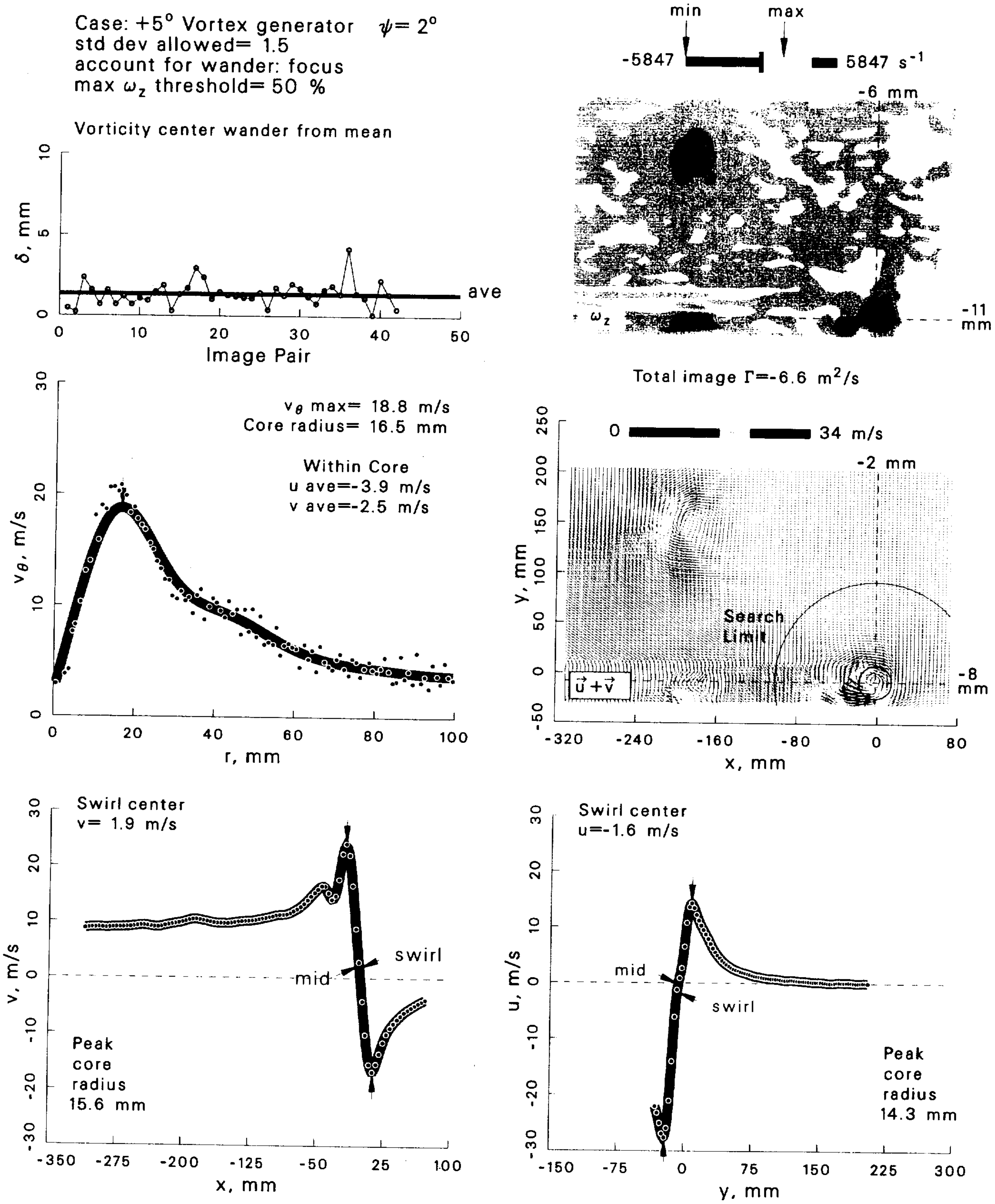

Figure 56: Vortex statistics at $\psi = 2°$ for the +5° vortex generator case.

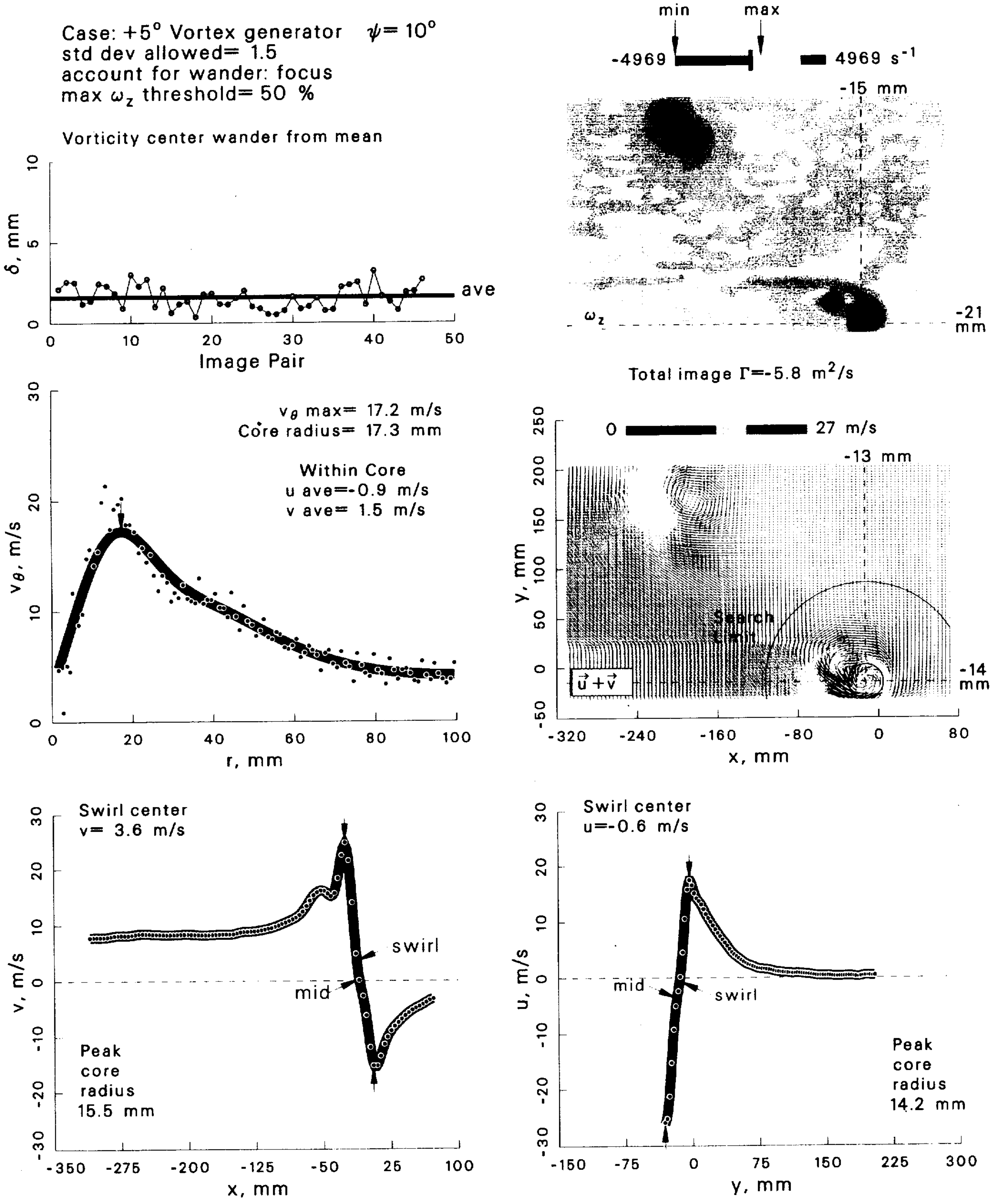

Figure 57: Vortex statistics at $\psi = 10°$ for the +5° vortex generator case.

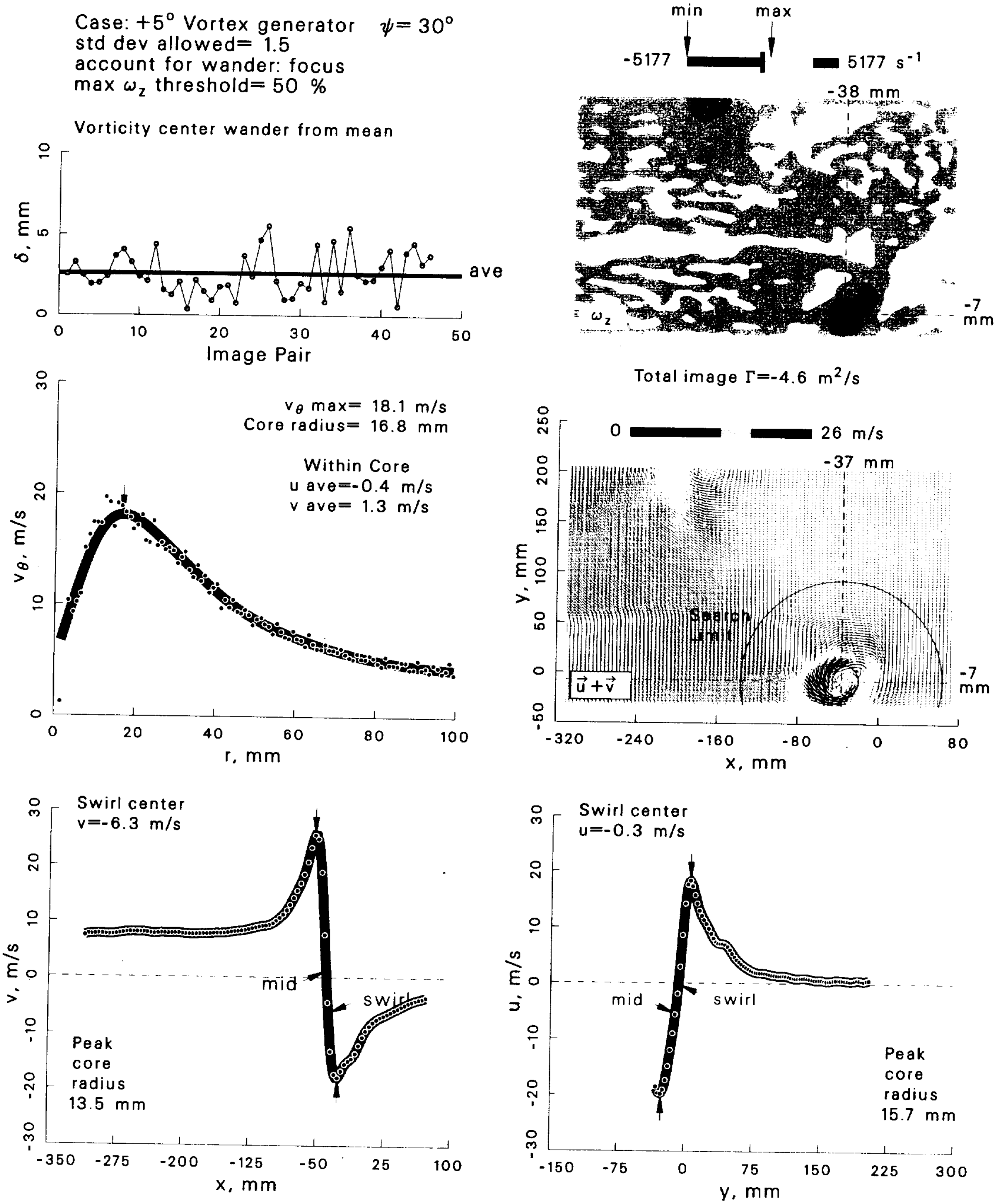

Figure 58: Vortex statistics at $\psi = 30°$ for the +5° vortex generator case.

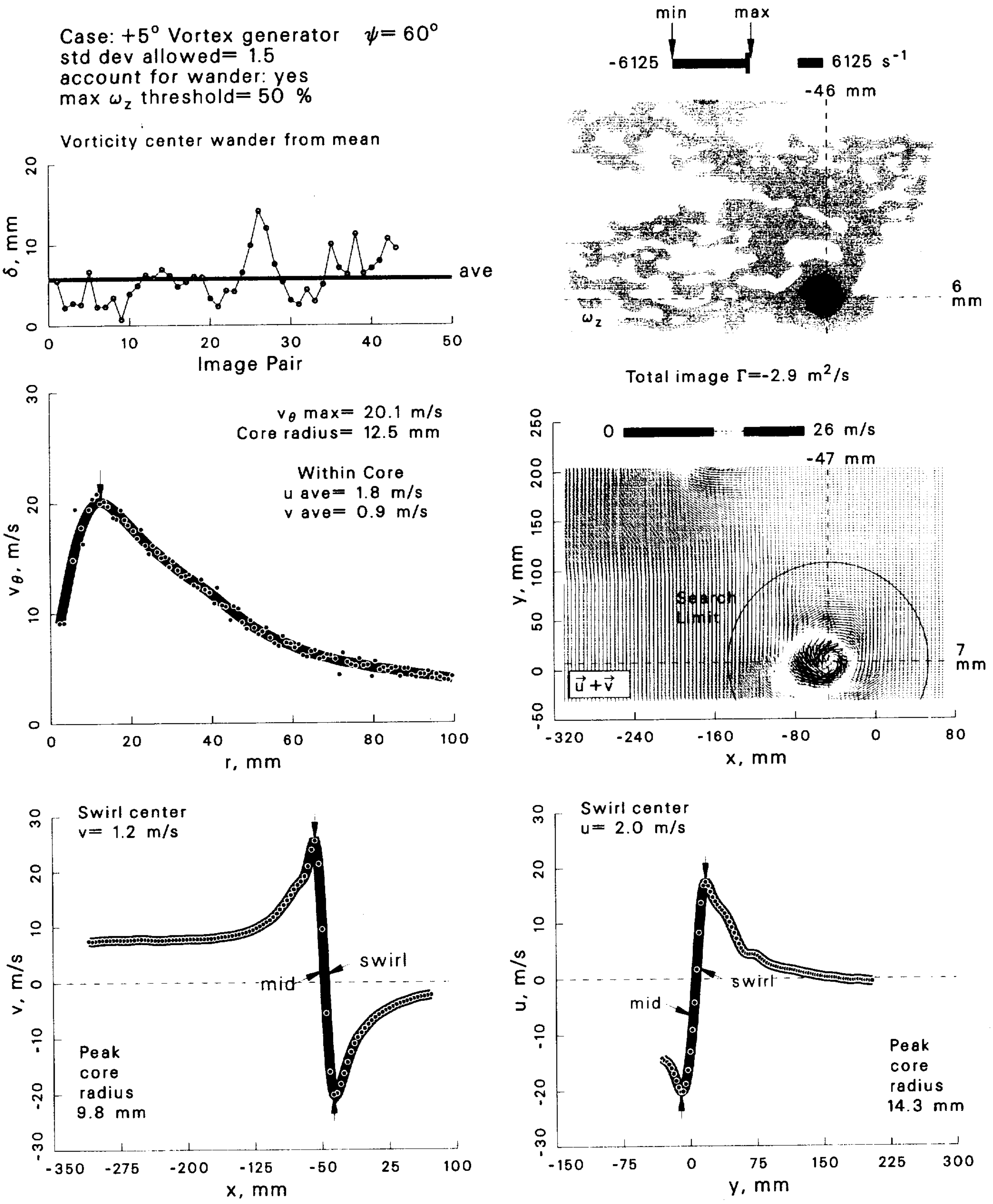

Figure 59: Vortex statistics at $\psi = 60°$ for the +5° vortex generator case.

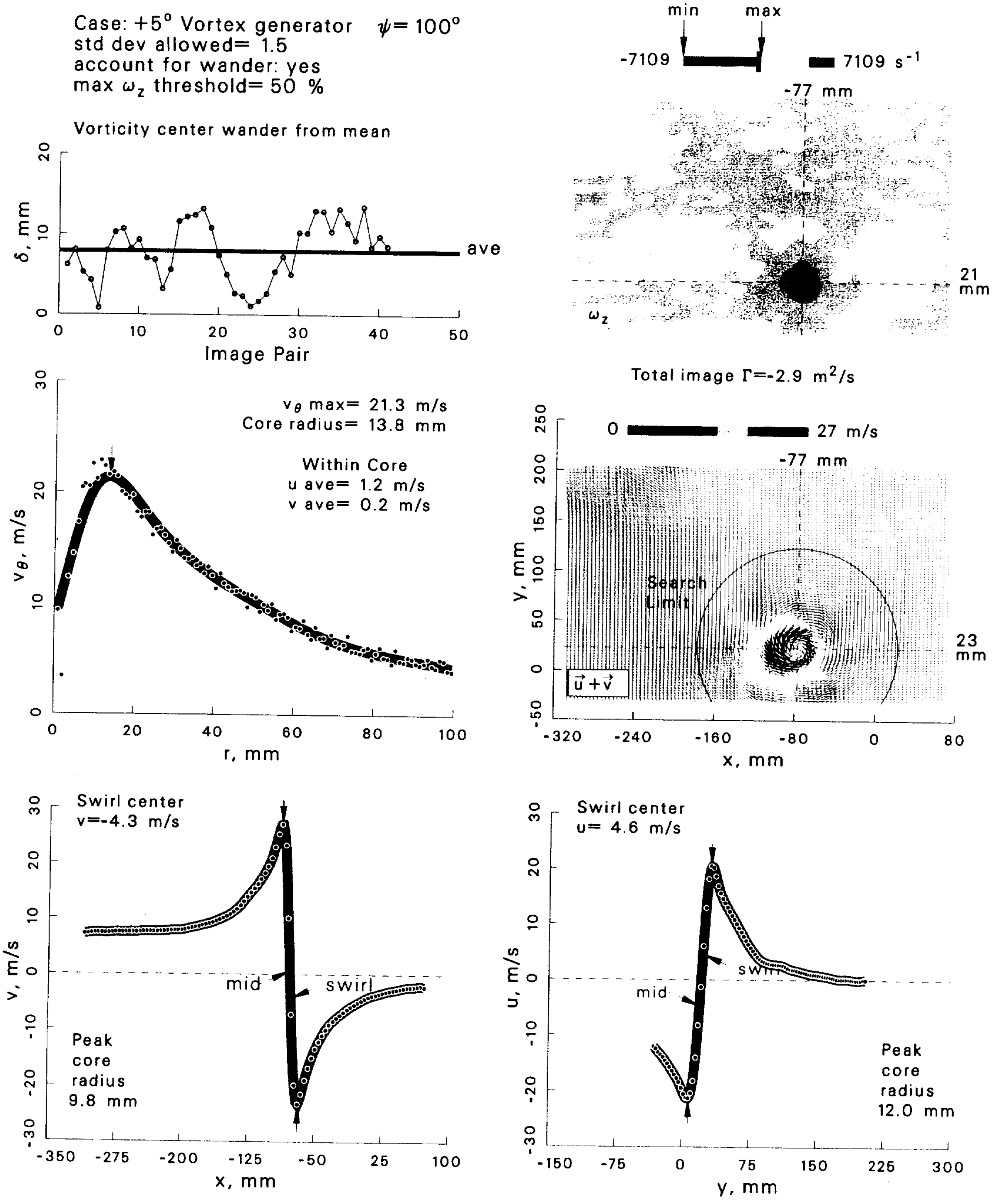

Figure 60: Vortex statistics at $\psi = 100°$ for the +5° vortex generator case.

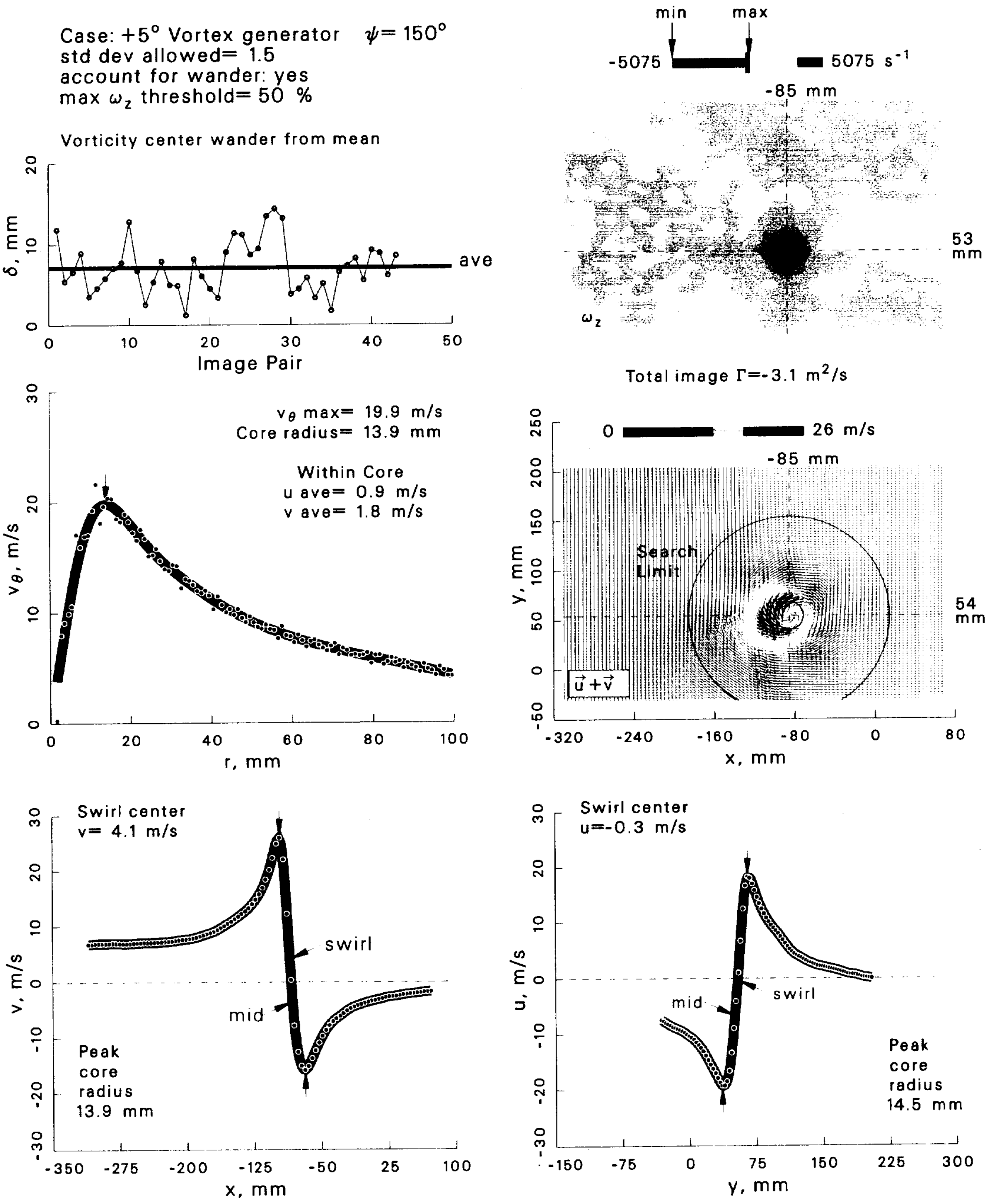

Figure 61: Vortex statistics at $\psi = 150°$ for the +5° vortex generator case.

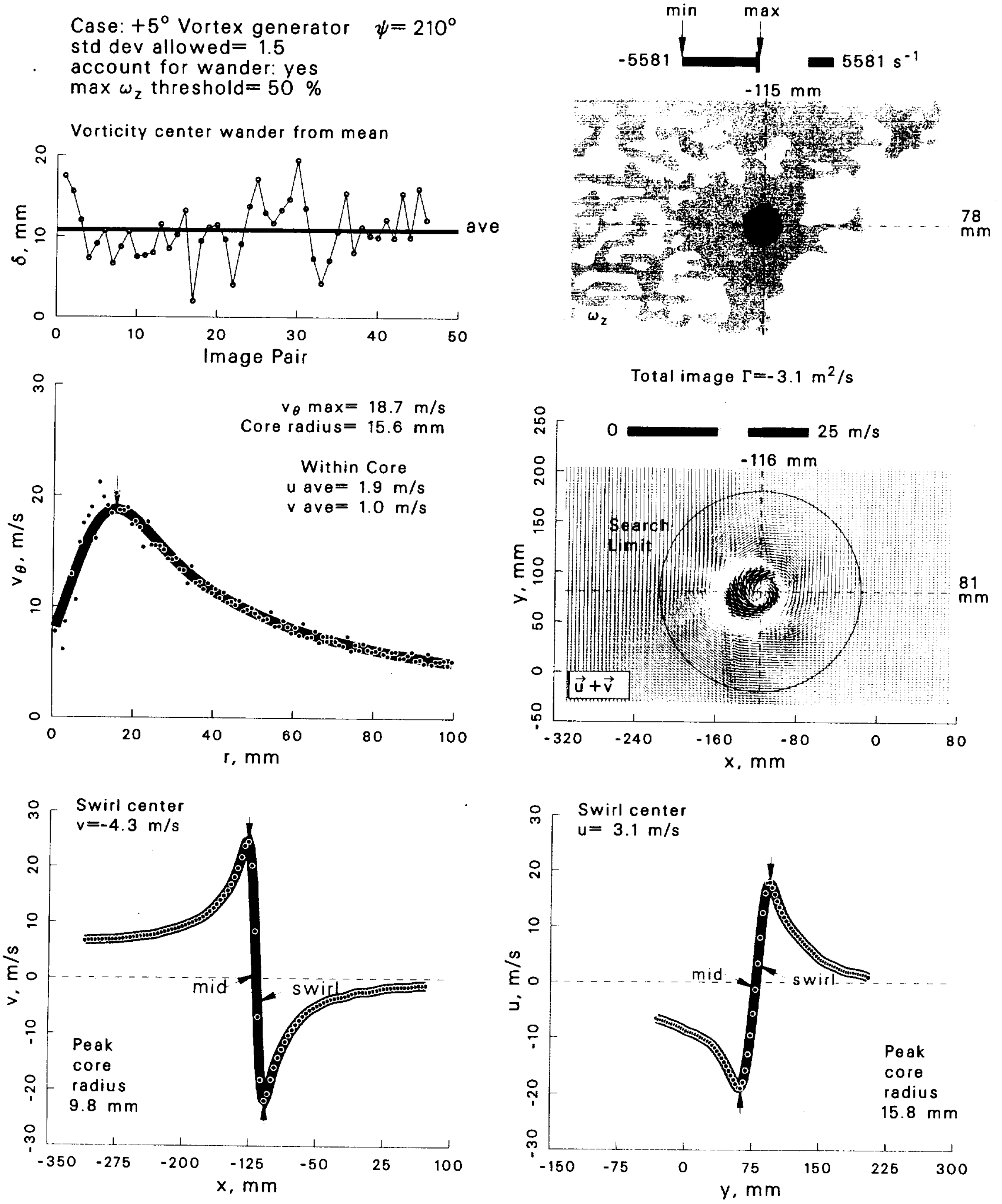

Figure 62: Vortex statistics at $\psi = 210^\circ$ for the $+5^\circ$ vortex generator case.

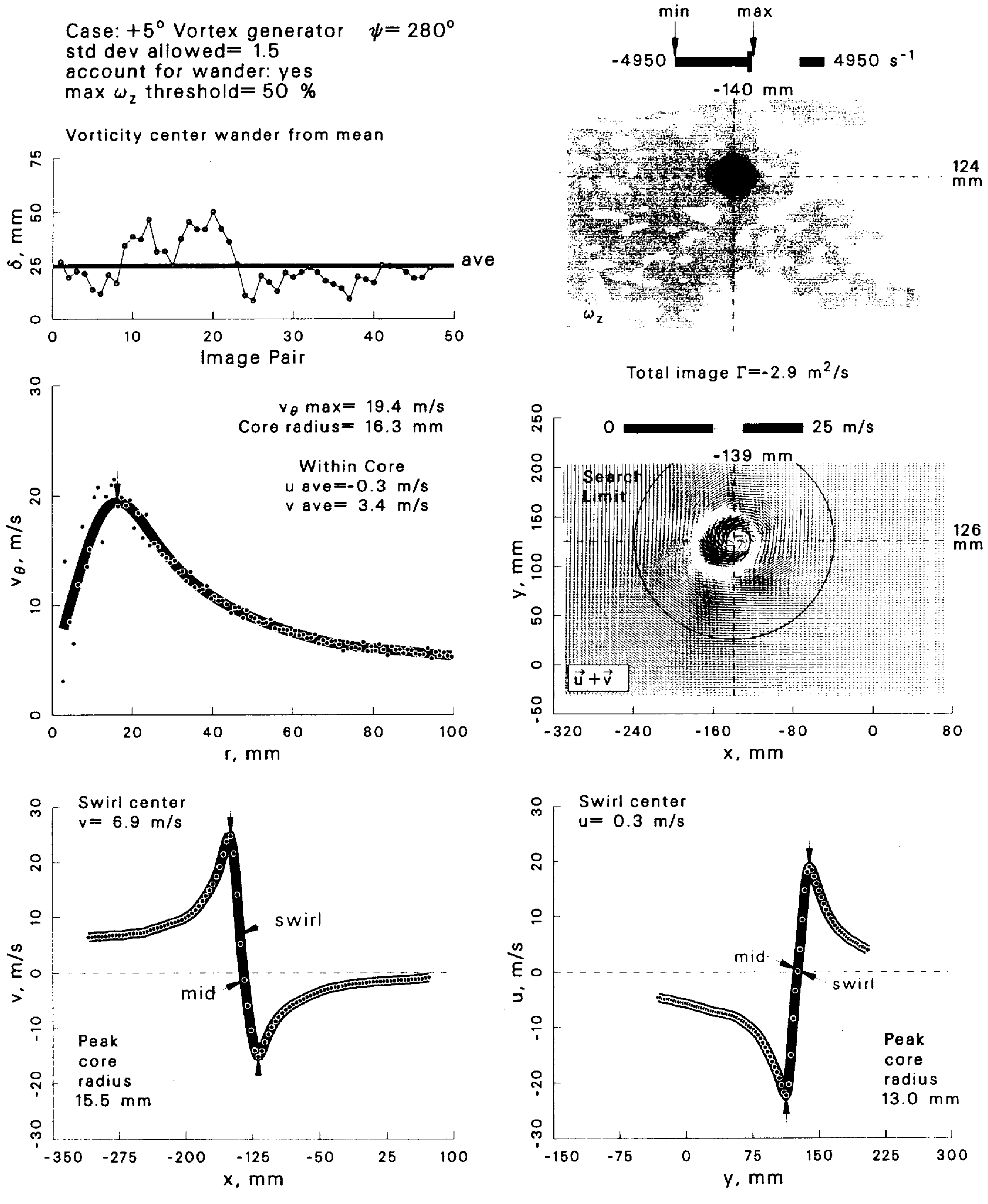

Figure 63: Vortex statistics at $\psi = 280°$ for the +5° vortex generator case.

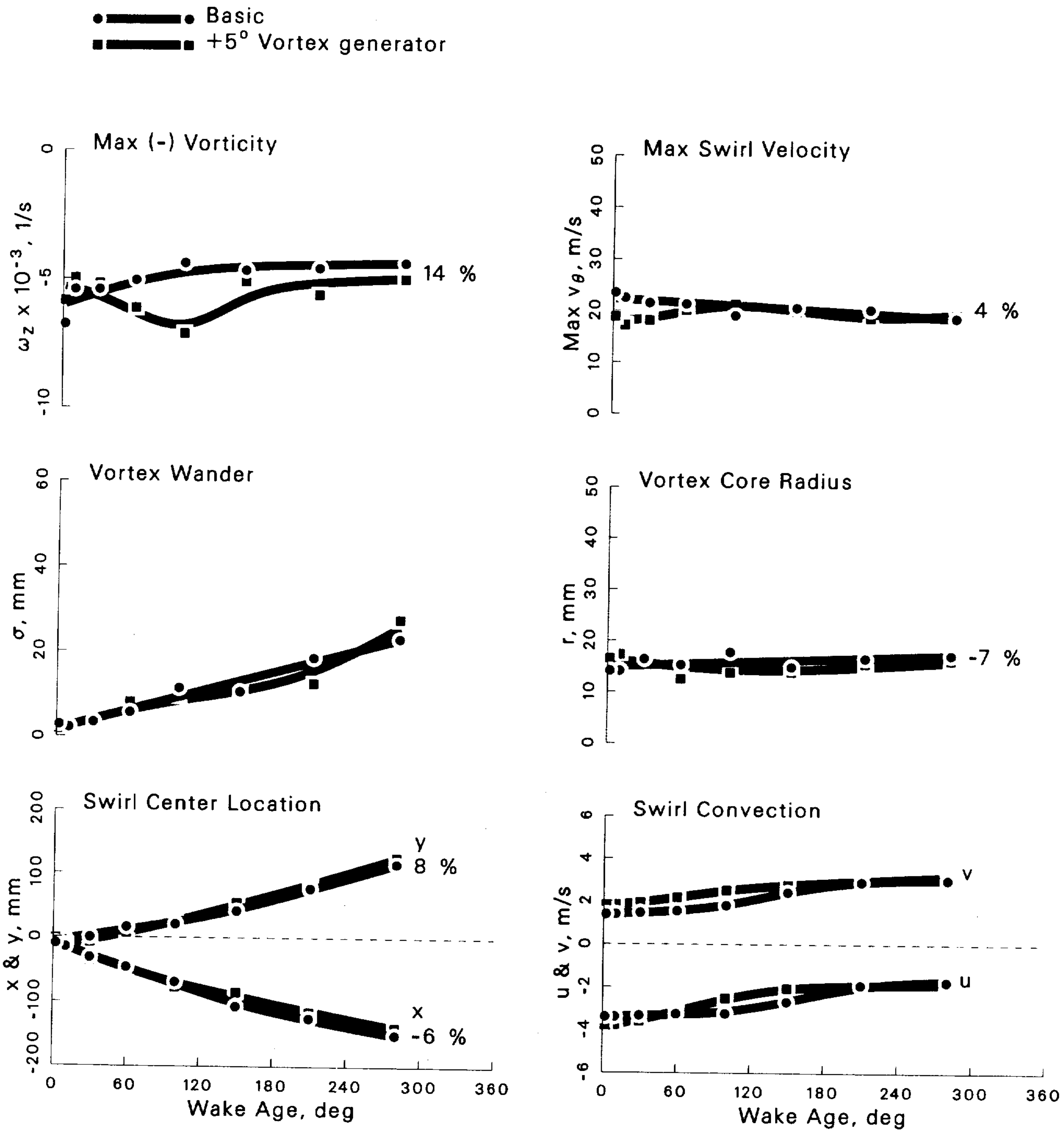

Figure 64: Summary of vortex development from $\psi = 2° \rightarrow 280°$ for the +5° vortex generator case.

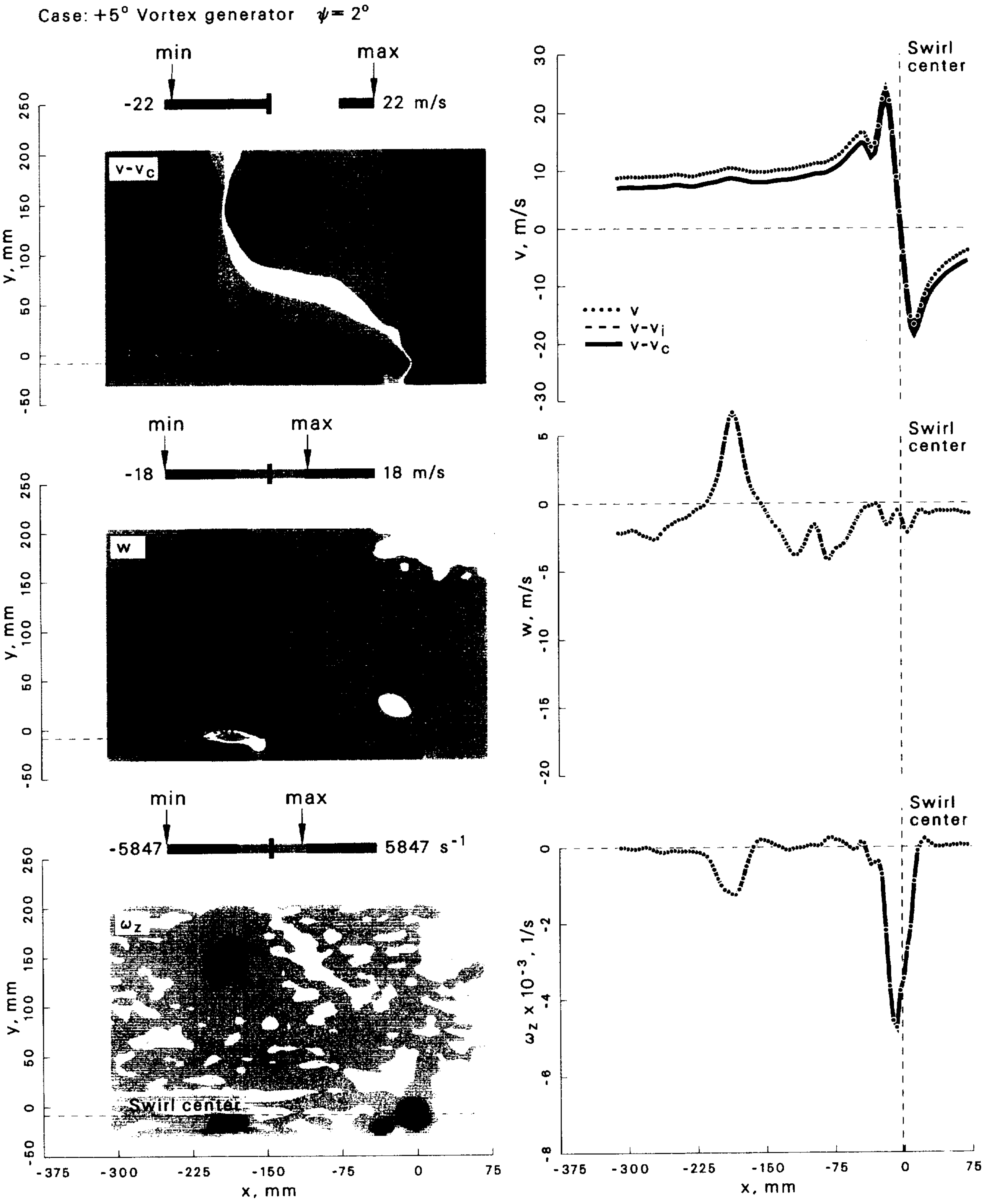

Figure 65: Velocity and vorticity components at $\psi = 2°$ for the $+5°$ vortex generator case.

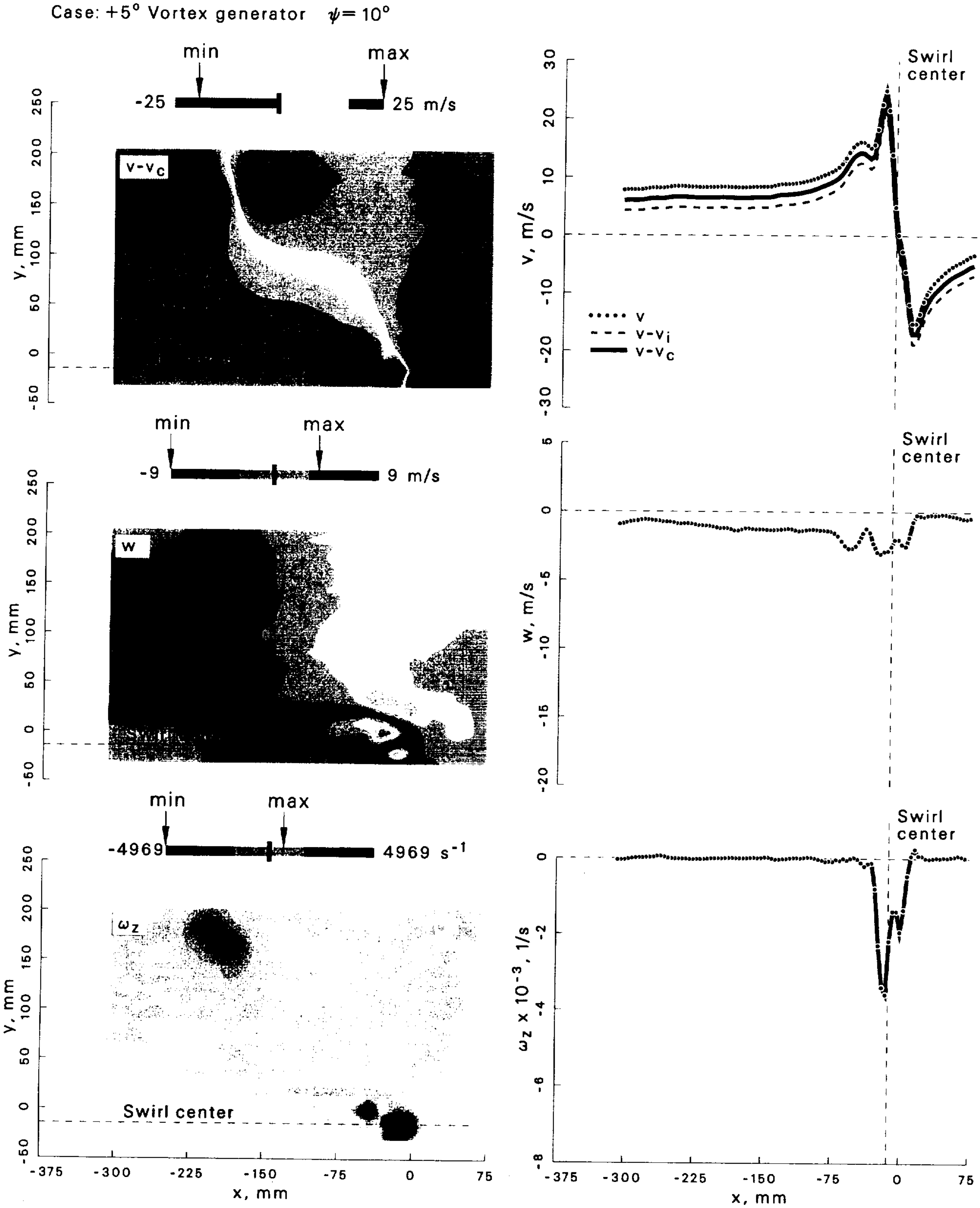

Figure 66: Velocity and vorticity components at $\psi = 10°$ for the +5° vortex generator case.

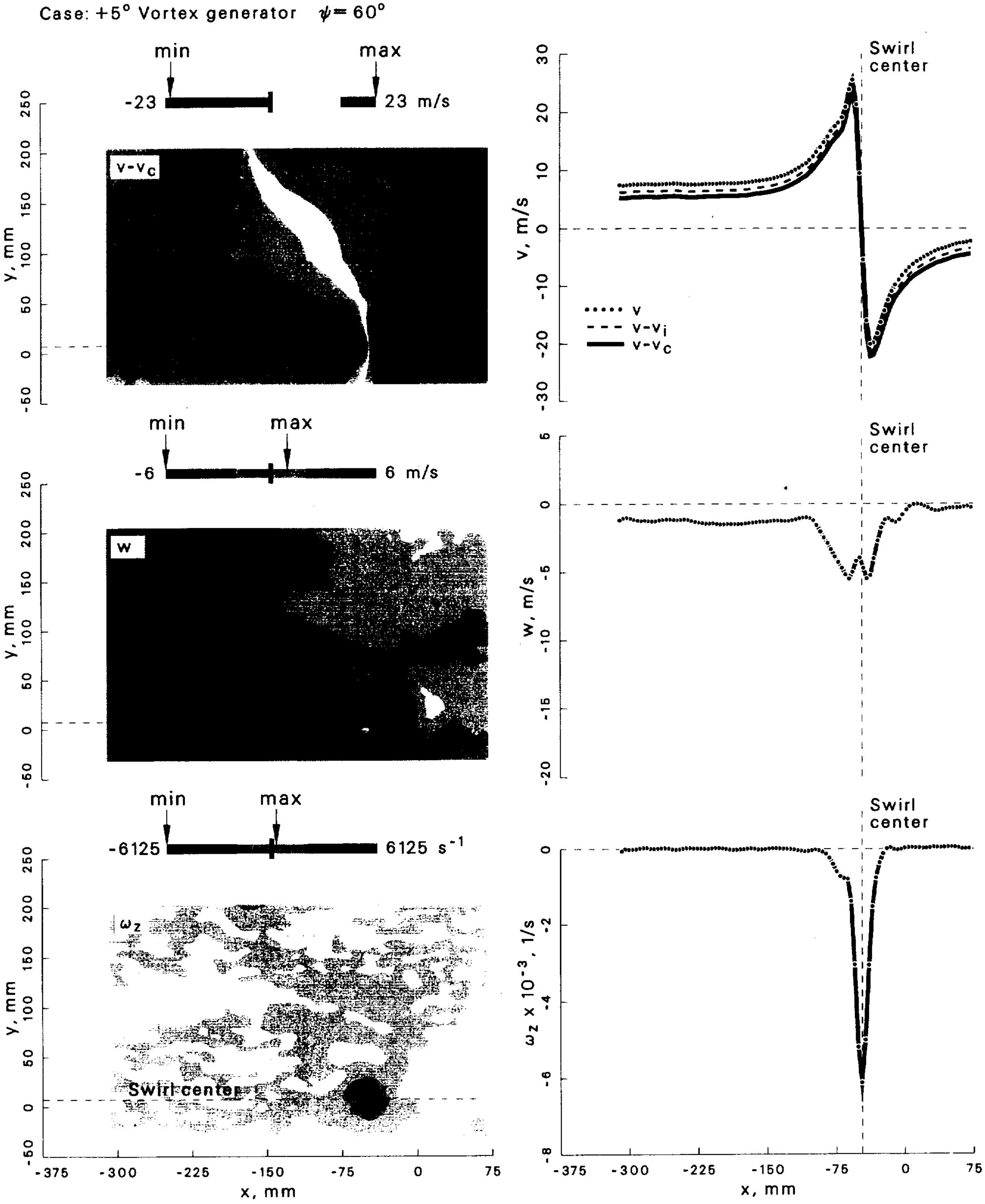

Figure 67: Velocity and vorticity components at $\psi = 60°$ for the $+5°$ vortex generator case.

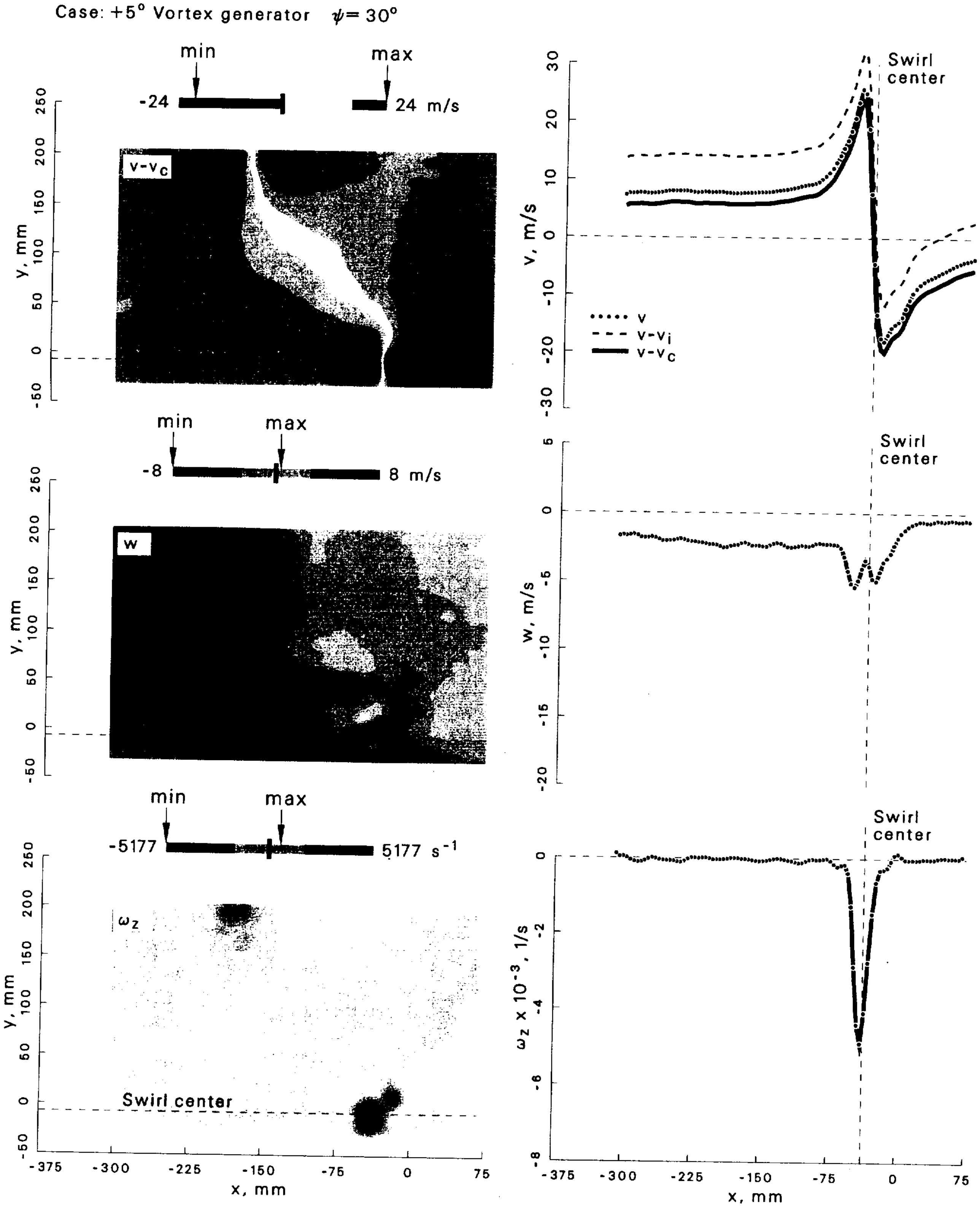

Figure 68: Velocity and vorticity components at $\psi = 30°$ for the $+5°$ vortex generator case.

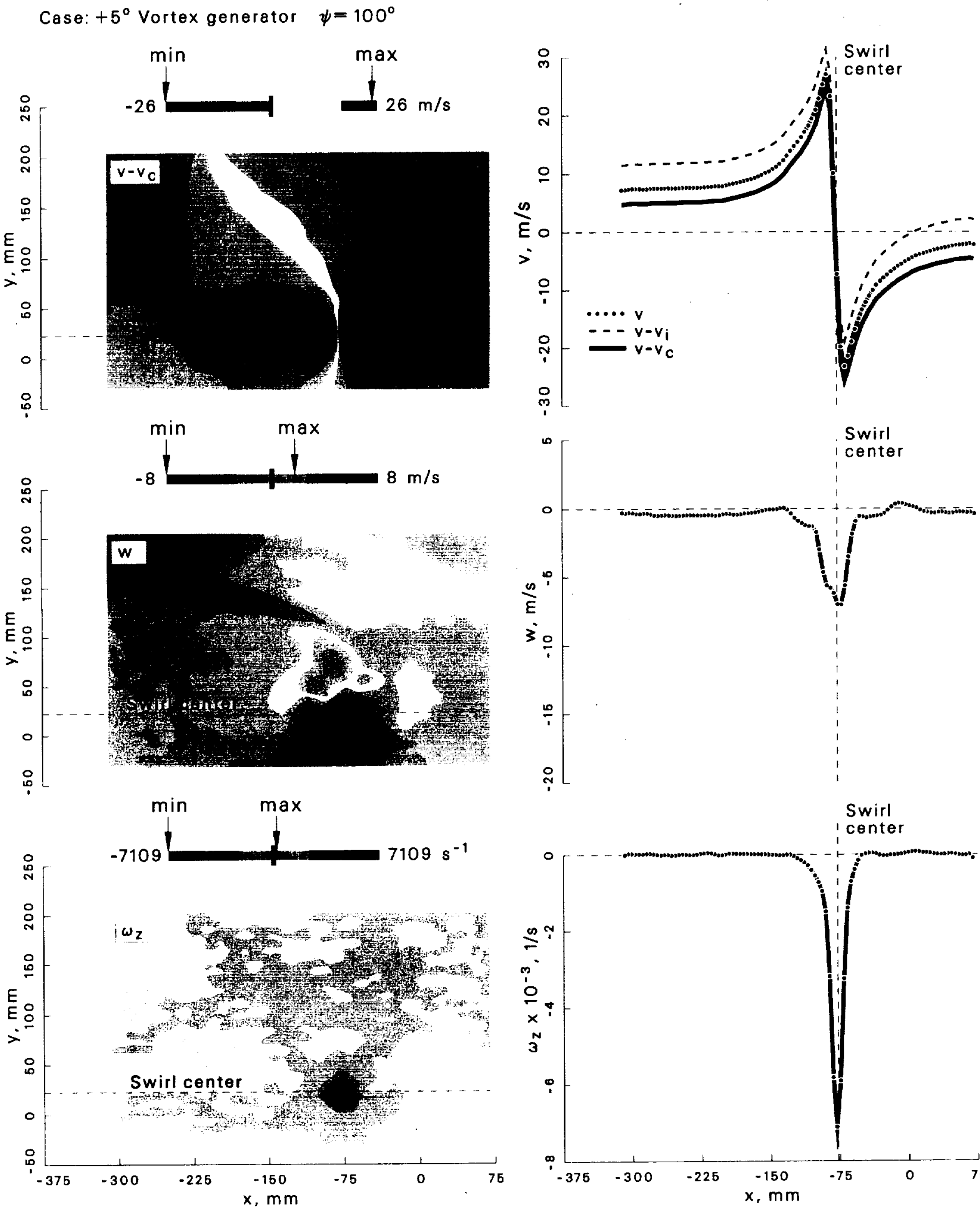

Figure 69: Velocity and vorticity components at $\psi = 100°$ for the +5° vortex generator case.

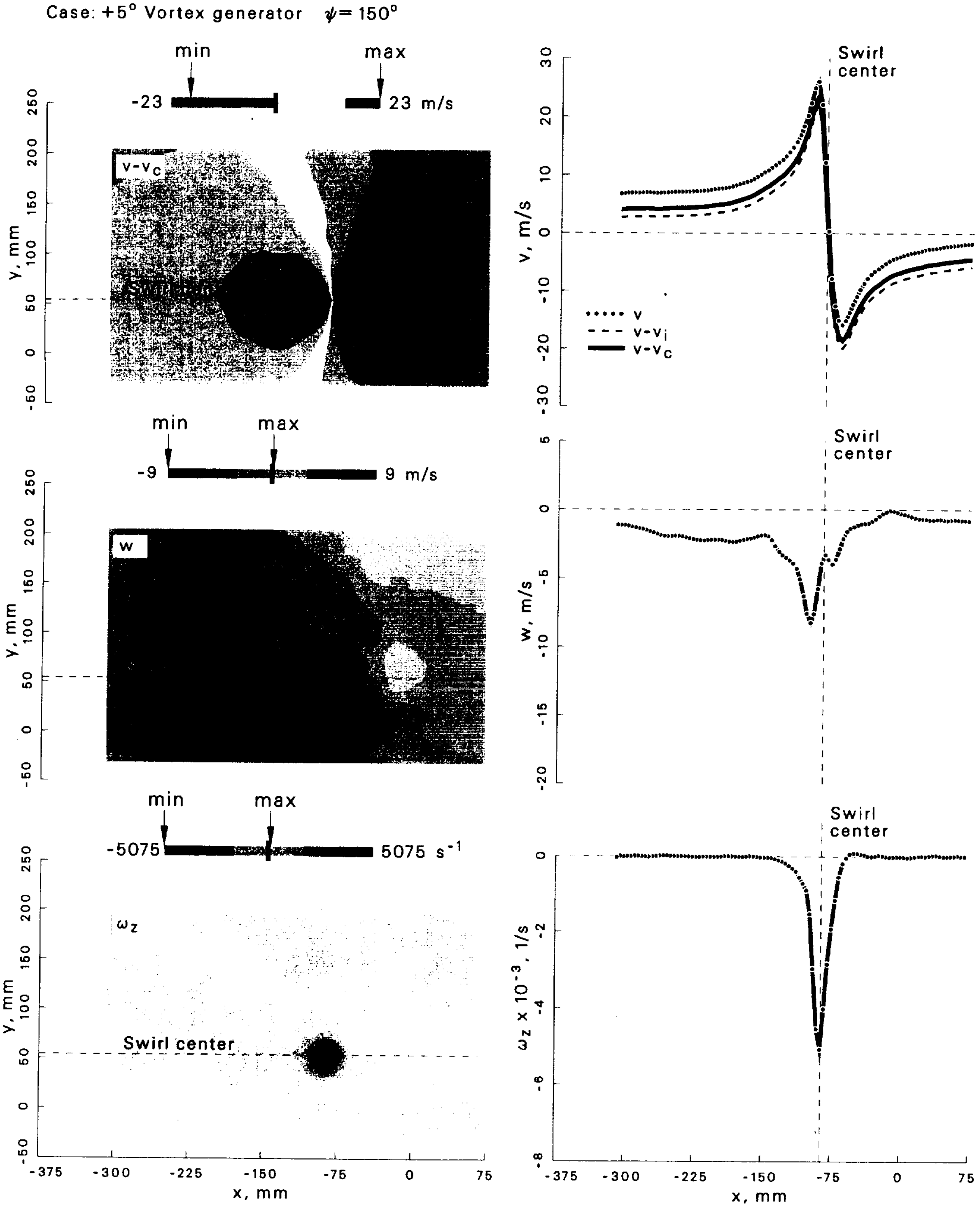

Figure 70: Velocity and vorticity components at $\psi = 150°$ for the $+5°$ vortex generator case.

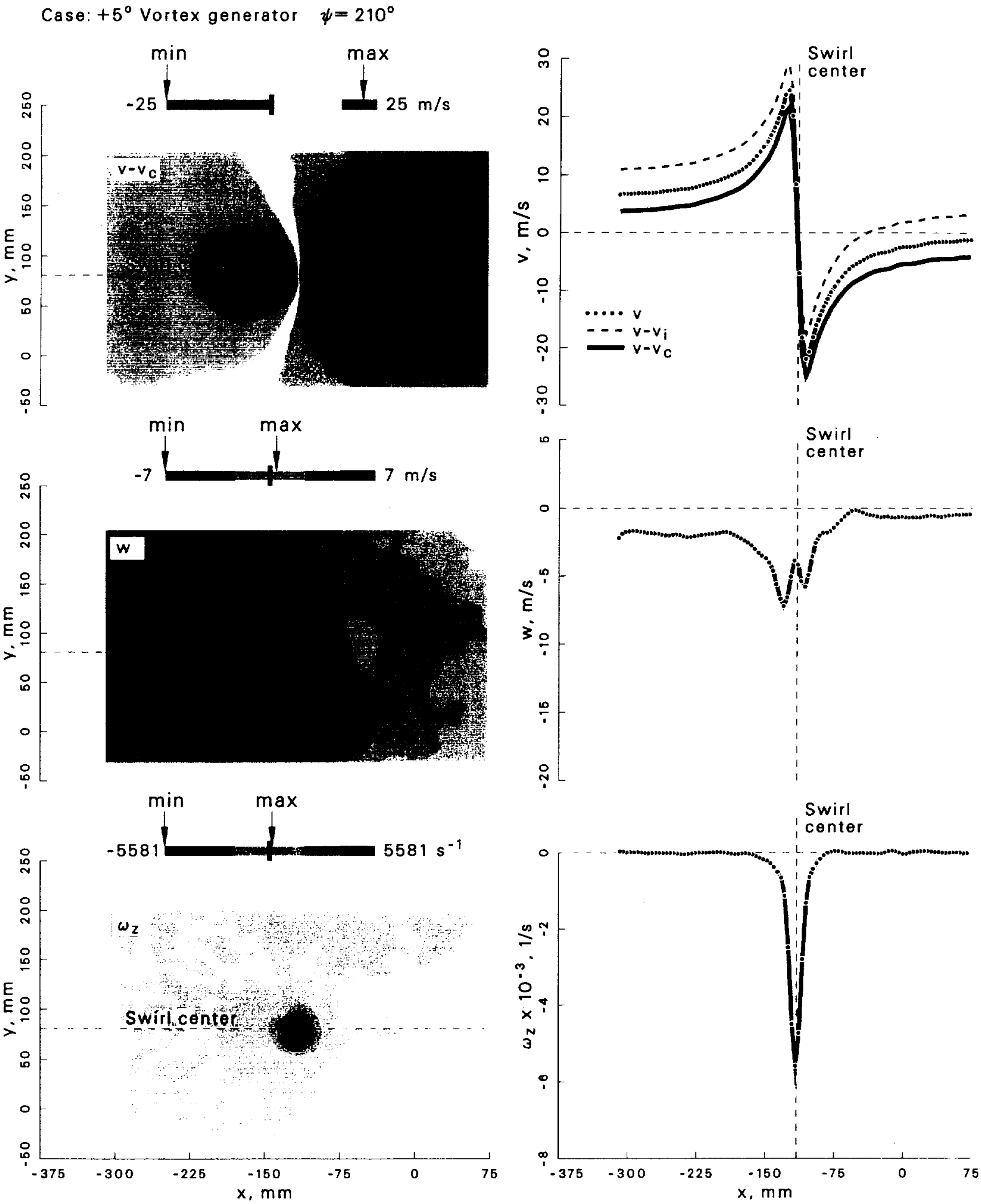

Figure 71: Velocity and vorticity components at $\psi = 210^\circ$ for the $+5^\circ$ vortex generator case.

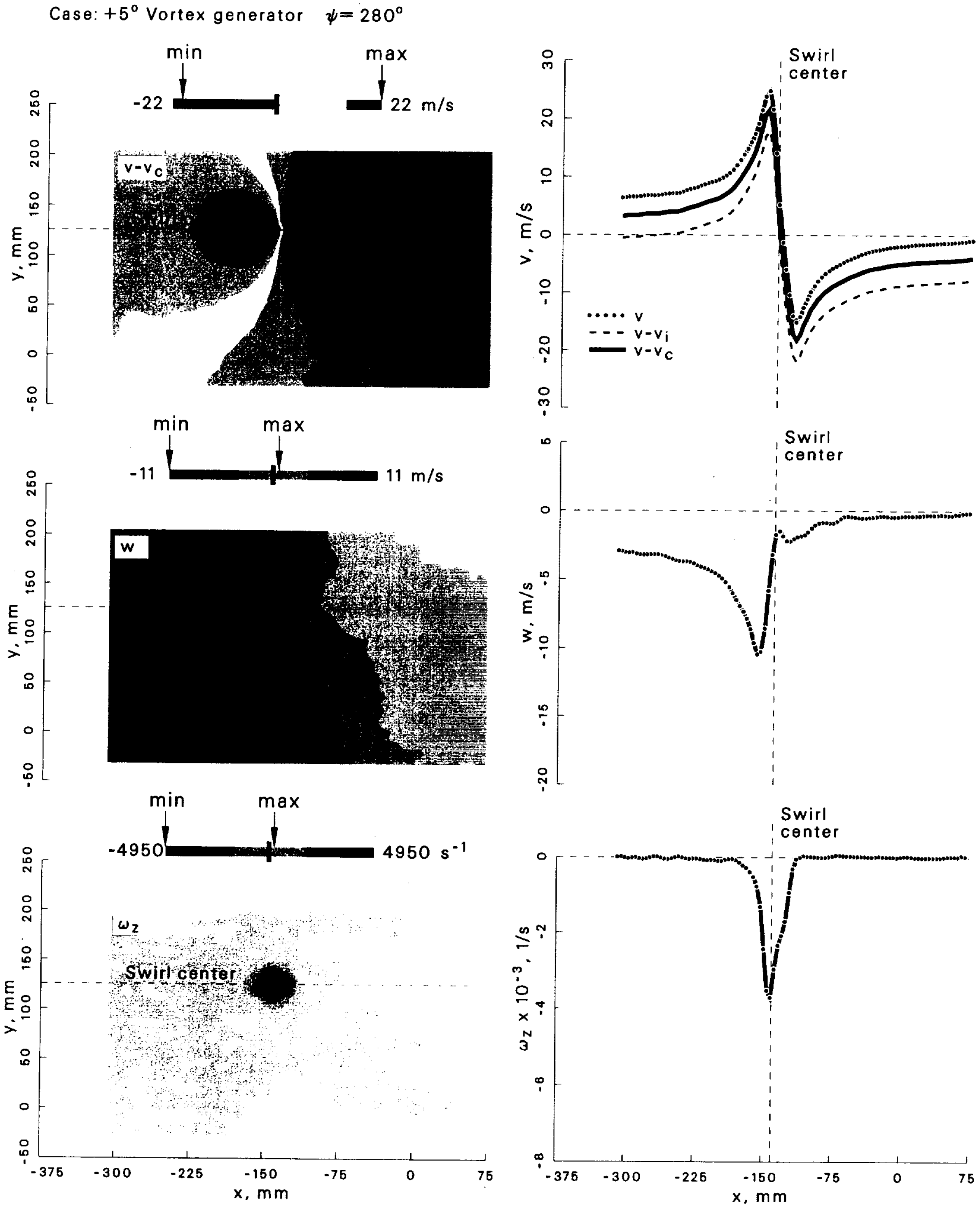

Figure 72: Velocity and vorticity components at $\psi = 280°$ for the +5° vortex generator case.

Case: +10° Vortex generator

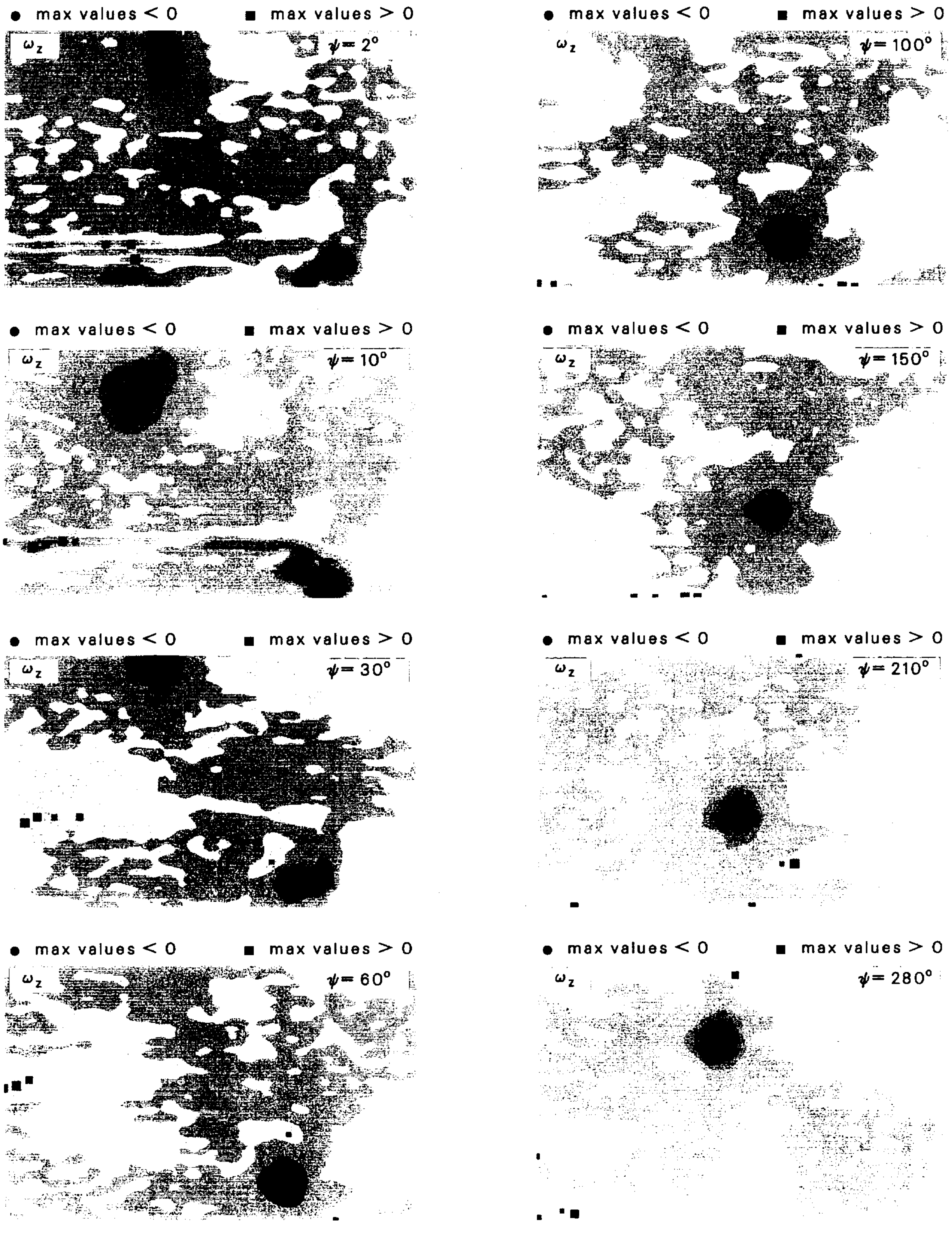

Figure 73: Locations of ω_z extrema at $\psi = 2° \rightarrow 280°$ for the +10° vortex generator case.

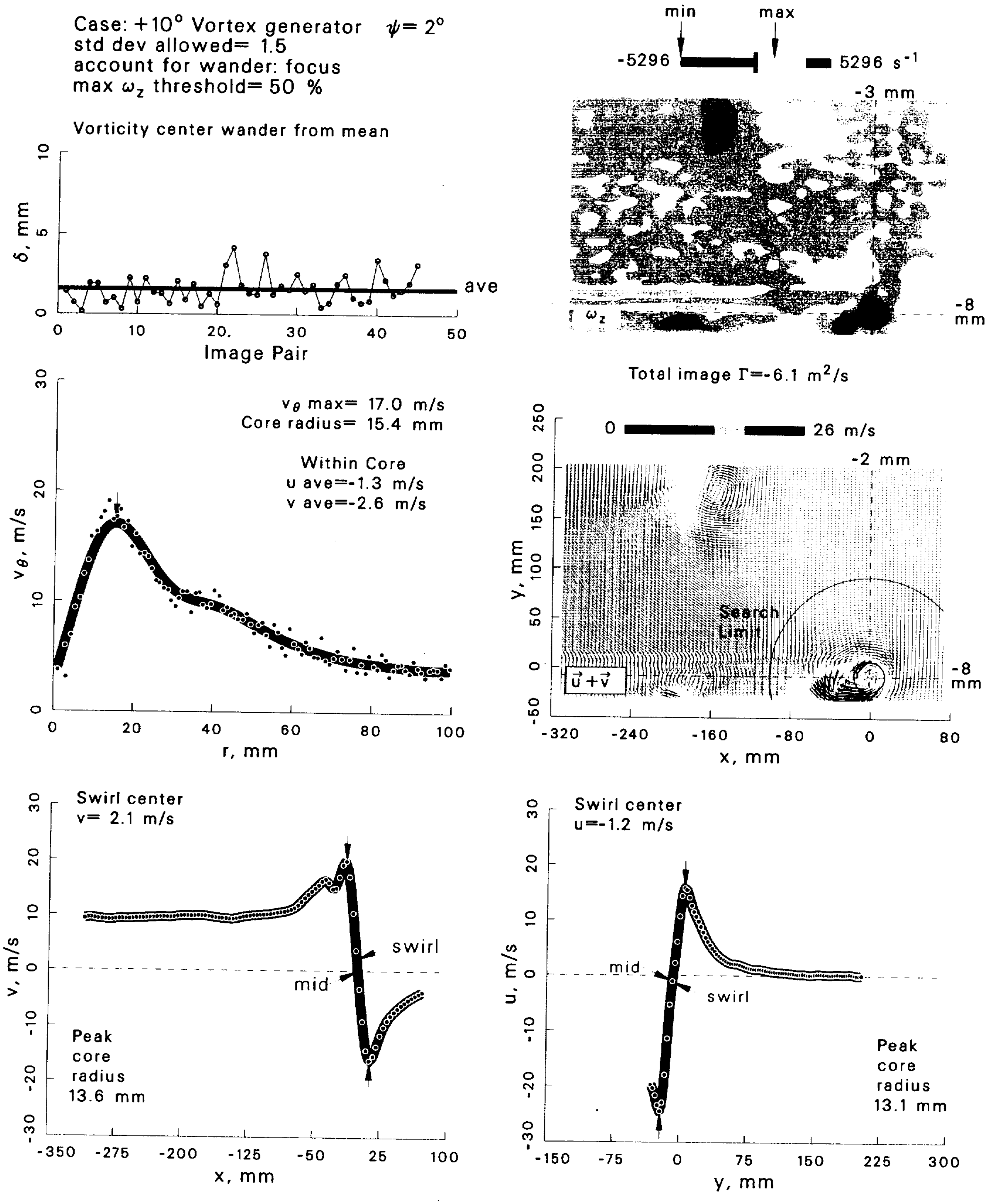

Figure 74: Vortex statistics at $\psi = 2°$ for the +10° vortex generator case.

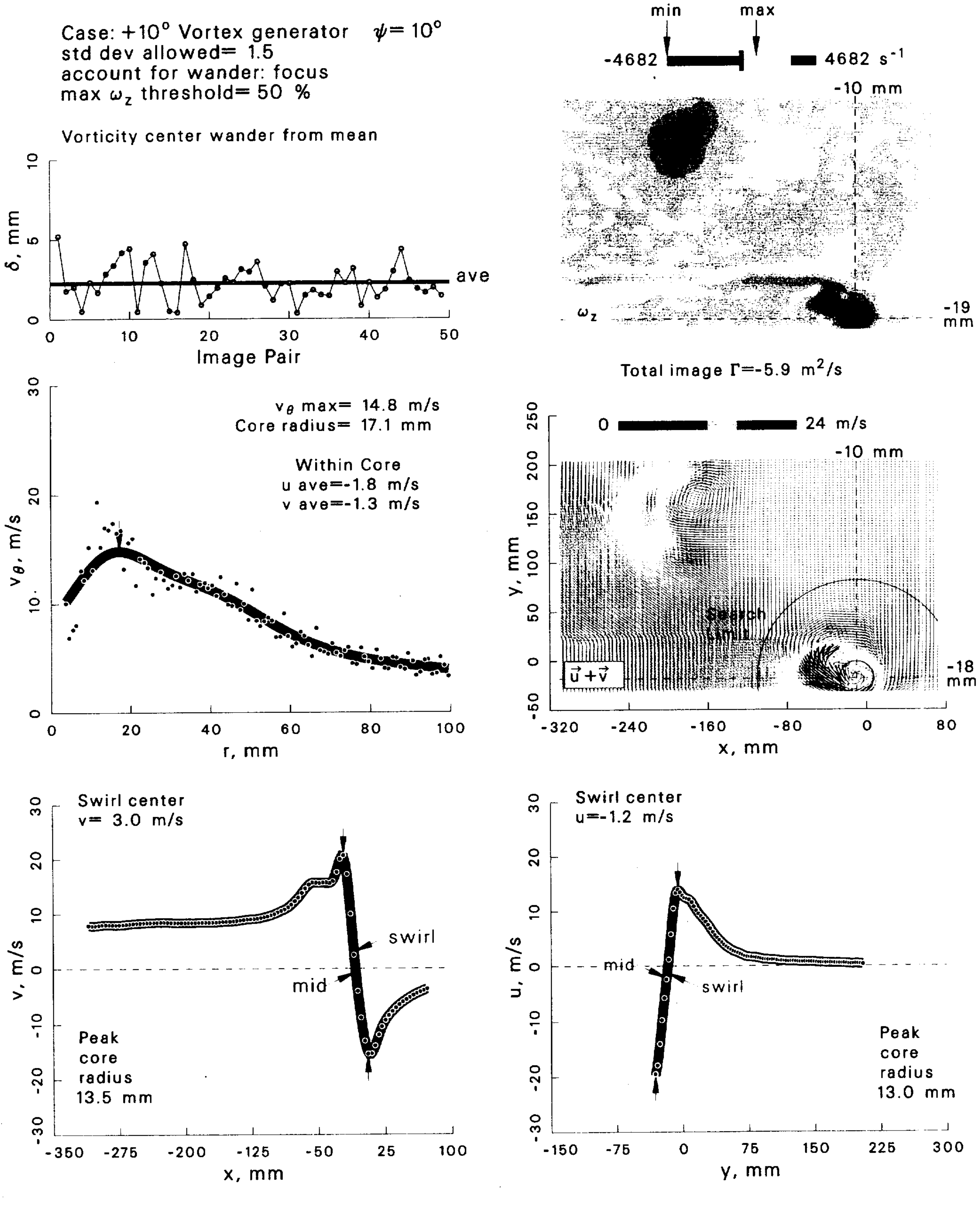

Figure 75: Vortex statistics at $\psi = 10°$ for the +10° vortex generator case.

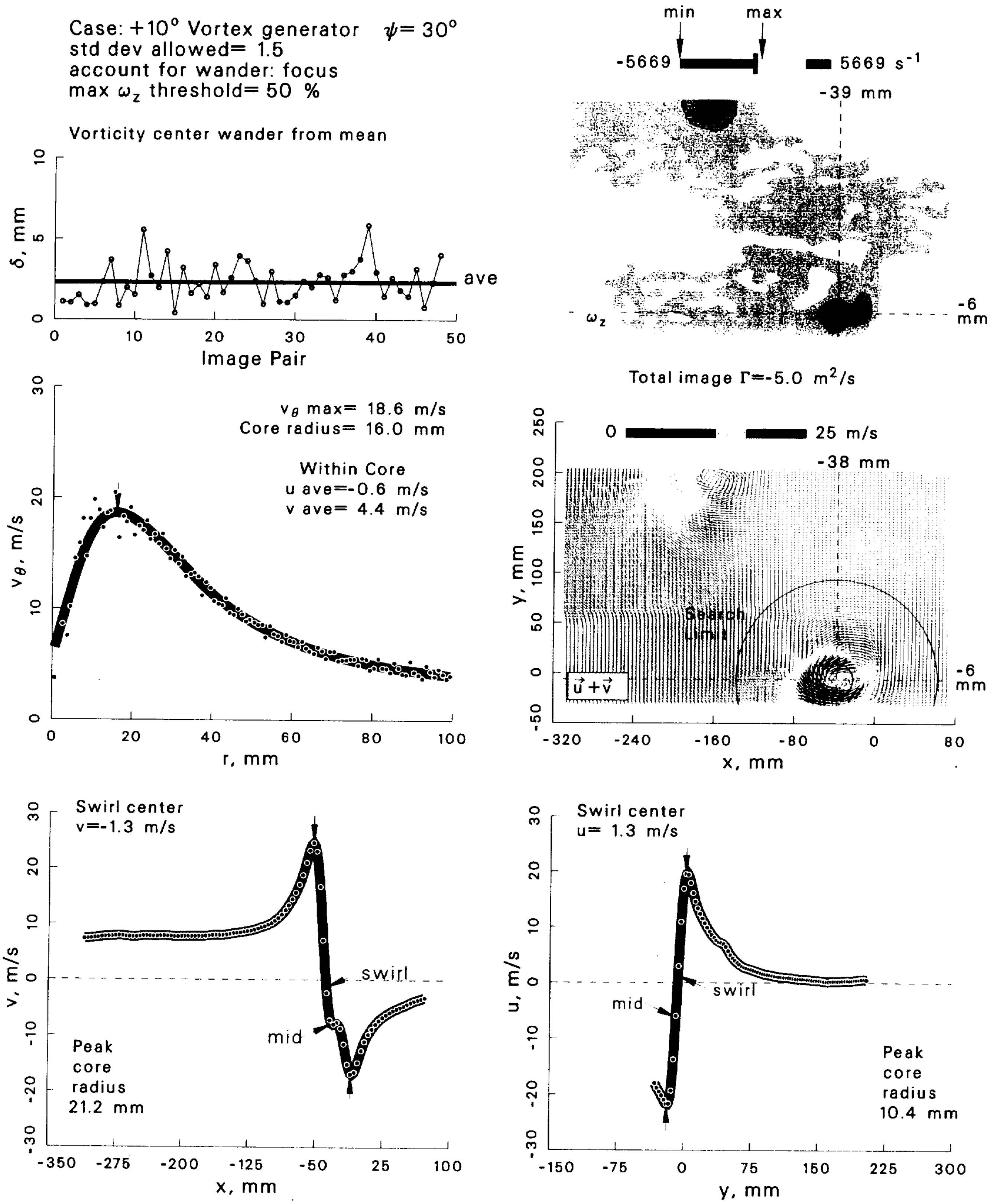

Figure 76: Vortex statistics at $\psi = 30°$ for the +10° vortex generator case.

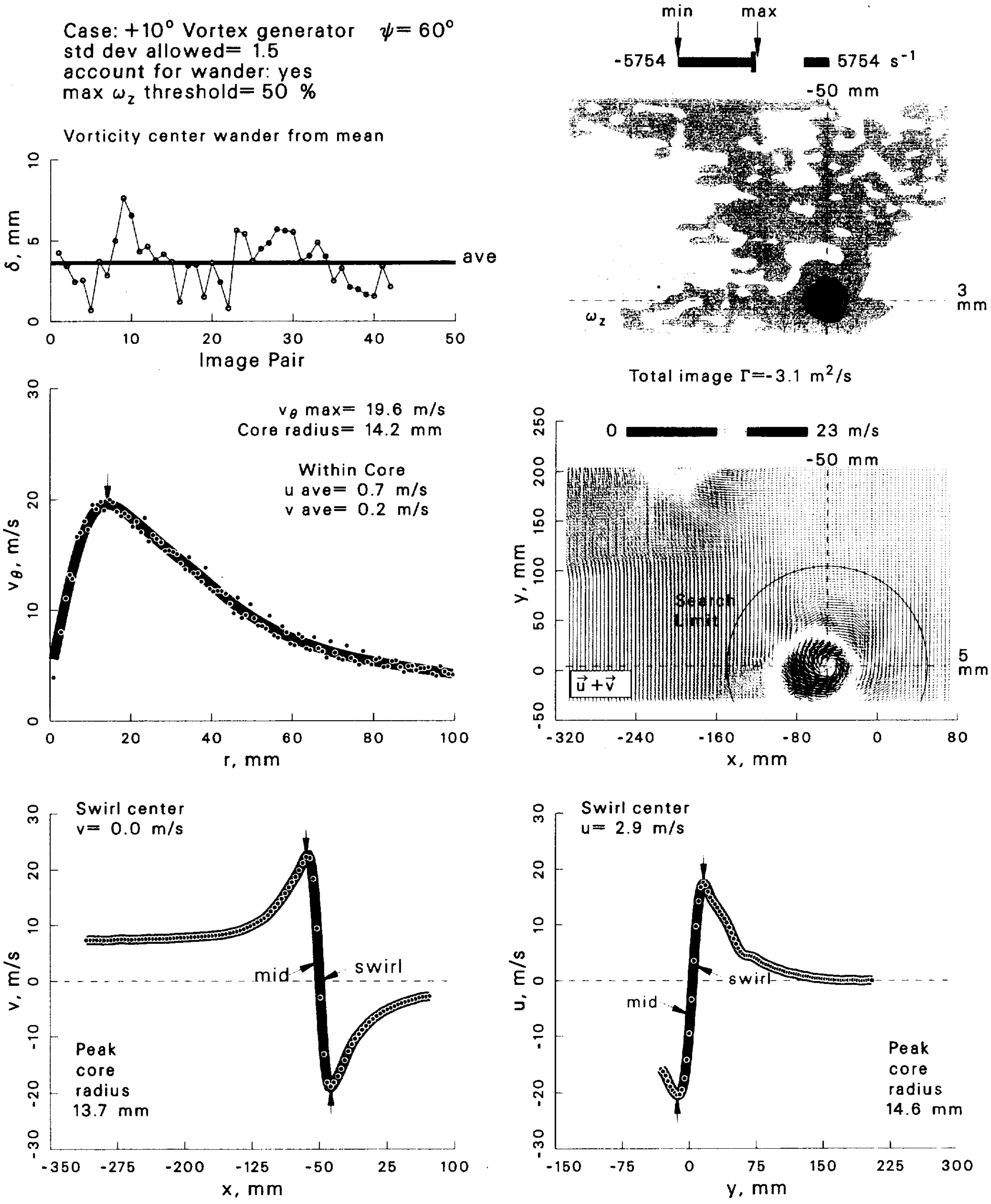

Figure 77: Vortex statistics at $\psi = 60°$ for the $+10°$ vortex generator case.

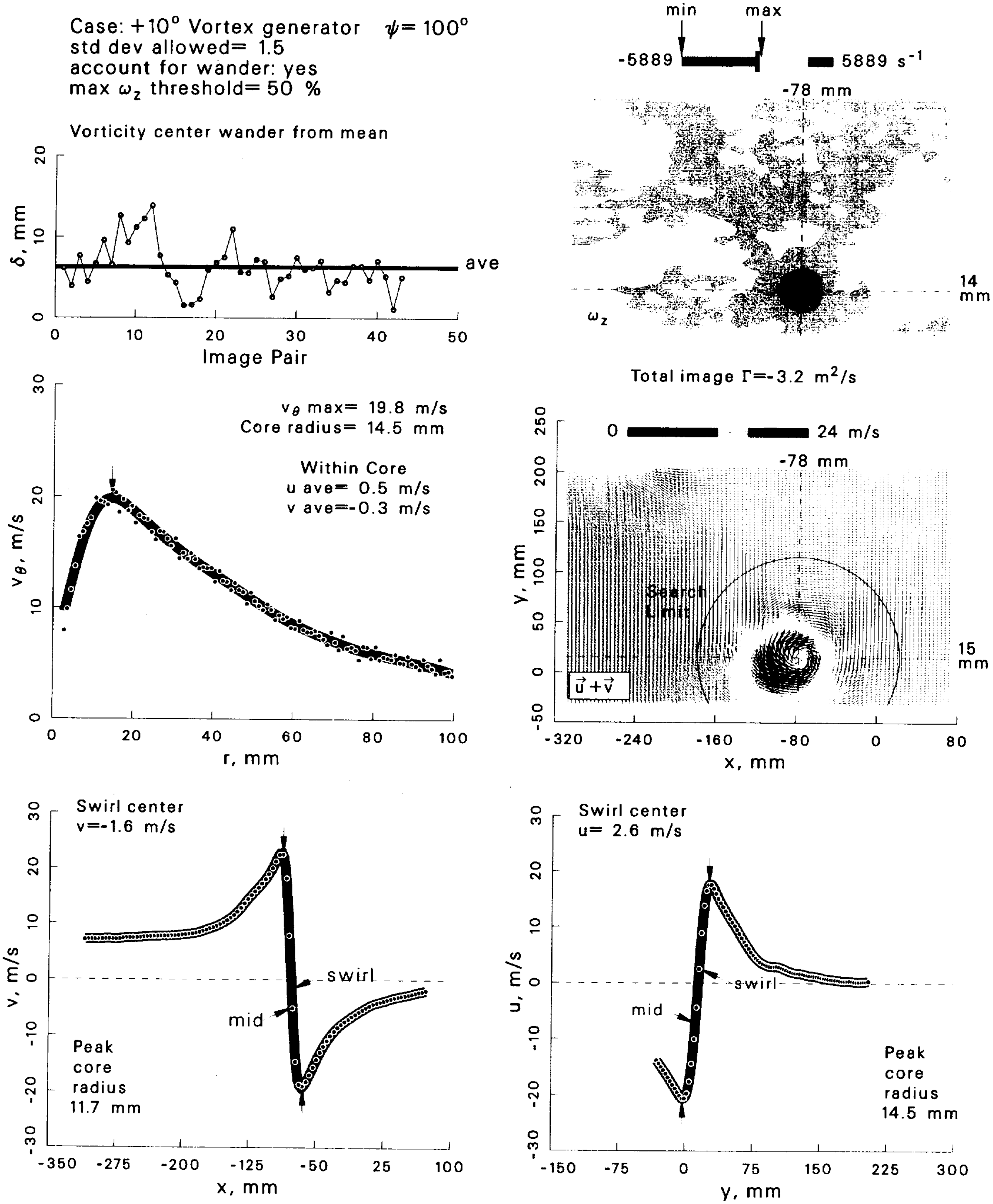

Figure 78: Vortex statistics at $\psi = 100^\circ$ for the +10° vortex generator case.

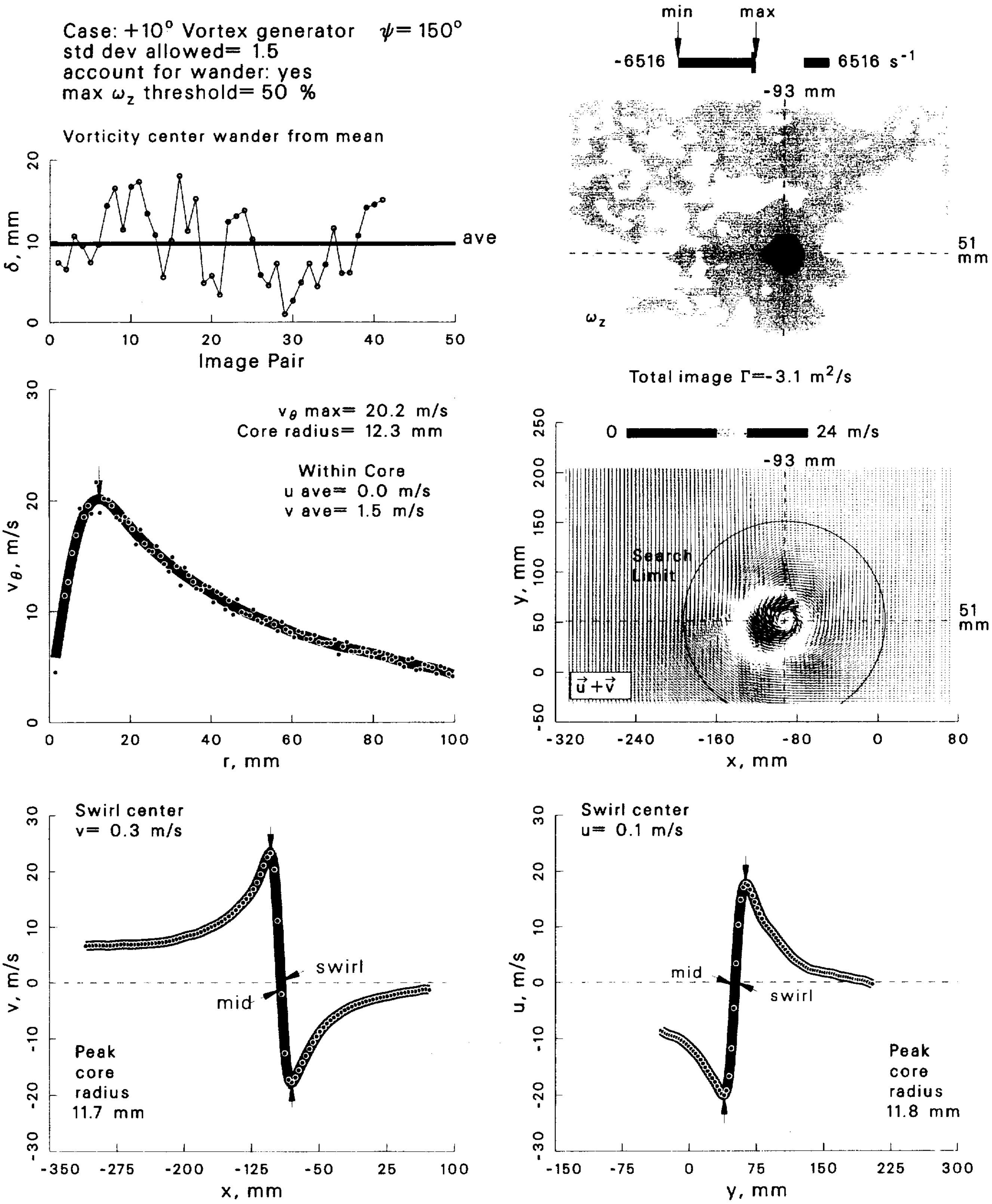

Figure 79: Vortex statistics at $\psi = 150°$ for the +10° vortex generator case.

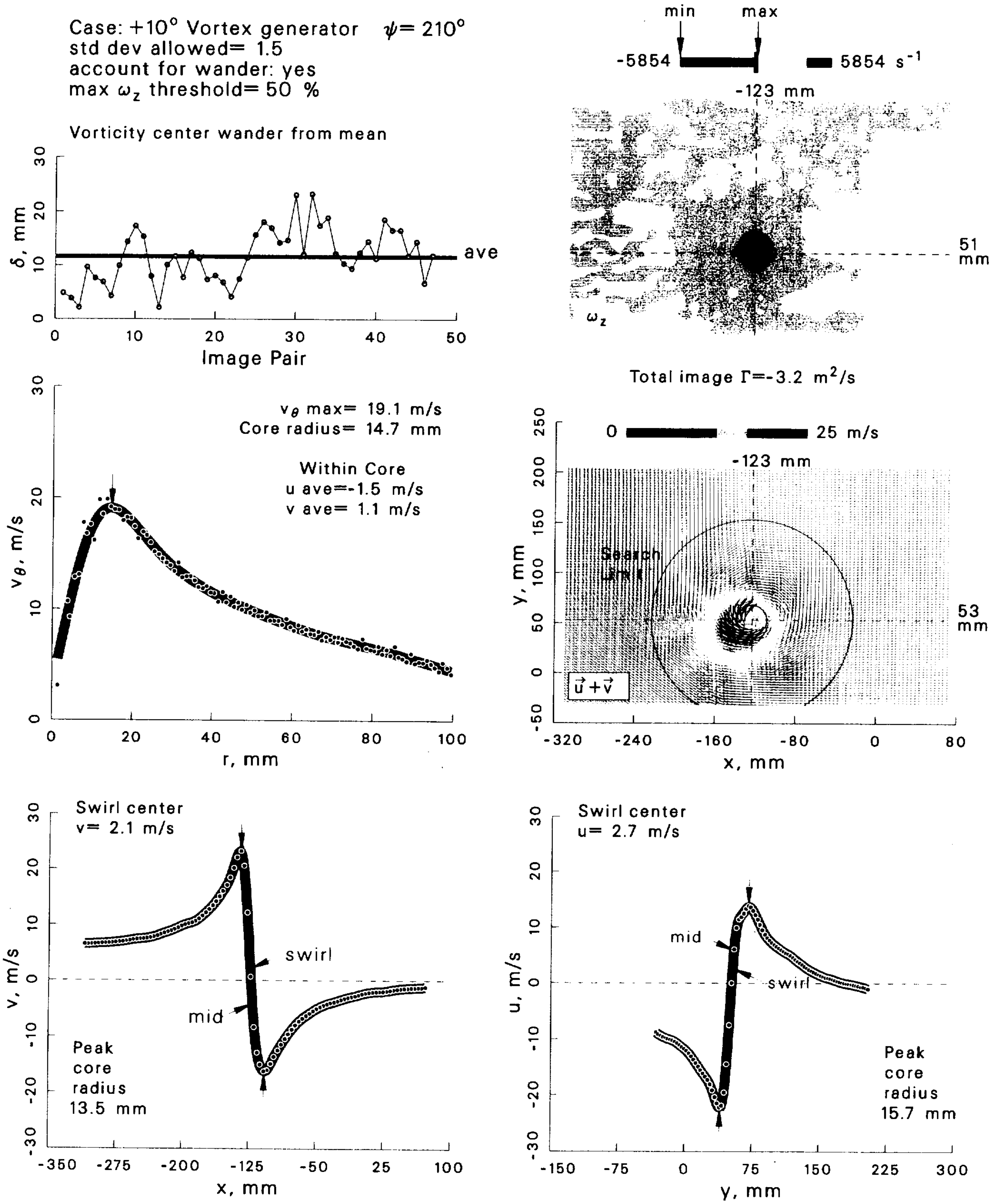

Figure 80: Vortex statistics at $\psi = 210°$ for the +10° vortex generator case.

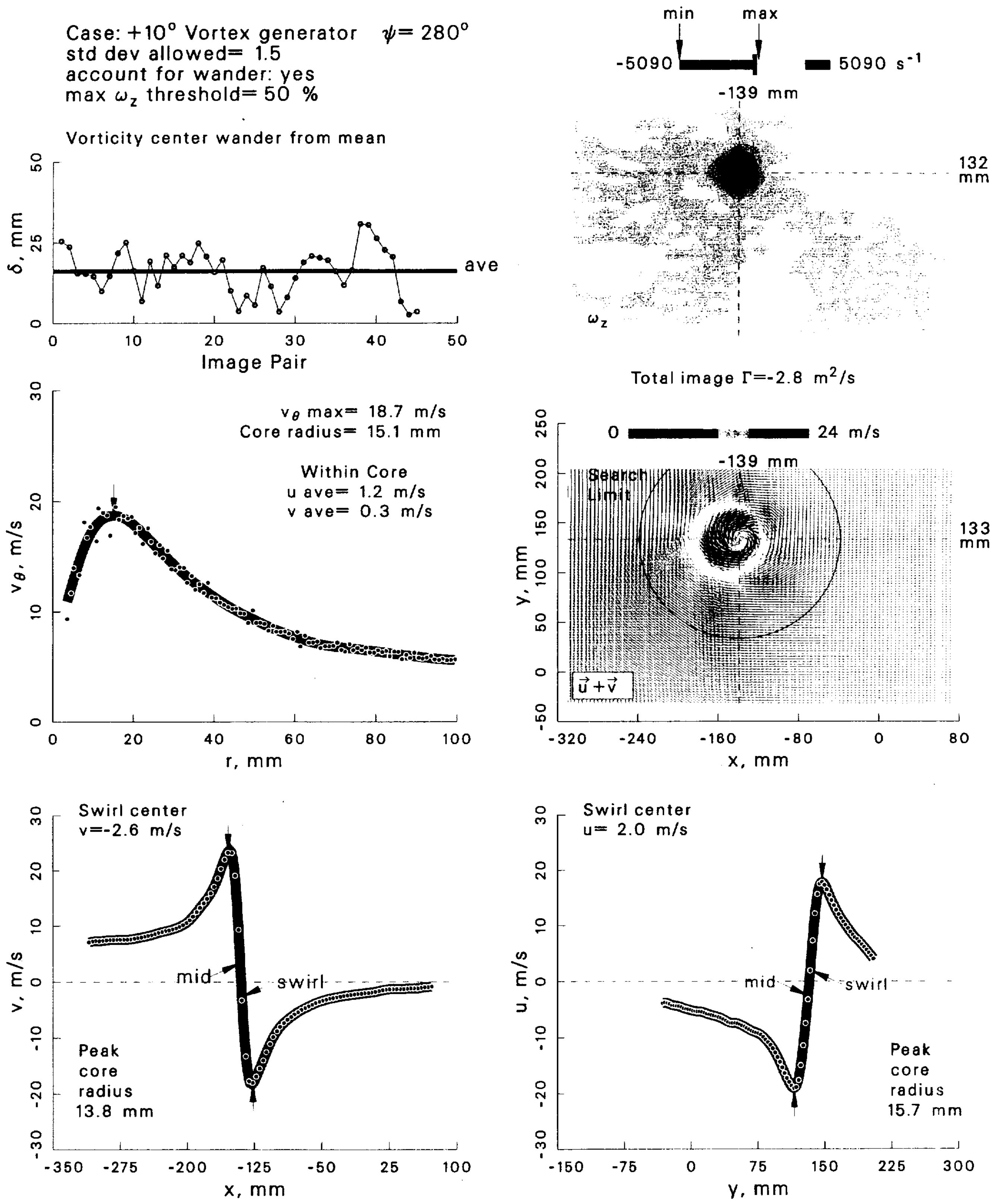

Figure 81: Vortex statistics at $\psi = 280°$ for the +10° vortex generator case.

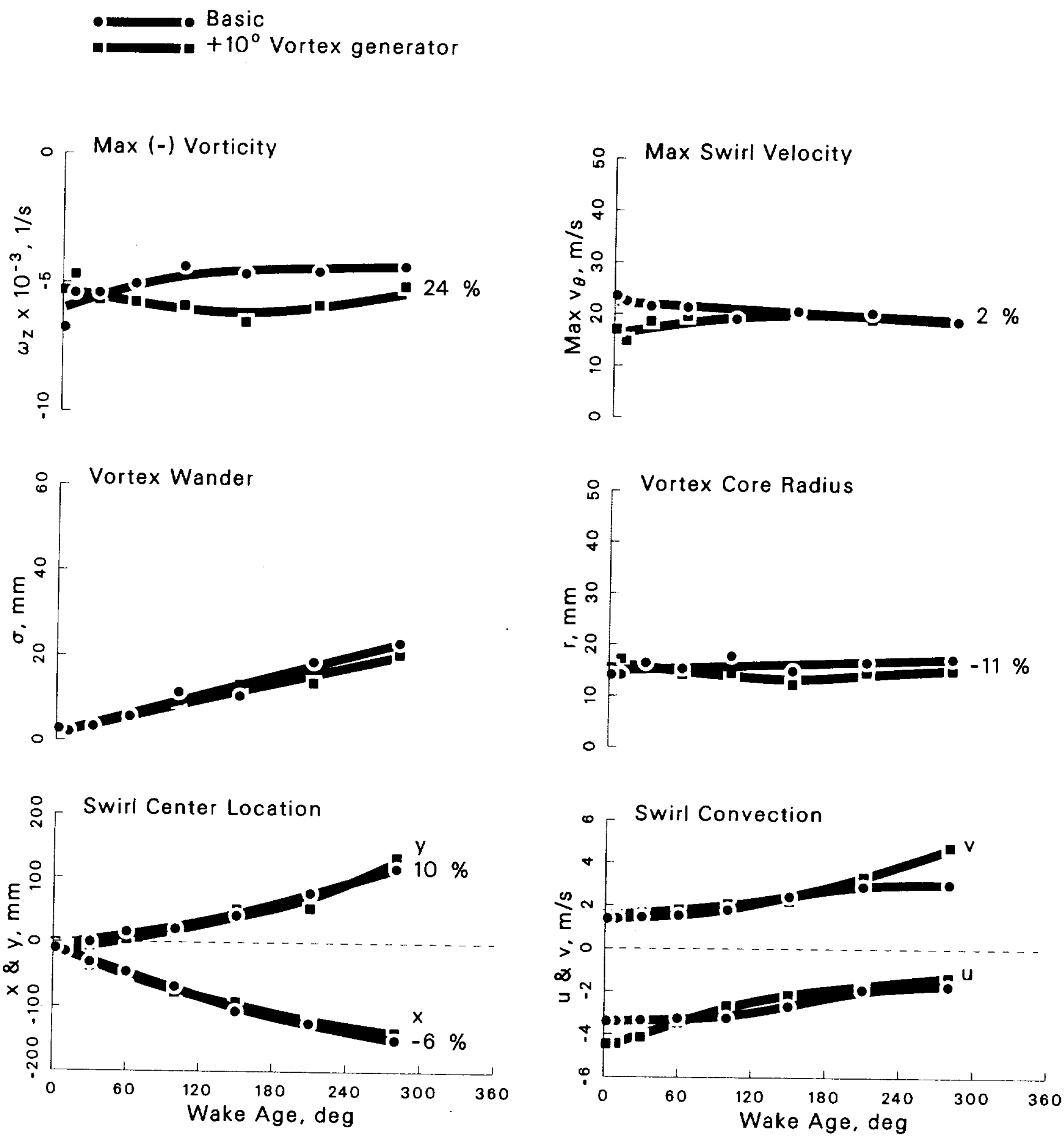

Figure 82: Summary of vortex development from $\psi = 2° \rightarrow 280°$ for the +10° vortex generator case.

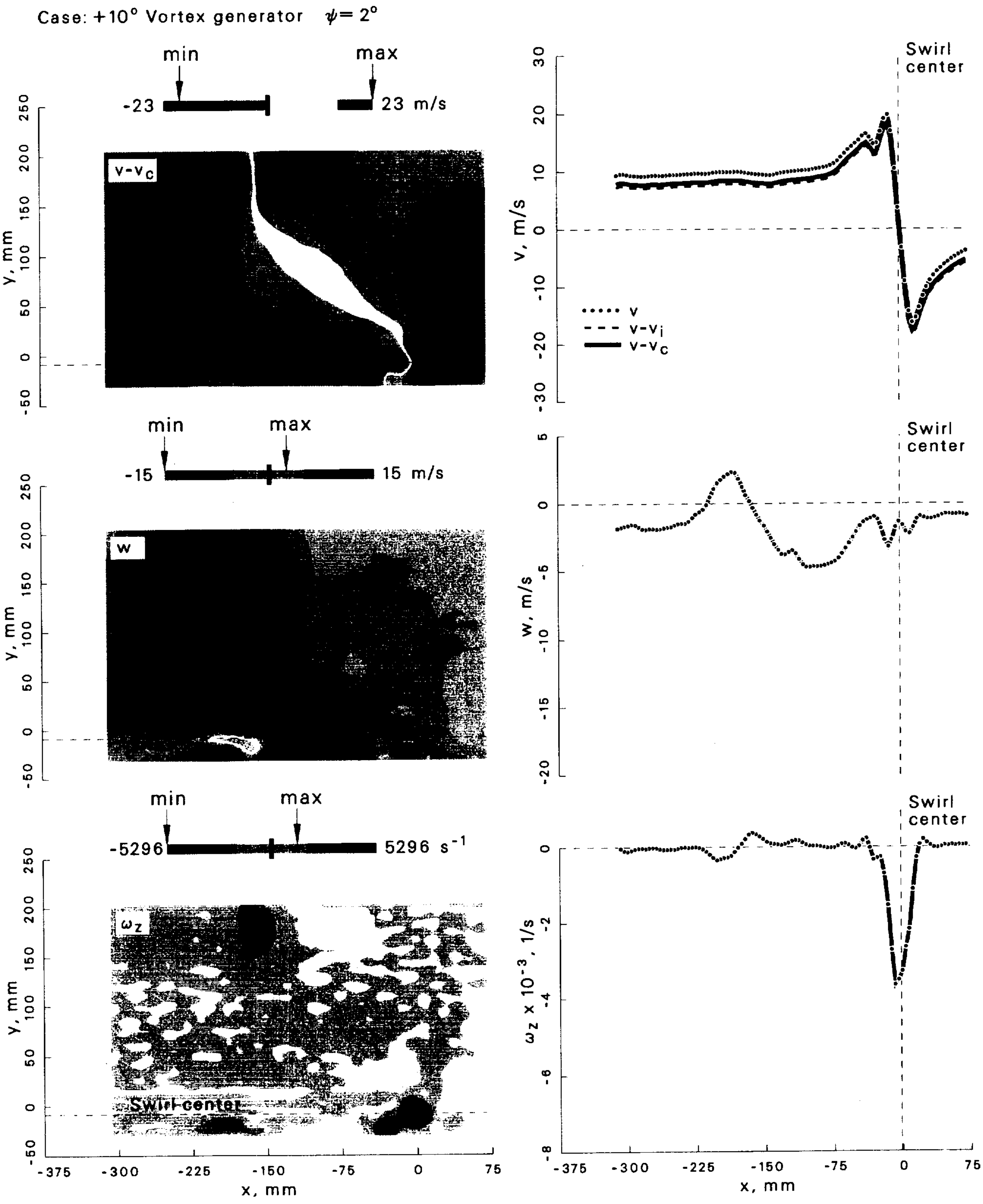

Figure 83: Velocity and vorticity components at $\psi = 2°$ for the +10° vortex generator case.

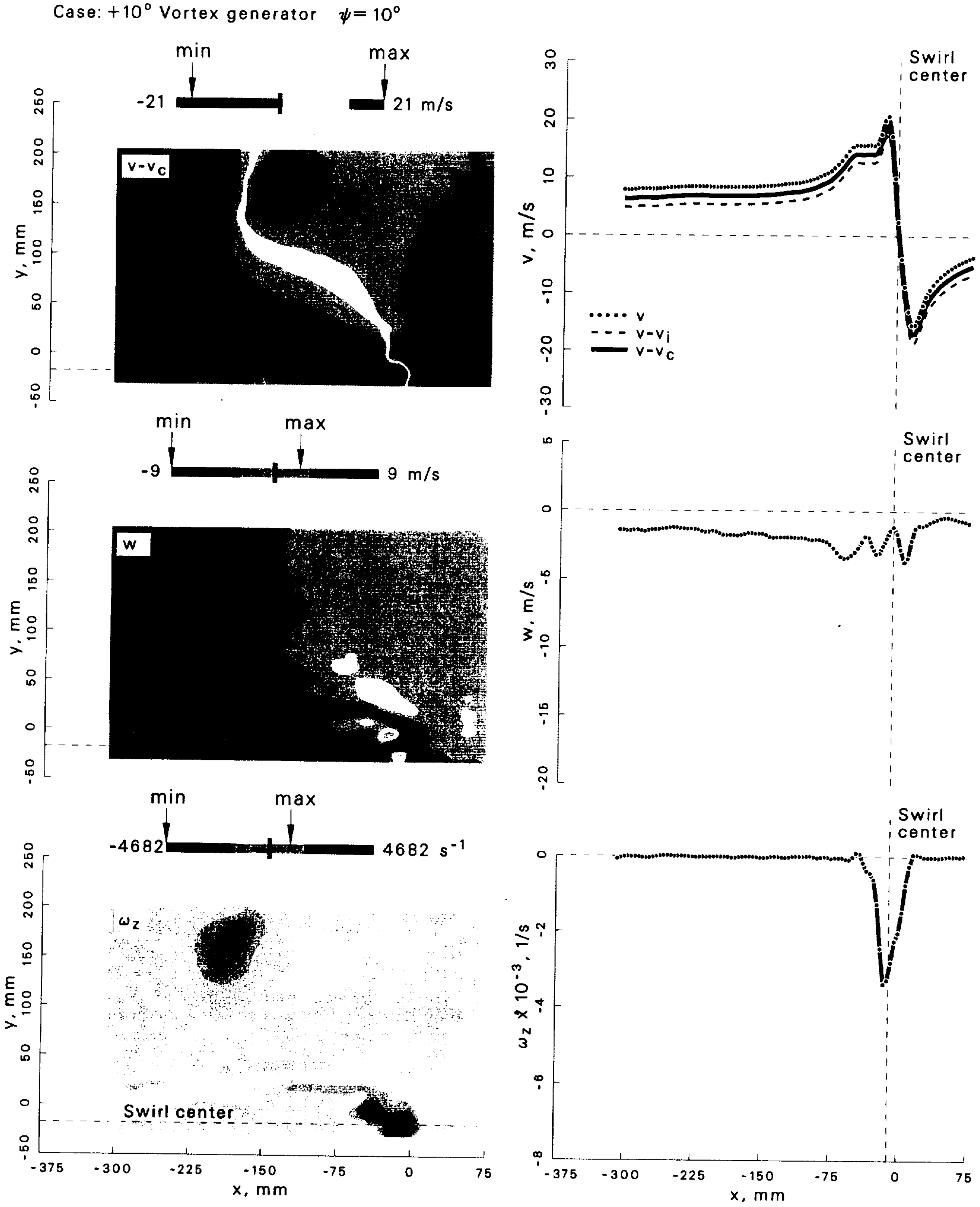

Figure 84: Velocity and vorticity components at $\psi = 10°$ for the +10° vortex generator case.

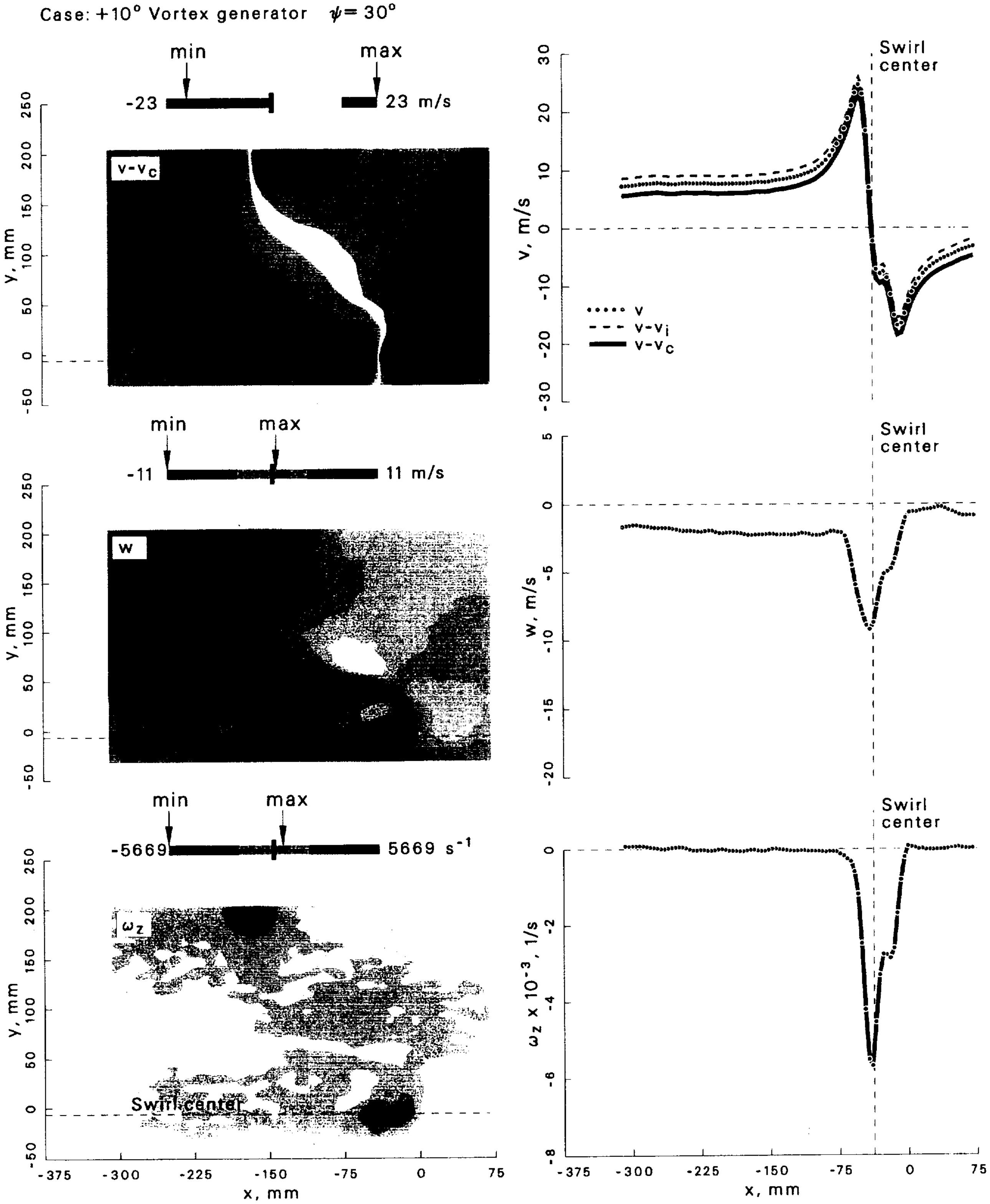

Figure 85: Velocity and vorticity components at $\psi = 30°$ for the +10° vortex generator case.

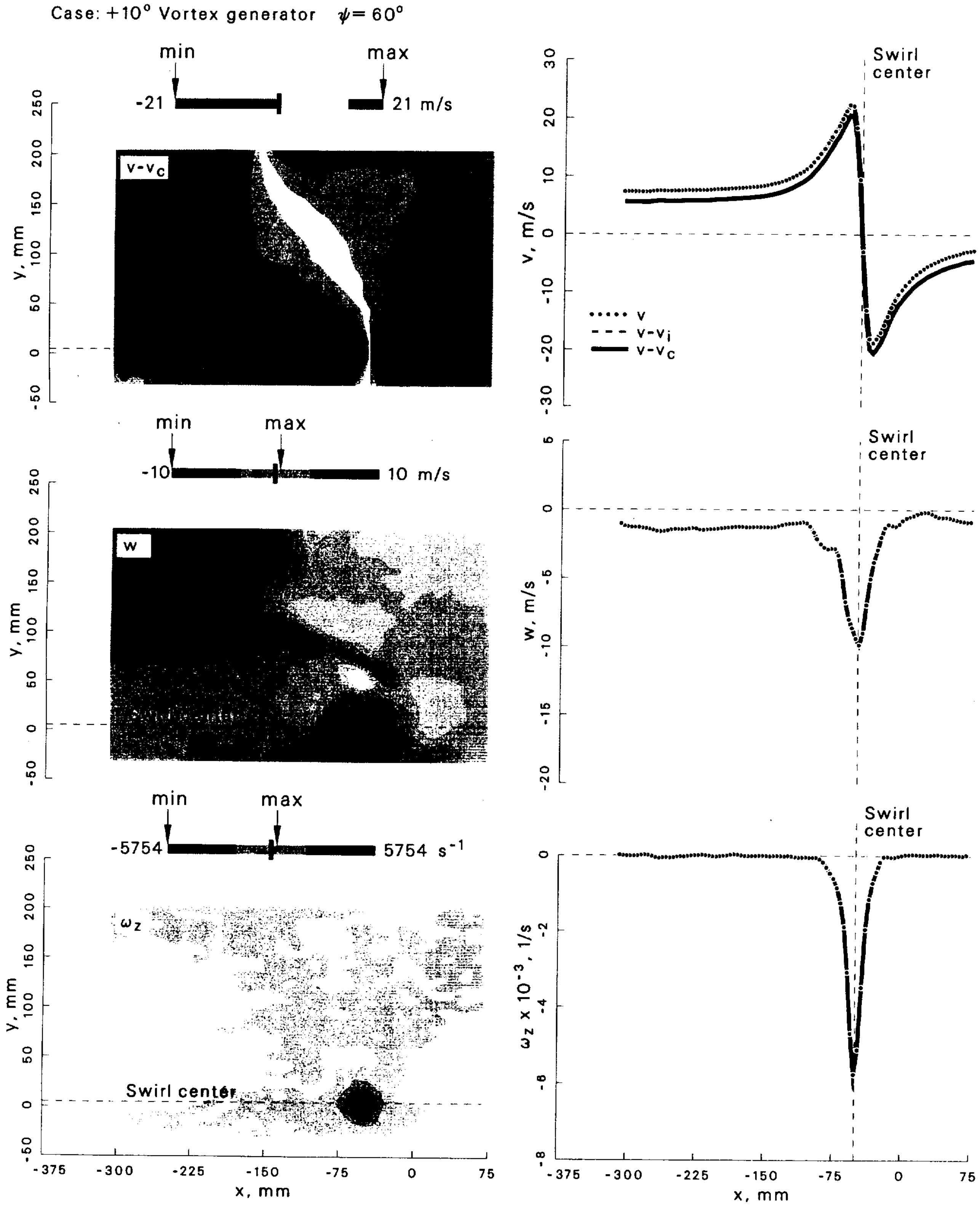

Figure 86: Velocity and vorticity components at $\psi = 60°$ for the $+10°$ vortex generator case.

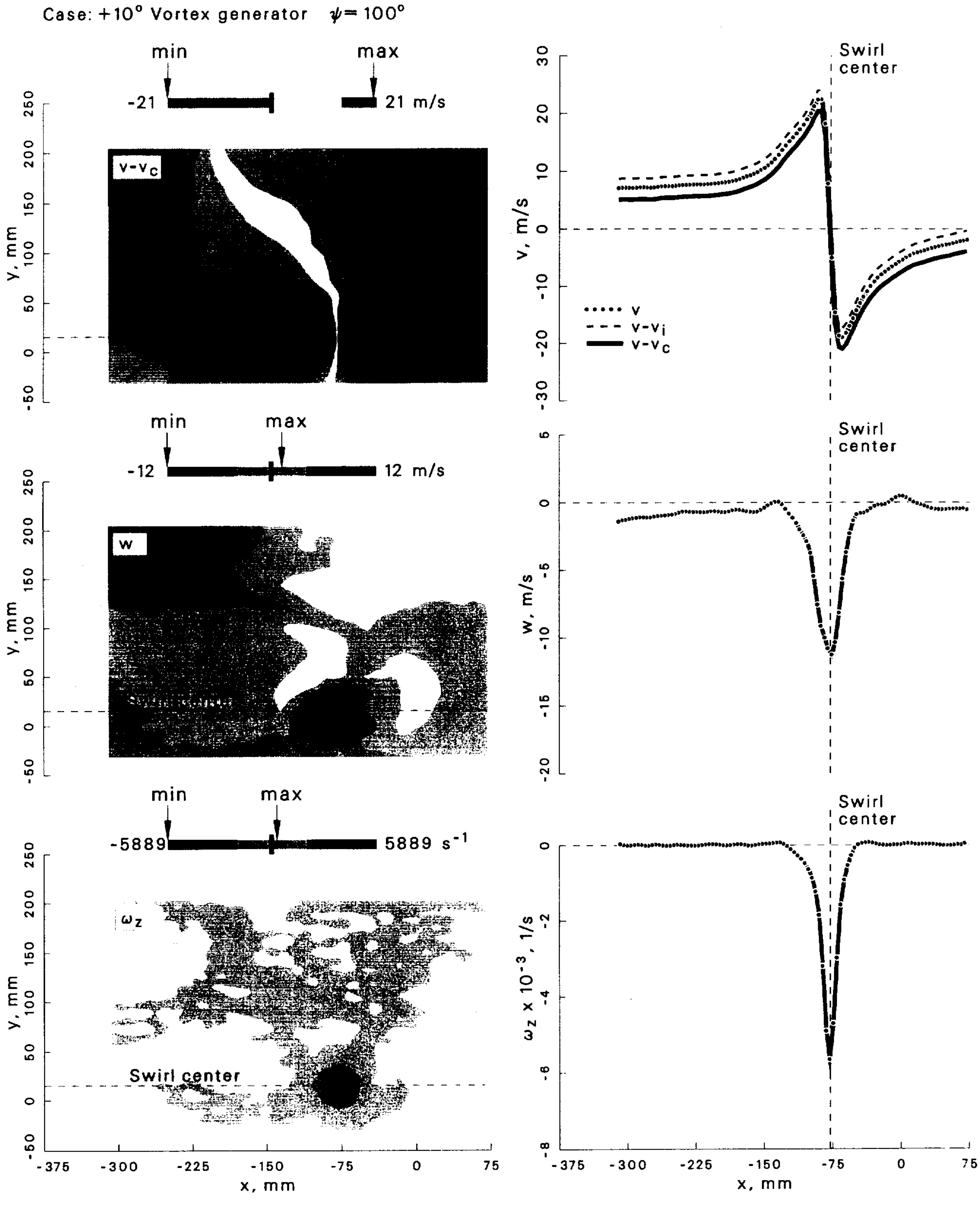

Figure 87: Velocity and vorticity components at $\psi = 100°$ for the $+10°$ vortex generator case.

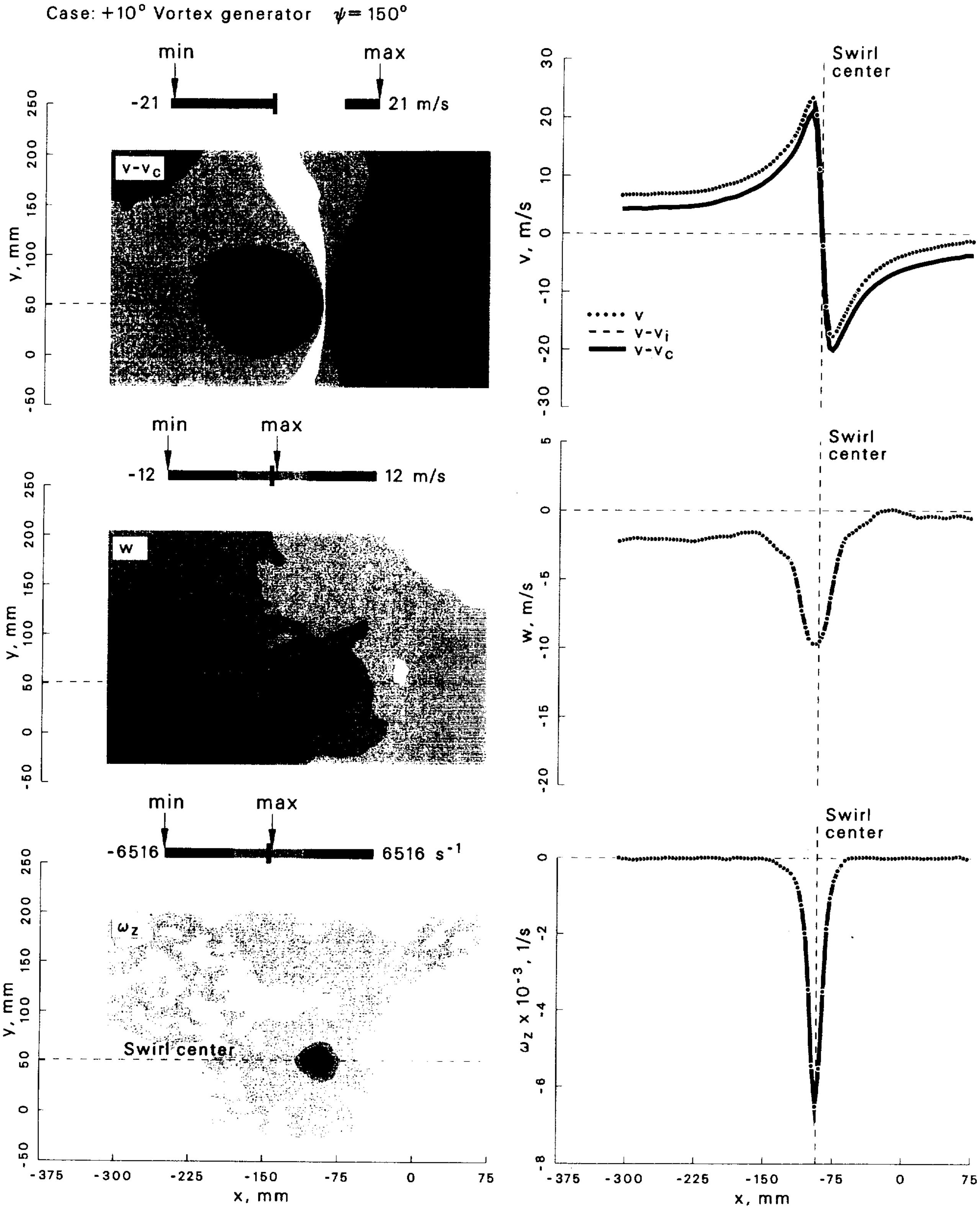

Figure 88: Velocity and vorticity components at $\psi = 150°$ for the +10° vortex generator case.

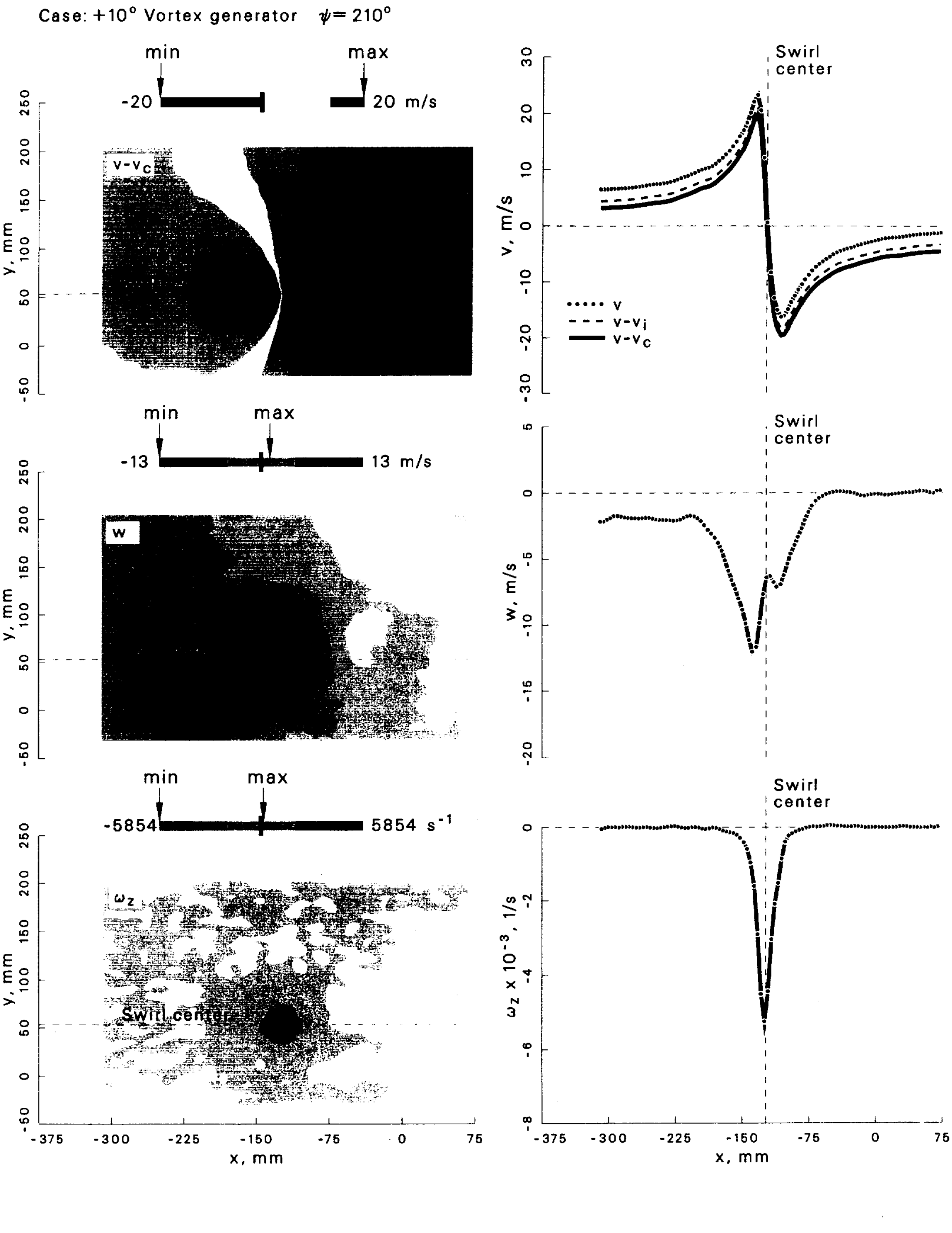

Figure 89: Velocity and vorticity components at $\psi = 210^\circ$ for the $+10^\circ$ vortex generator case.

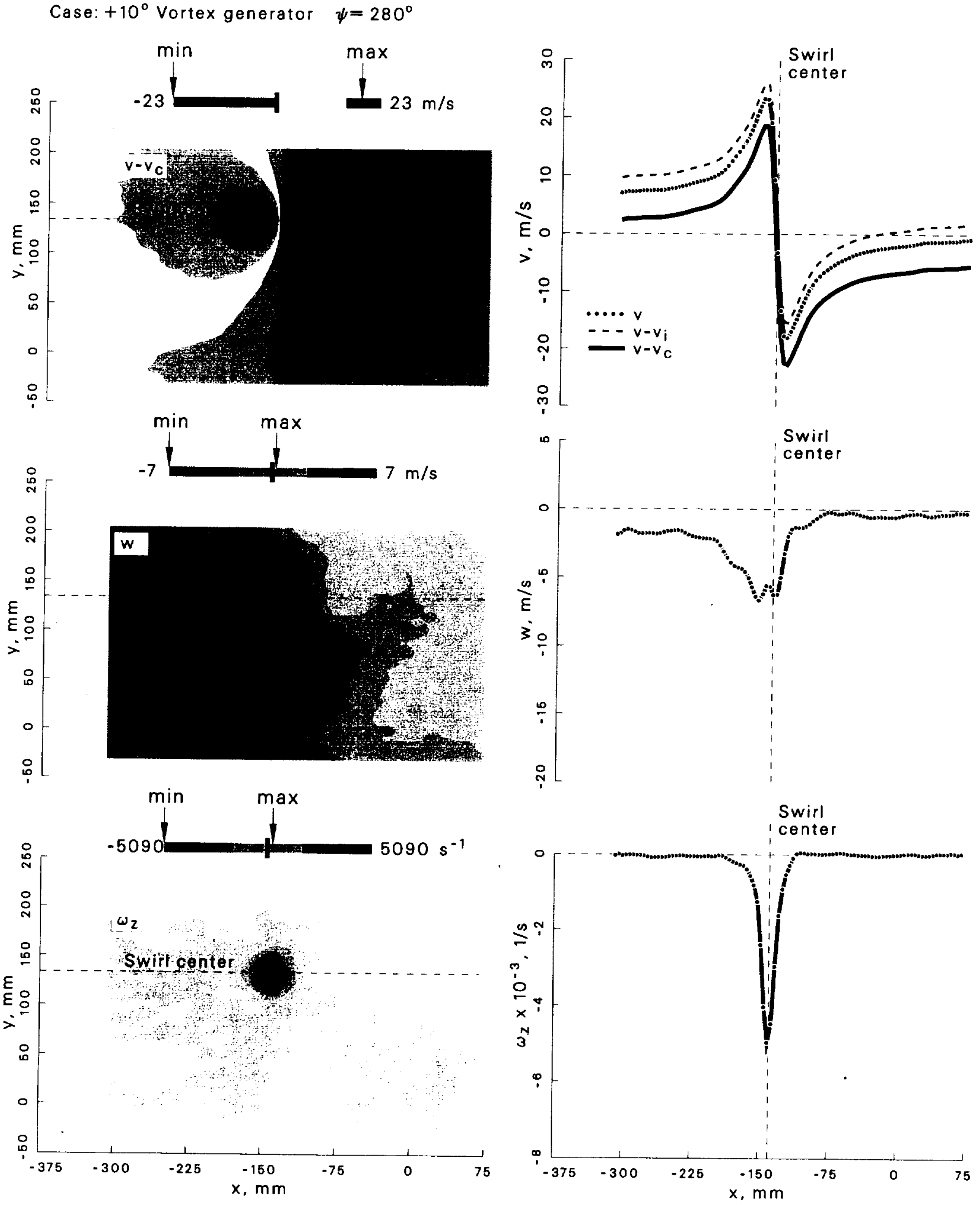

Figure 90: Velocity and vorticity components at $\psi = 280°$ for the +10° vortex generator case.

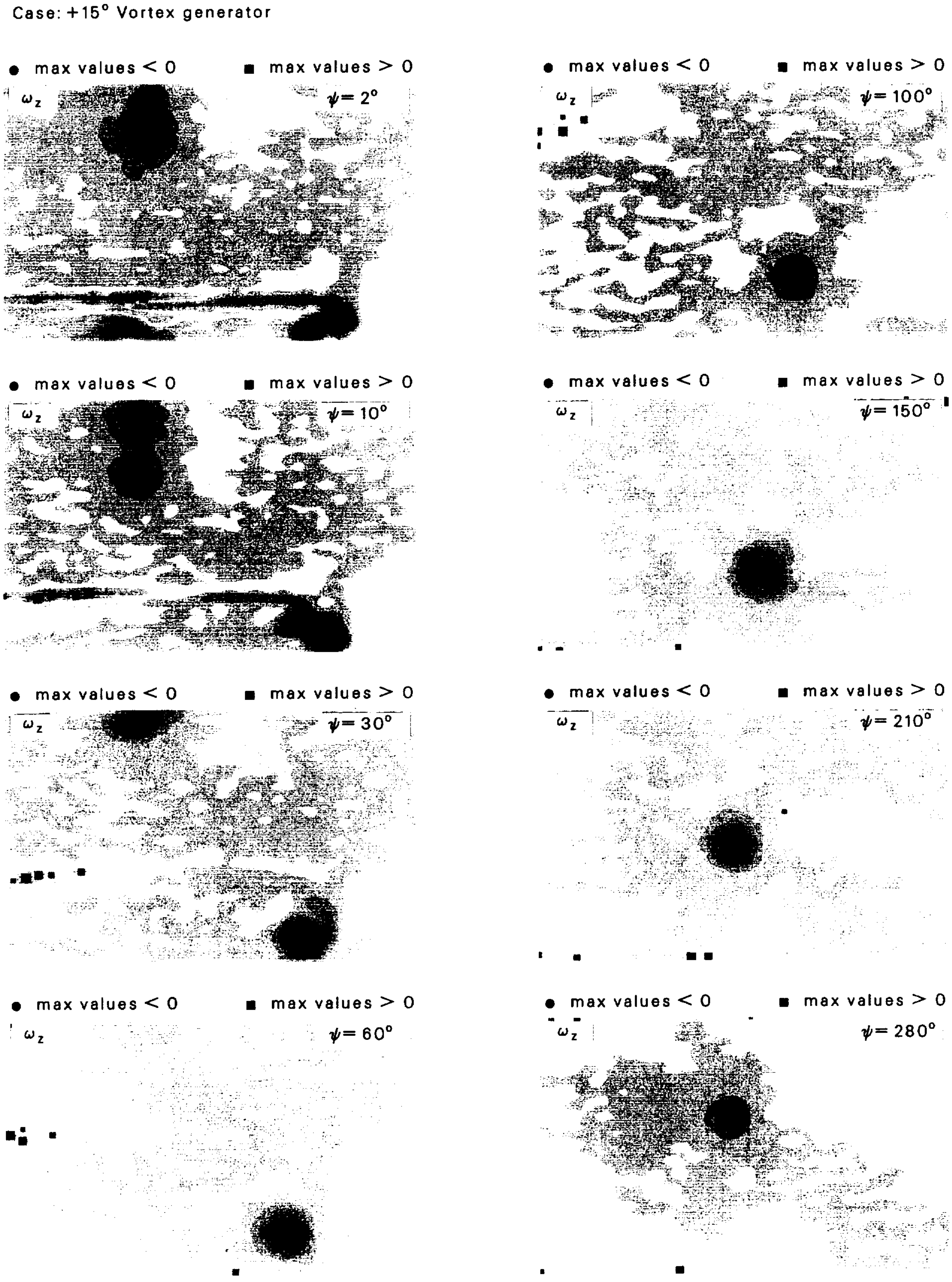

Figure 91: Locations of ω_z extrema at $\psi = 2° \rightarrow 280°$ for the +15° vortex generator case.

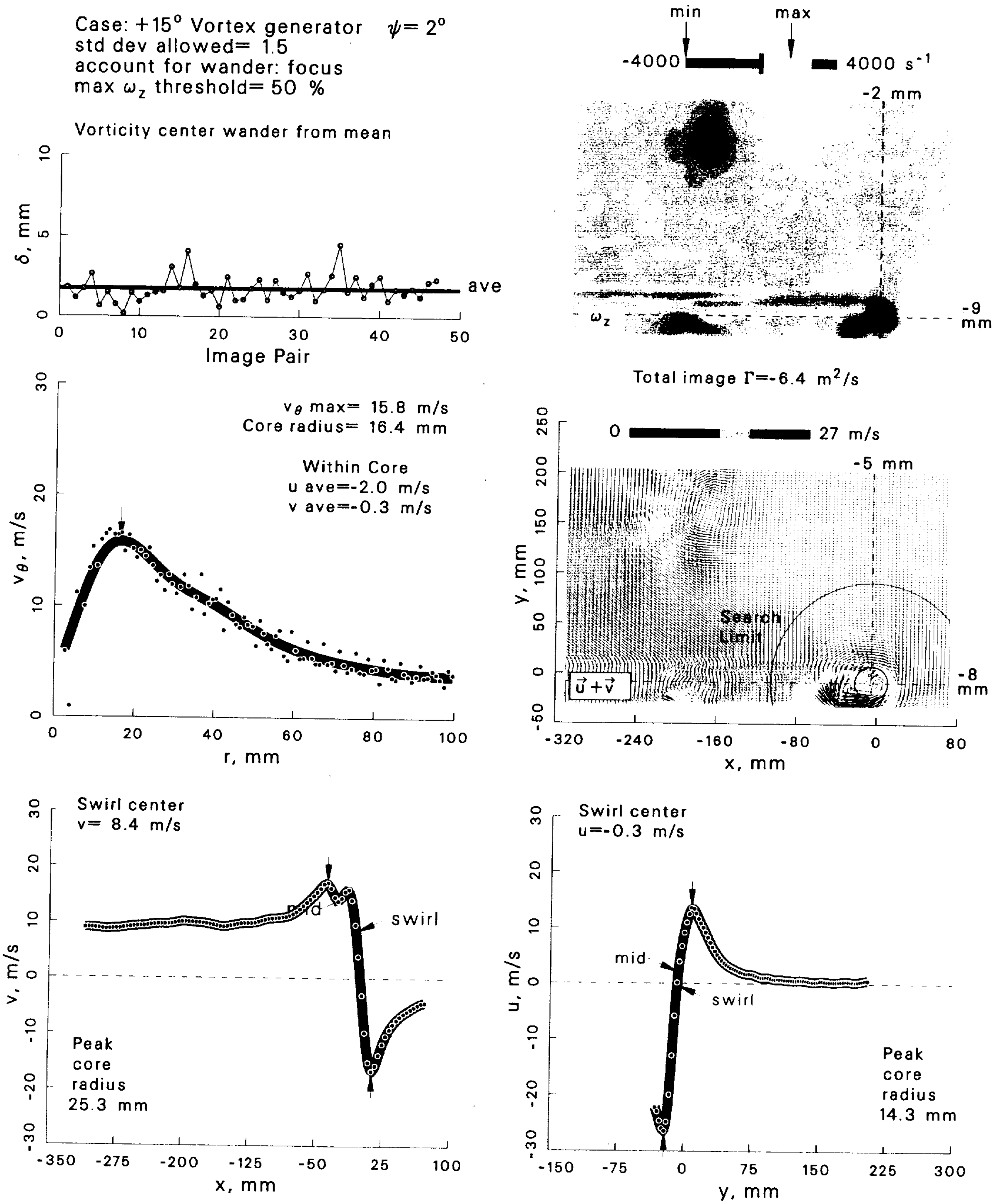

Figure 92: Vortex statistics at $\psi = 2°$ for the +15° vortex generator case.

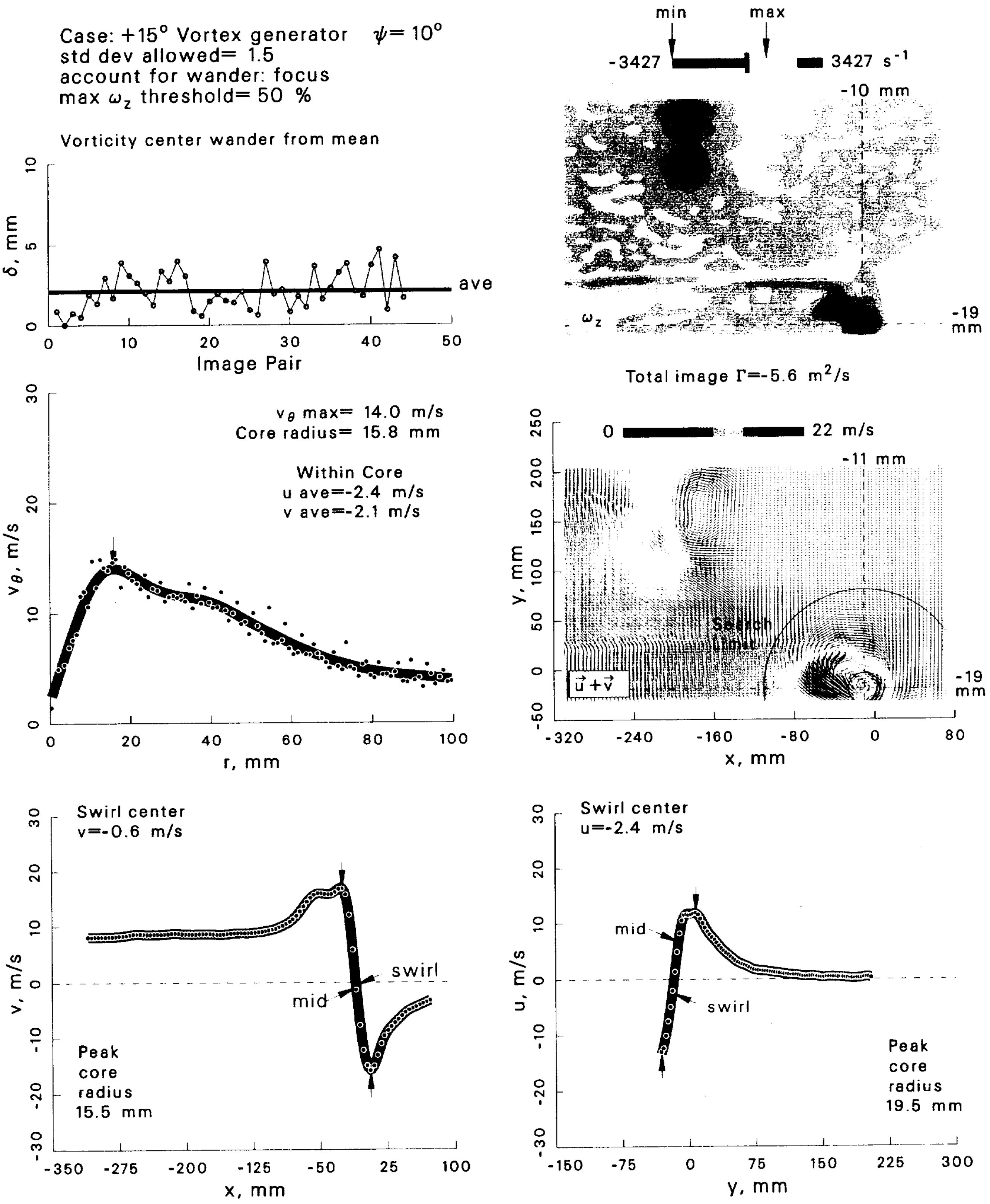

Figure 93: Vortex statistics at $\psi = 10°$ for the +15° vortex generator case.

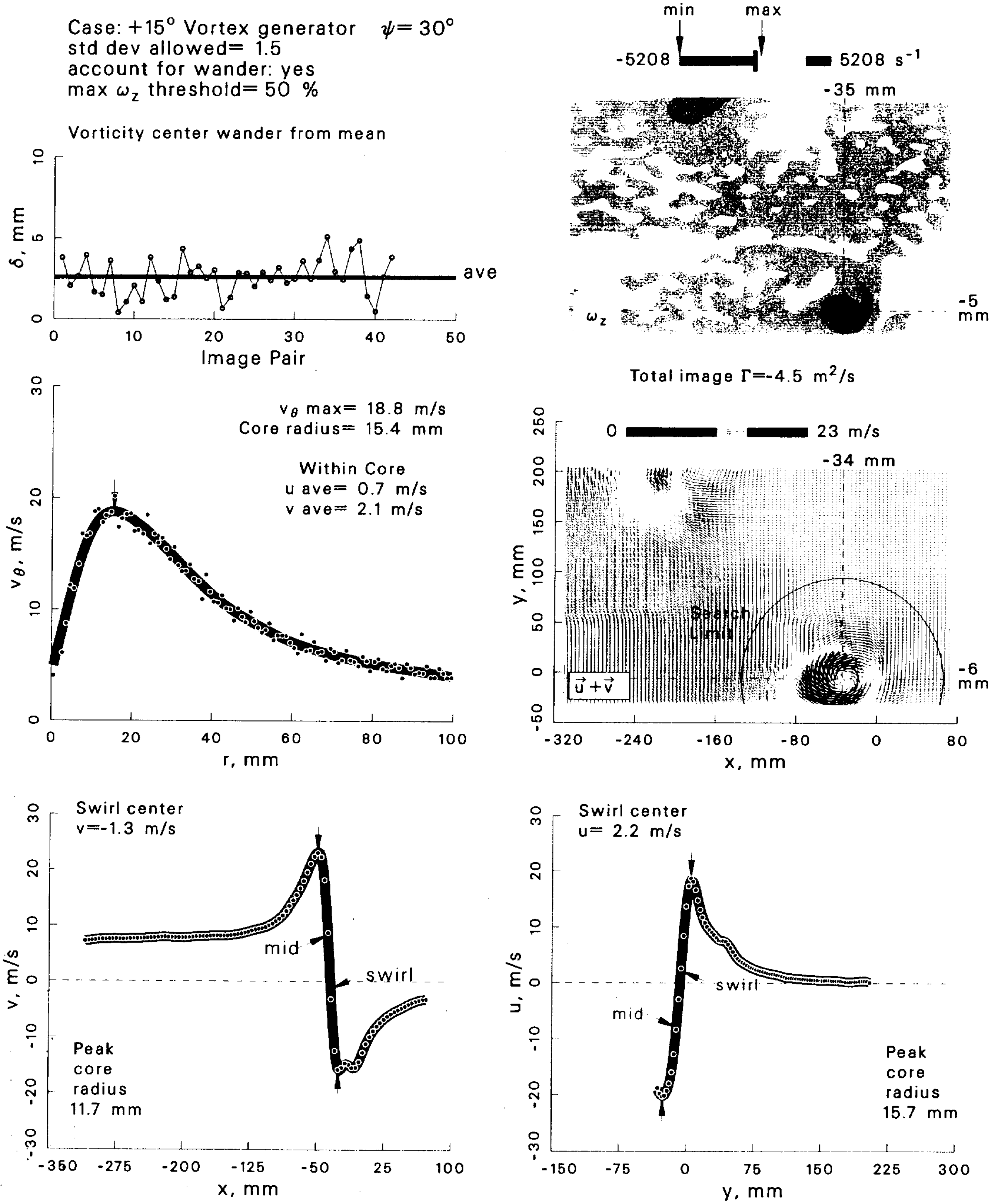

Figure 94: Vortex statistics at $\psi = 30°$ for the +15° vortex generator case.

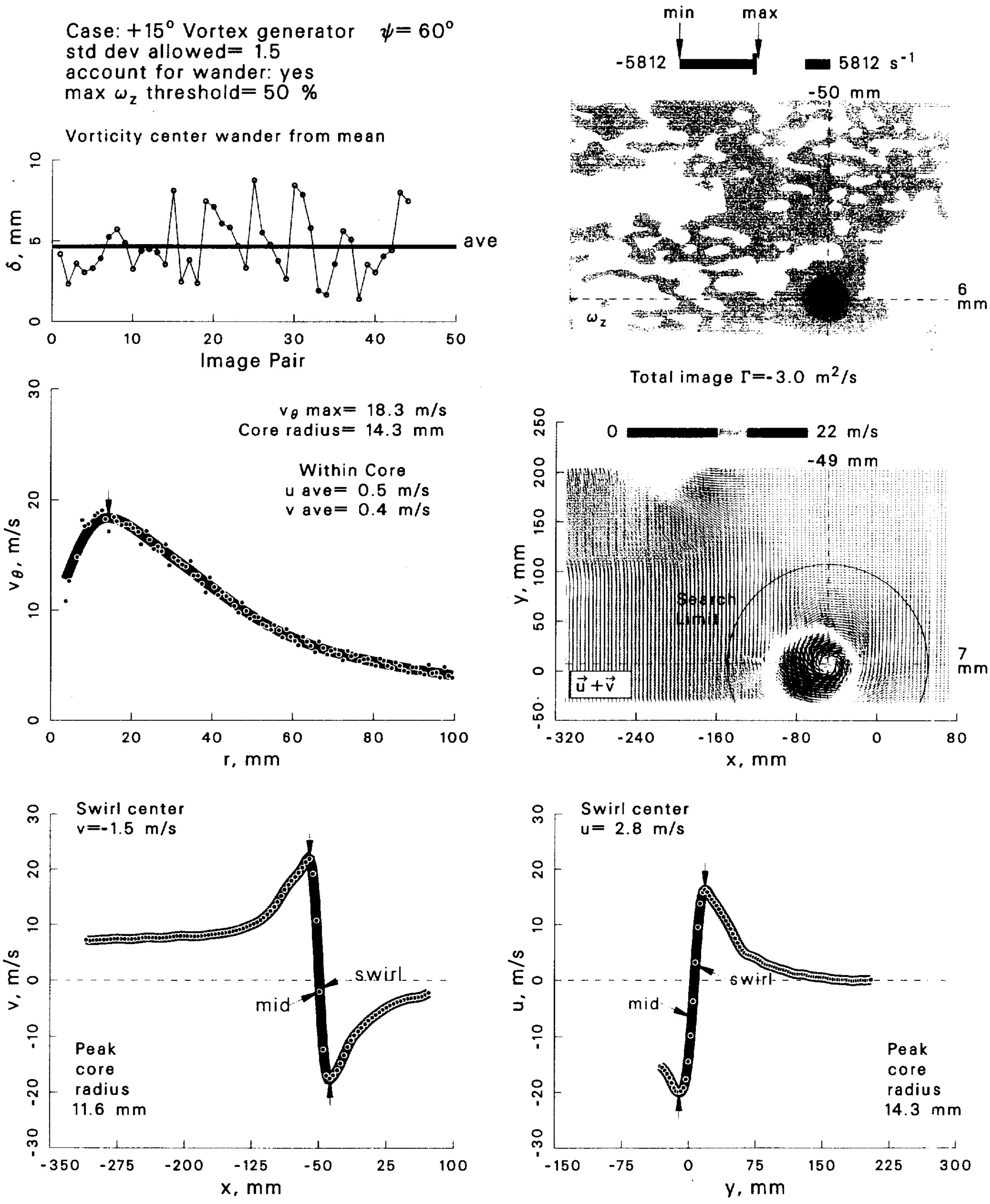

Figure 95: Vortex statistics at $\psi = 60°$ for the +15° vortex generator case.

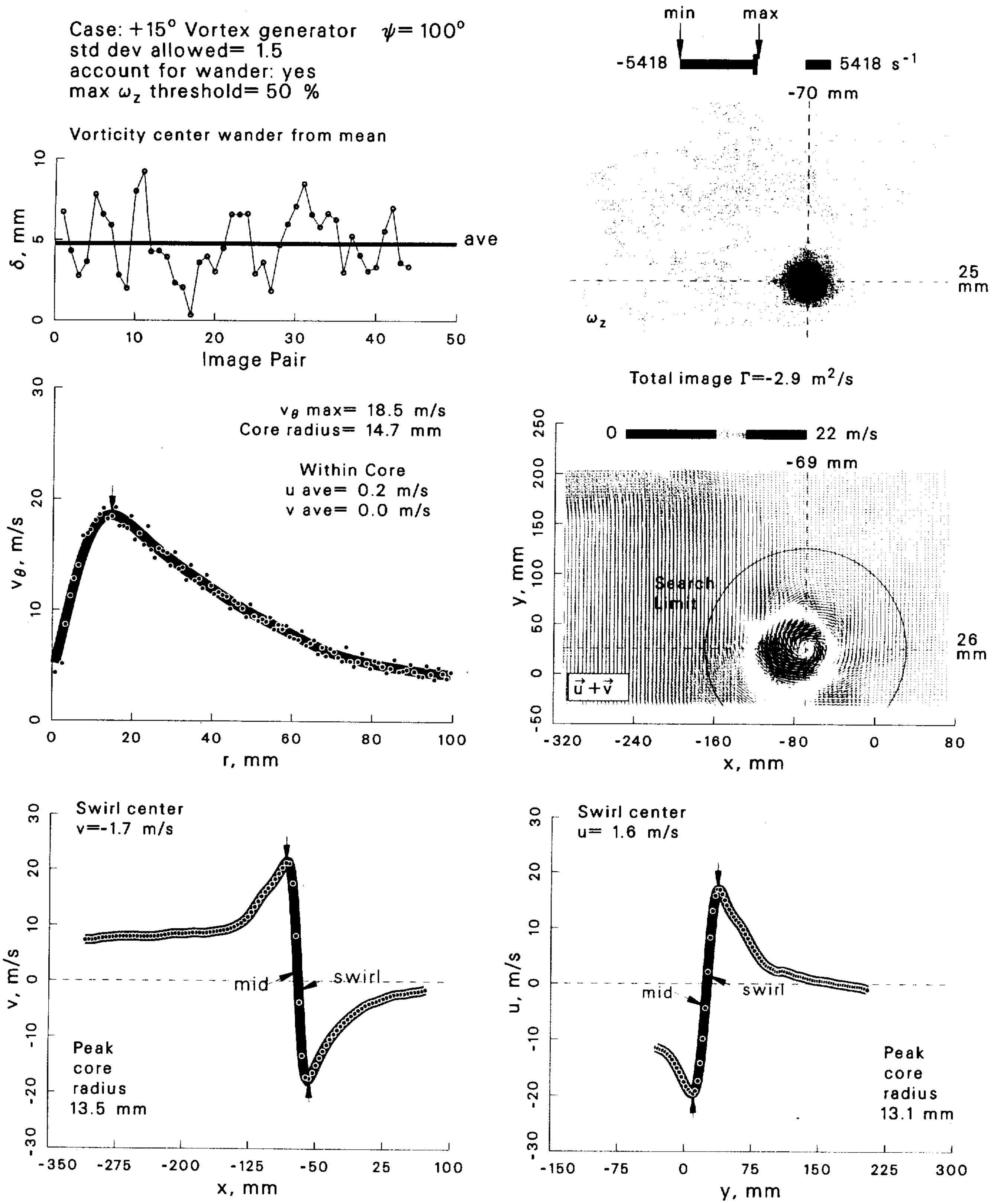

Figure 96: Vortex statistics at $\psi = 100°$ for the +15° vortex generator case.

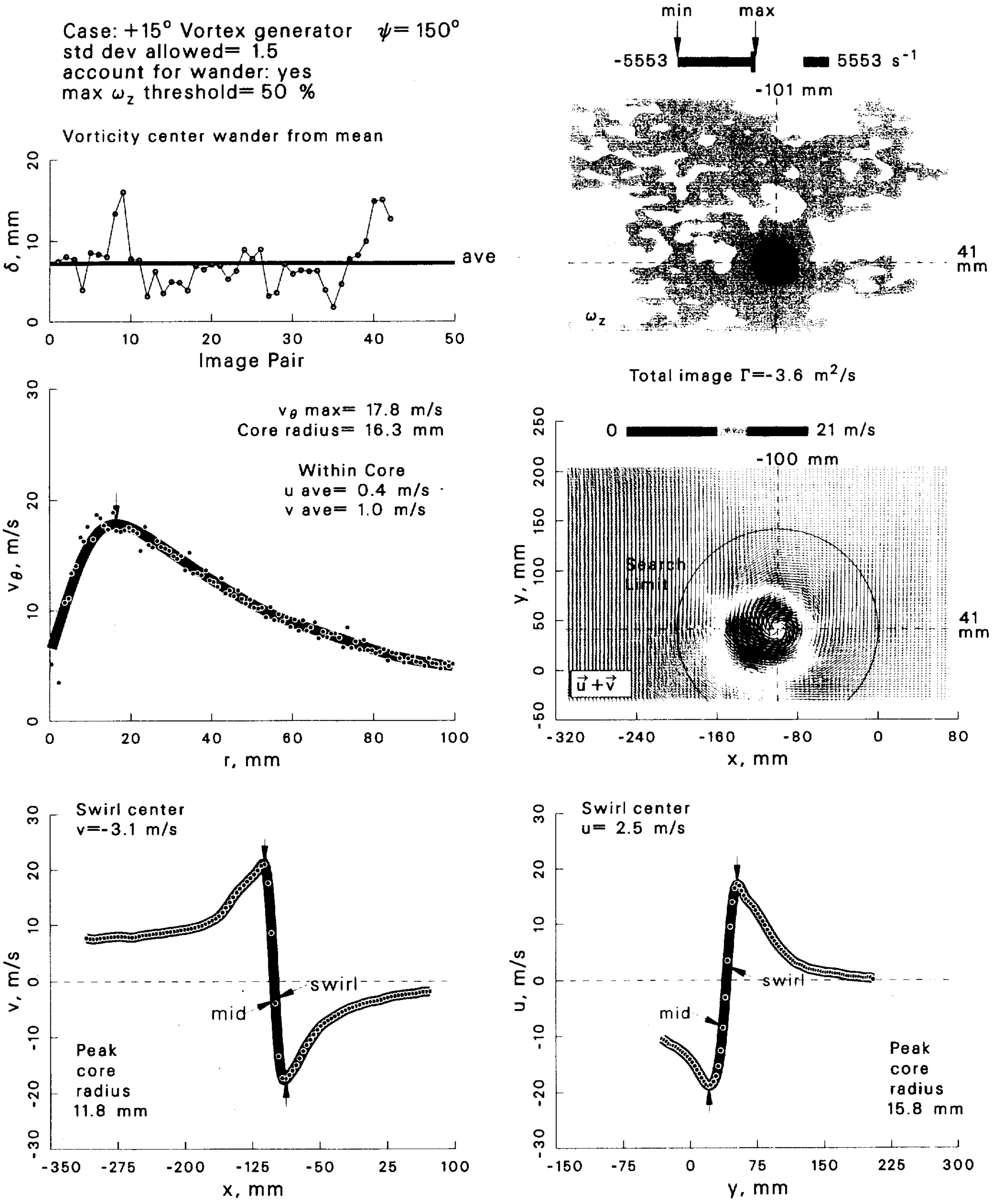

Figure 97: Vortex statistics at $\psi = 150°$ for the +15° vortex generator case.

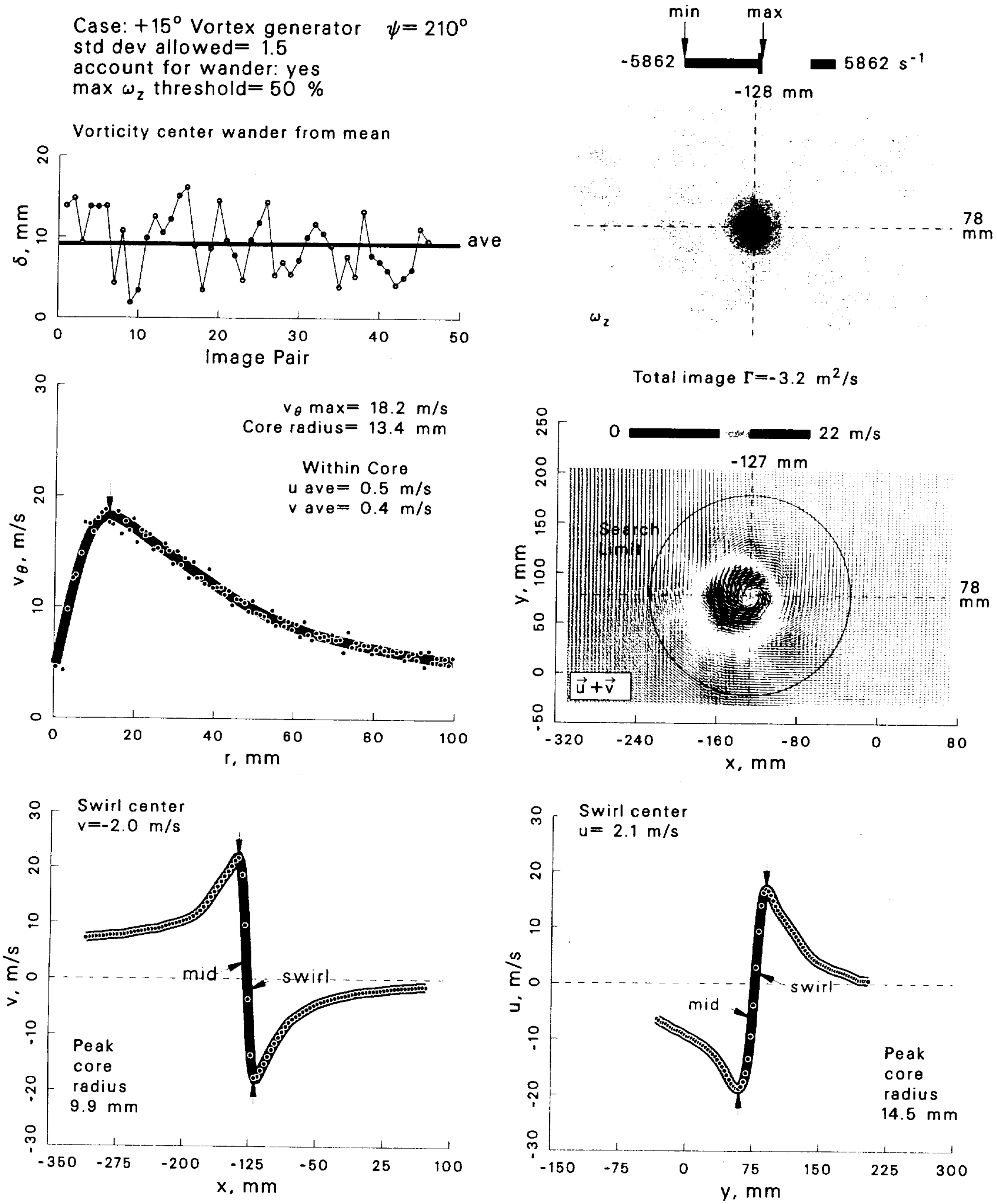

Figure 98: Vortex statistics at $\psi = 210°$ for the +15° vortex generator case.

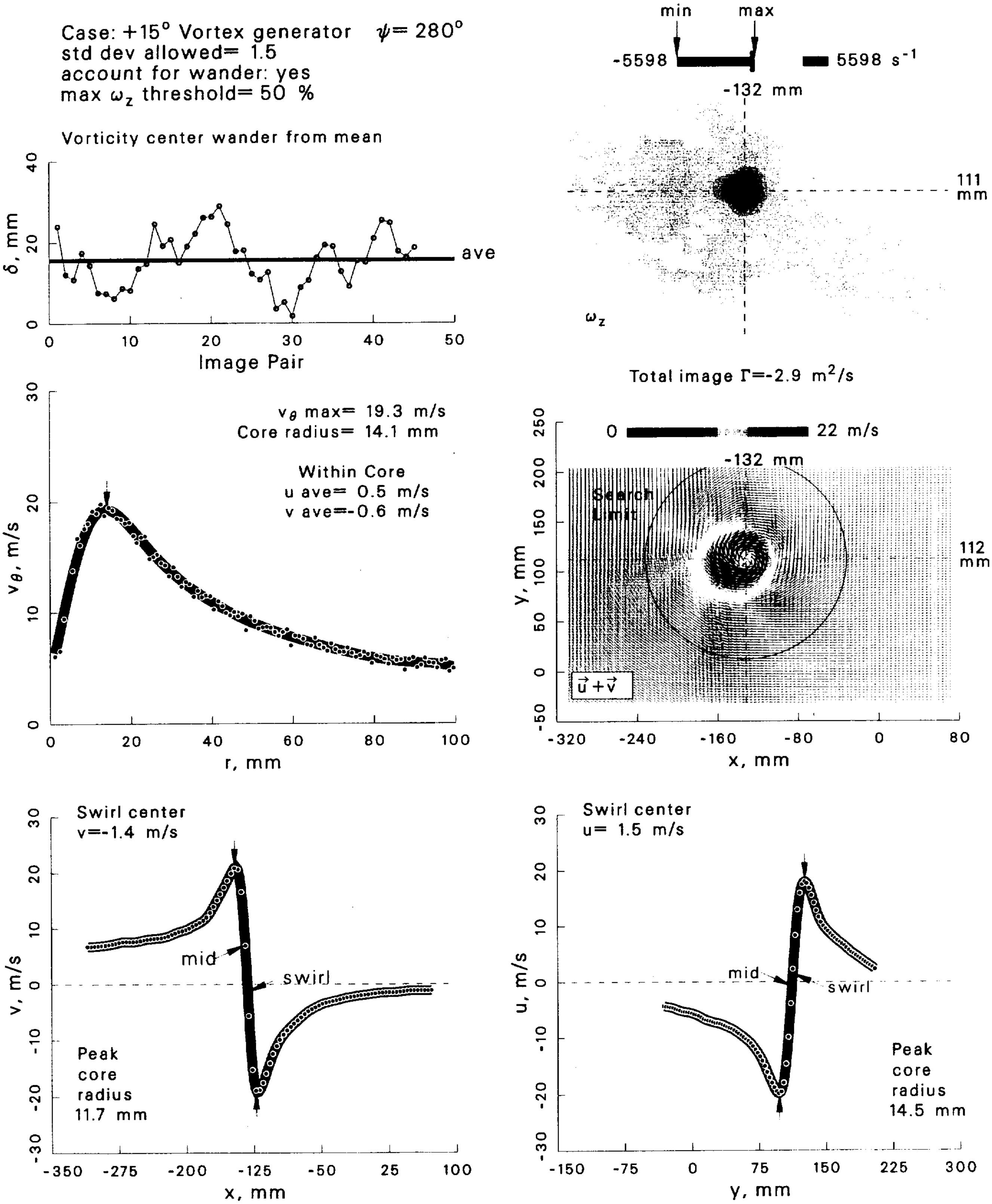

Figure 99: Vortex statistics at $\psi = 280°$ for the +15° vortex generator case.

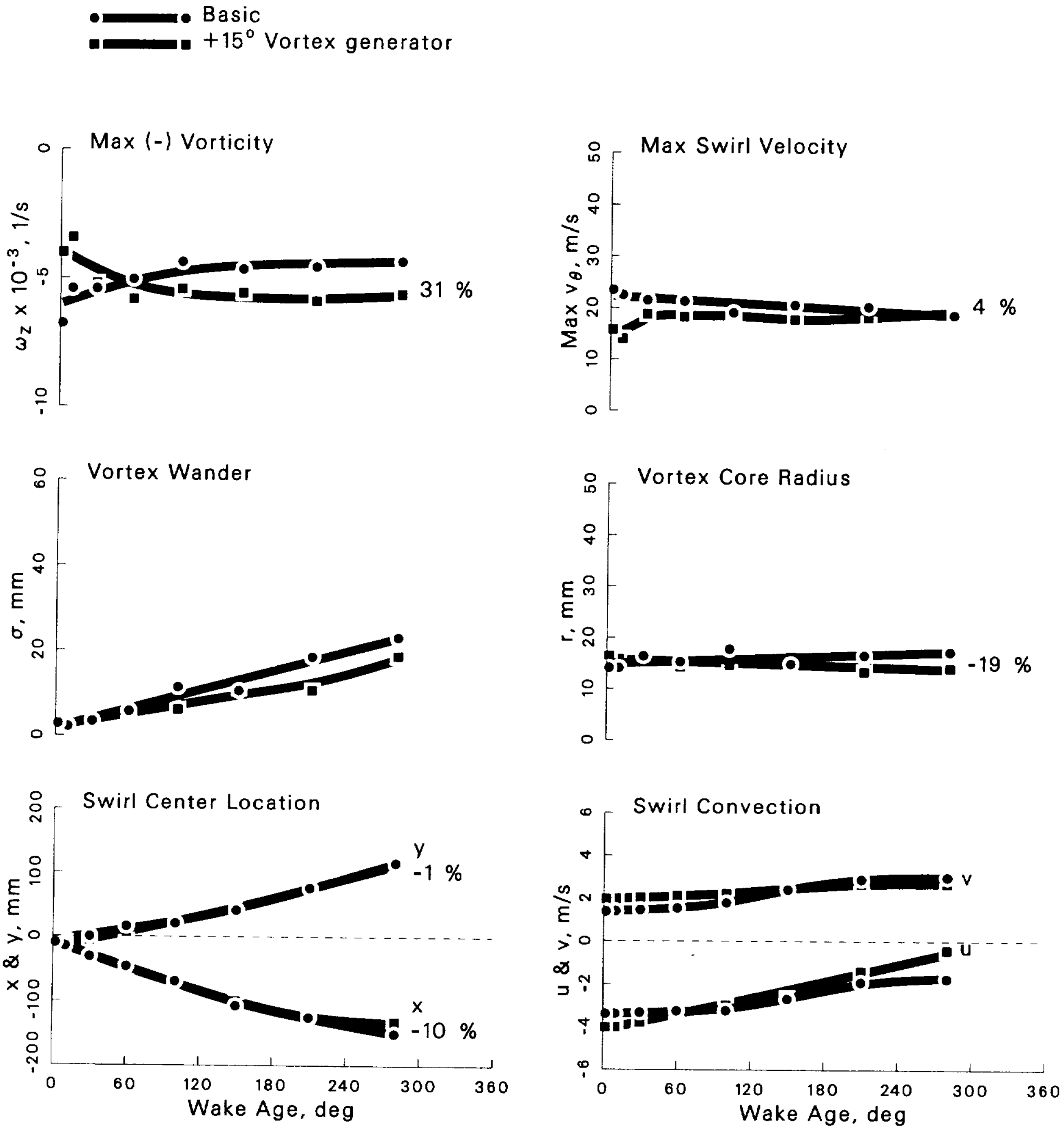

Figure 100: Summary of vortex development from $\psi = 2° \rightarrow 280°$ for the +15° vortex generator case.

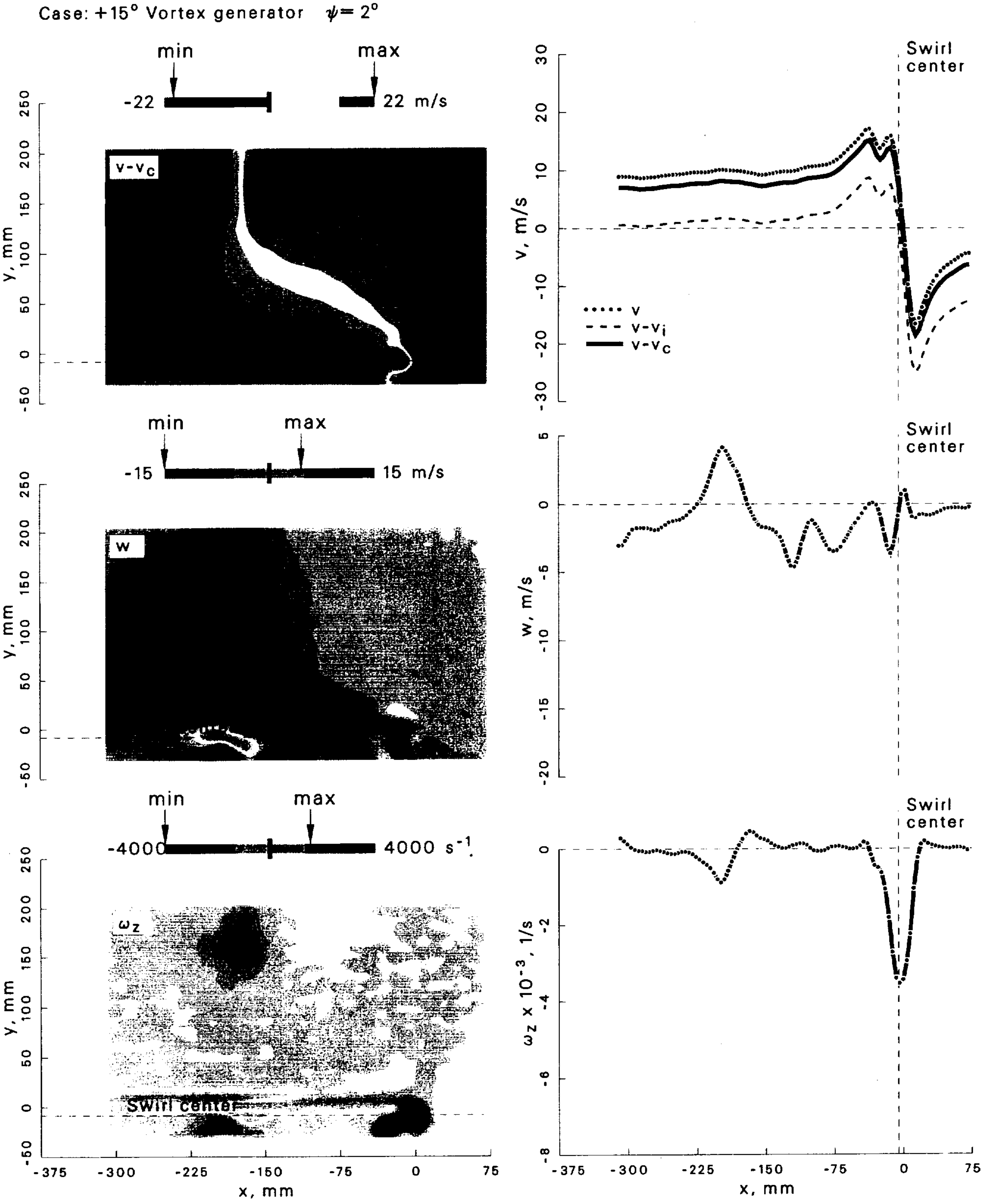

Figure 101: Velocity and vorticity components at $\psi = 2°$ for the +15° vortex generator case.

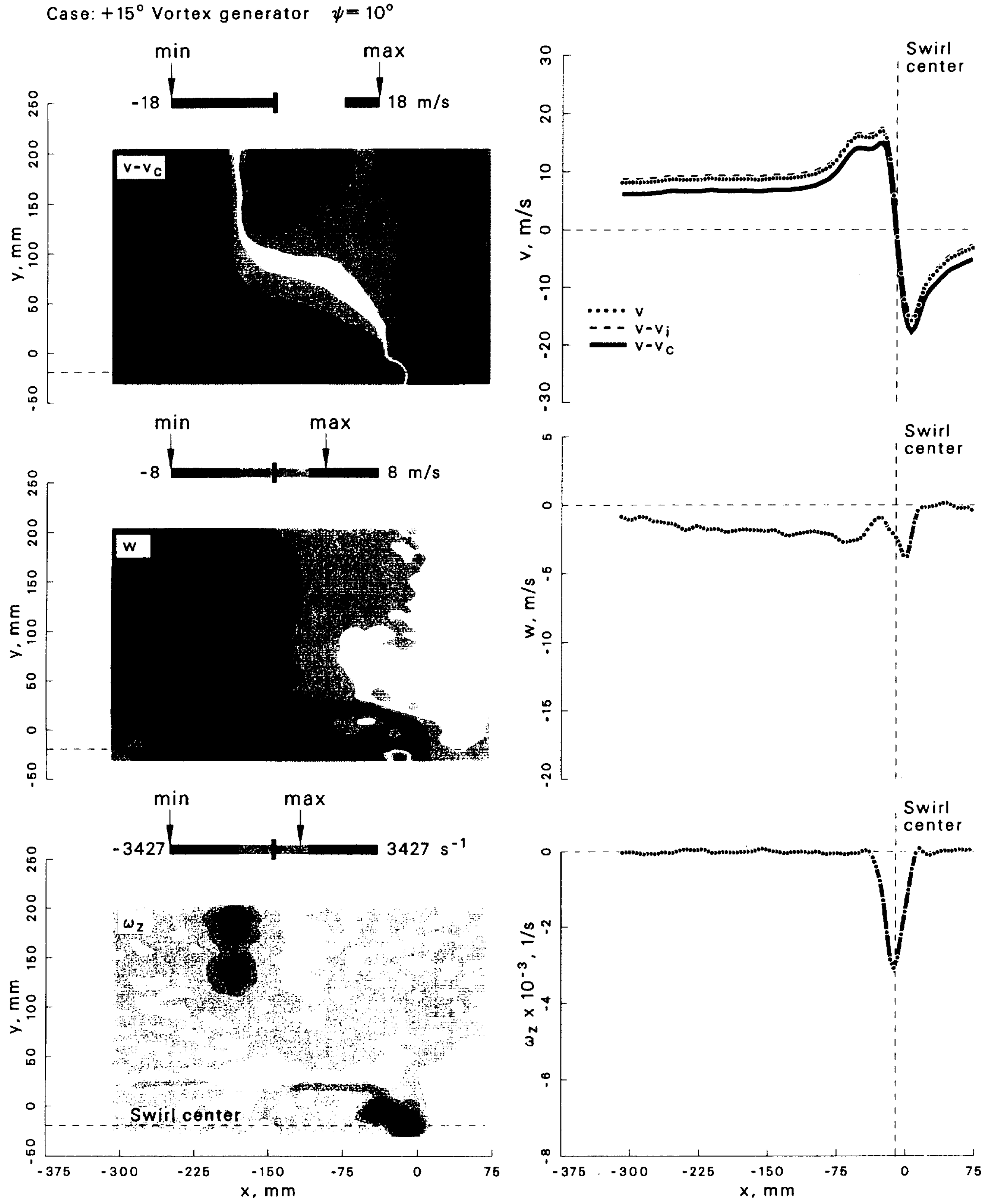

Figure 102: Velocity and vorticity components at $\psi = 10°$ for the $+15°$ vortex generator case.

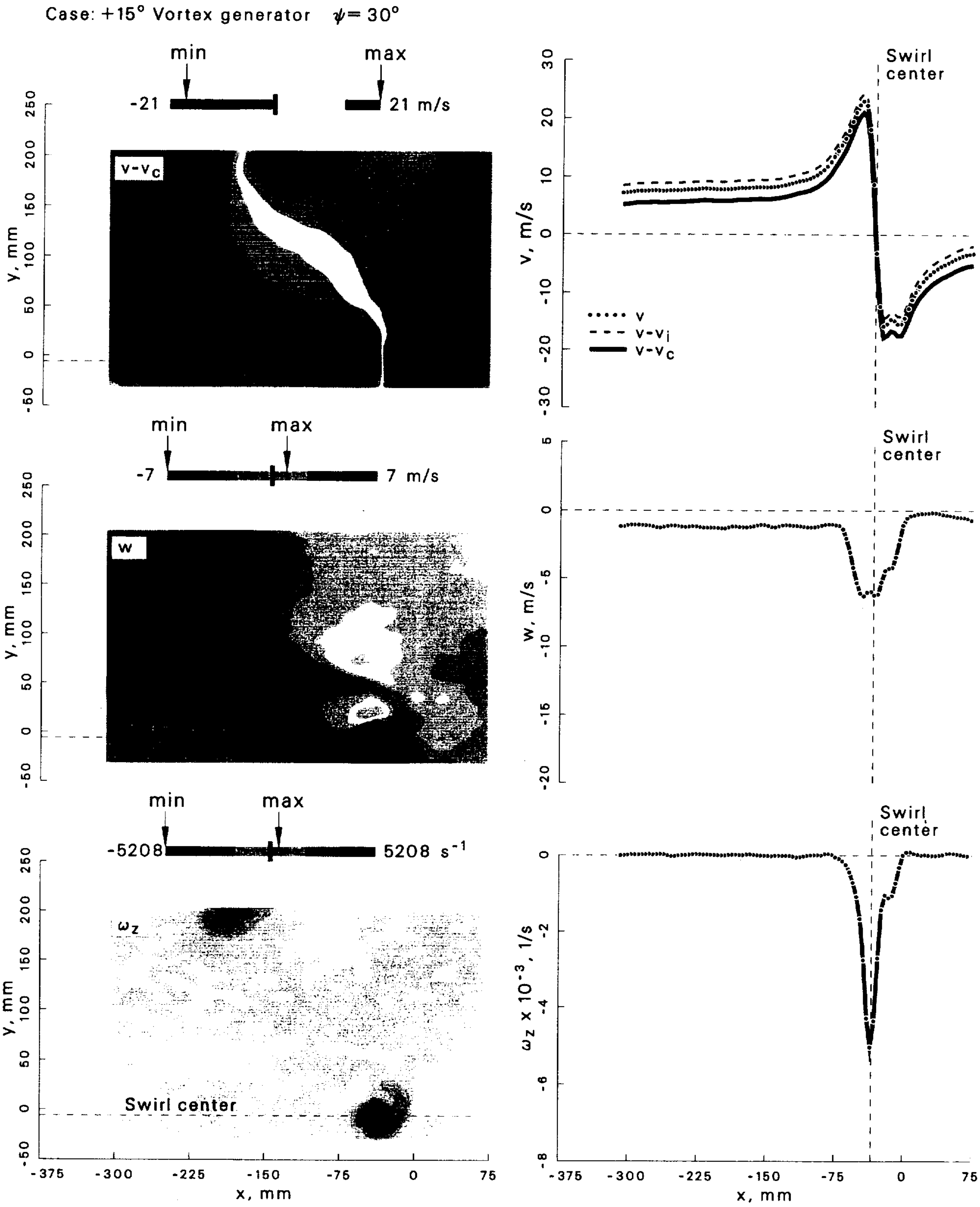

Figure 103: Velocity and vorticity components at $\psi = 30°$ for the +15° vortex generator case.

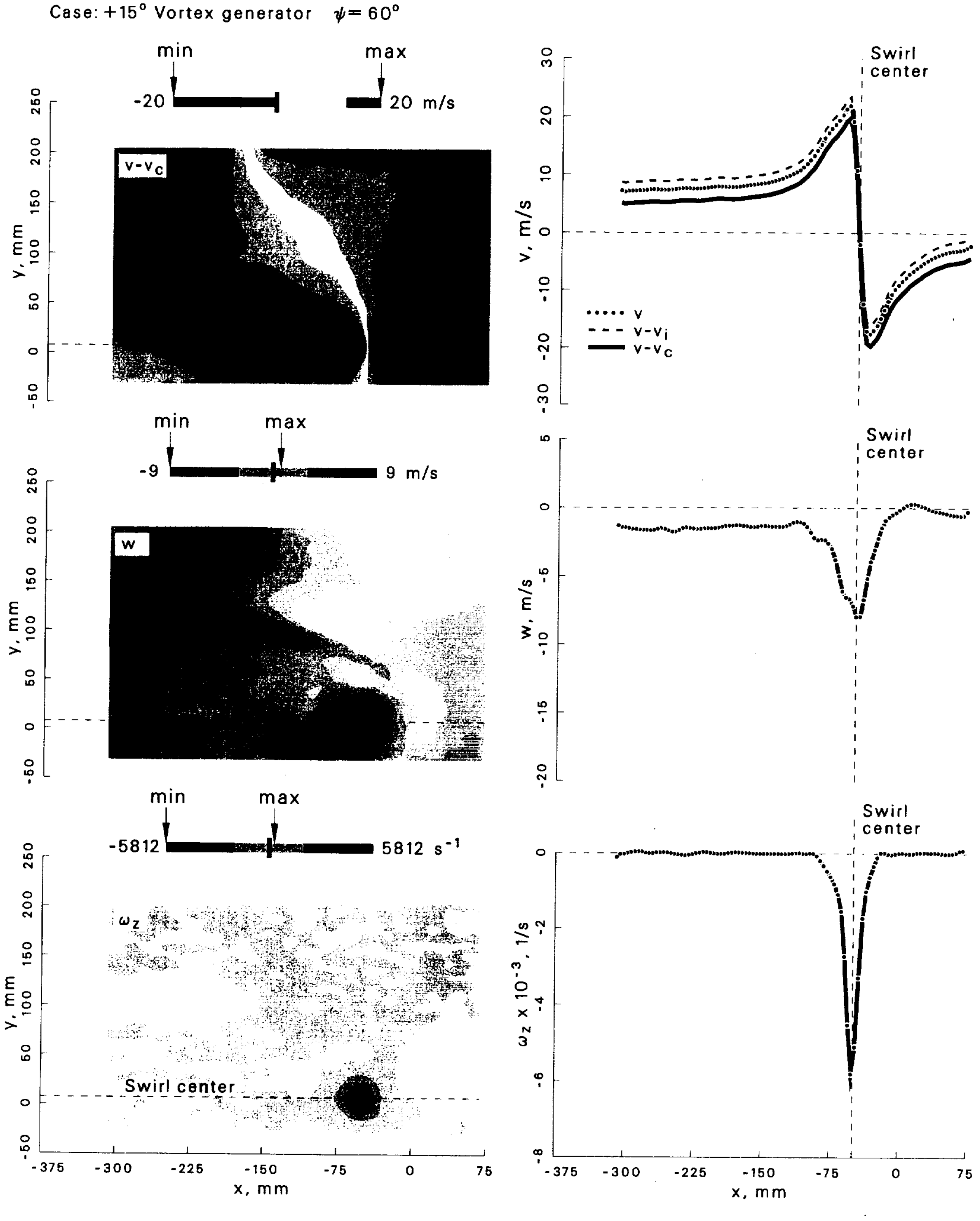

Figure 104: Velocity and vorticity components at $\psi = 60°$ for the $+15°$ vortex generator case.

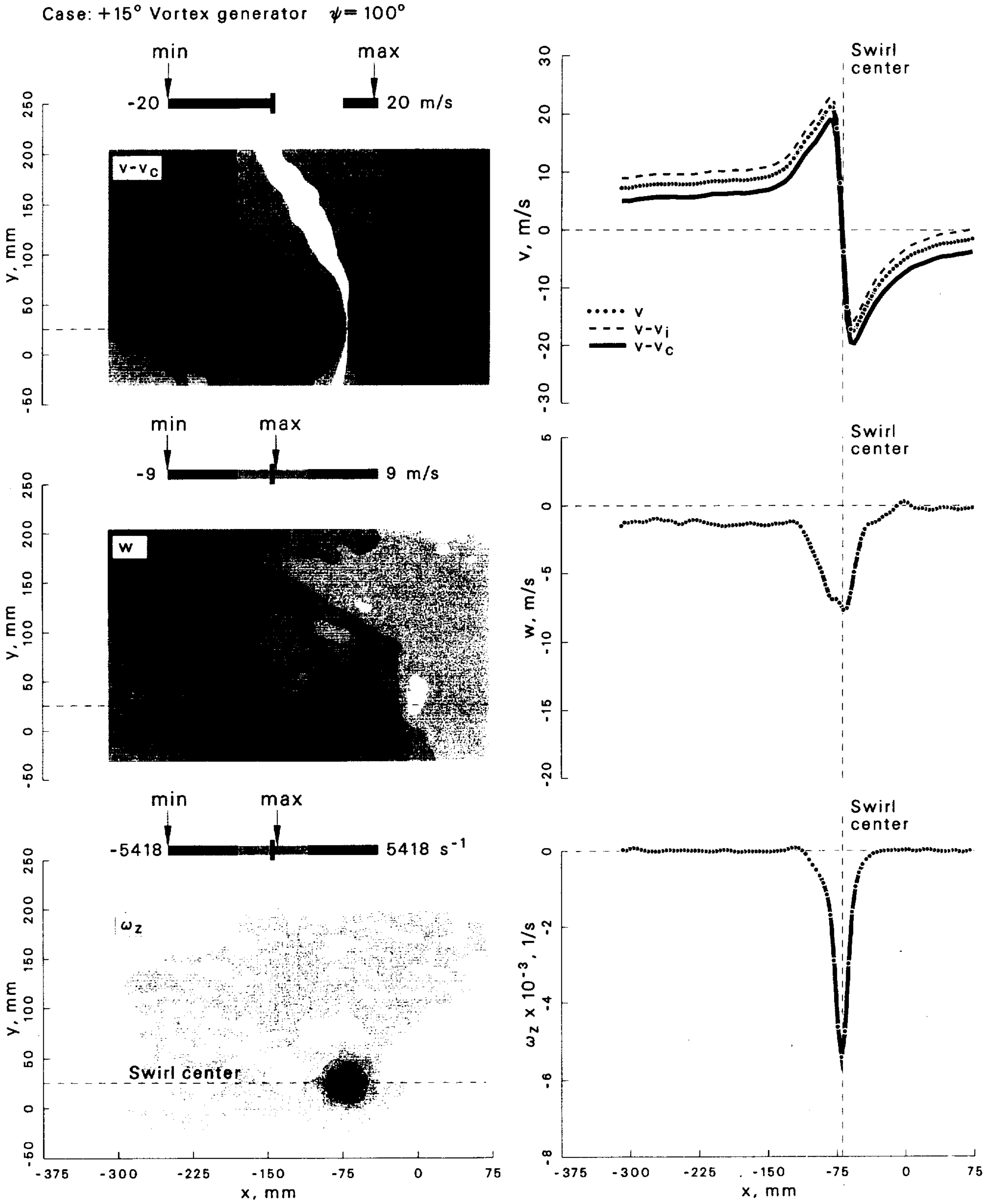

Figure 105: Velocity and vorticity components at $\psi = 100°$ for the +15° vortex generator case.

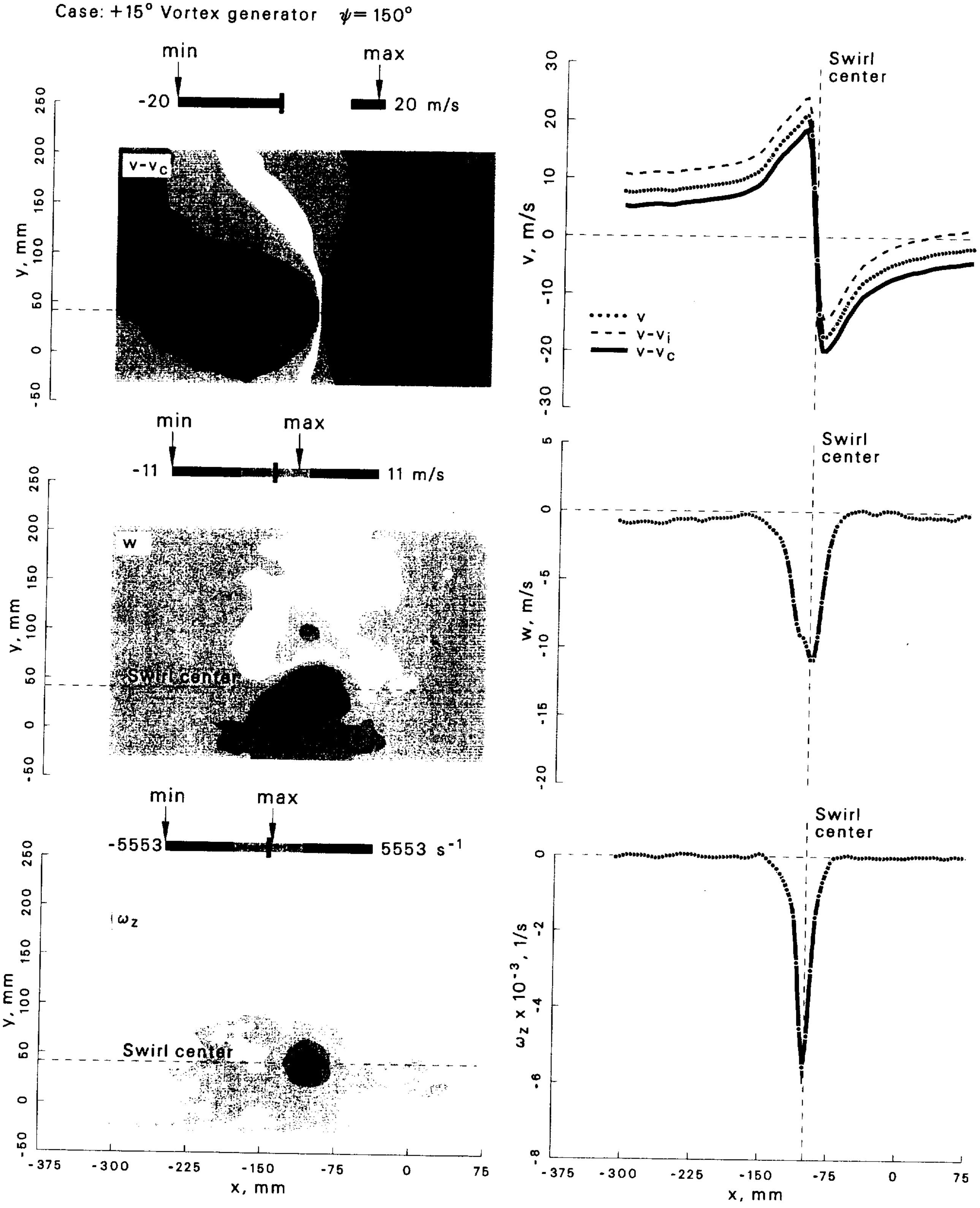

Figure 106: Velocity and vorticity components at $\psi = 150°$ for the +15° vortex generator case.

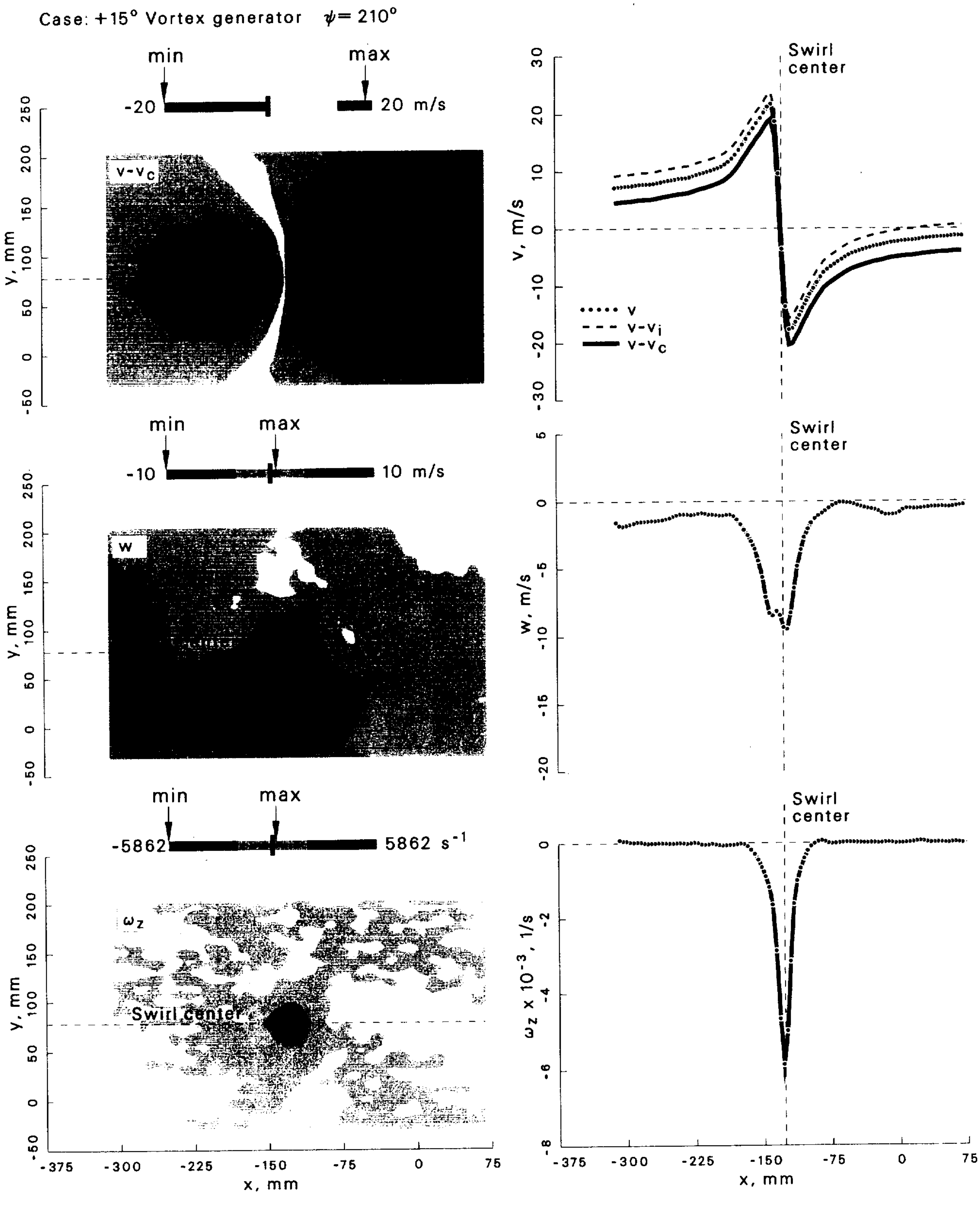

Figure 107: Velocity and vorticity components at $\psi = 210°$ for the $+15°$ vortex generator case.

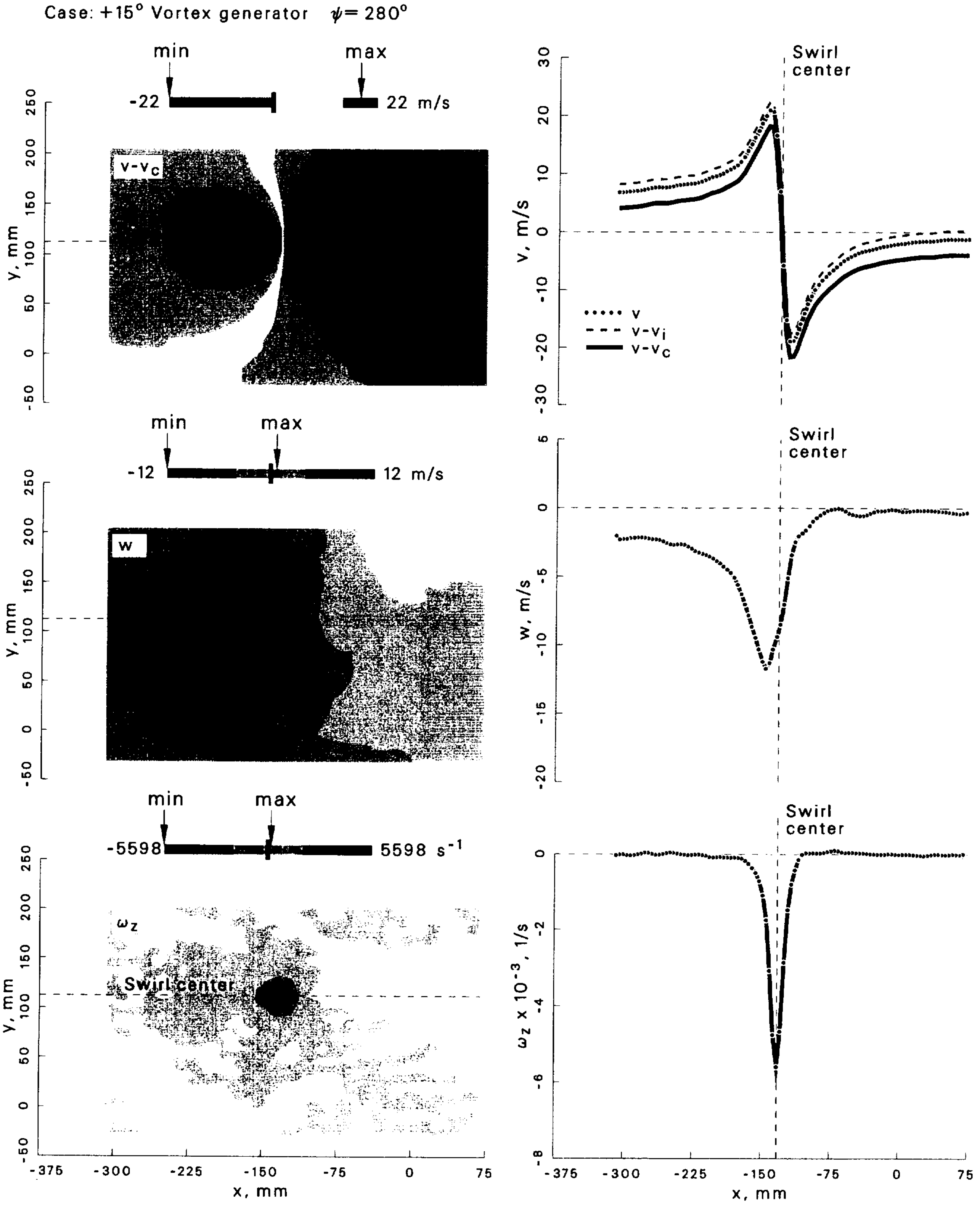

Figure 108: Velocity and vorticity components at ψ = 280° for the +15° vortex generator case.

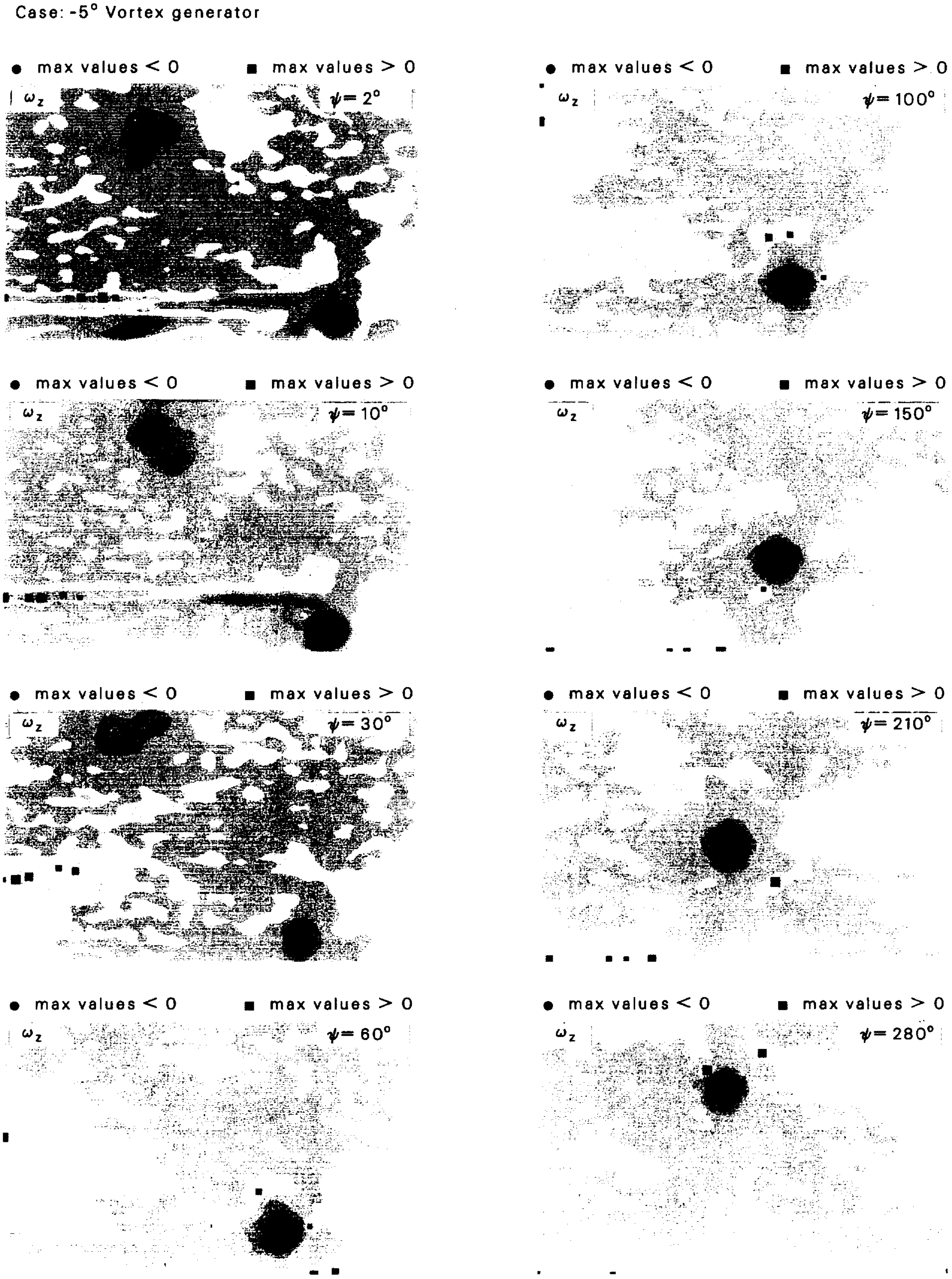

Figure 109: Locations of ω_z extrema at $\psi = 2^\circ \rightarrow 280^\circ$ for the -5° vortex generator case.

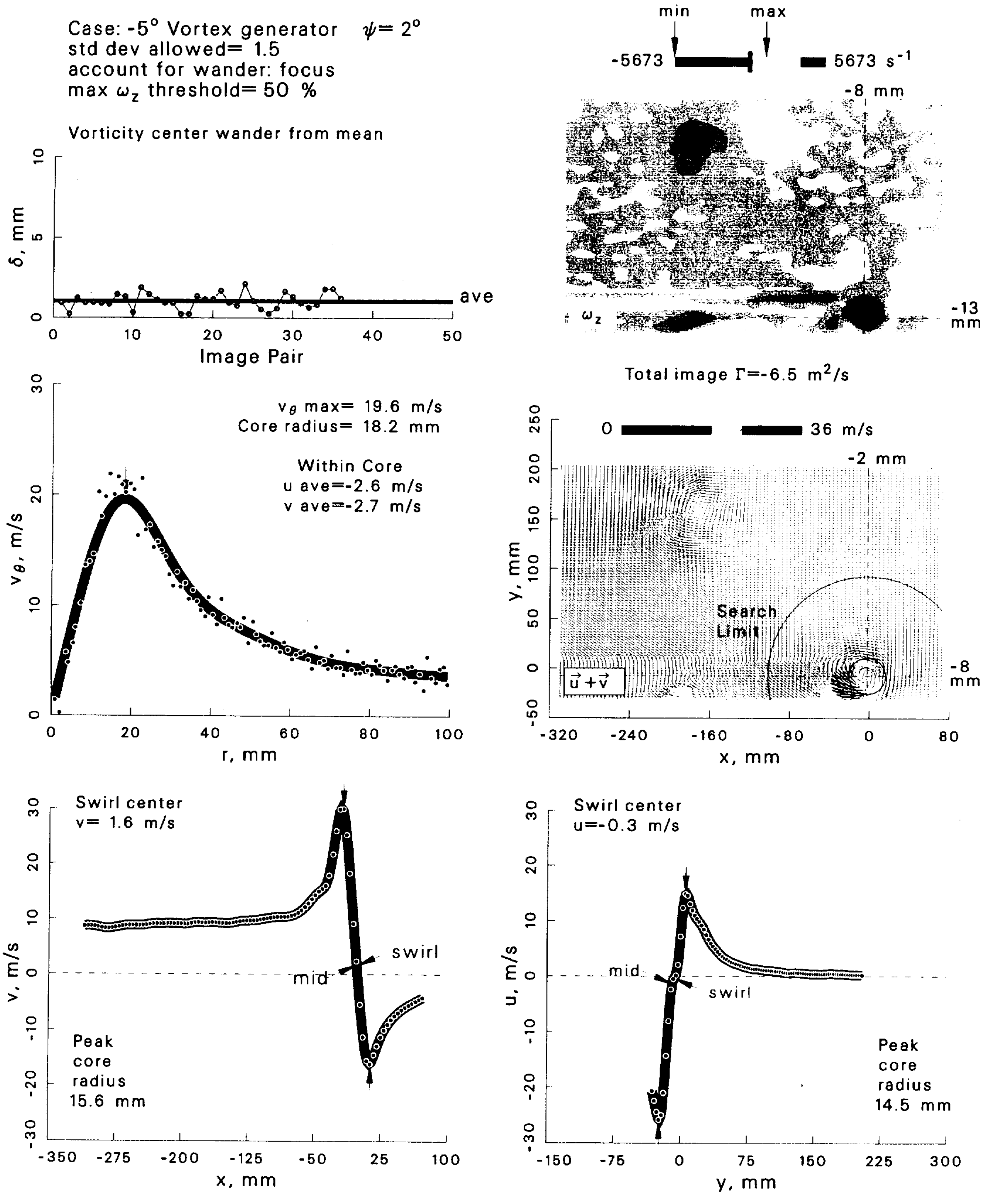

Figure 110: Vortex statistics at $\psi = 2^\circ$ for the -5° vortex generator case.

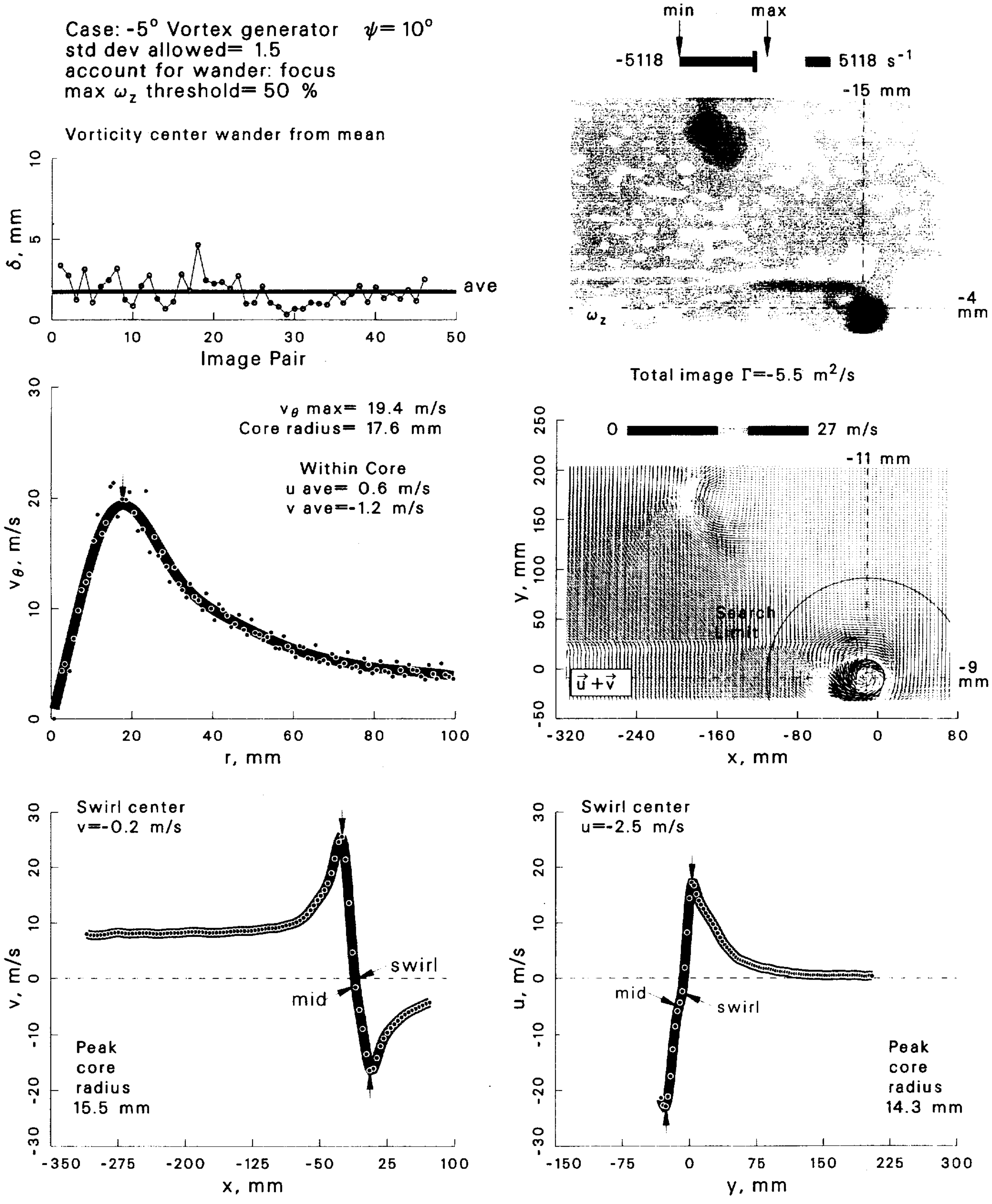

Figure 111: Vortex statistics at $\psi = 10°$ for the $-5°$ vortex generator case.

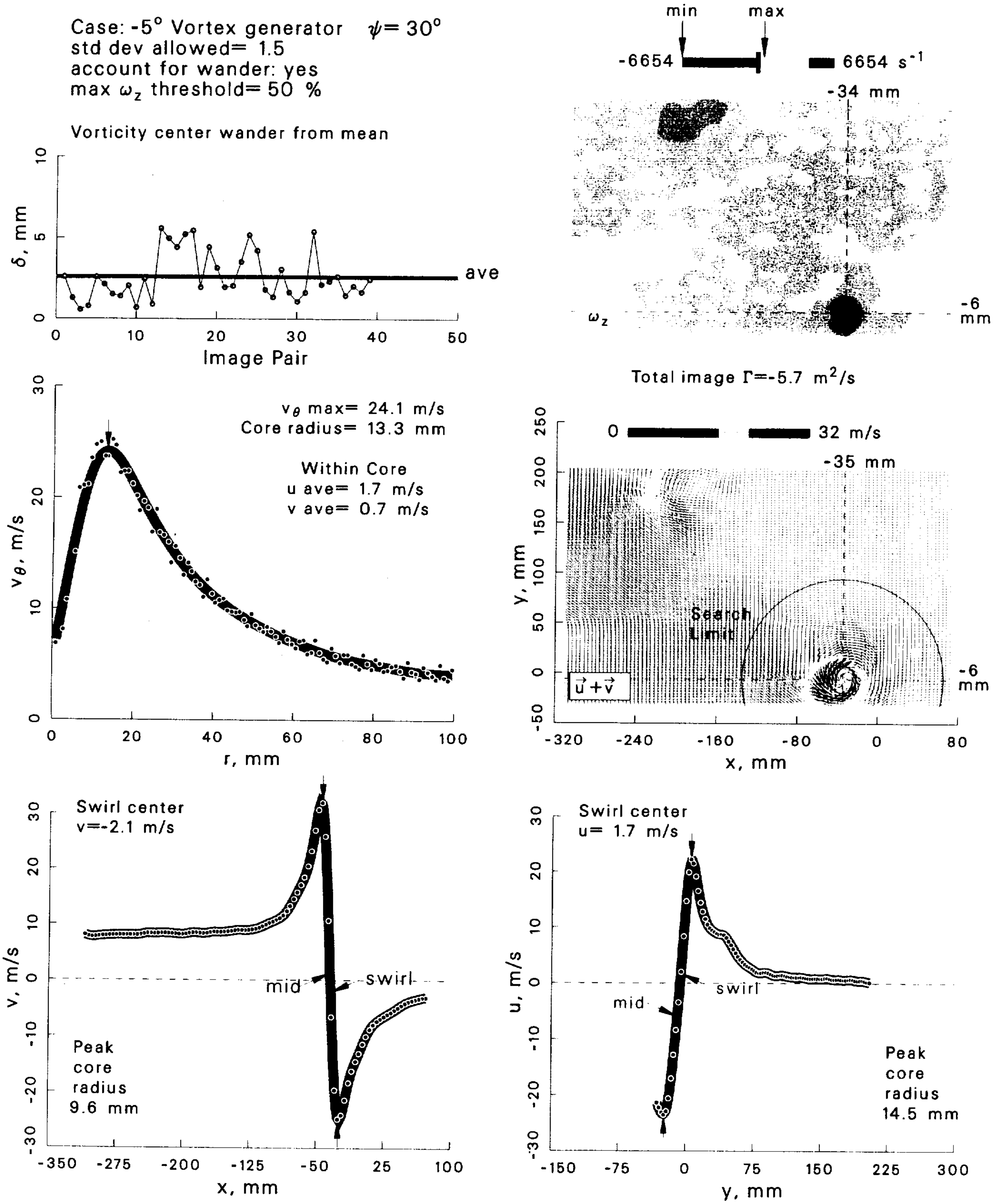

Figure 112: Vortex statistics at $\psi = 30°$ for the $-5°$ vortex generator case.

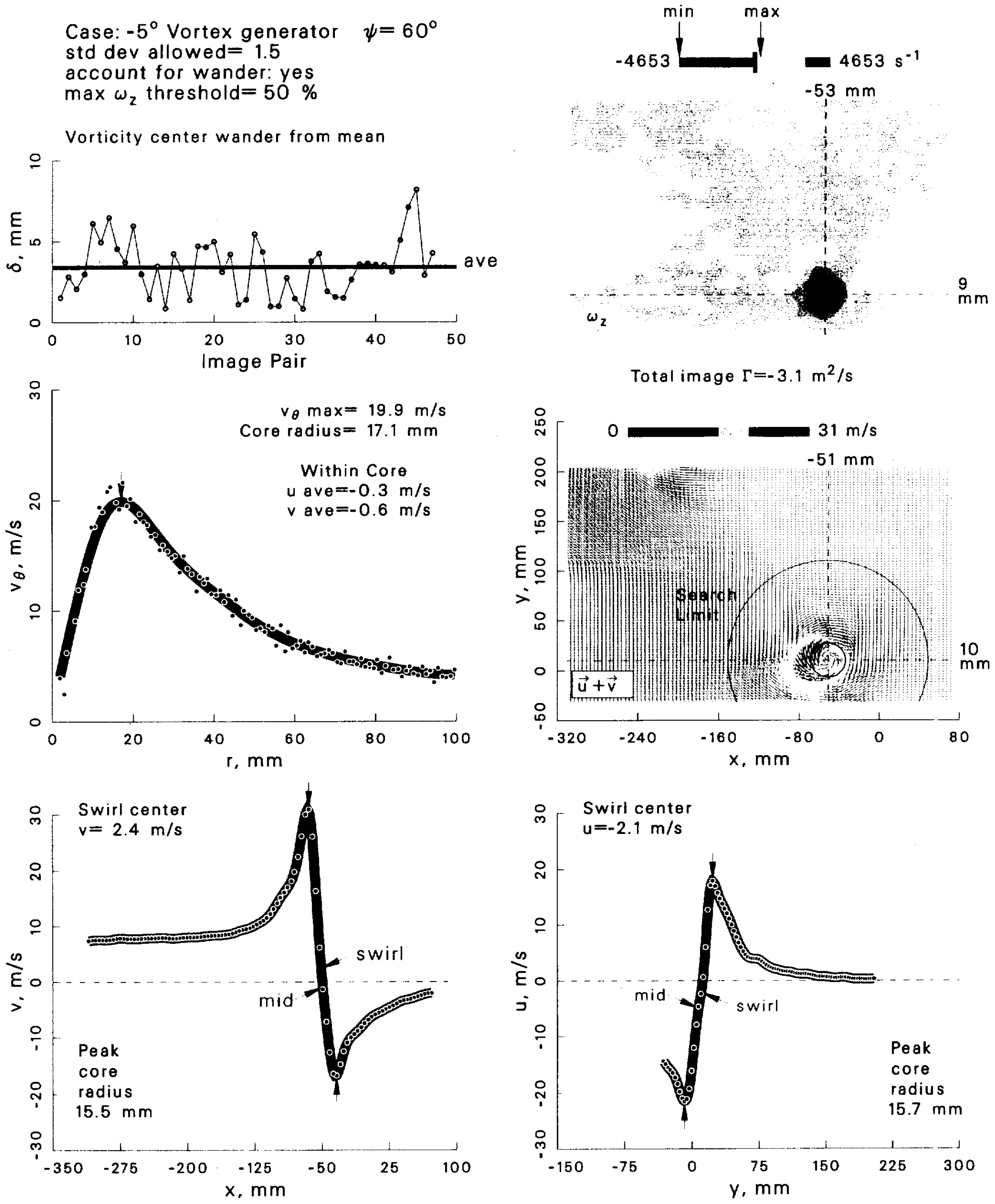

Figure 113: Vortex statistics at $\psi = 60°$ for the $-5°$ vortex generator case.

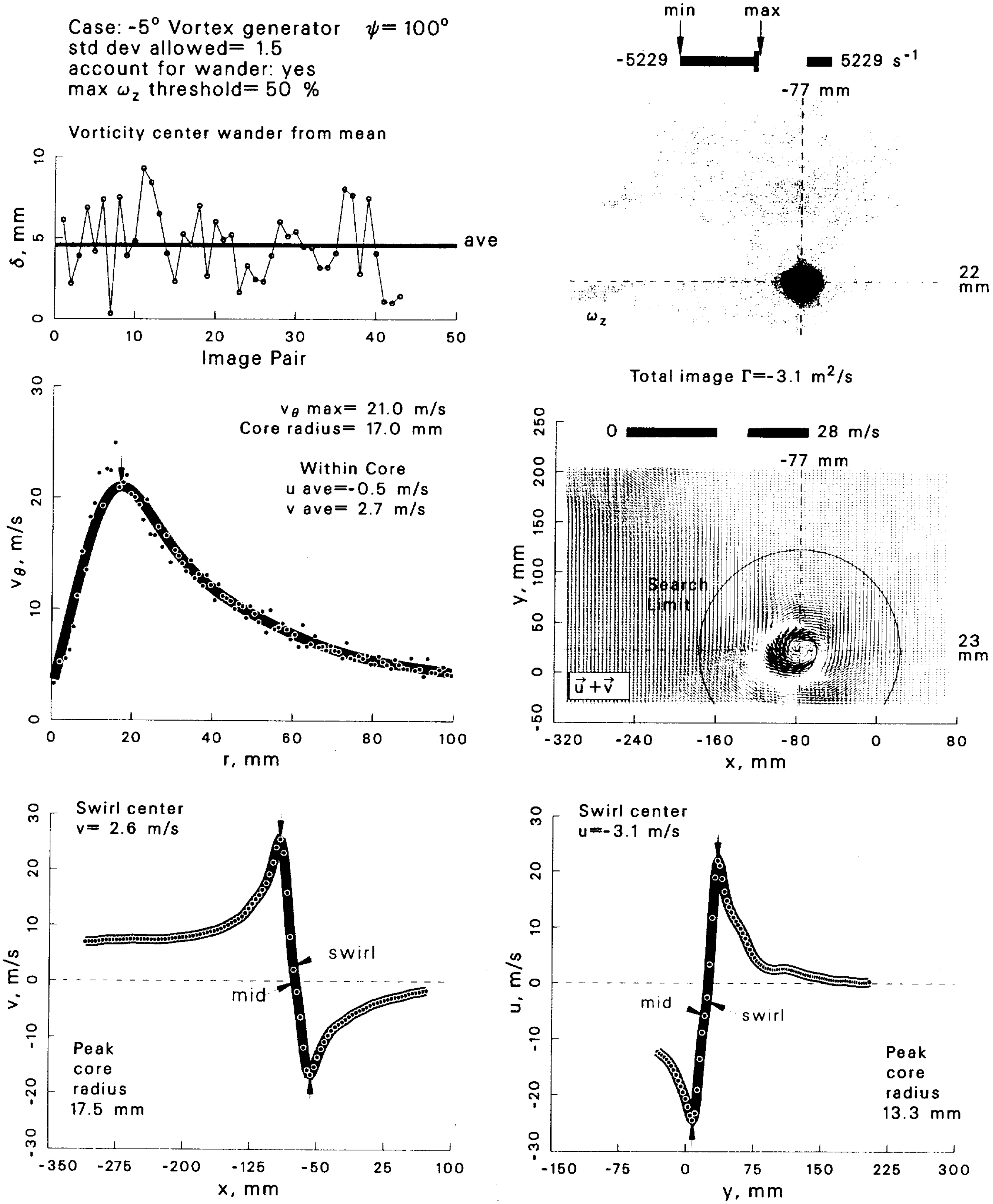

Figure 114: Vortex statistics at $\psi = 100°$ for the $-5°$ vortex generator case.

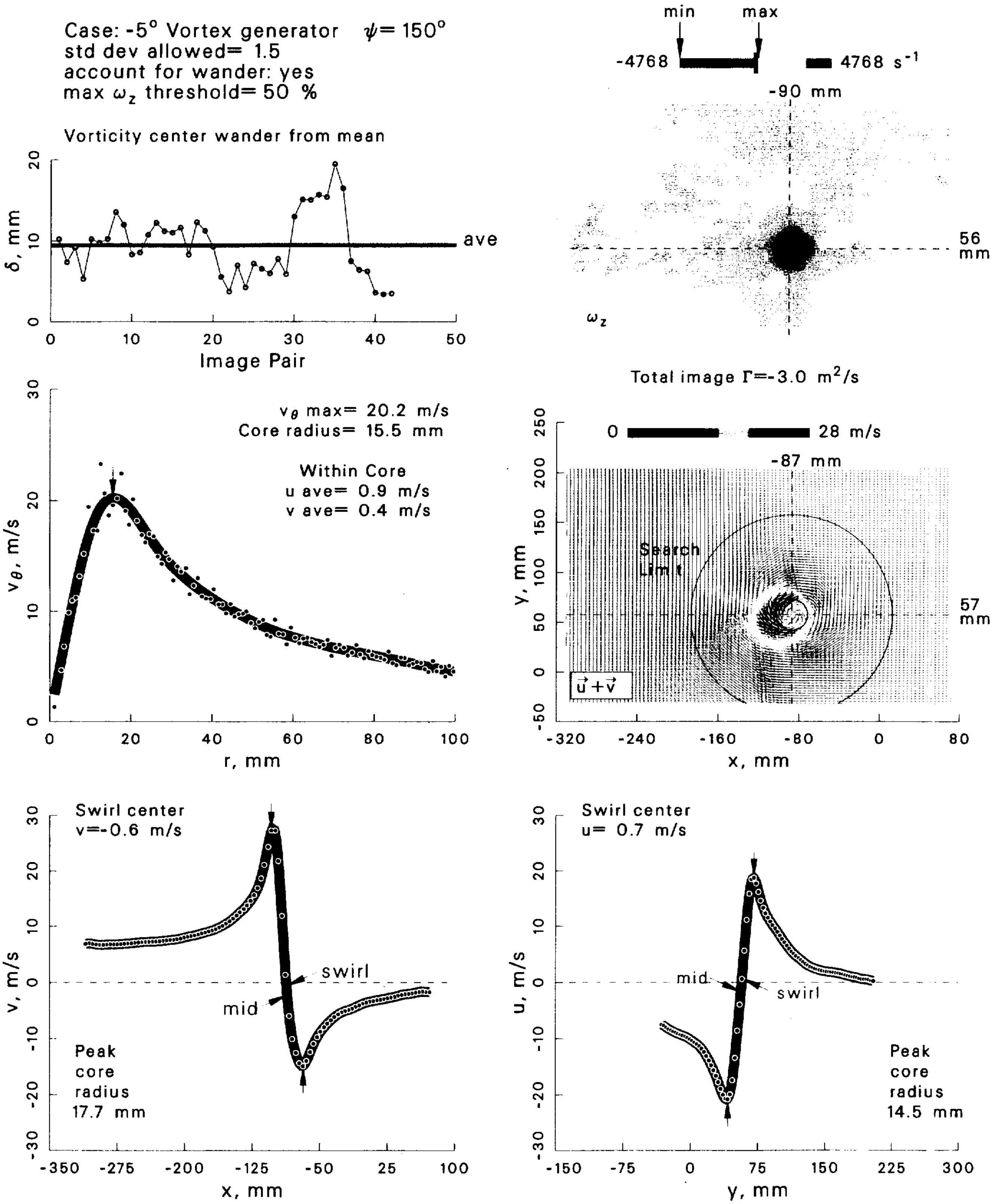

Figure 115: Vortex statistics at $\psi = 150°$ for the $-5°$ vortex generator case.

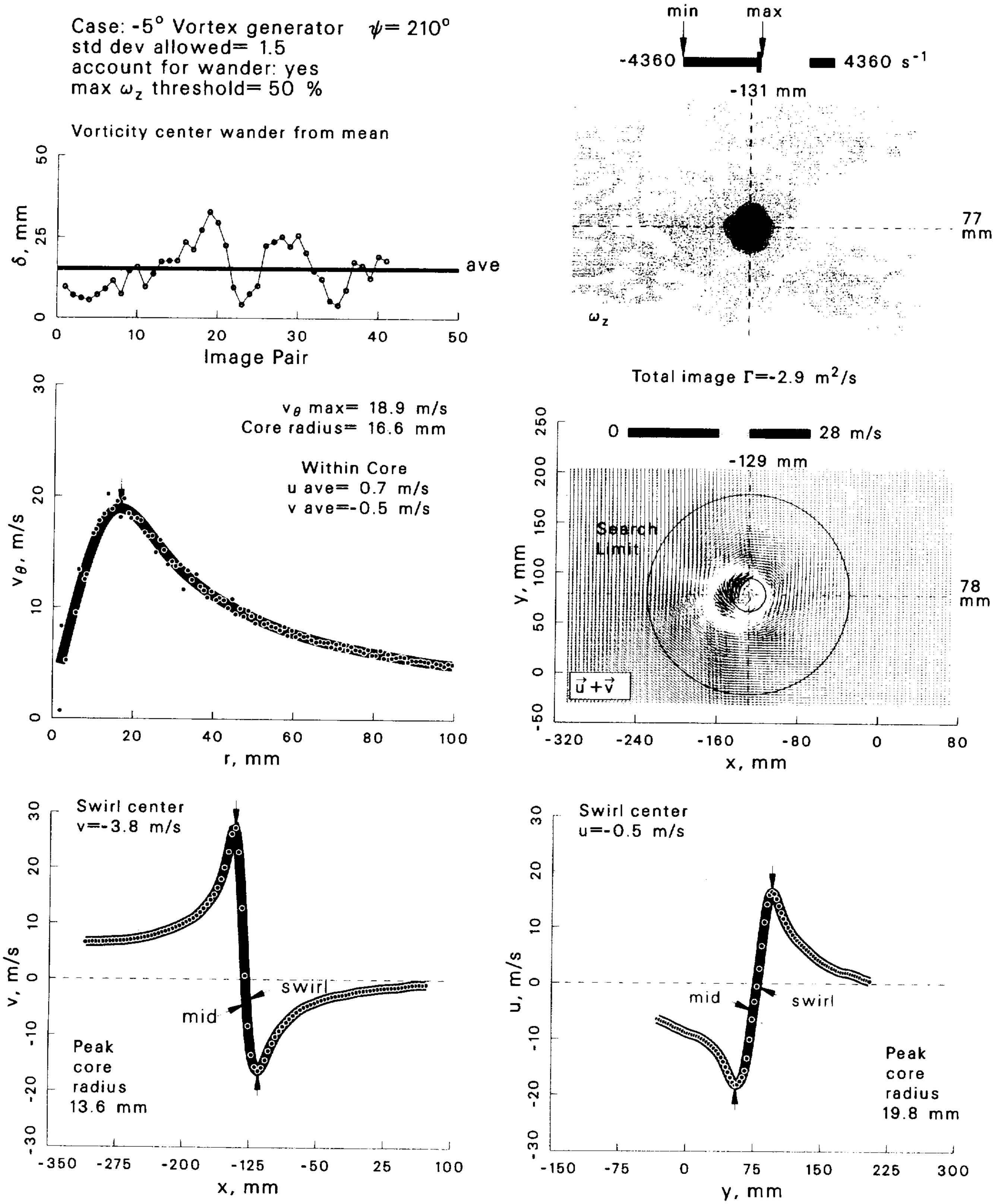

Figure 116: Vortex statistics at $\psi = 210°$ for the $-5°$ vortex generator case.

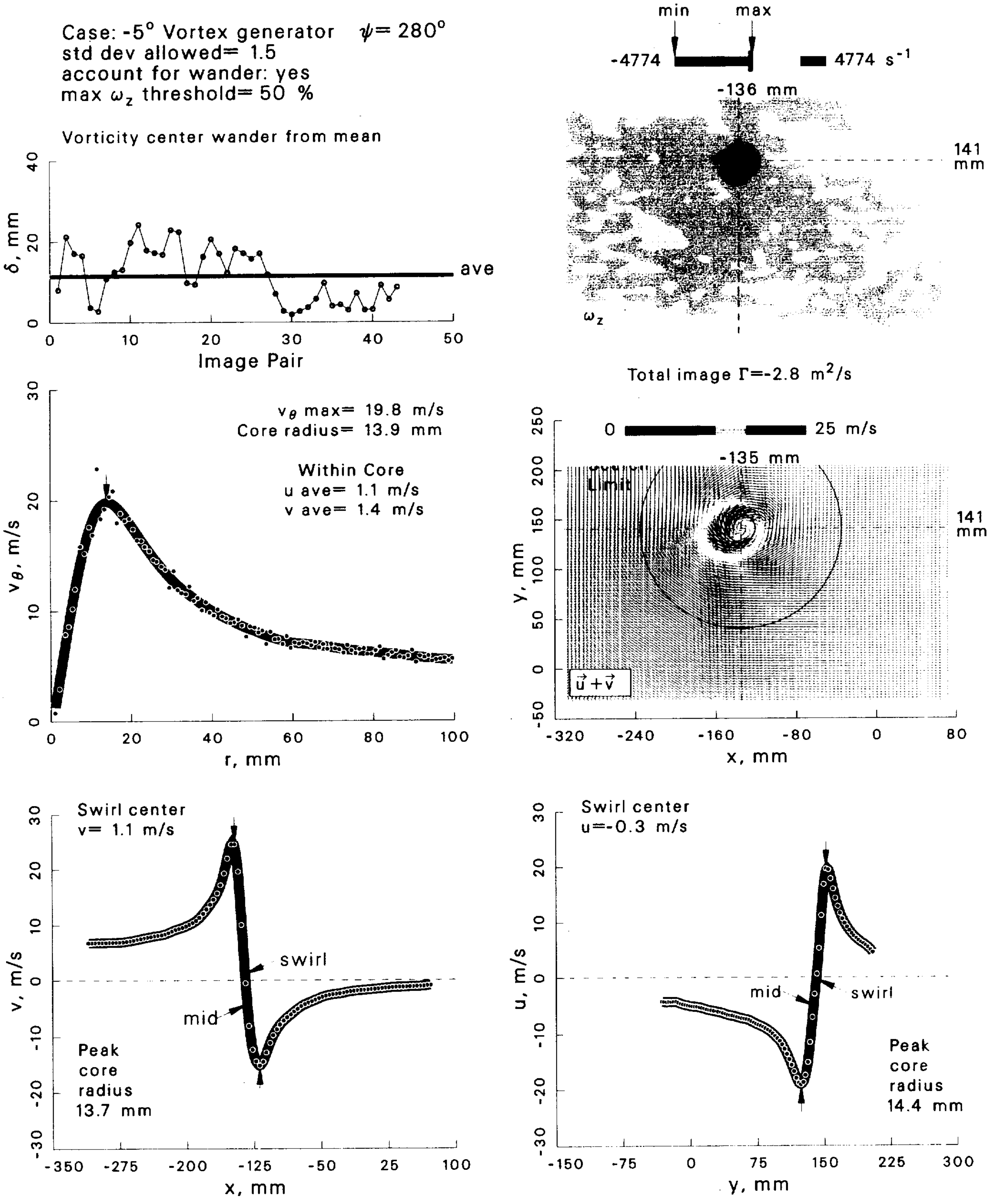

Figure 117: Vortex statistics at $\psi = 280°$ for the $-5°$ vortex generator case.

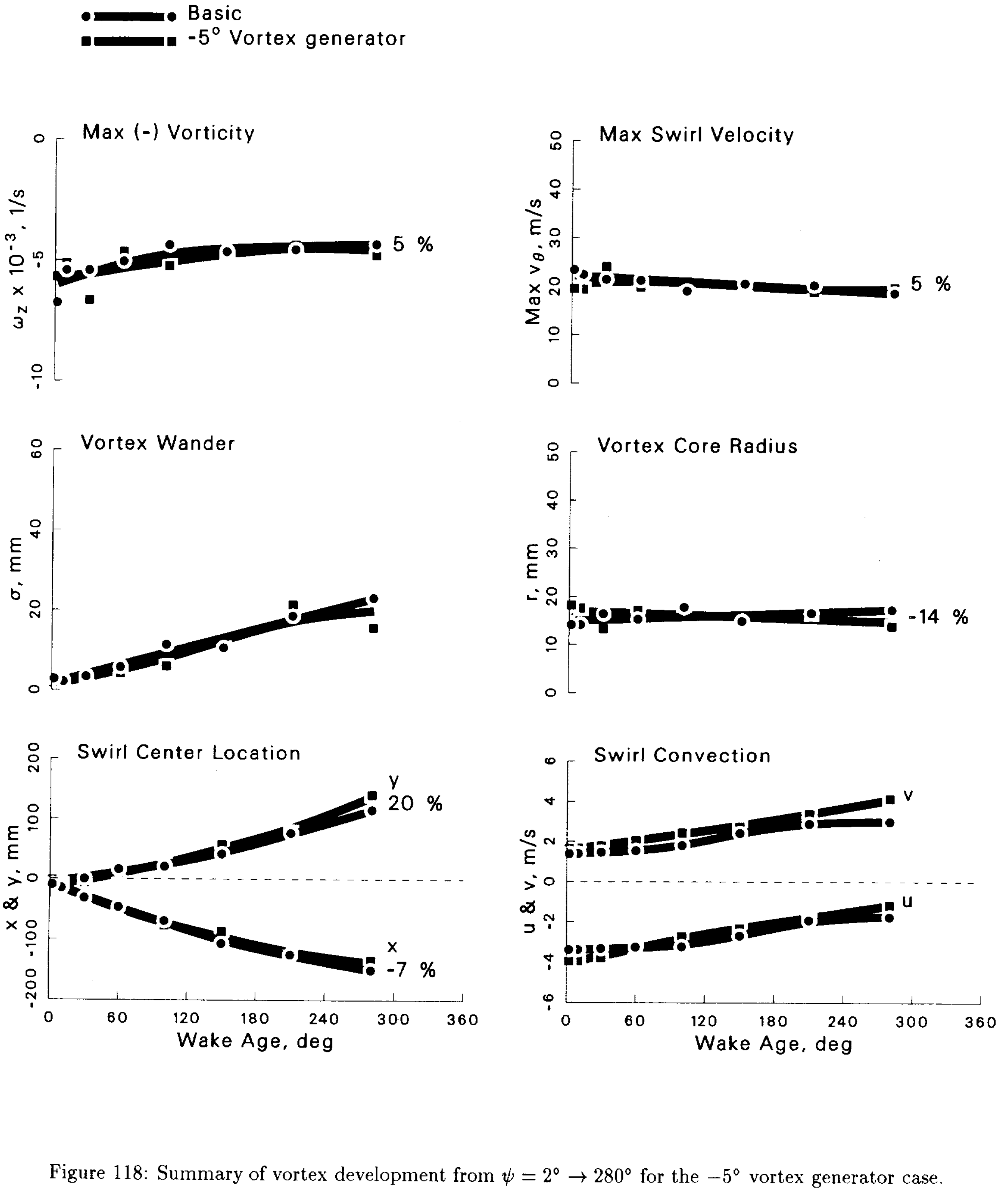

Figure 118: Summary of vortex development from $\psi = 2° \rightarrow 280°$ for the $-5°$ vortex generator case.

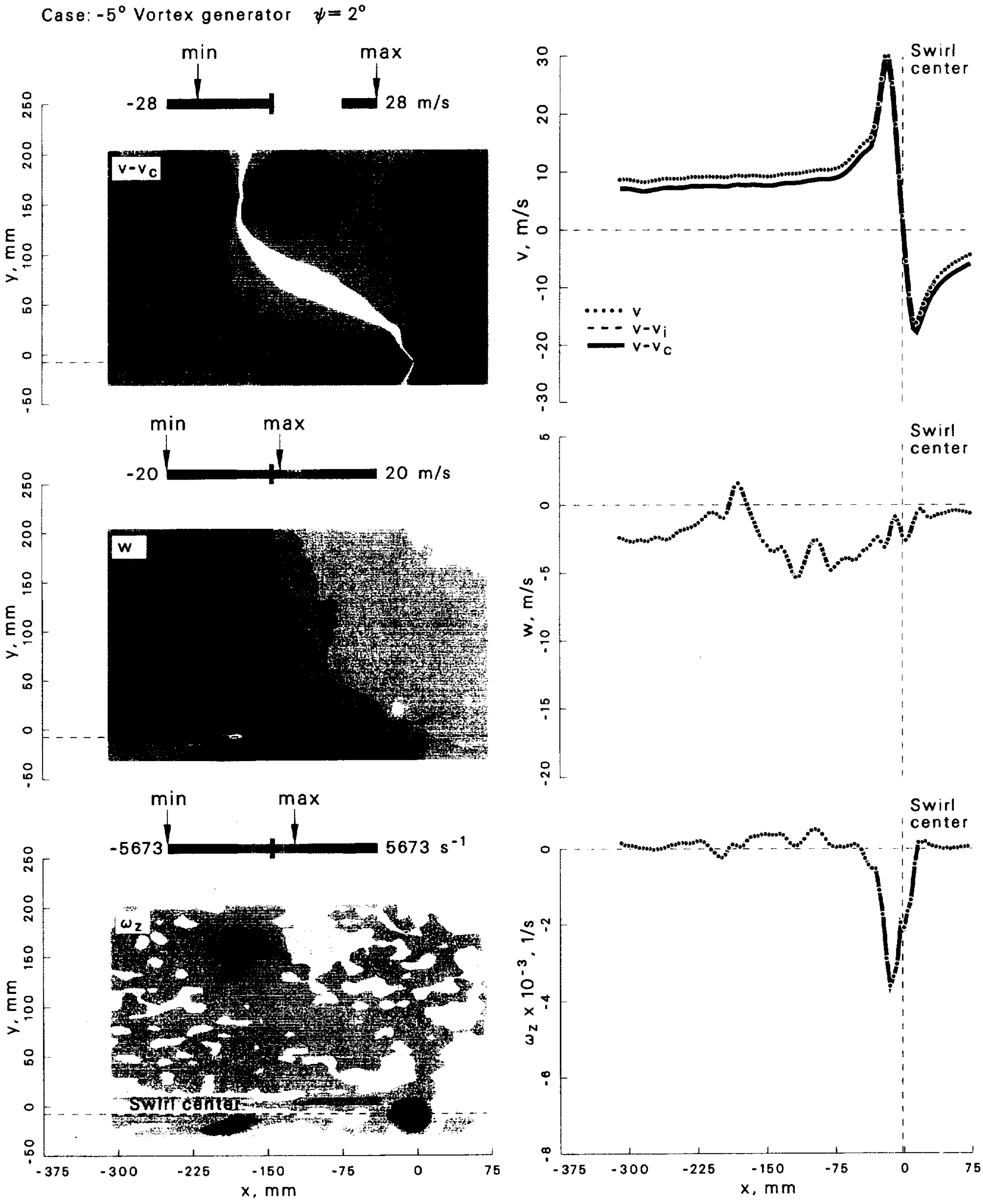

Figure 119: Velocity and vorticity components at $\psi = 2°$ for the $-5°$ vortex generator case.

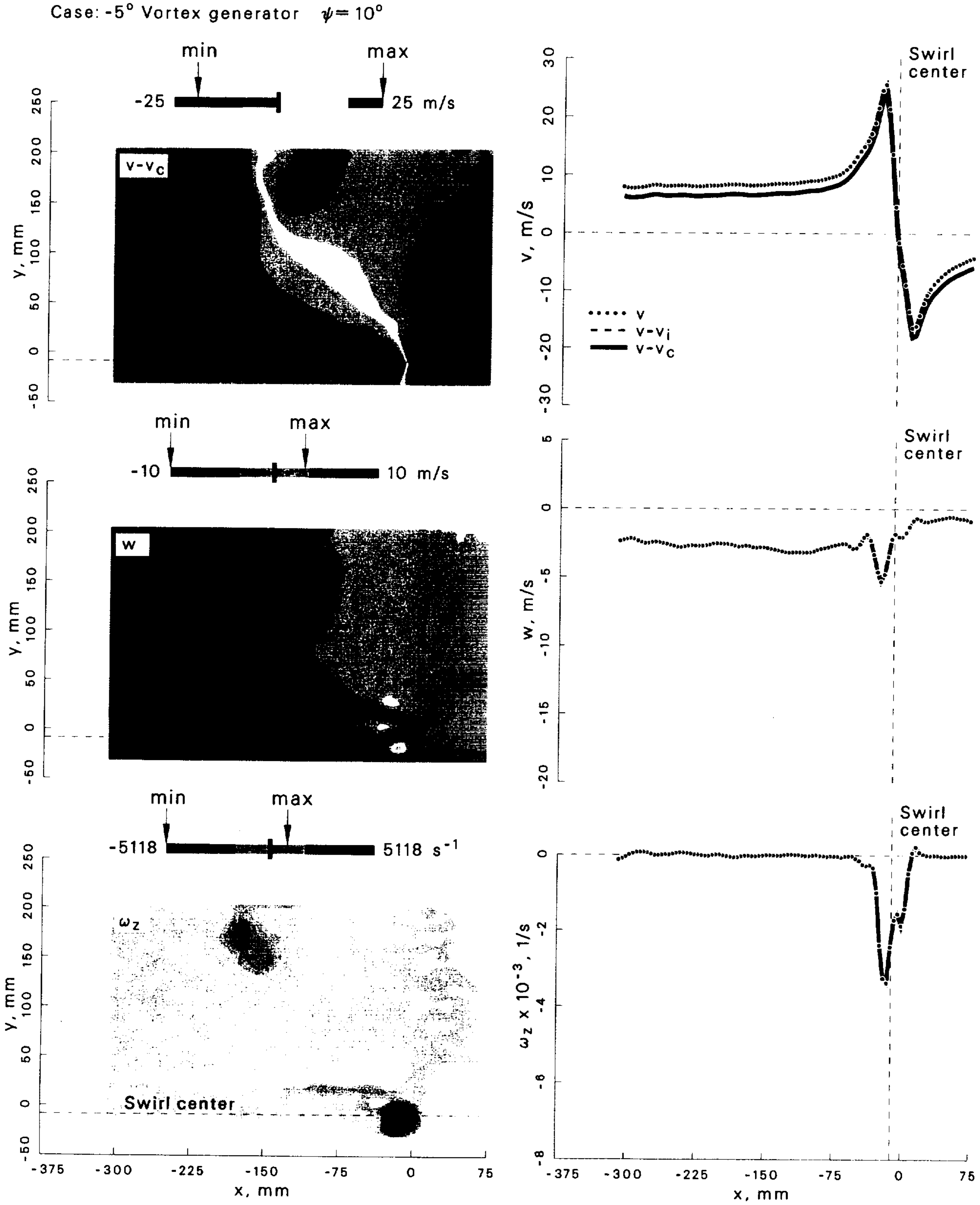

Figure 120: Velocity and vorticity components at $\psi = 10°$ for the $-5°$ vortex generator case.

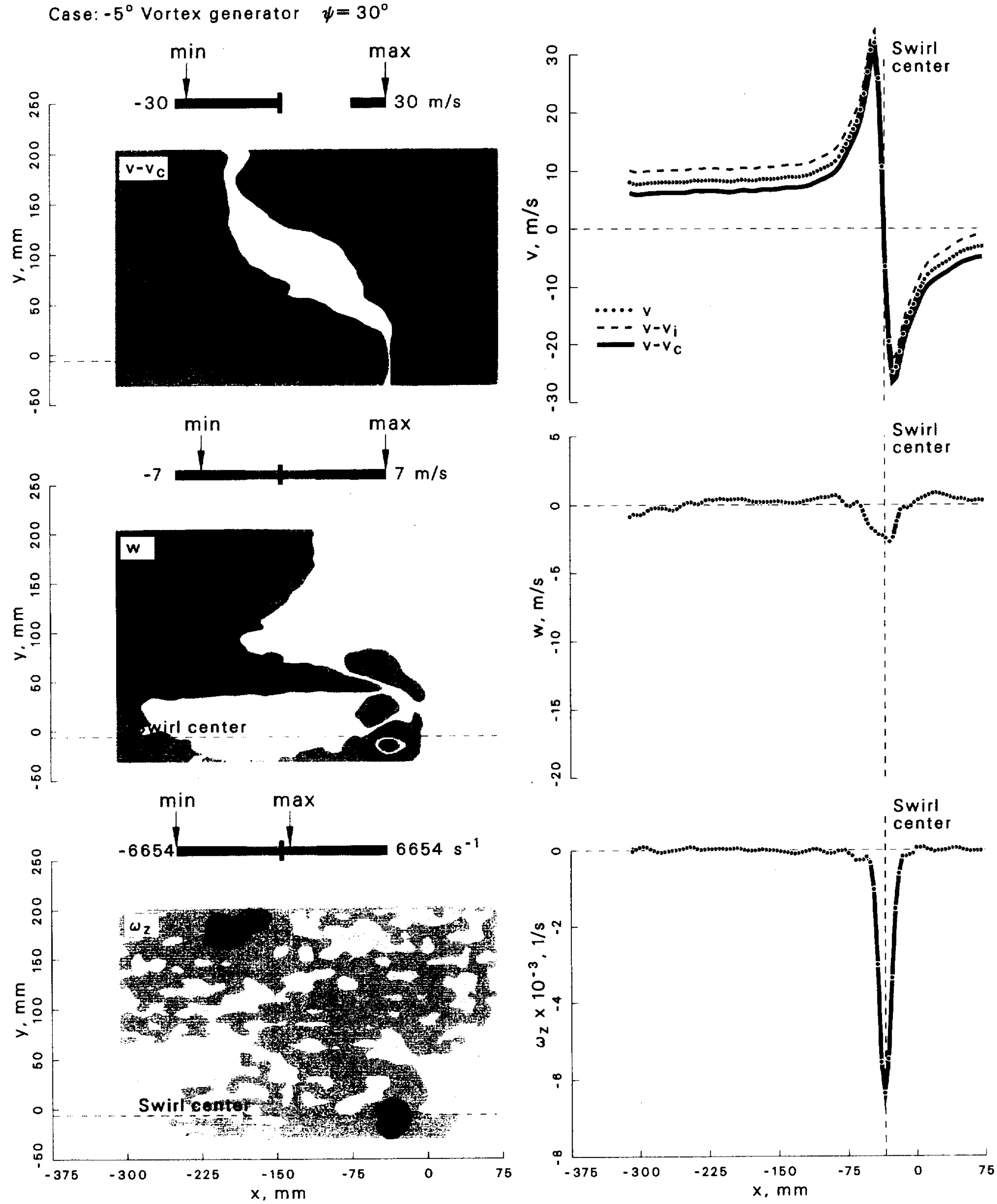

Figure 121: Velocity and vorticity components at $\psi = 30^\circ$ for the -5° vortex generator case.

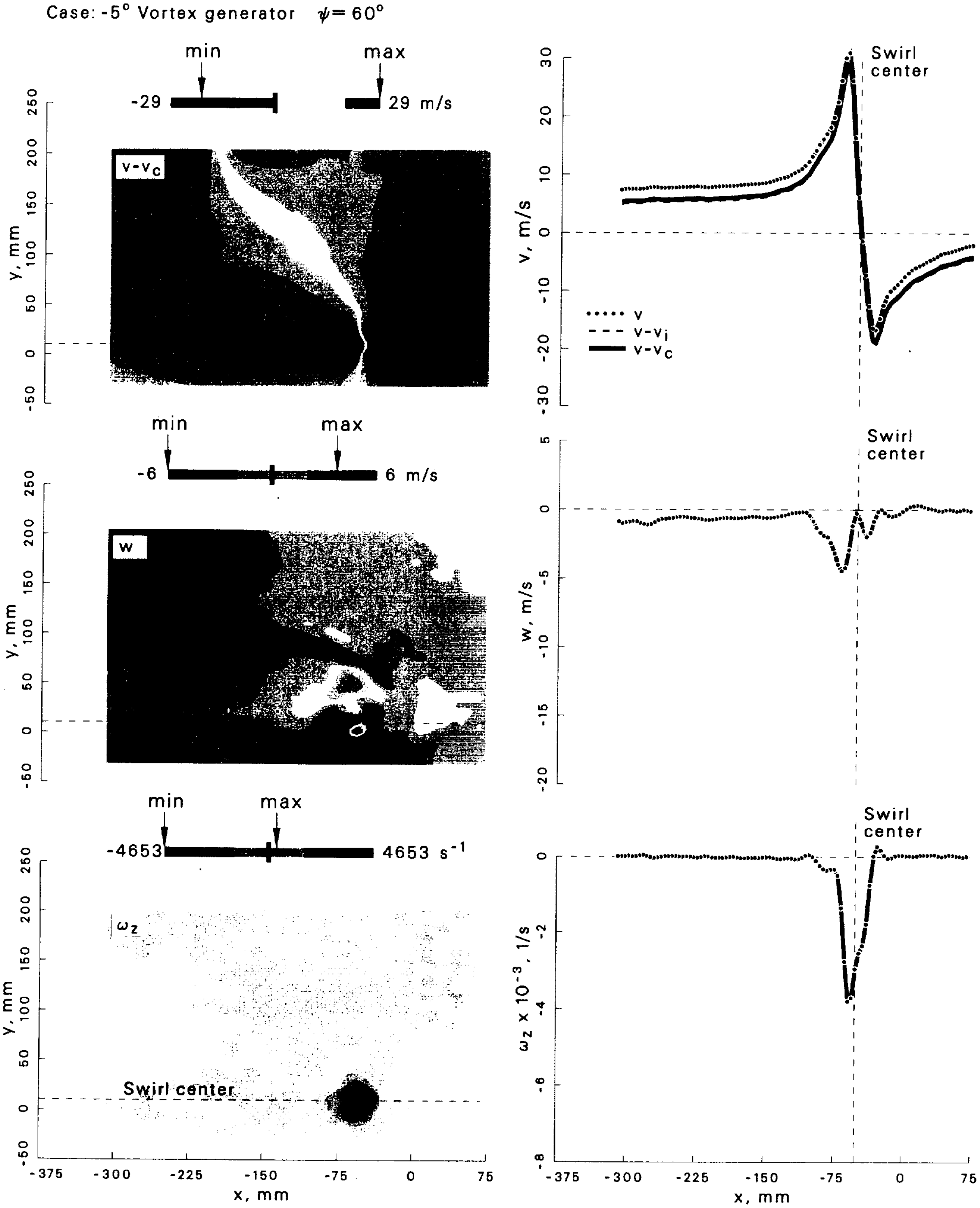

Figure 122: Velocity and vorticity components at $\psi = 60°$ for the $-5°$ vortex generator case.

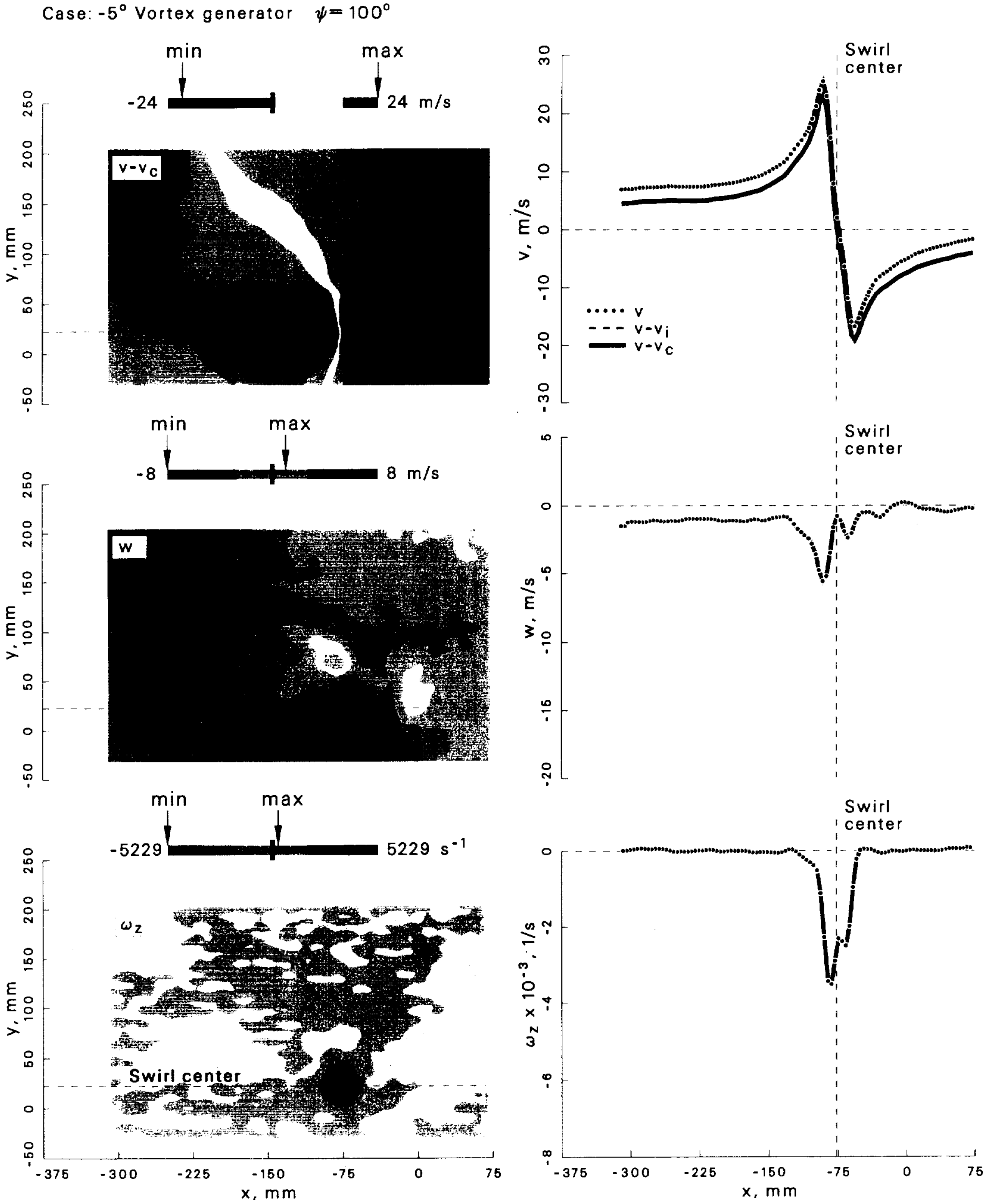

Figure 123: Velocity and vorticity components at $\psi = 100°$ for the $-5°$ vortex generator case.

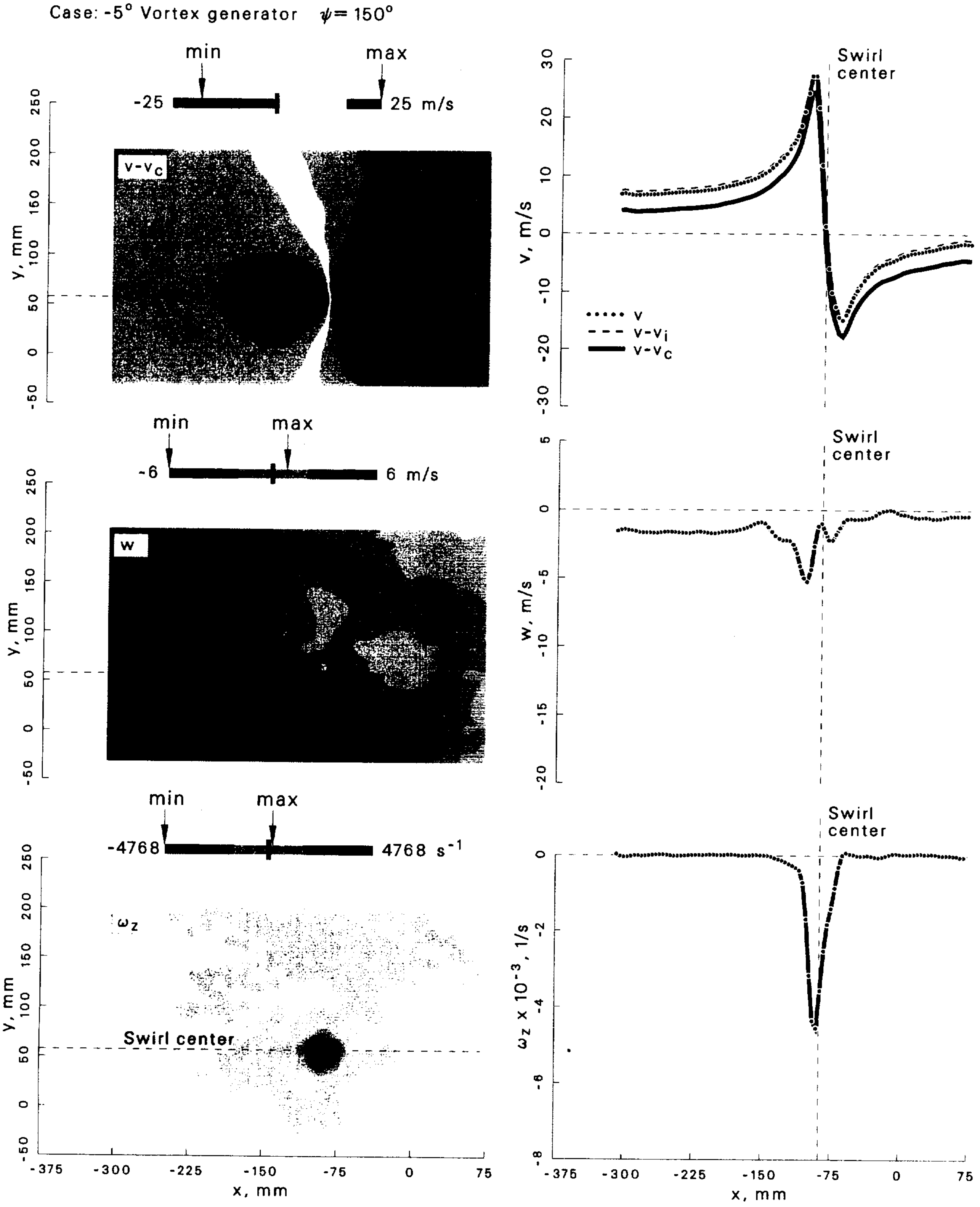

Figure 124: Velocity and vorticity components at $\psi = 150°$ for the $-5°$ vortex generator case.

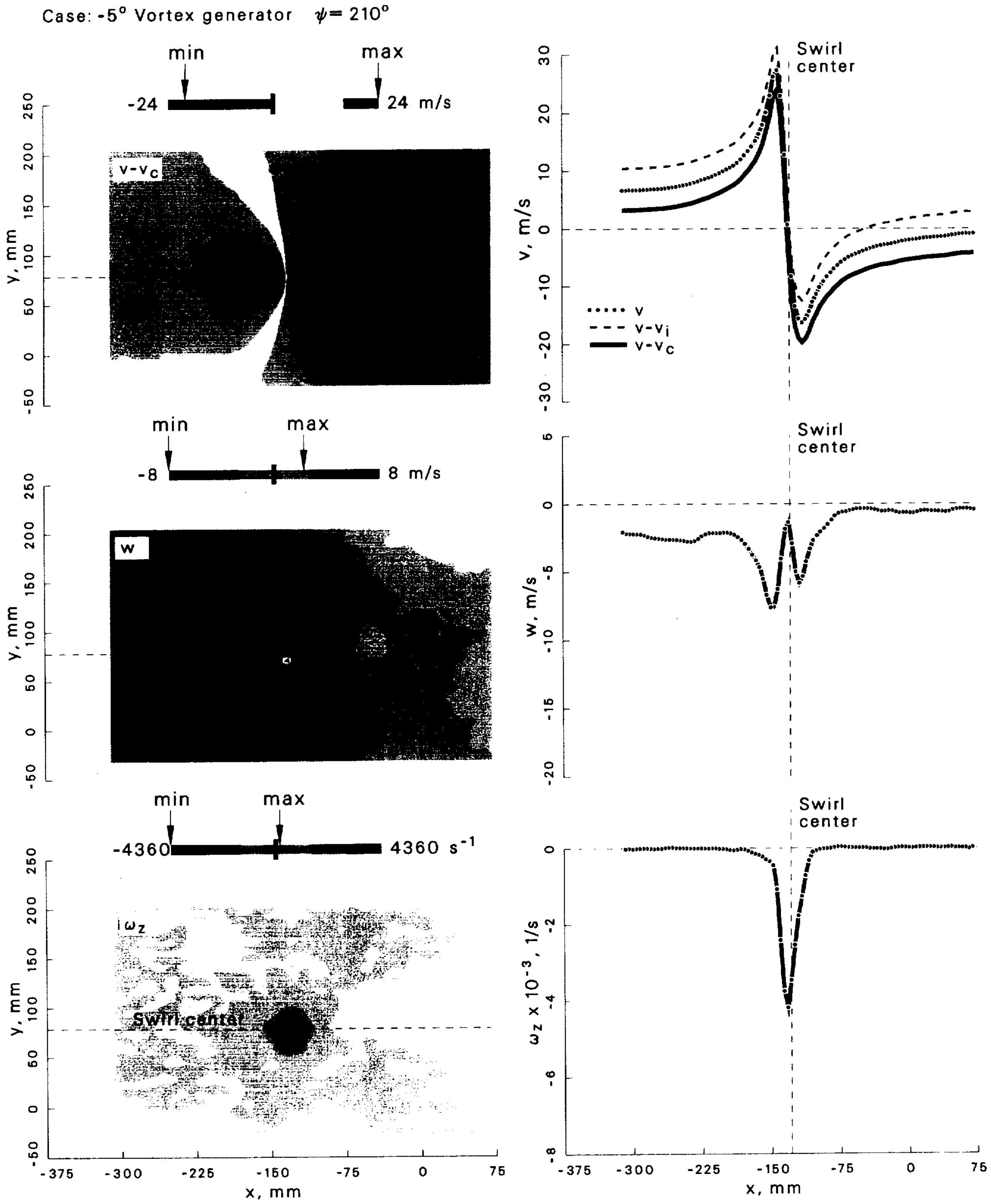

Figure 125: Velocity and vorticity components at $\psi = 210°$ for the $-5°$ vortex generator case.

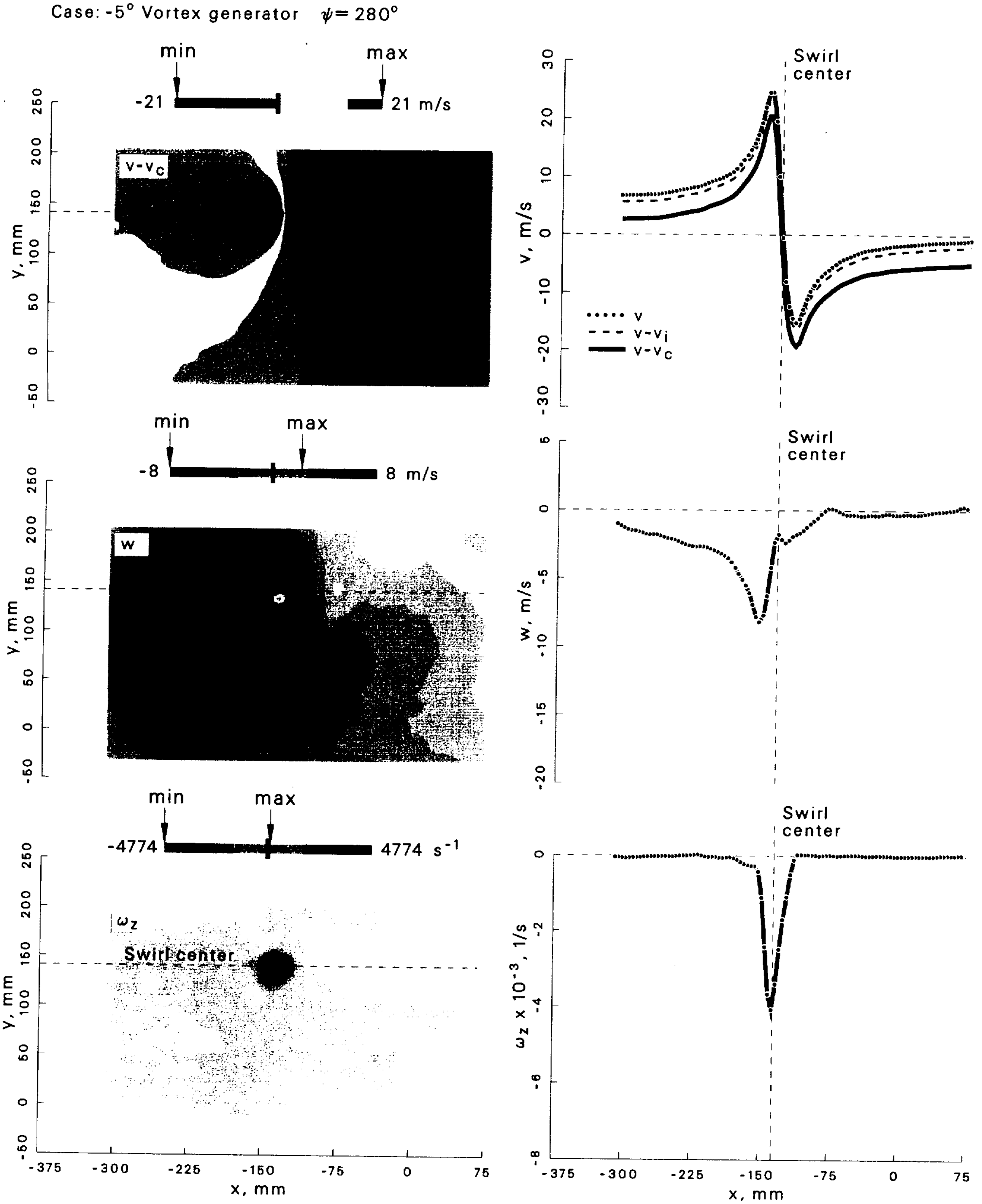

Figure 126: Velocity and vorticity components at $\psi = 280°$ for the $-5°$ vortex generator case.

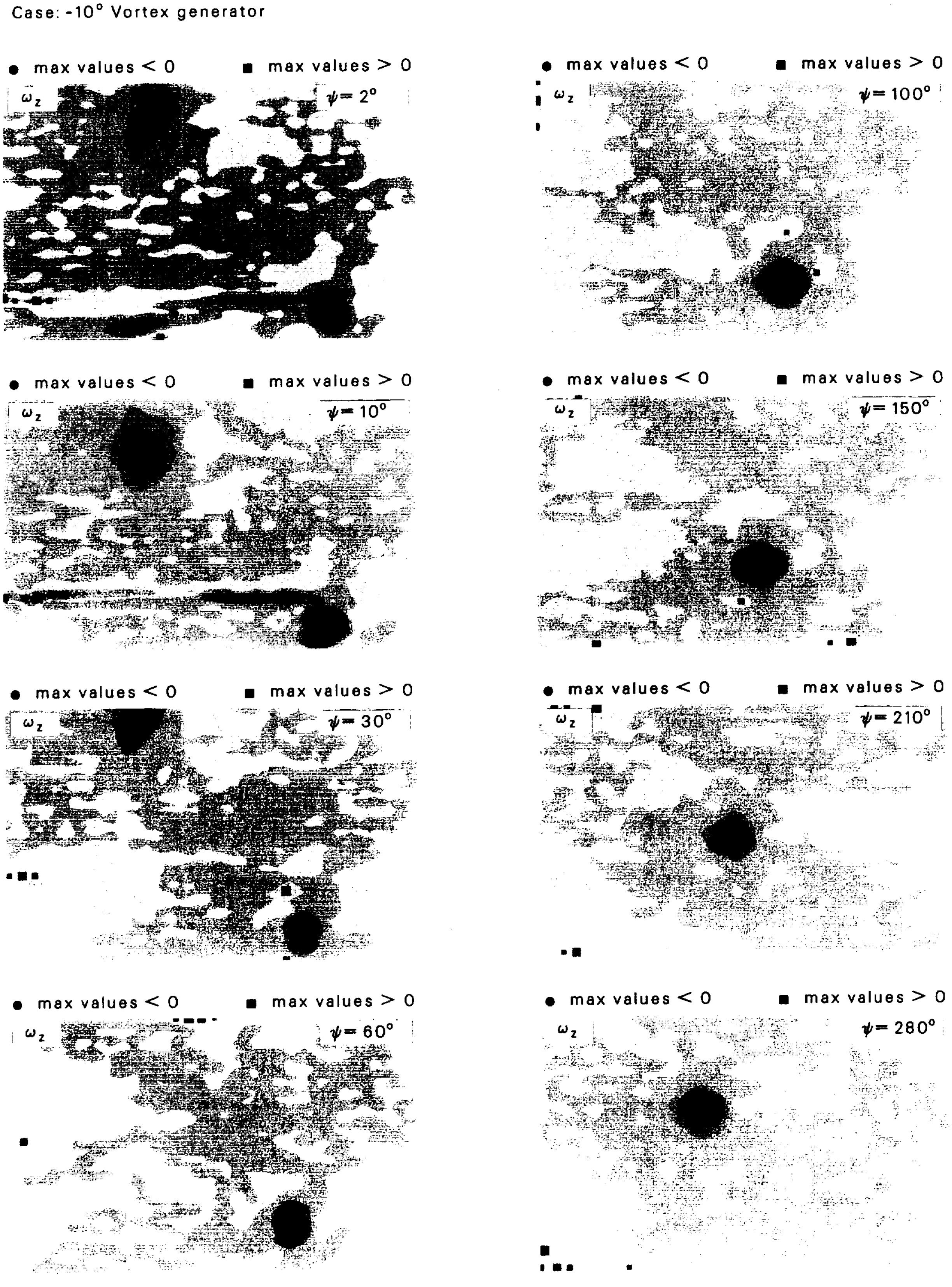

Figure 127: Locations of ω_z extrema at $\psi = 2^\circ \rightarrow 280^\circ$ for the -10° vortex generator case.

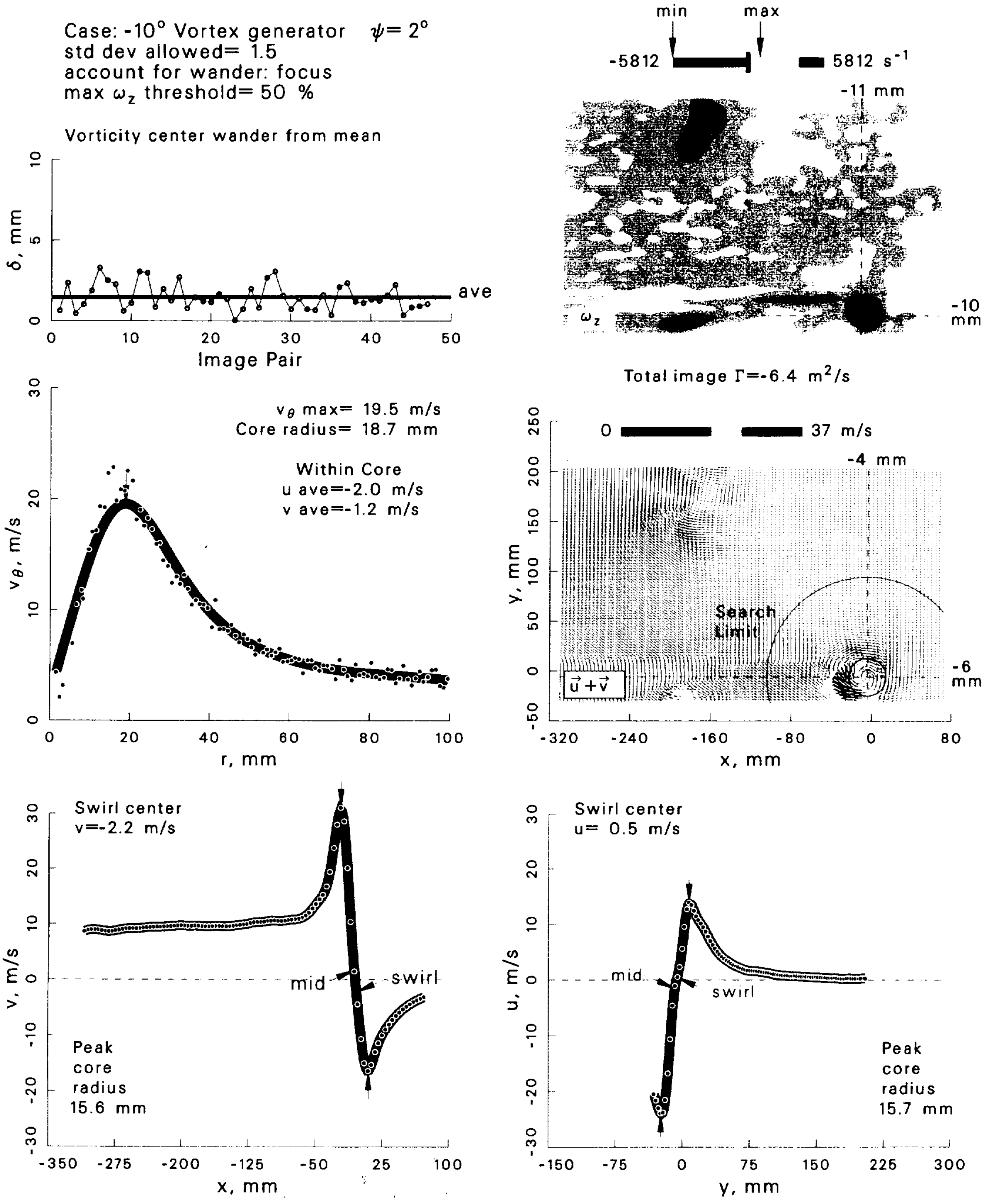

Figure 128: Vortex statistics at $\psi = 2°$ for the $-10°$ vortex generator case.

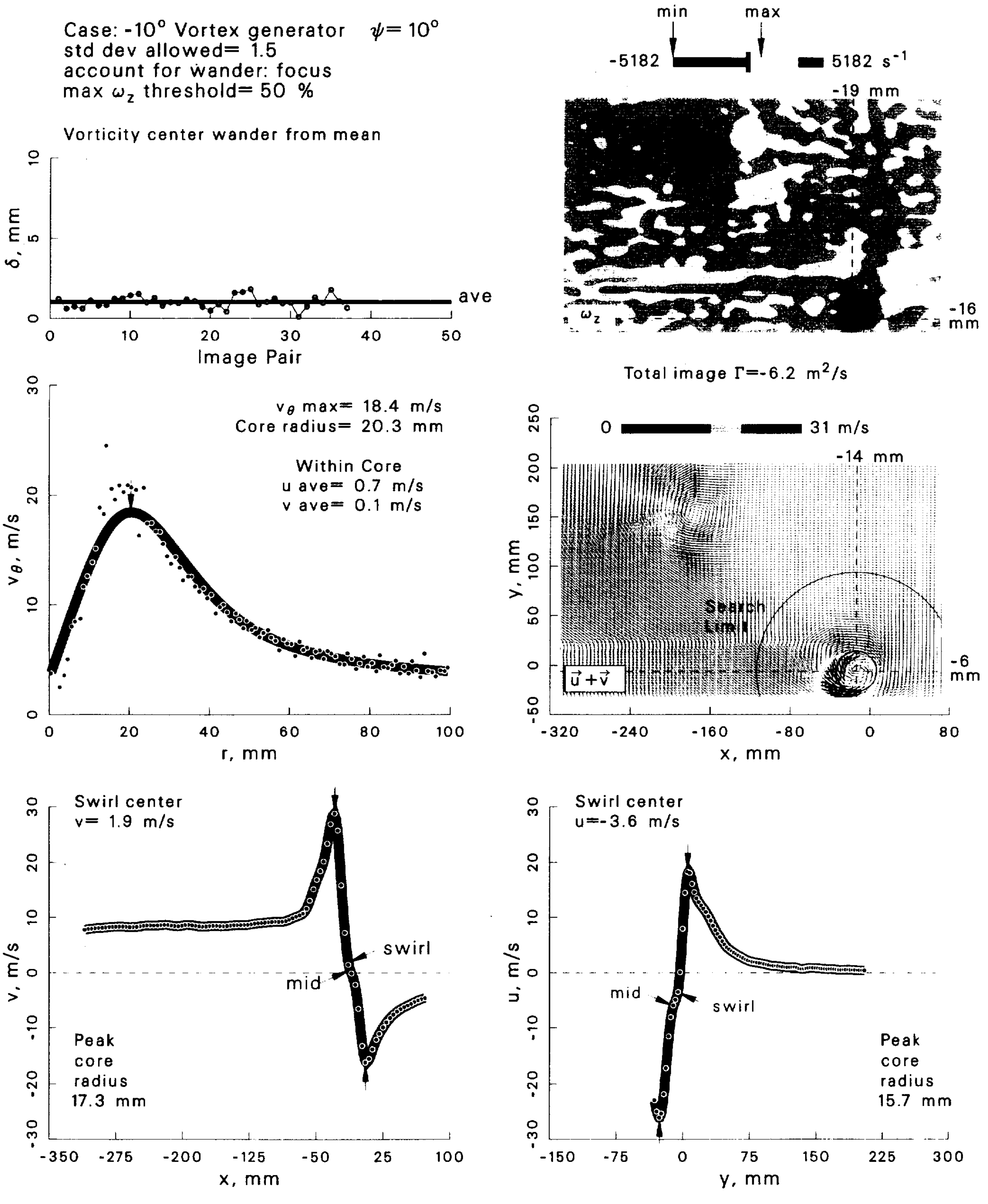

Figure 129: Vortex statistics at $\psi = 10°$ for the $-10°$ vortex generator case.

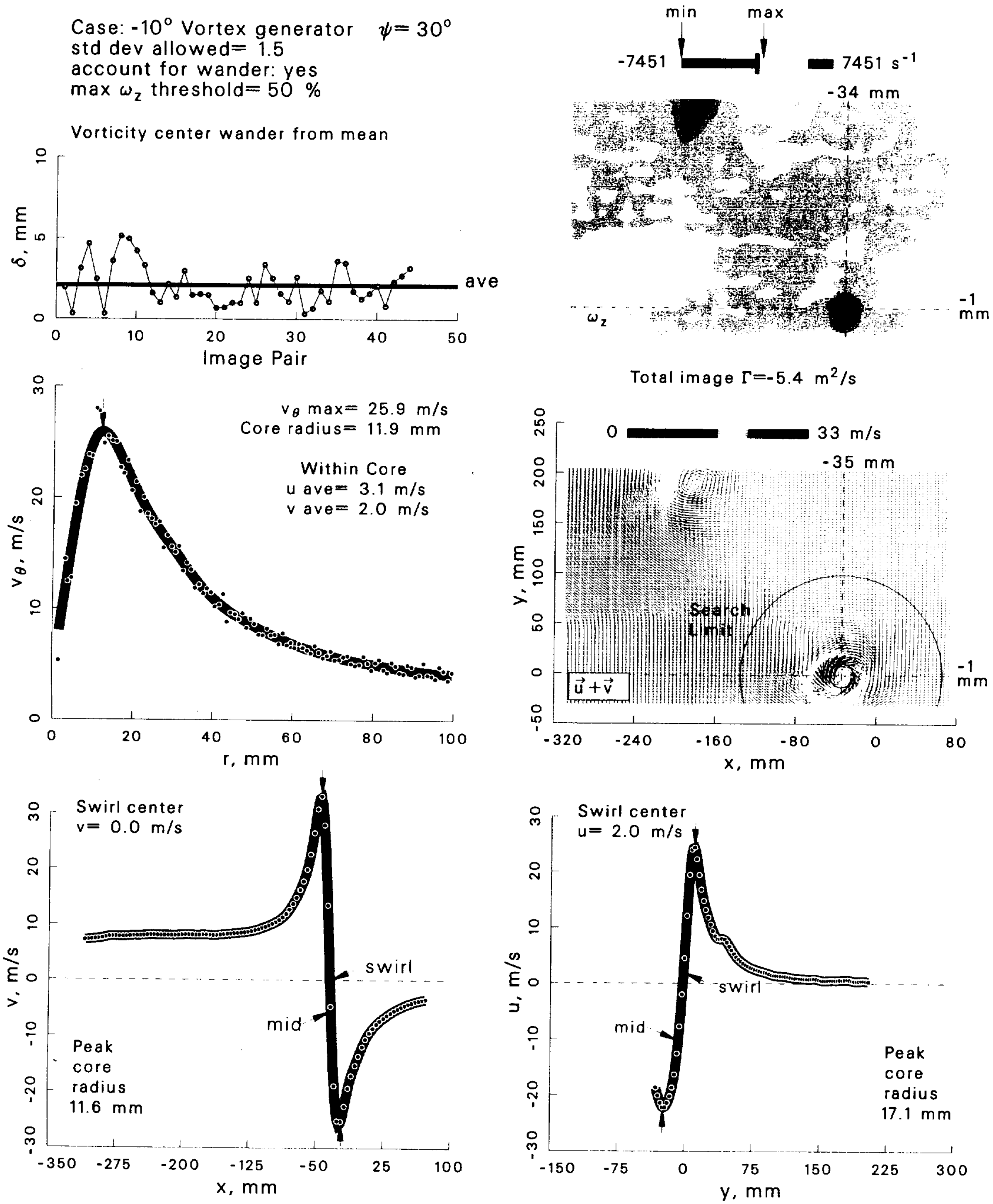

Figure 130: Vortex statistics at $\psi = 30°$ for the $-10°$ vortex generator case.

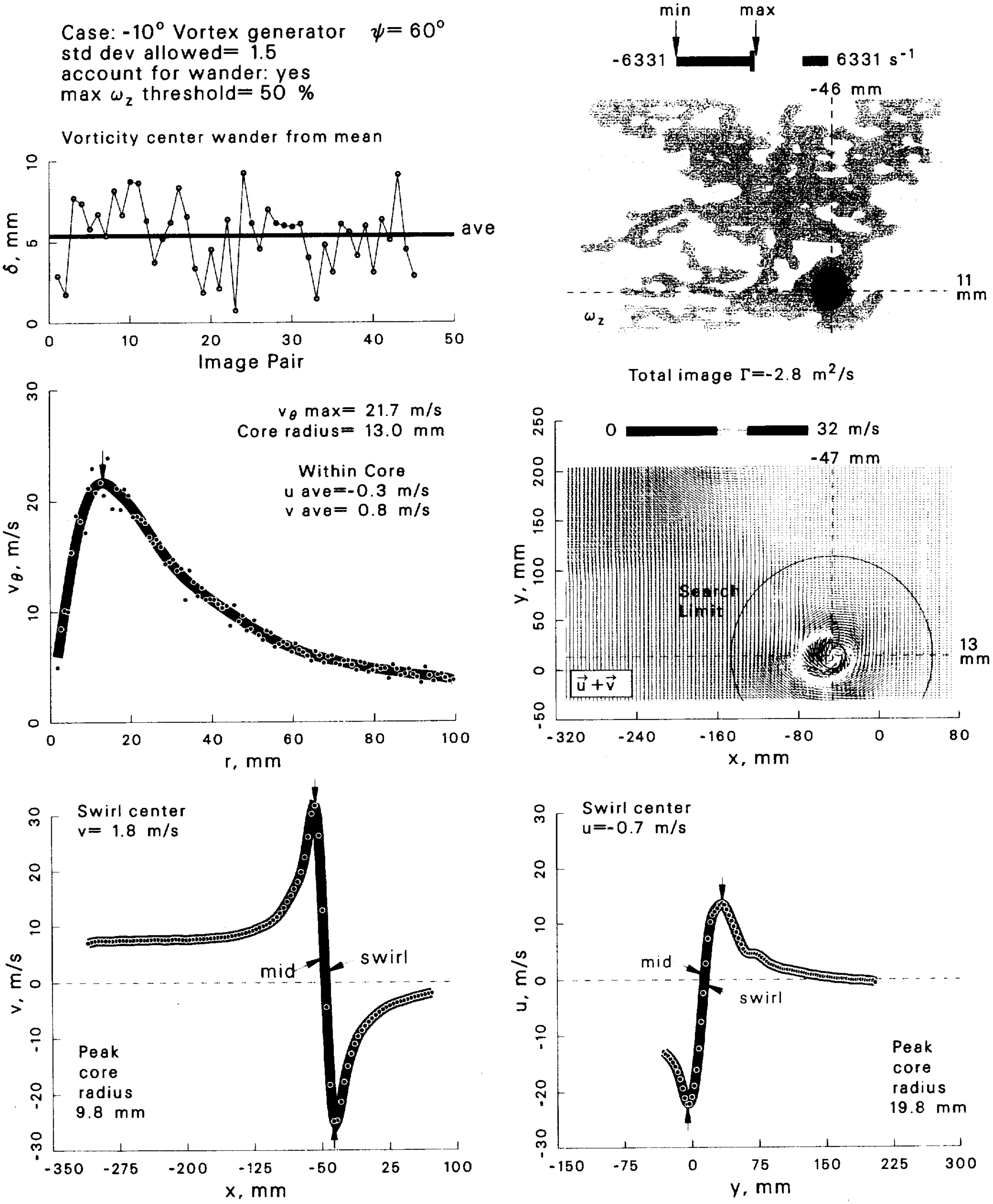

Figure 131: Vortex statistics at $\psi = 60°$ for the $-10°$ vortex generator case.

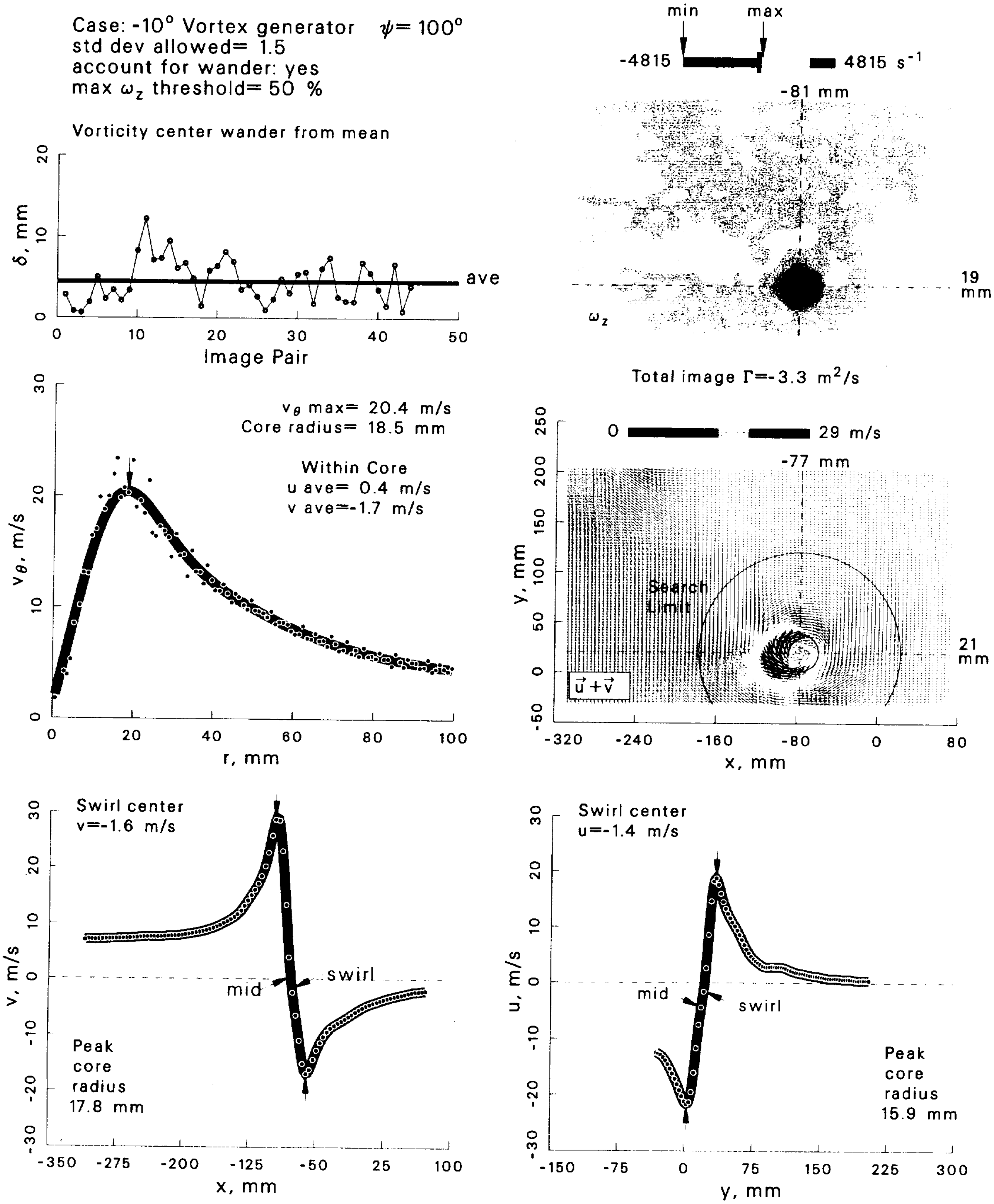

Figure 132: Vortex statistics at $\psi = 100°$ for the $-10°$ vortex generator case.

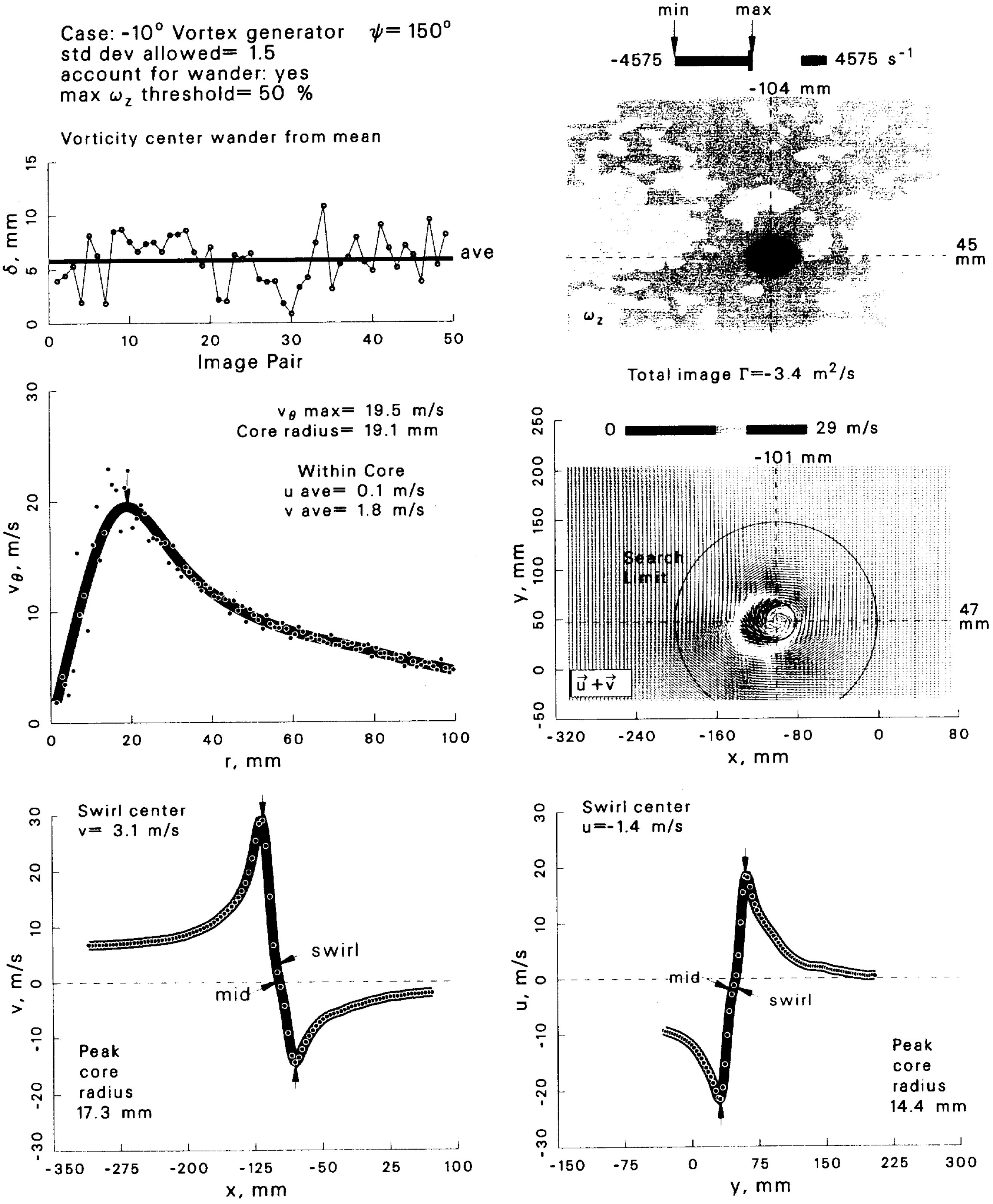

Figure 133: Vortex statistics at $\psi = 150°$ for the $-10°$ vortex generator case.

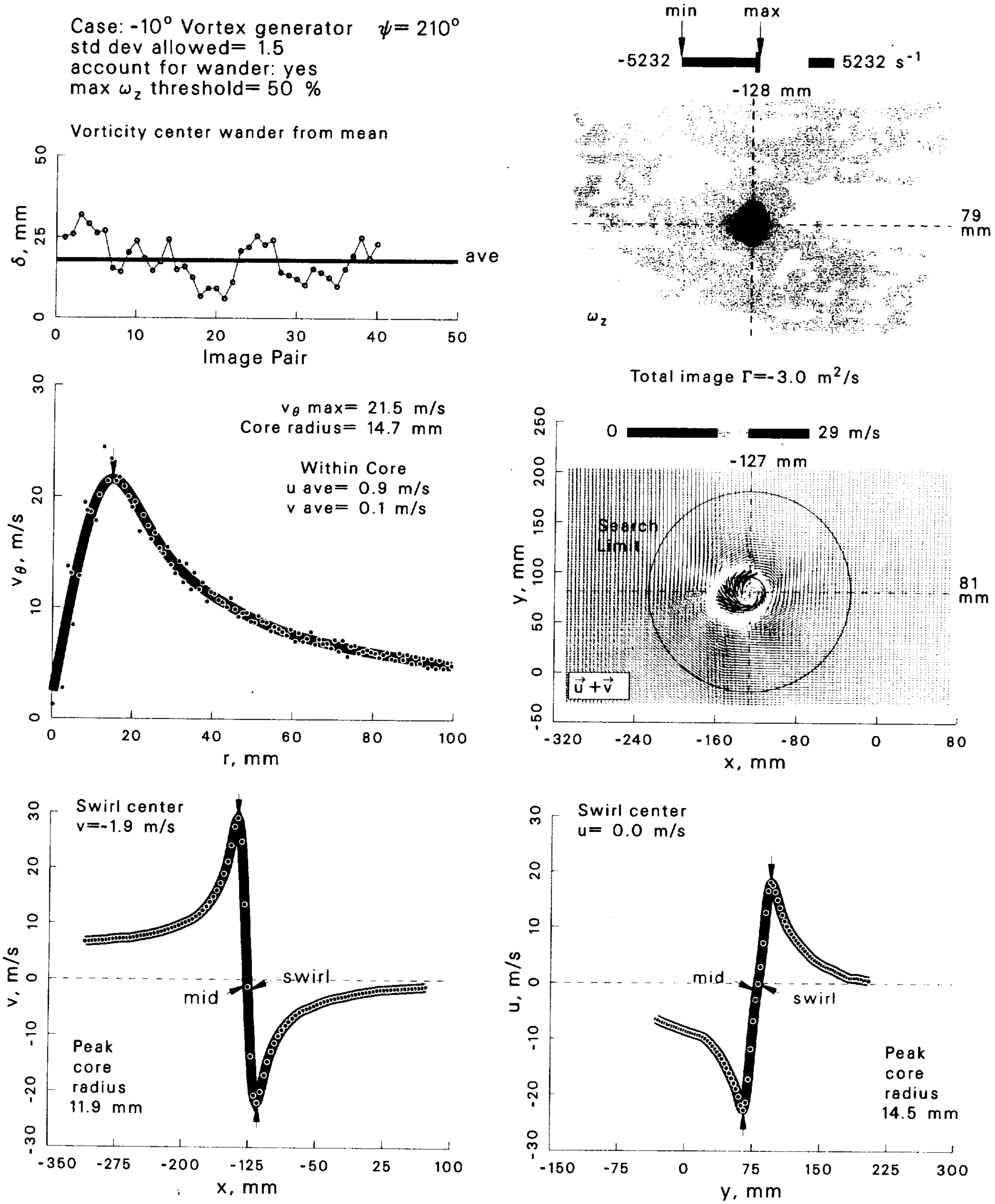

Figure 134: Vortex statistics at $\psi = 210^\circ$ for the -10° vortex generator case.

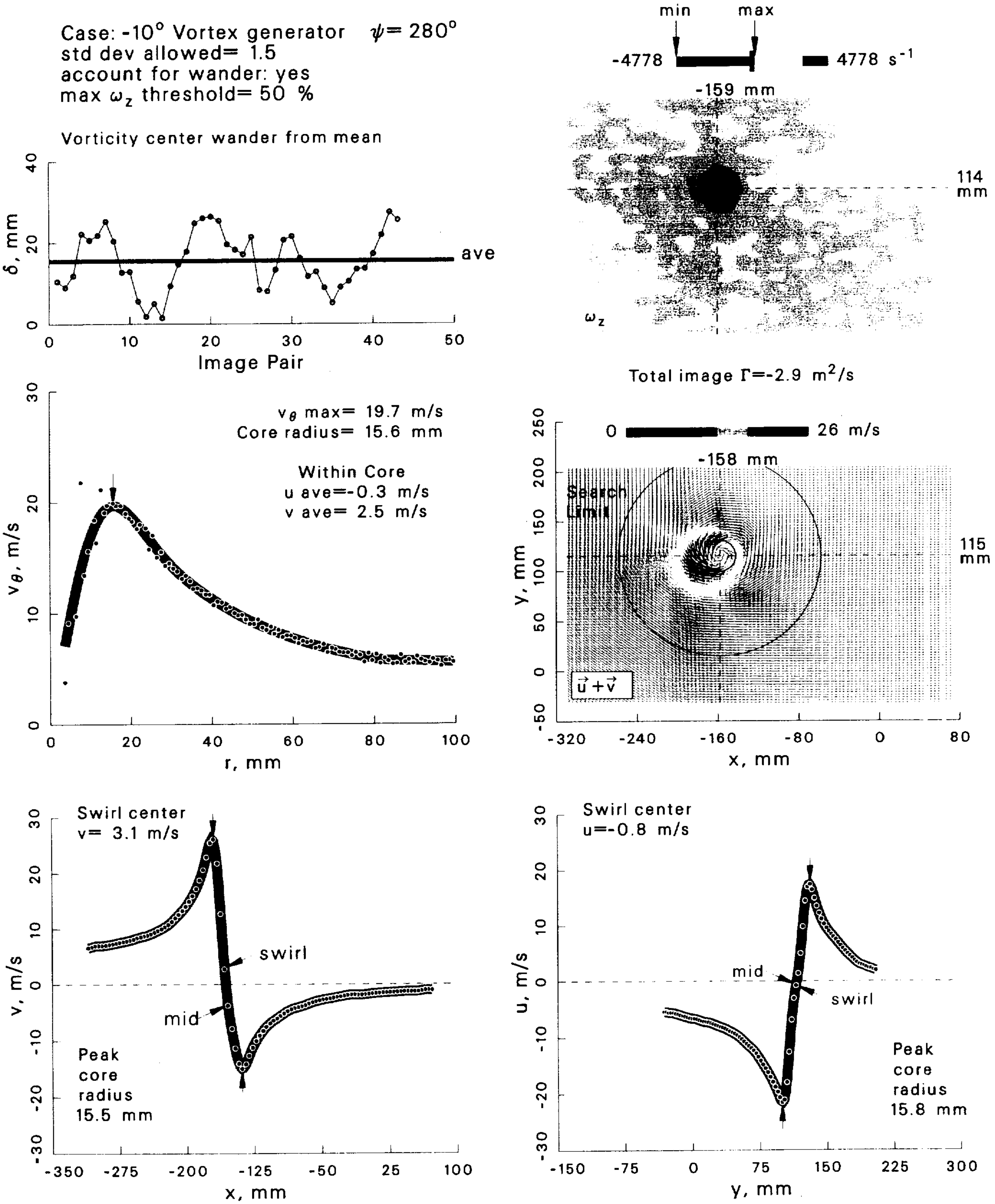

Figure 135: Vortex statistics at $\psi = 280°$ for the $-10°$ vortex generator case.

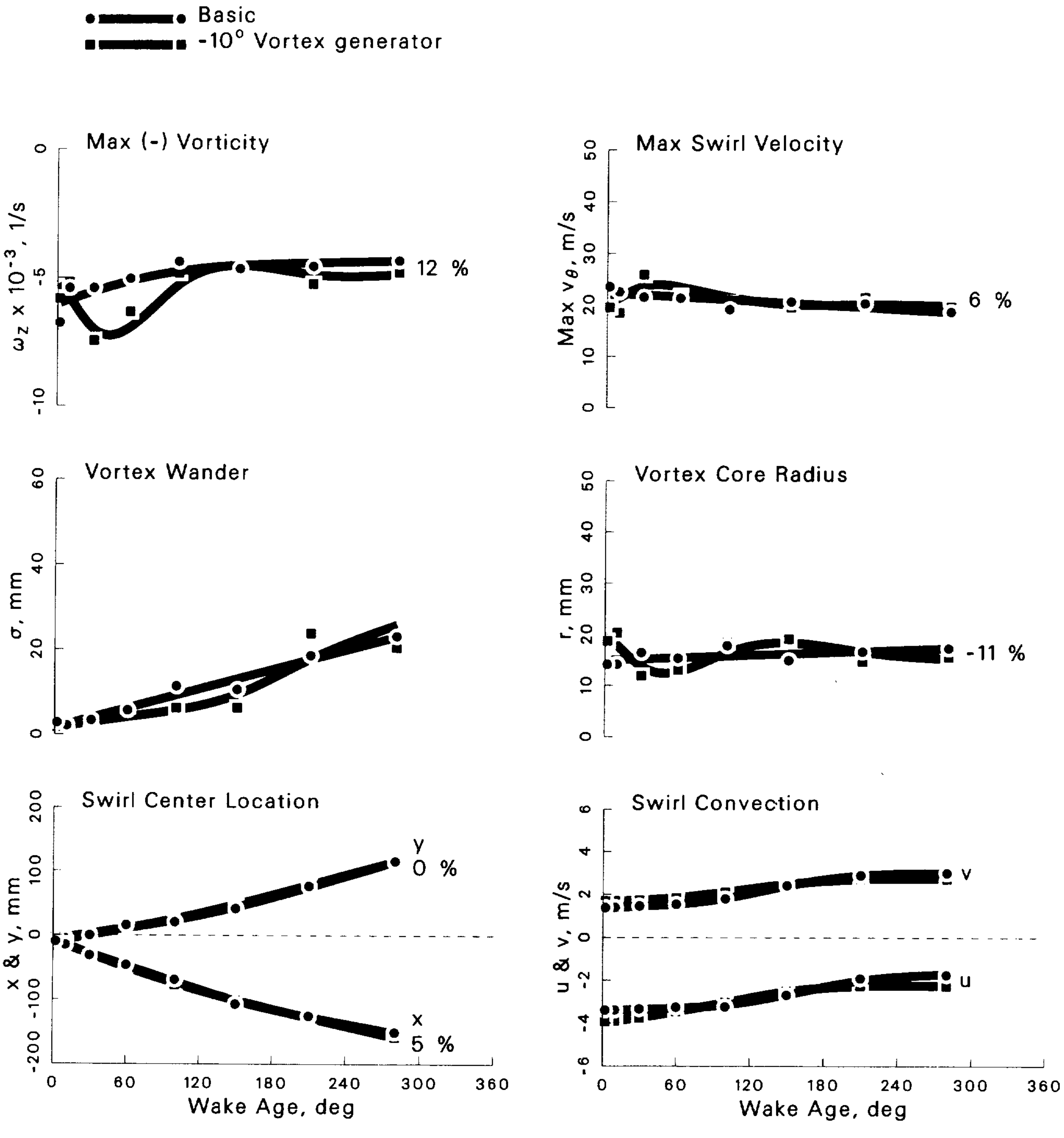

Figure 136: Summary of vortex development from $\psi = 2° \rightarrow 280°$ for the $-10°$ vortex generator case.

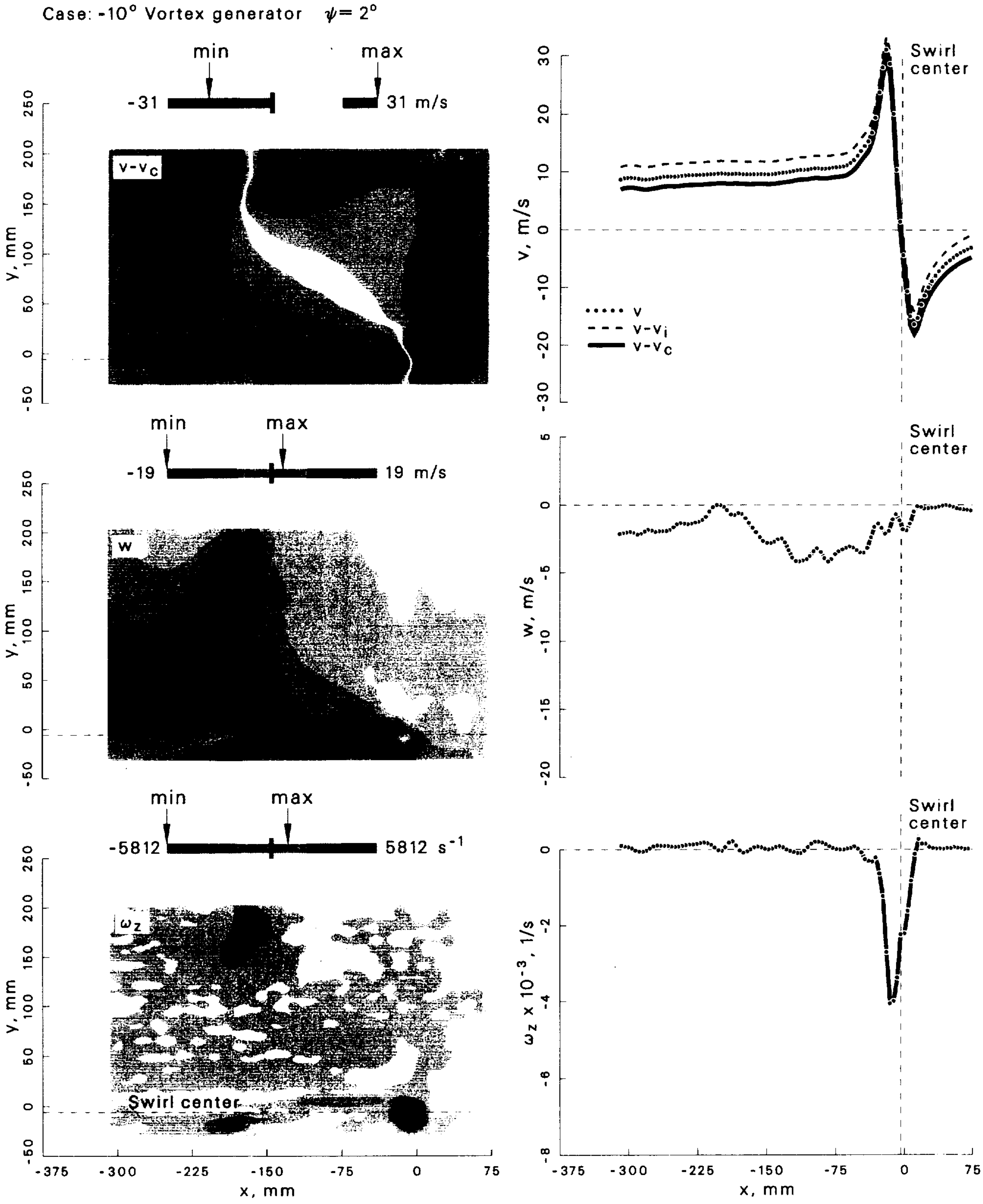

Figure 137: Velocity and vorticity components at $\psi = 2°$ for the $-10°$ vortex generator case.

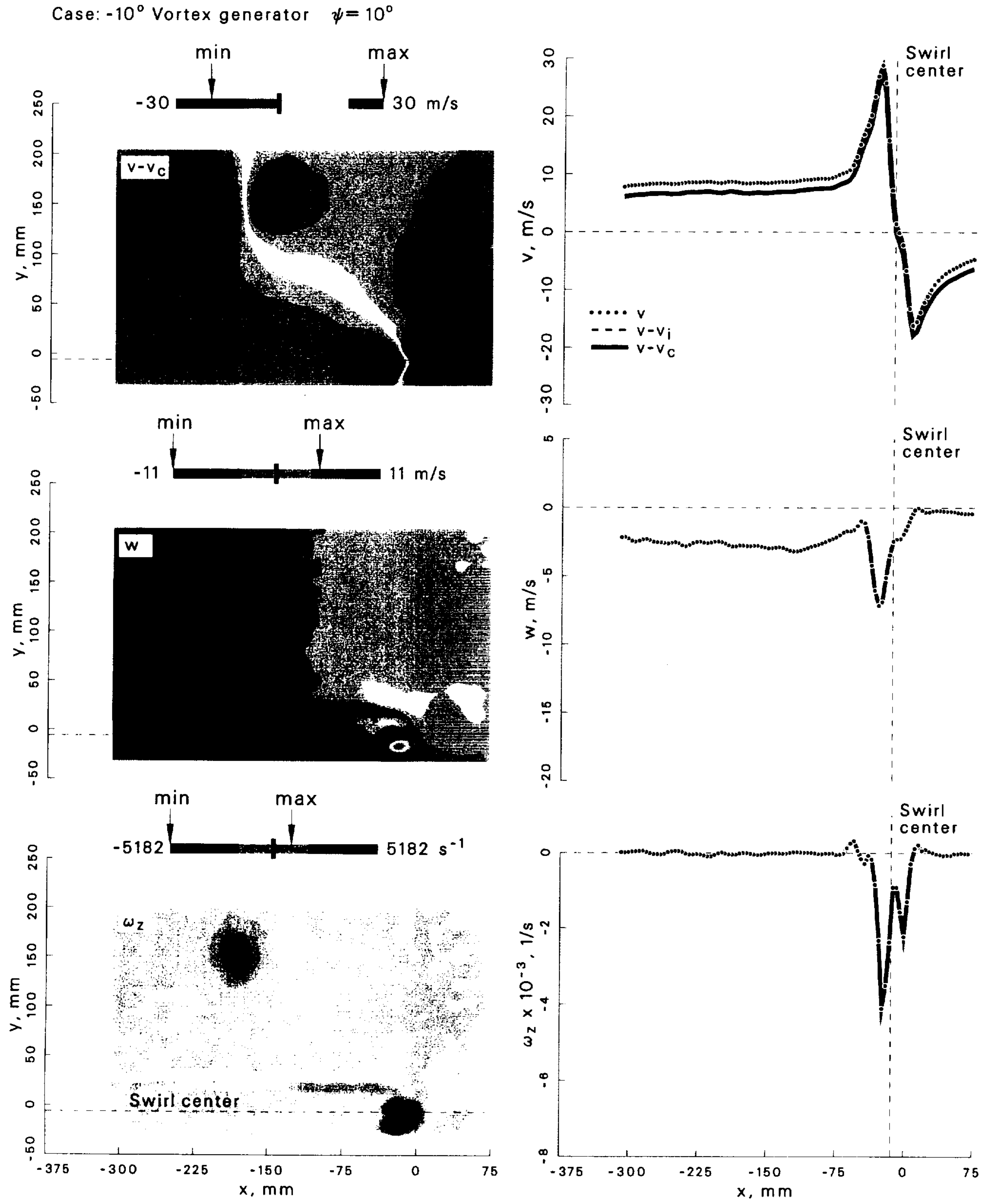

Figure 138: Velocity and vorticity components at $\psi = 10°$ for the $-10°$ vortex generator case.

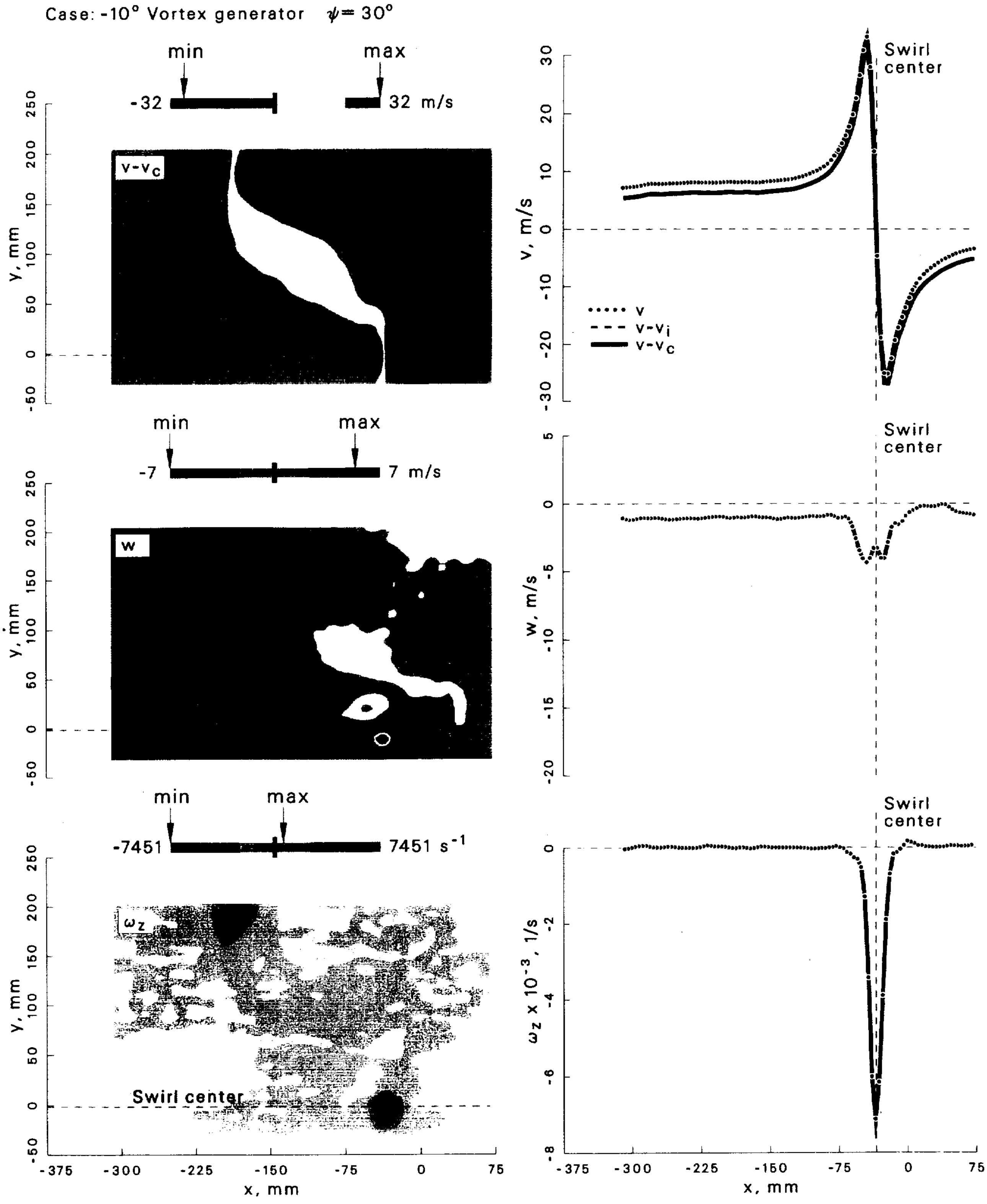

Figure 139: Velocity and vorticity components at $\psi = 30^\circ$ for the -10° vortex generator case.

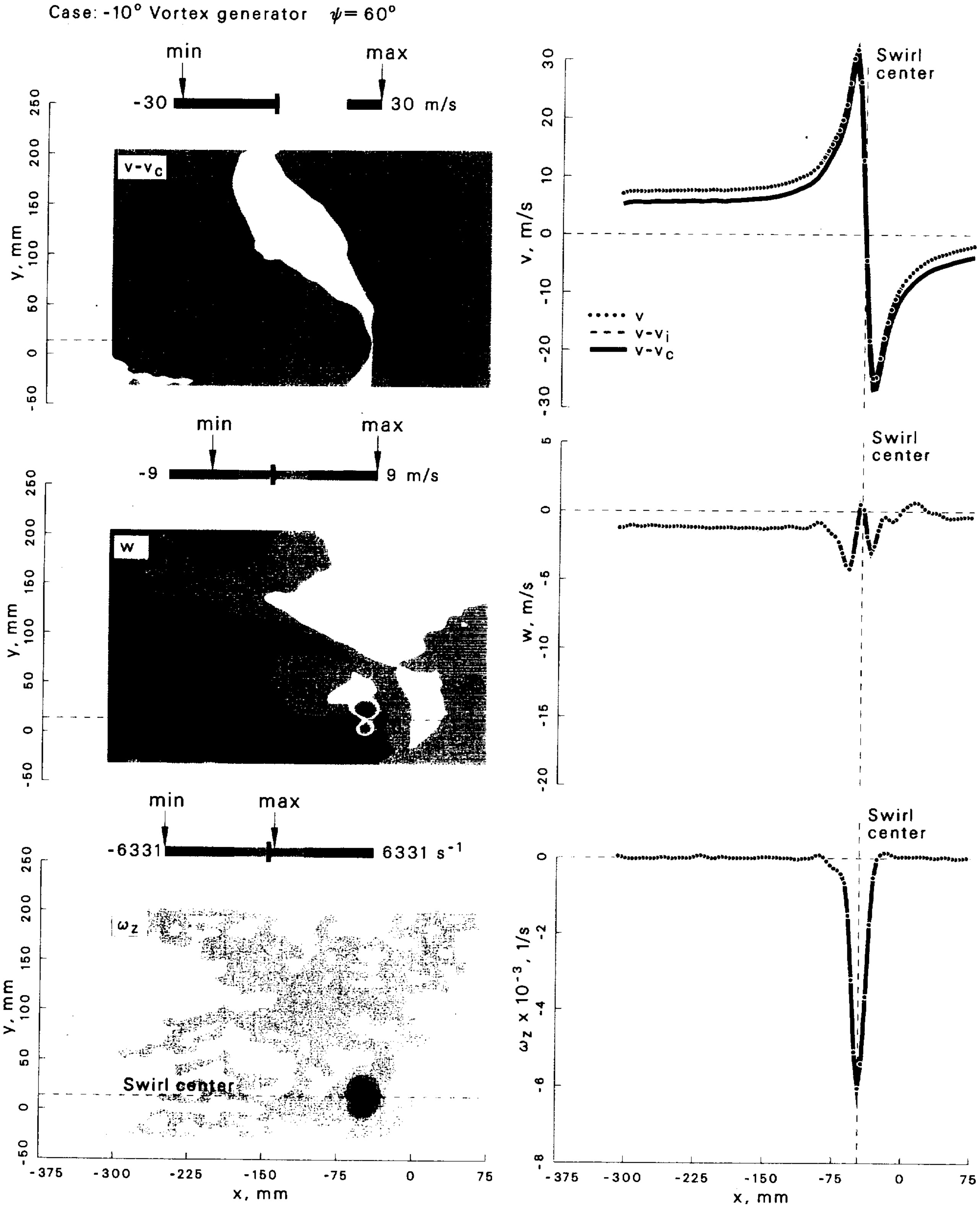

Figure 140: Velocity and vorticity components at $\psi = 60°$ for the $-10°$ vortex generator case.

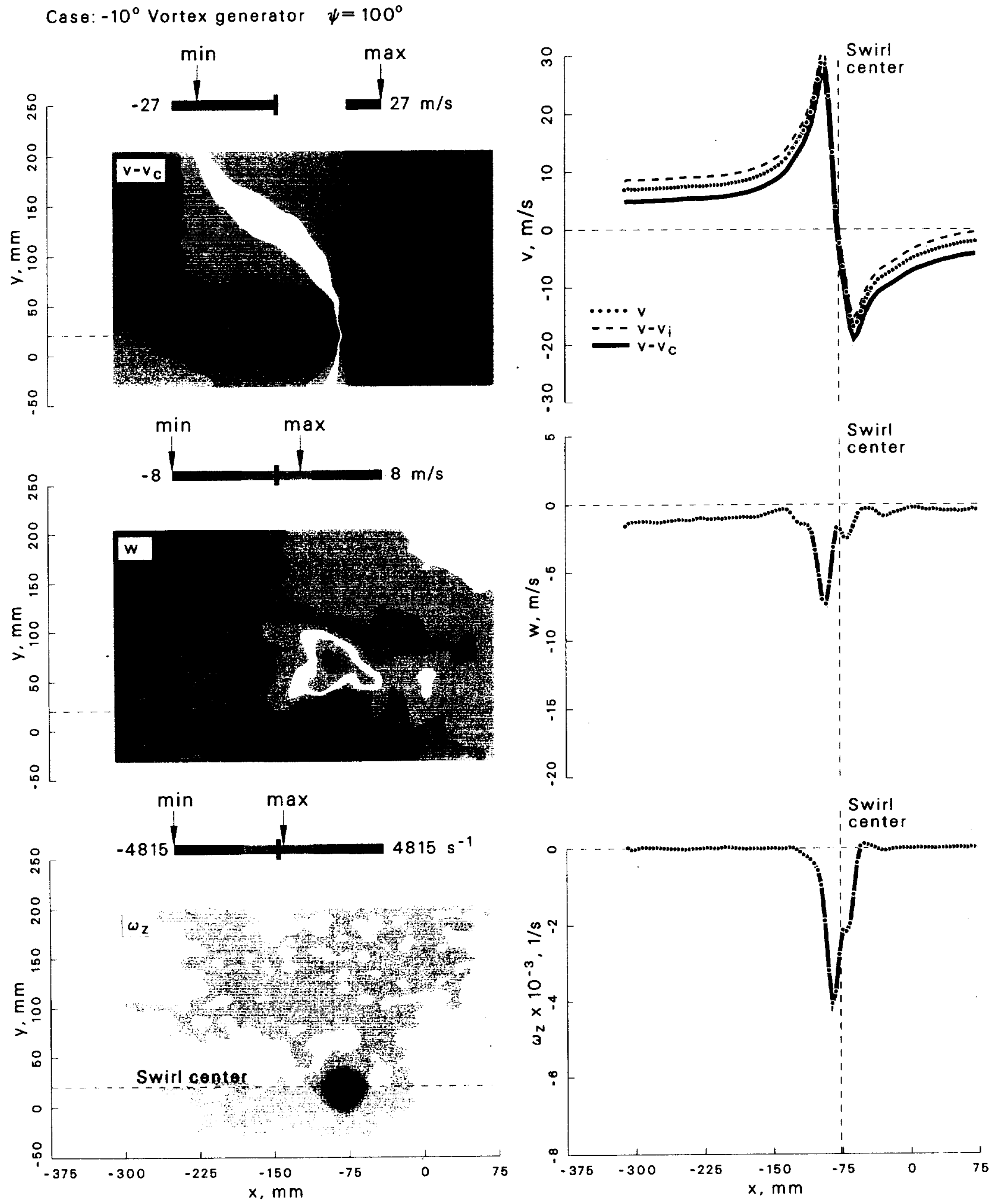

Figure 141: Velocity and vorticity components at $\psi = 100°$ for the $-10°$ vortex generator case.

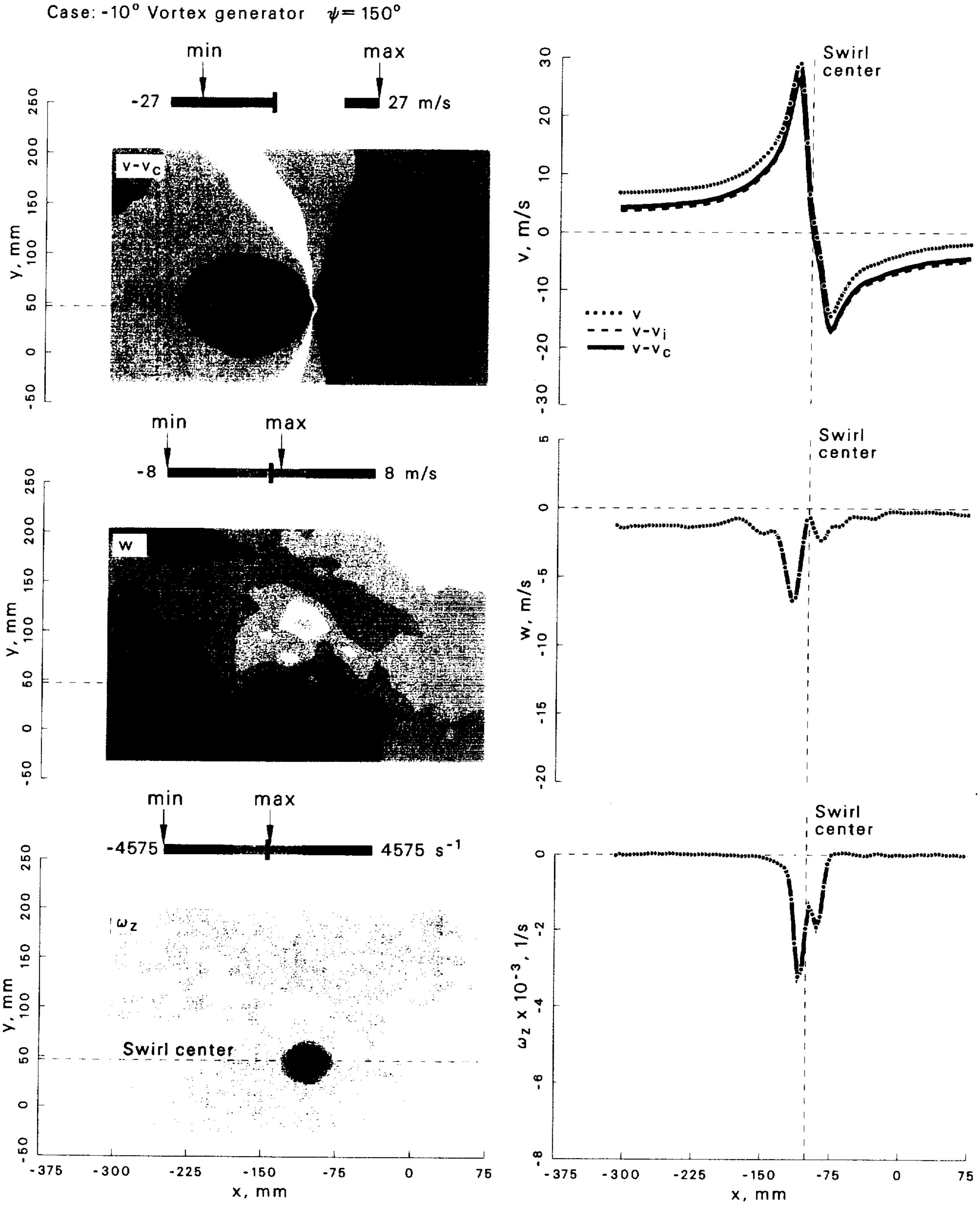

Figure 142: Velocity and vorticity components at $\psi = 150°$ for the $-10°$ vortex generator case.

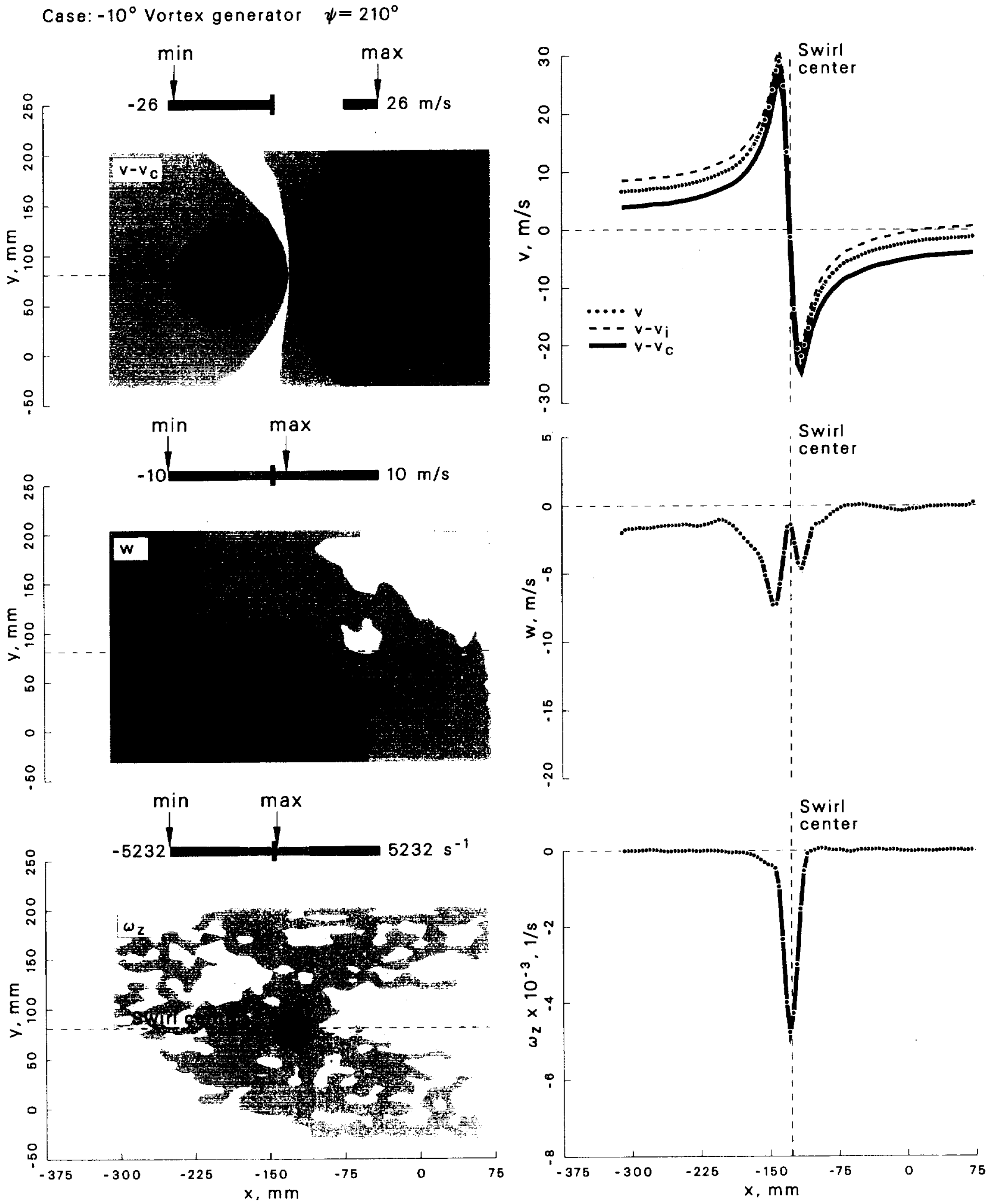

Figure 143: Velocity and vorticity components at $\psi = 210°$ for the $-10°$ vortex generator case.

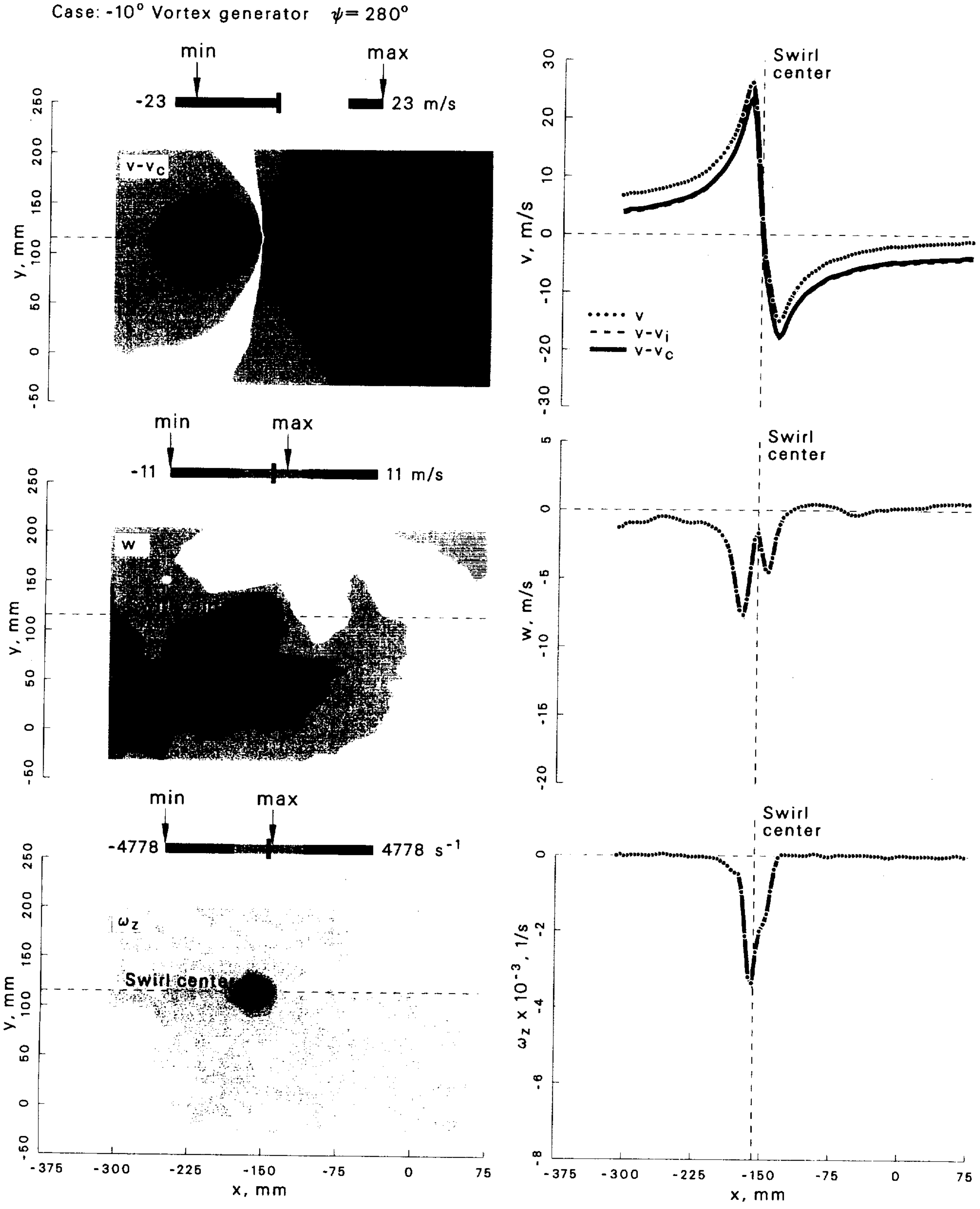

Figure 144: Velocity and vorticity components at $\psi = 280°$ for the $-10°$ vortex generator case.

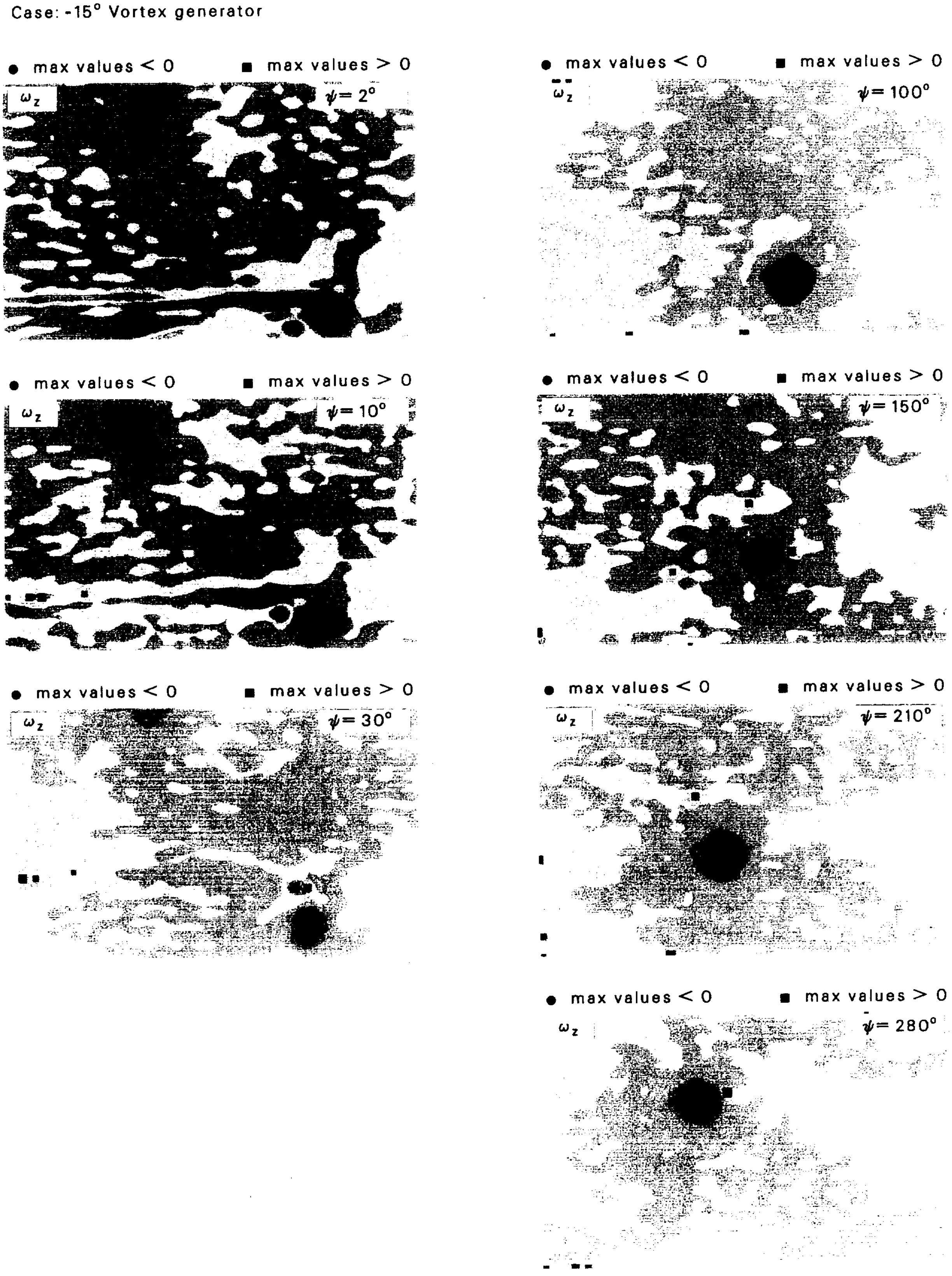

Figure 145: Locations of ω_z extrema at $\psi = 2° \rightarrow 280°$ for the $-15°$ vortex generator case.

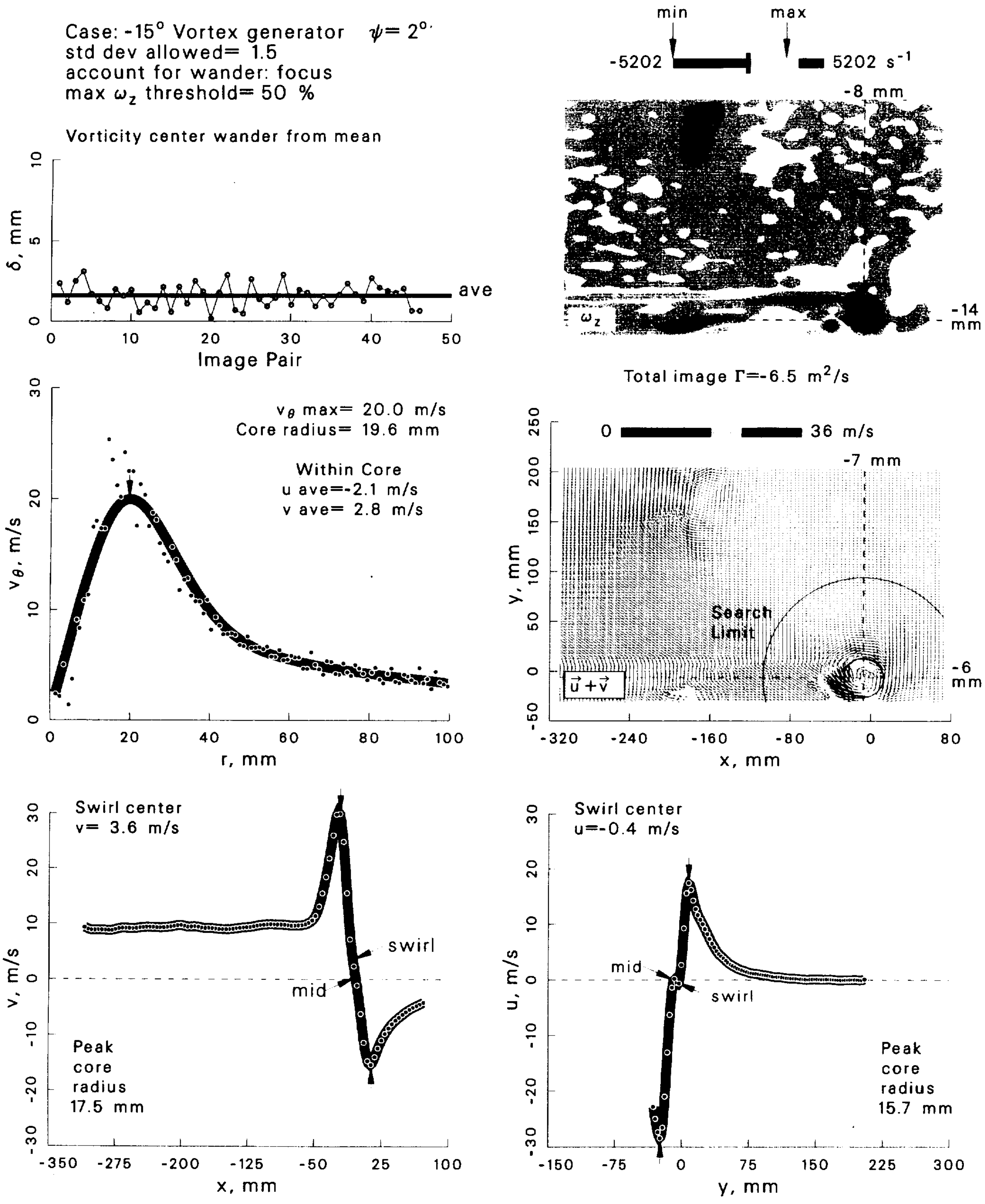

Figure 146: Vortex statistics at $\psi = 2°$ for the $-15°$ vortex generator case.

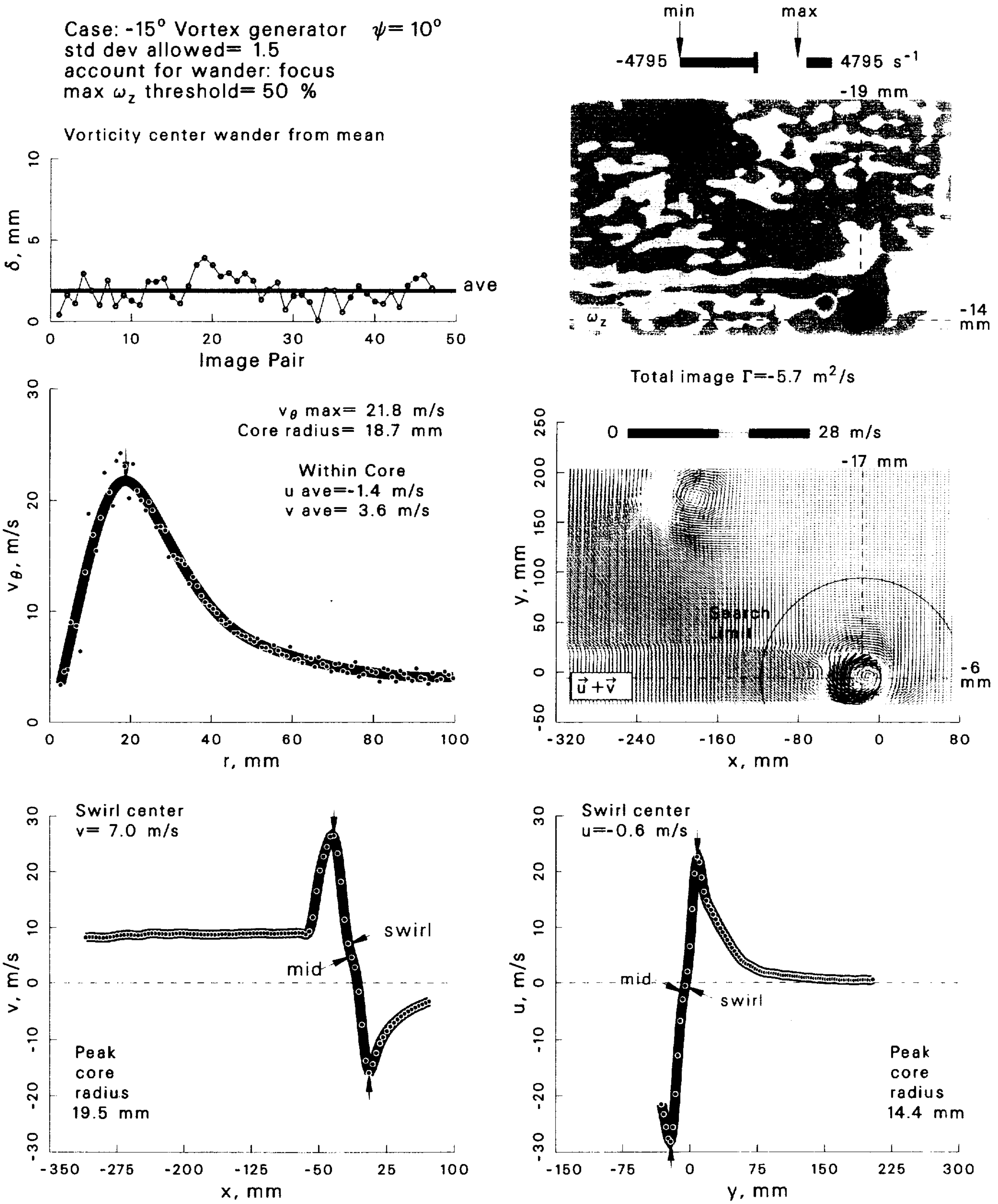

Figure 147: Vortex statistics at $\psi = 10°$ for the $-15°$ vortex generator case.

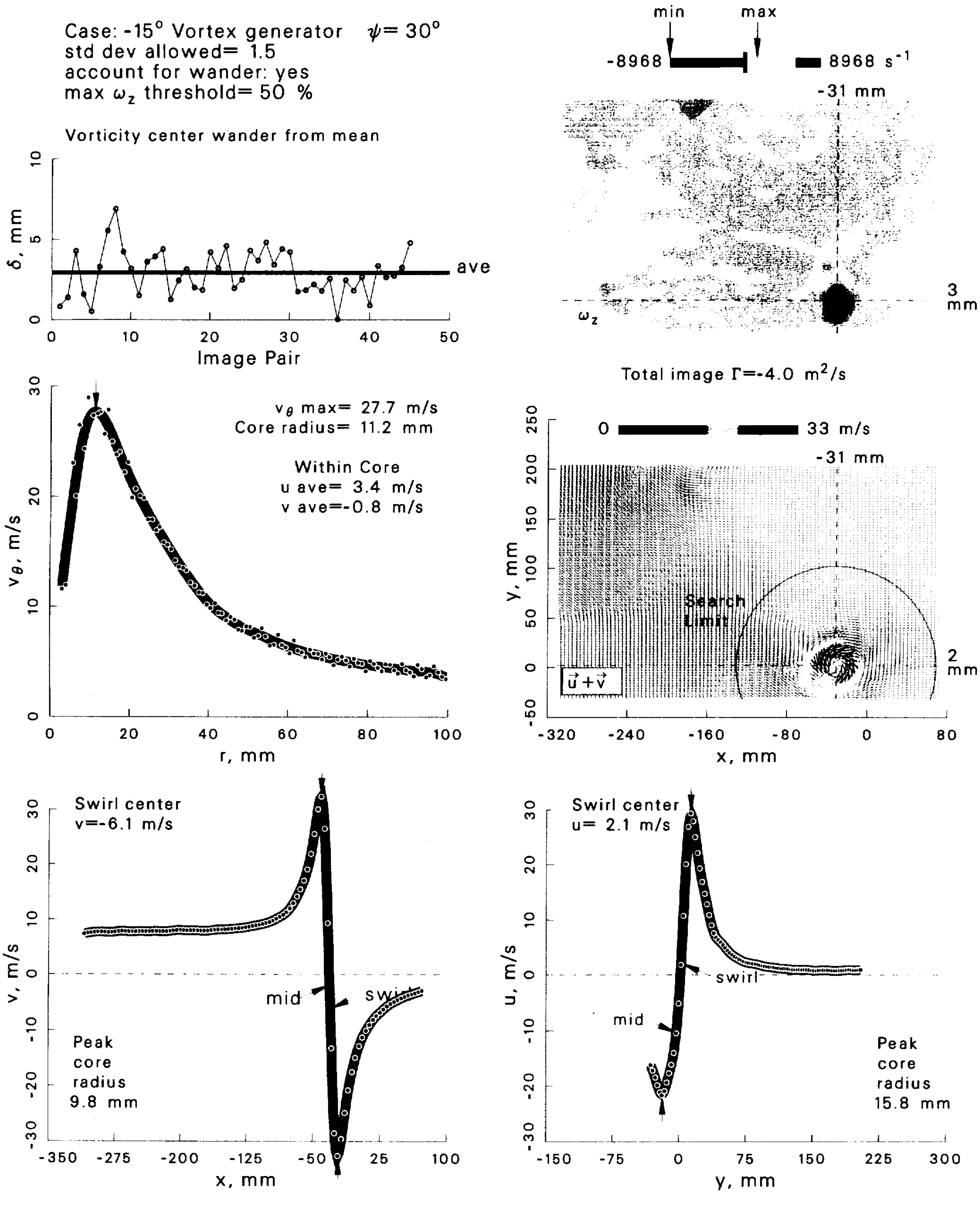

Figure 148: Vortex statistics at $\psi = 30°$ for the $-15°$ vortex generator case.

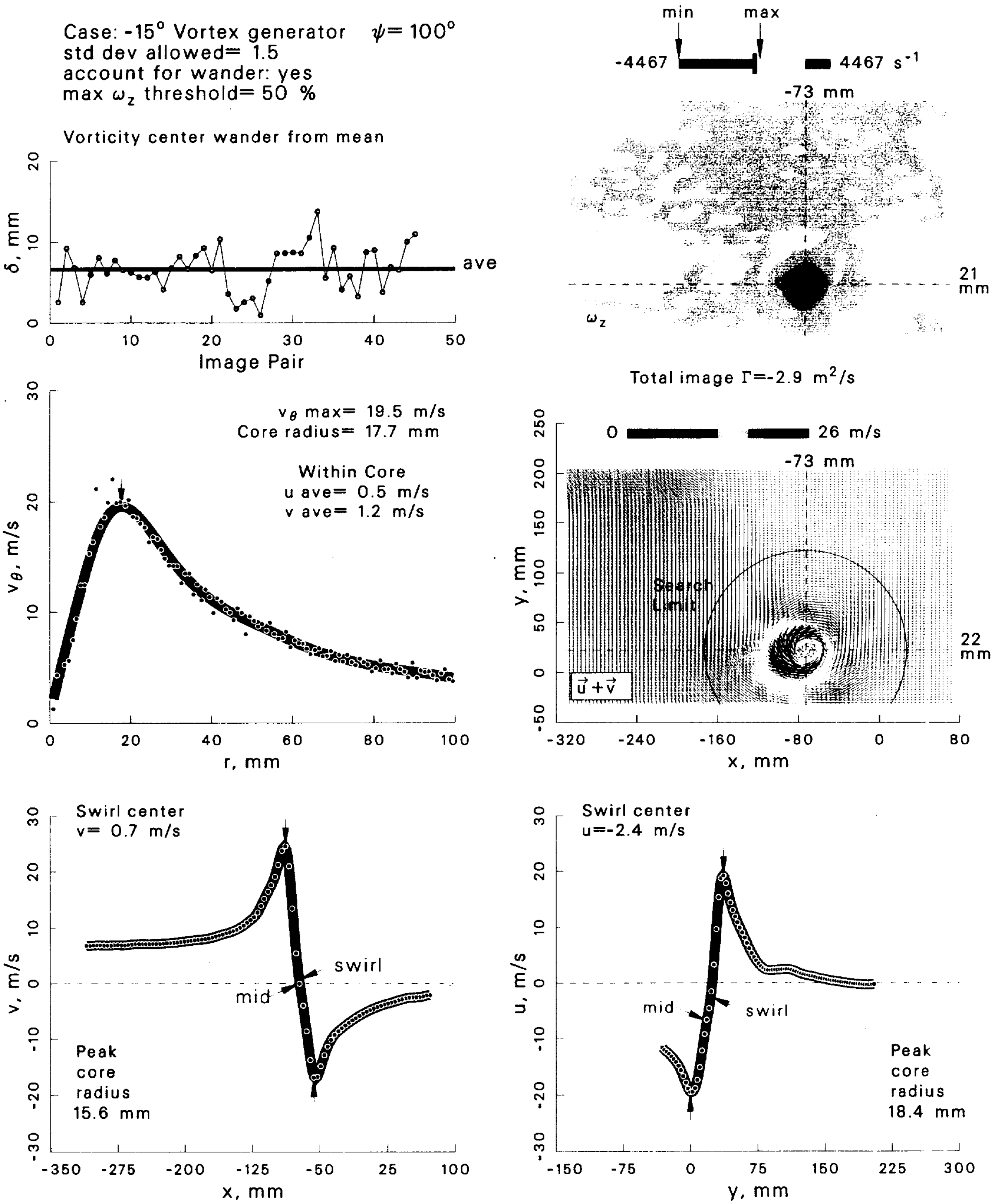

Figure 149: Vortex statistics at $\psi = 100°$ for the $-15°$ vortex generator case.

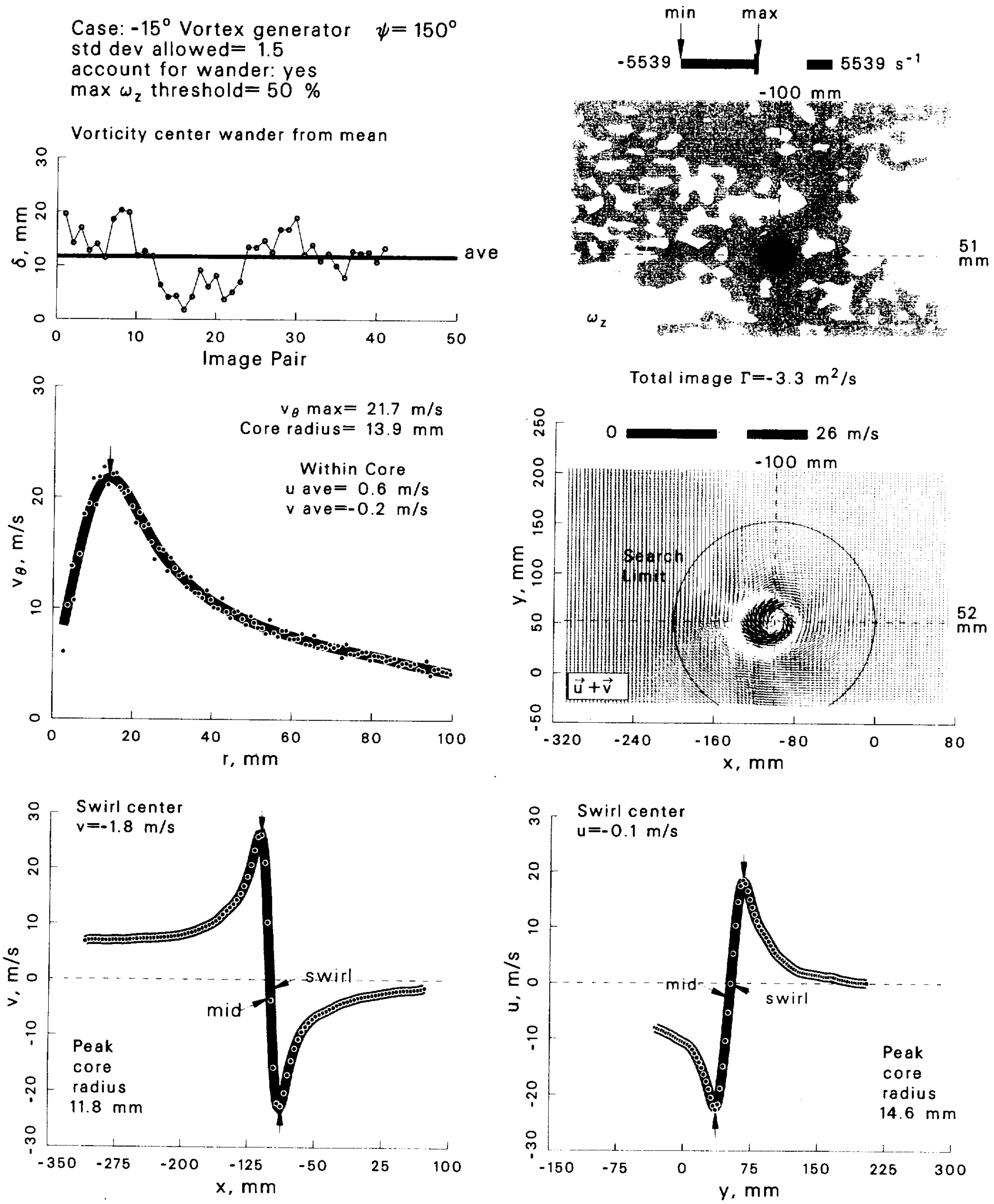

Figure 150: Vortex statistics at $\psi = 150°$ for the $-15°$ vortex generator case.

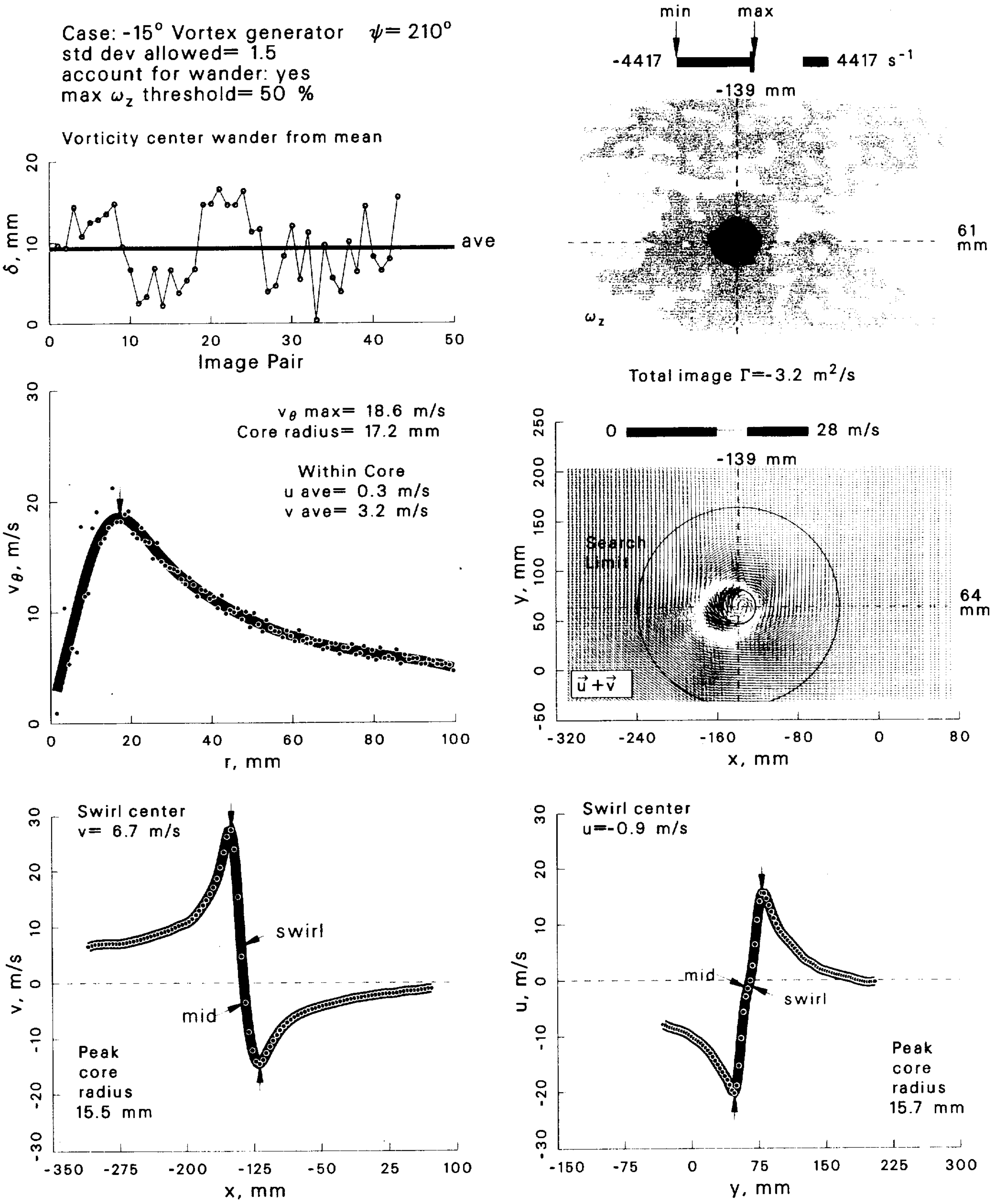

Figure 151: Vortex statistics at $\psi = 210°$ for the $-15°$ vortex generator case.

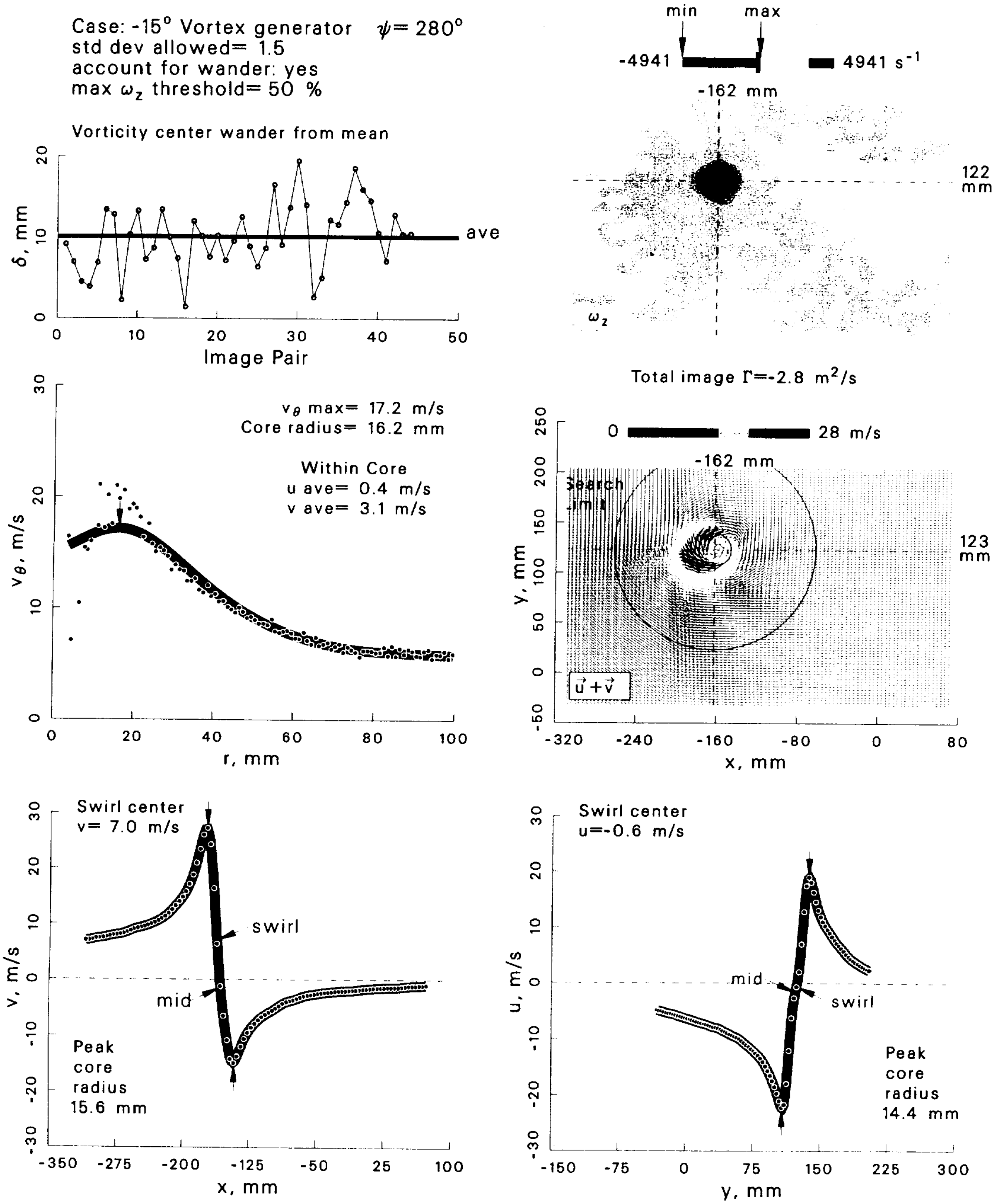

Figure 152: Vortex statistics at $\psi = 280°$ for the $-15°$ vortex generator case.

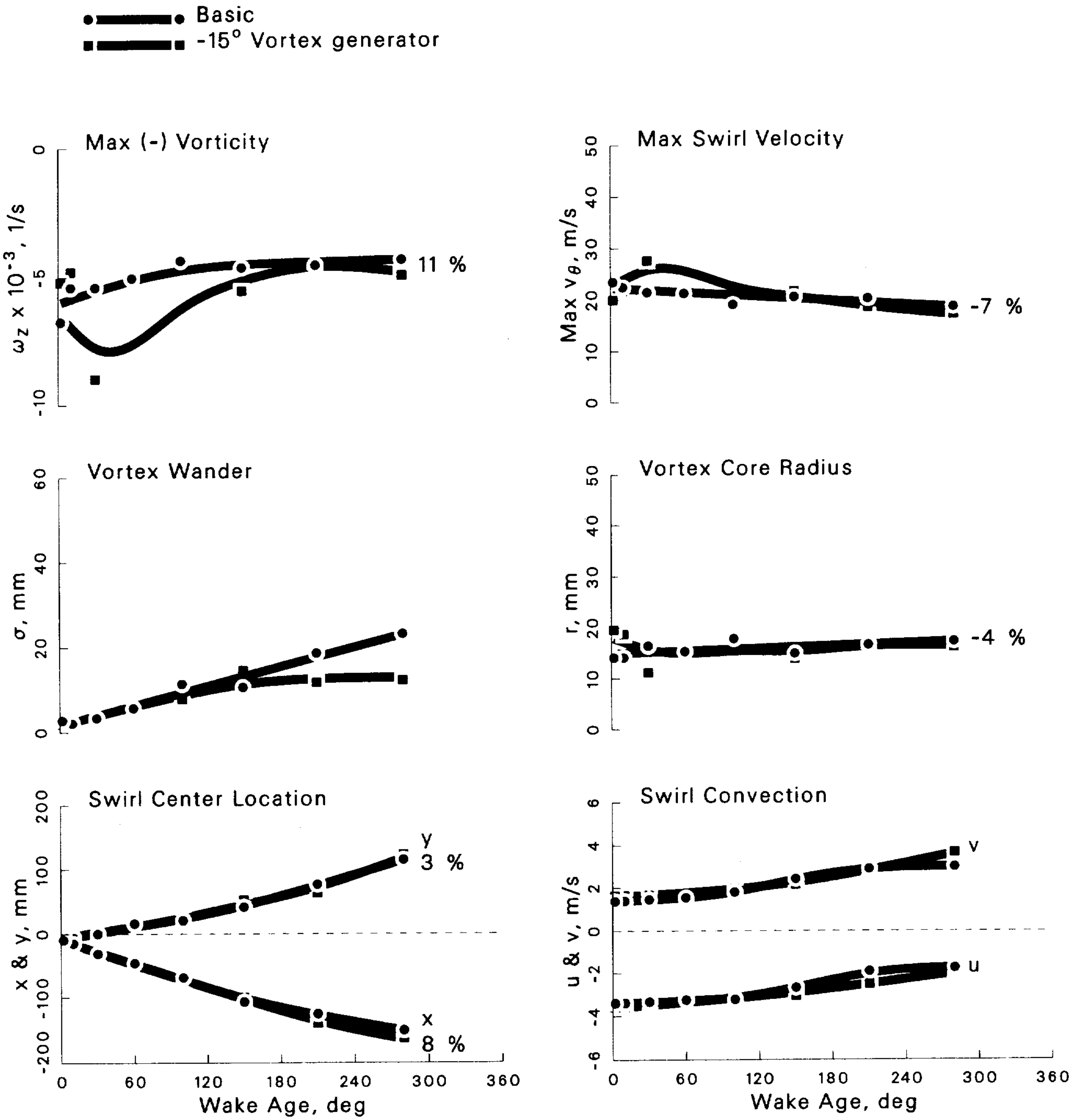

Figure 153: Summary of vortex development from $\psi = 2° \rightarrow 280°$ for the $-15°$ vortex generator case.

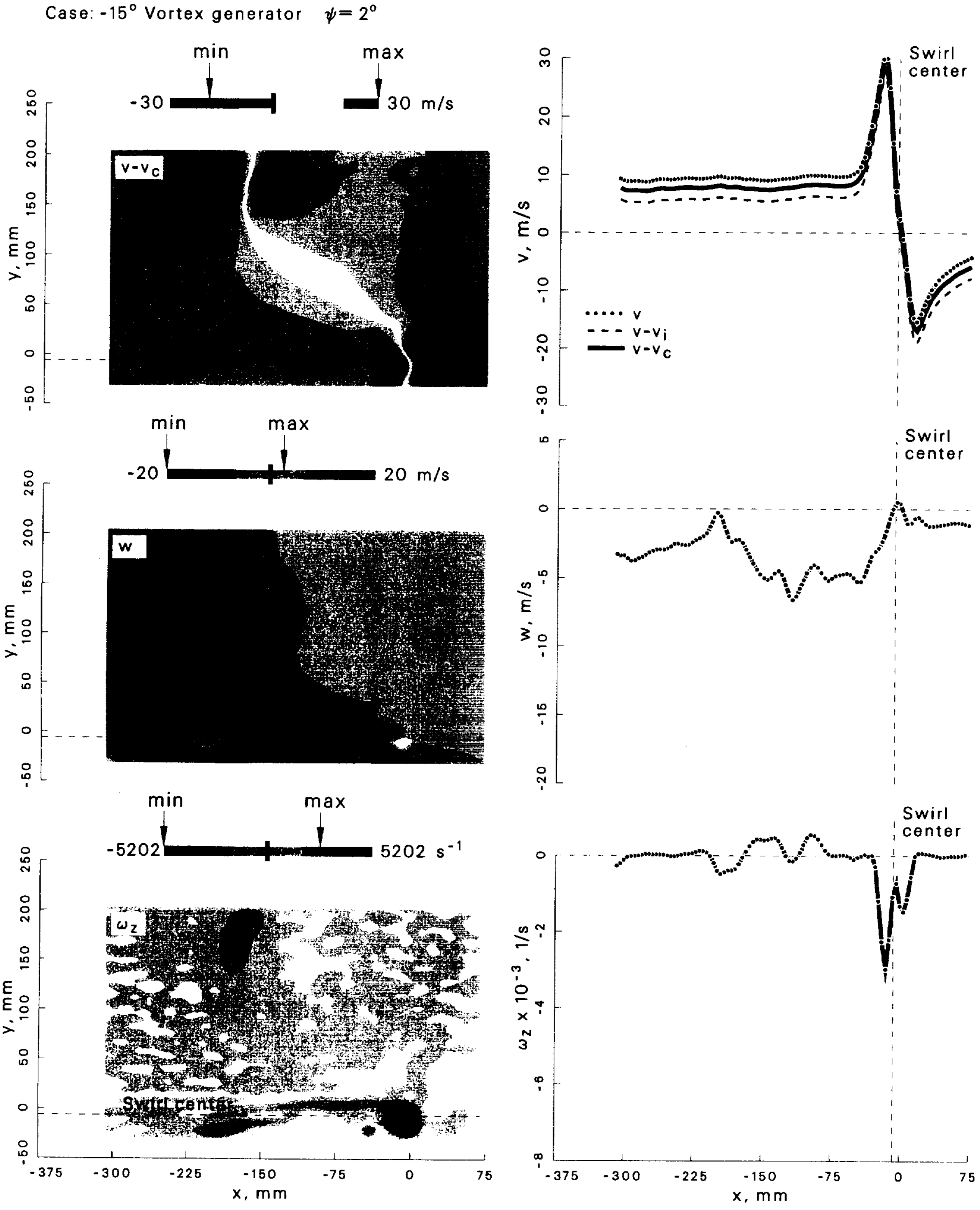

Figure 154: Velocity and vorticity components at $\psi = 2°$ for the $-15°$ vortex generator case.

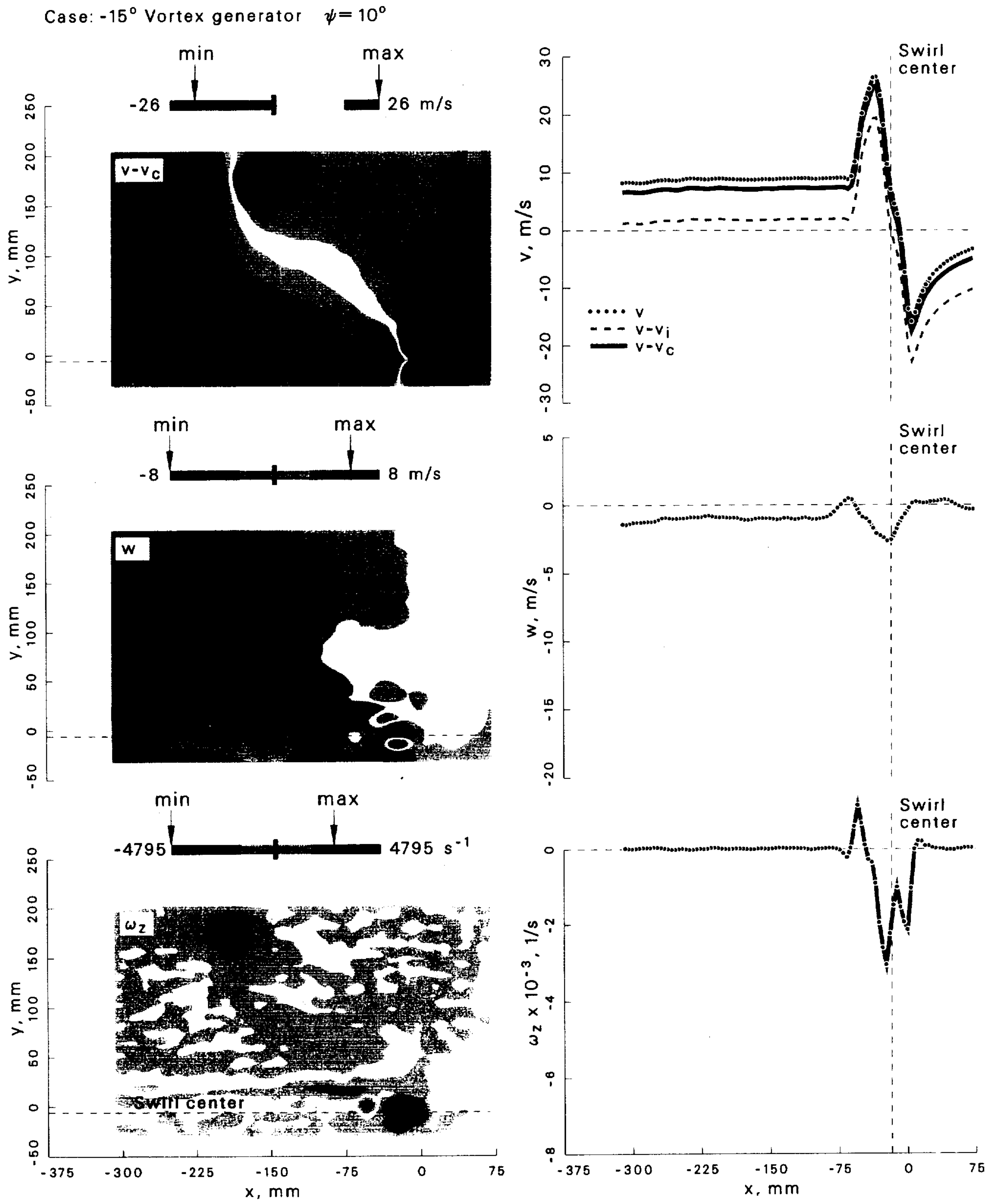

Figure 155: Velocity and vorticity components at $\psi = 10°$ for the $-15°$ vortex generator case.

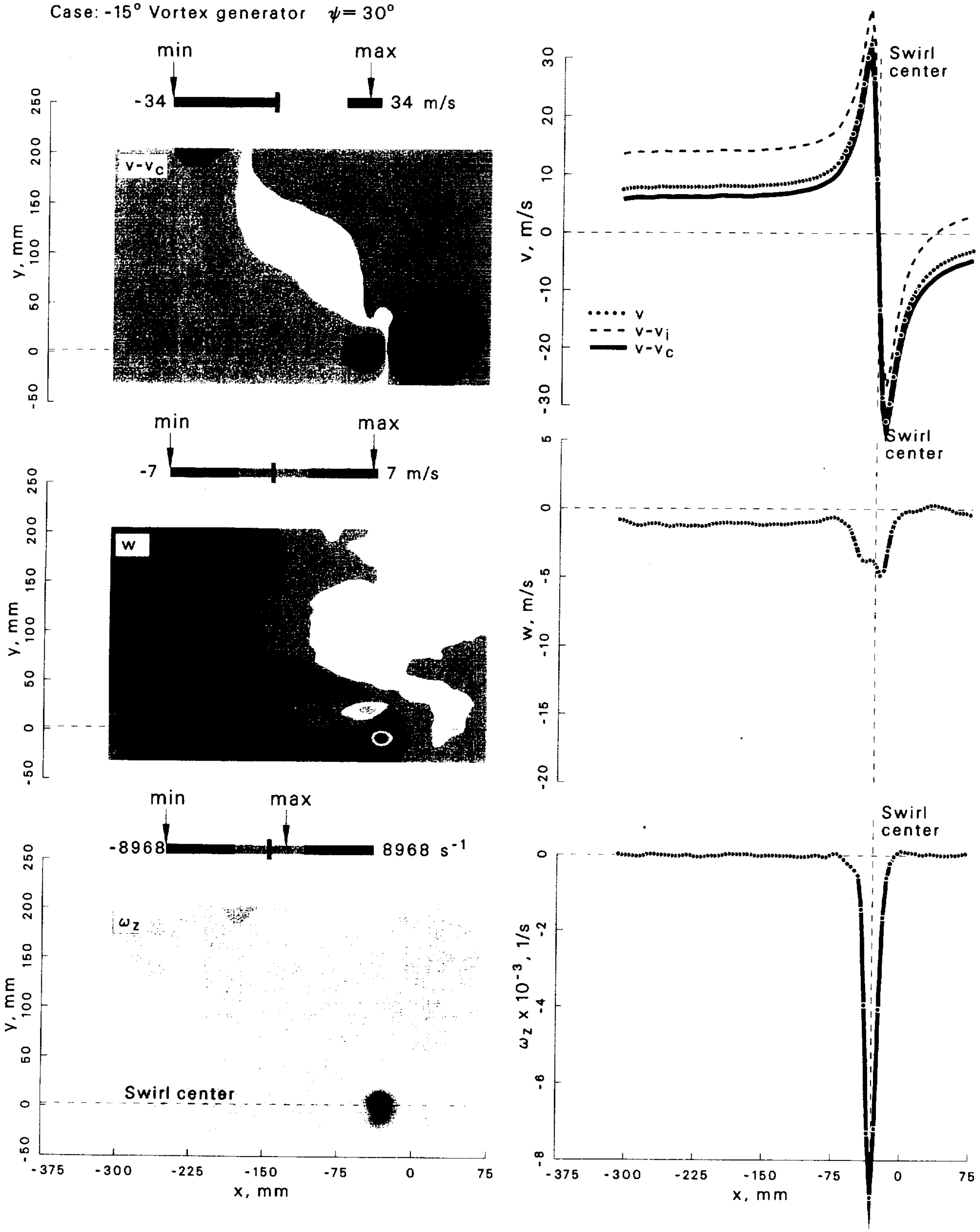

Figure 156: Velocity and vorticity components at $\psi = 30°$ for the $-15°$ vortex generator case.

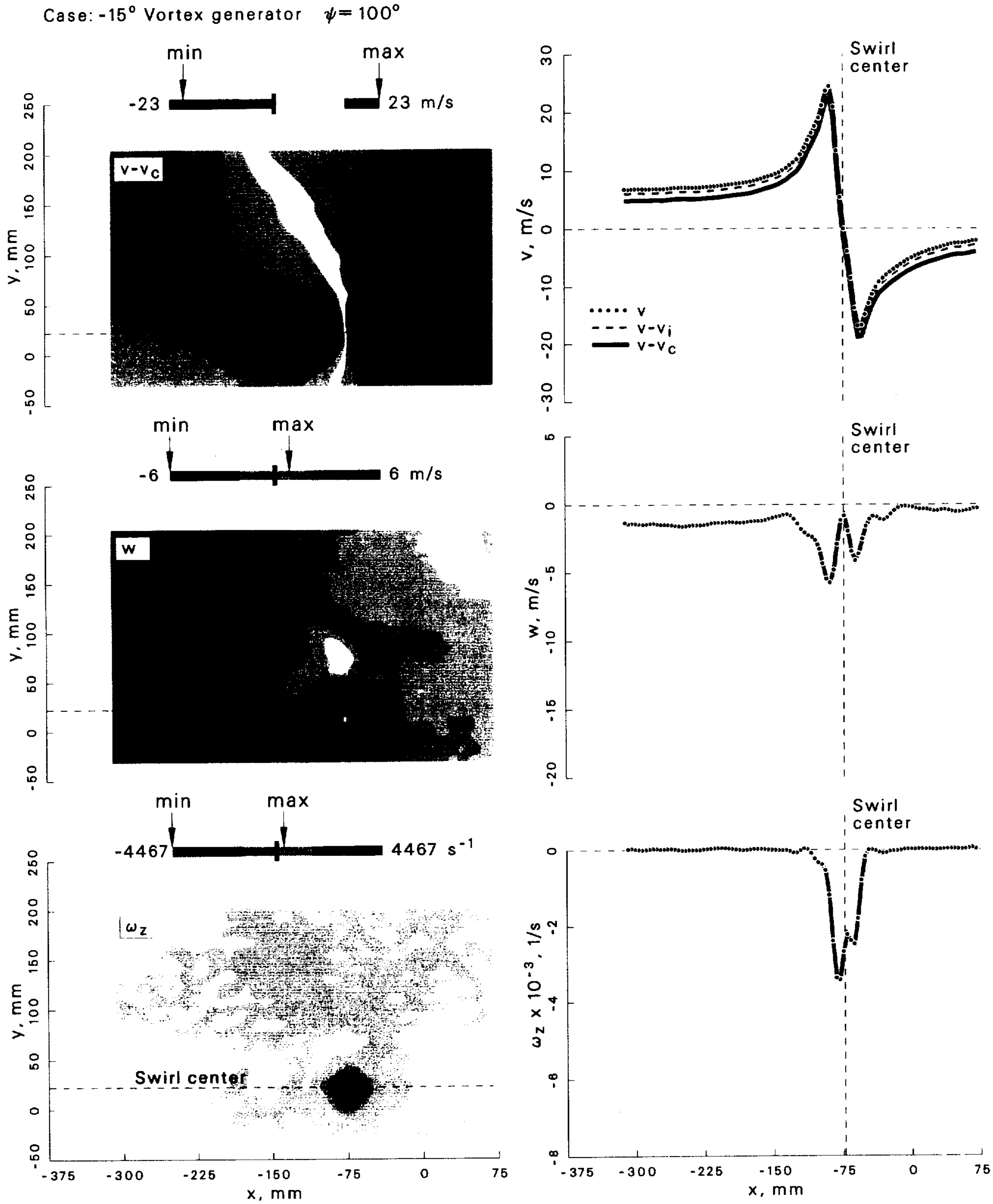

Figure 157: Velocity and vorticity components at $\psi = 100°$ for the $-15°$ vortex generator case.

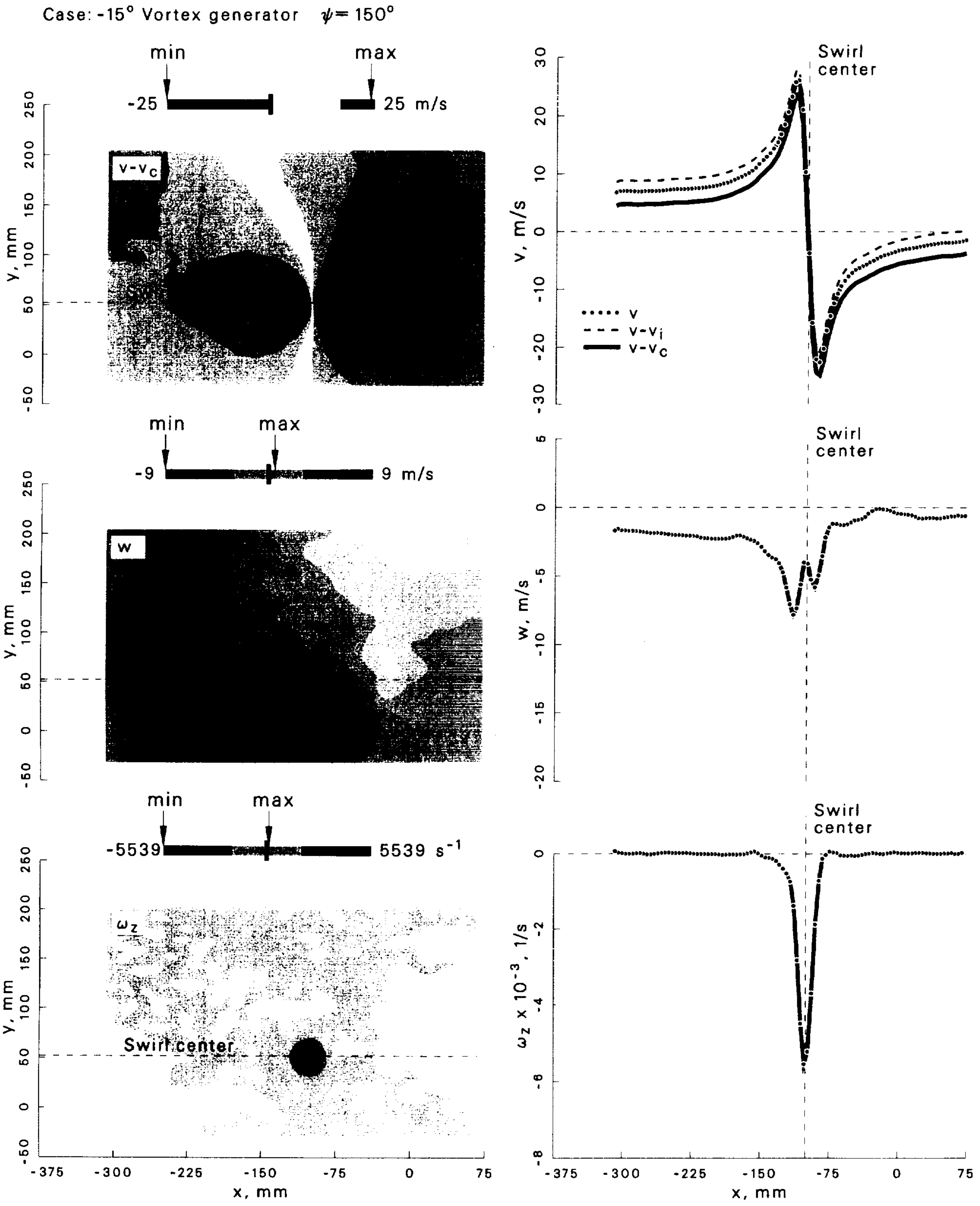

Figure 158: Velocity and vorticity components at $\psi = 150°$ for the $-15°$ vortex generator case.

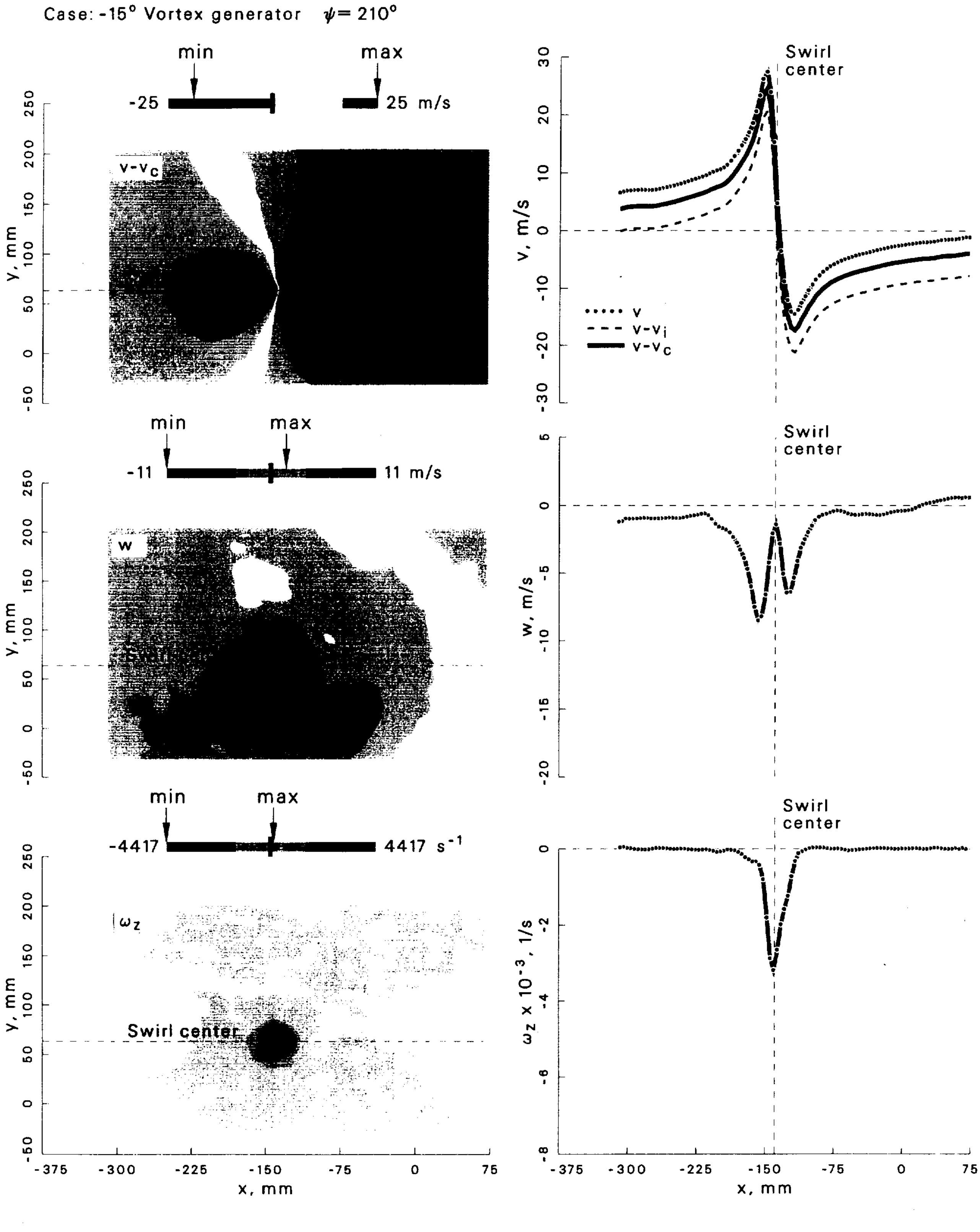

Figure 159: Velocity and vorticity components at $\psi = 210°$ for the $-15°$ vortex generator case.

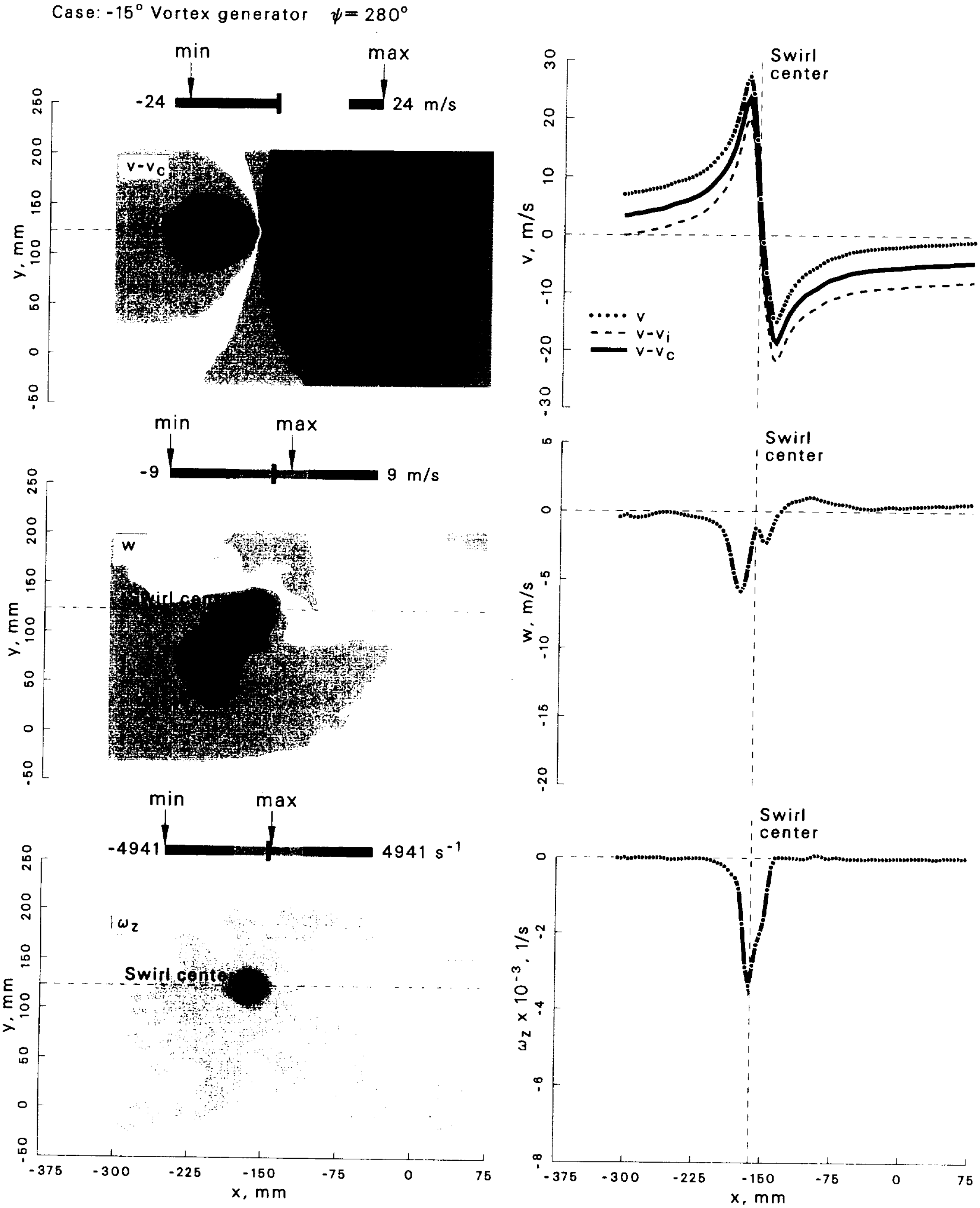

Figure 160: Velocity and vorticity components at $\psi = 280°$ for the $-15°$ vortex generator case.

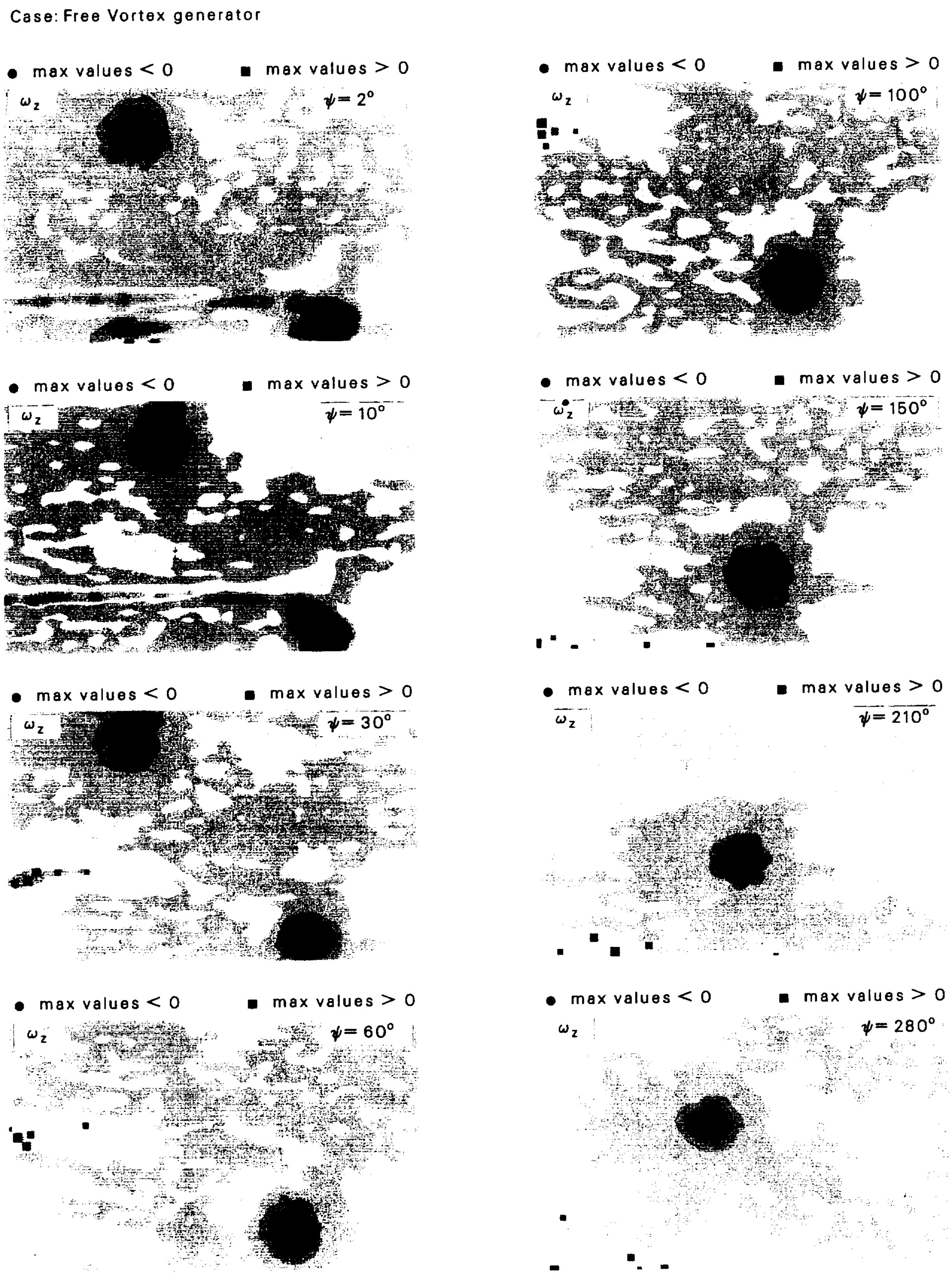

Figure 161: Locations of ω_z extrema at $\psi = 2^\circ \rightarrow 280^\circ$ for the free vortex generator case.

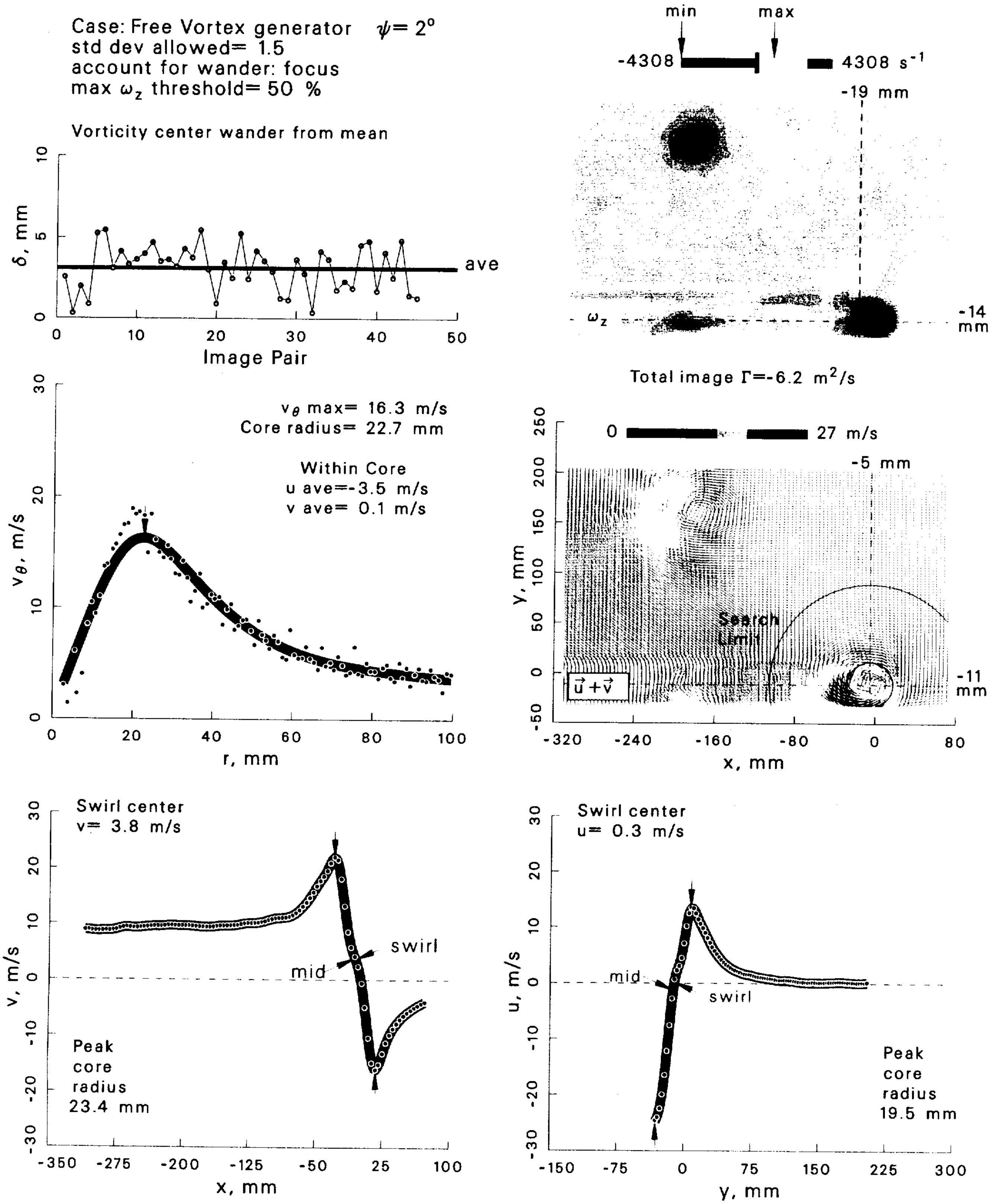

Figure 162: Vortex statistics at $\psi = 2°$ for the free vortex generator case.

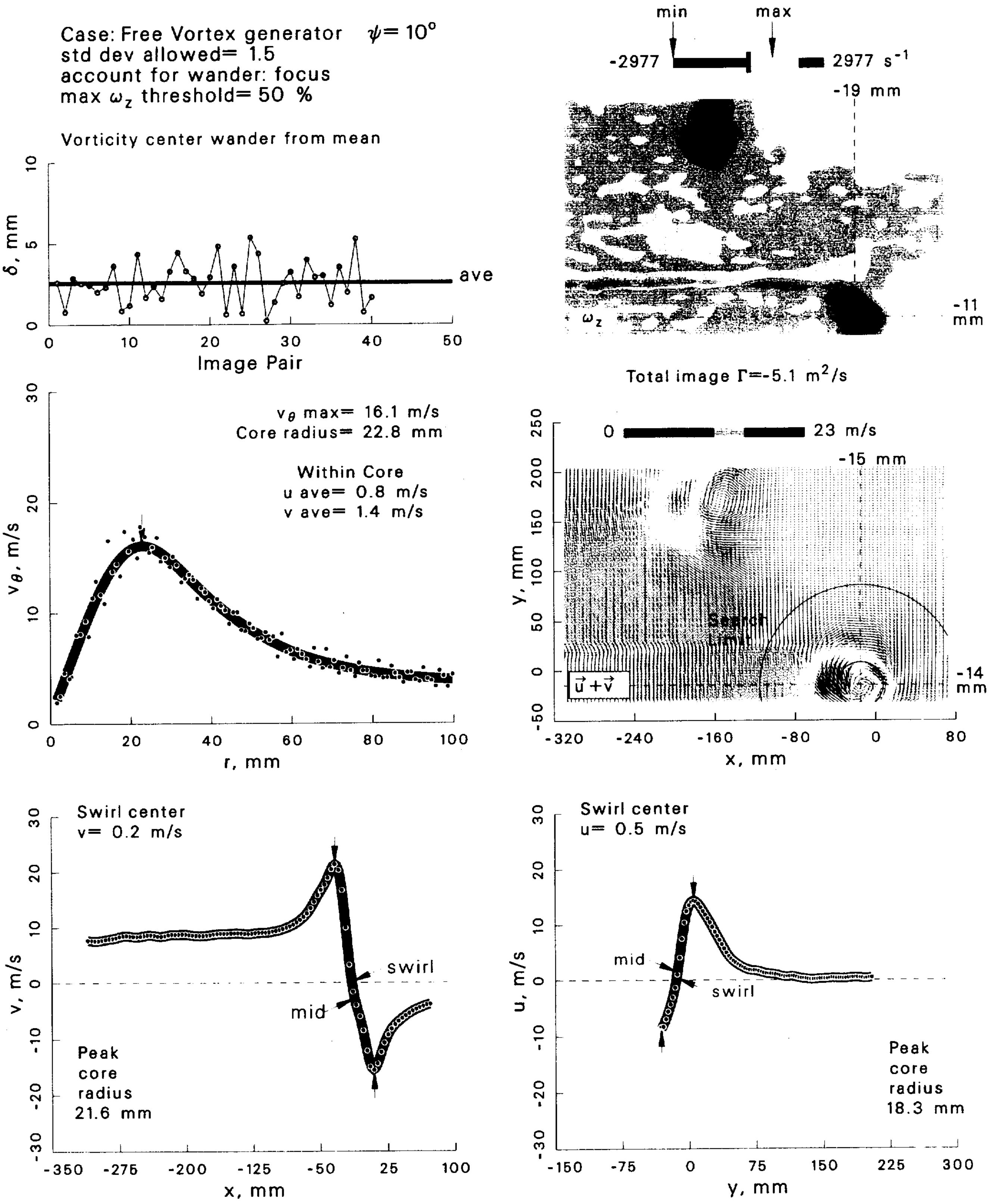

Figure 163: Vortex statistics at $\psi = 10°$ for the free vortex generator case.

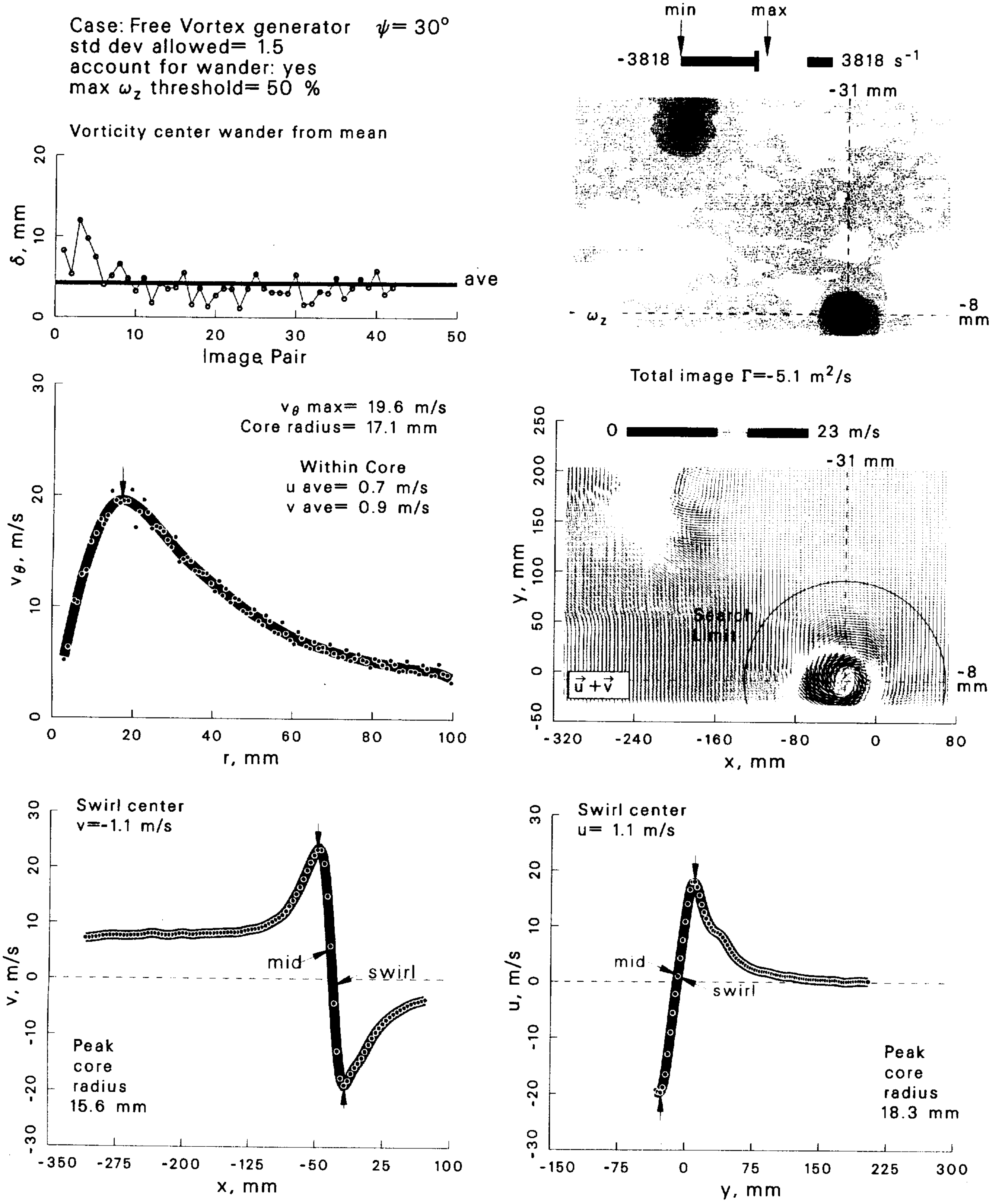

Figure 164: Vortex statistics at $\psi = 30°$ for the free vortex generator case.

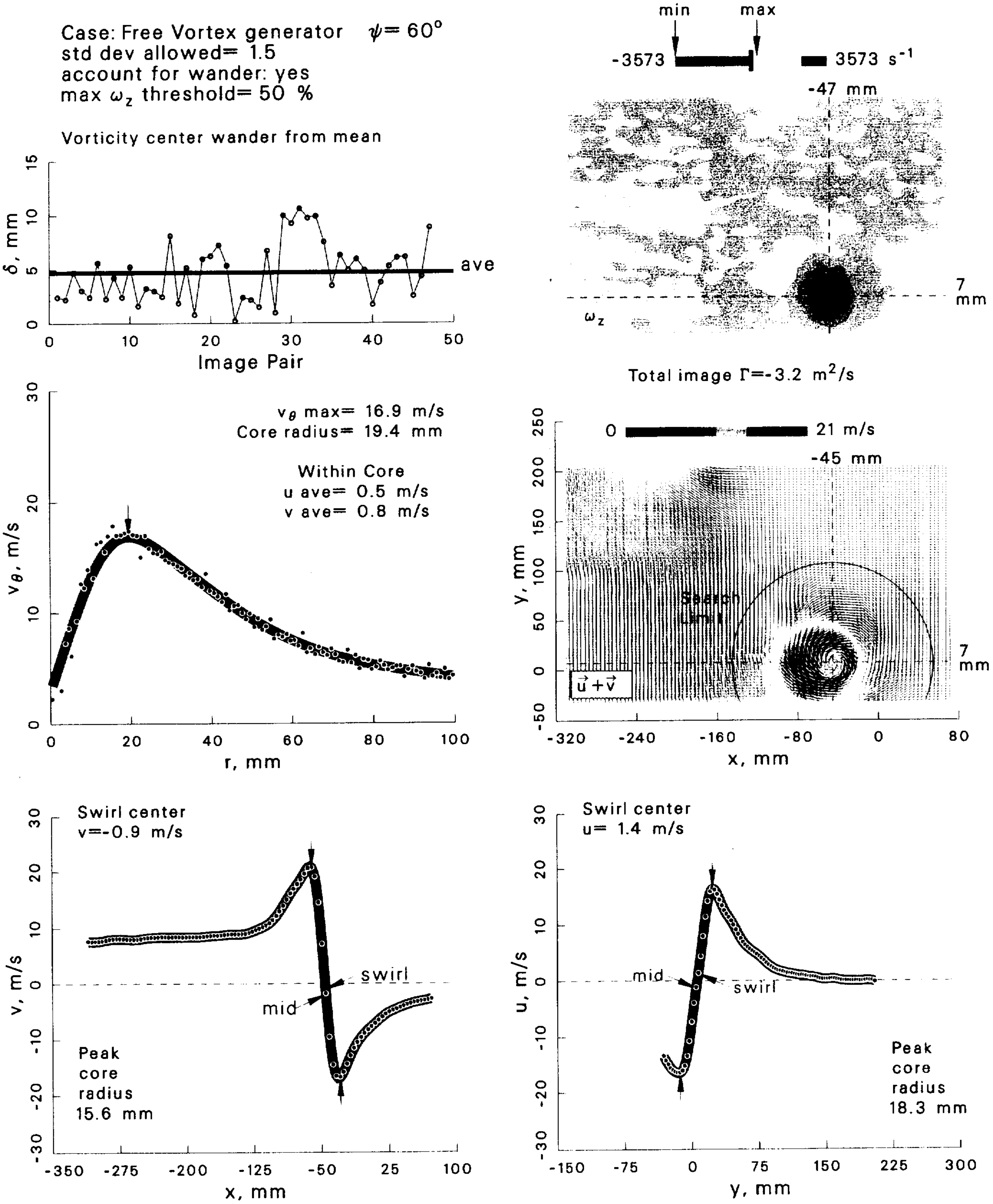

Figure 165: Vortex statistics at $\psi = 60°$ for the free vortex generator case.

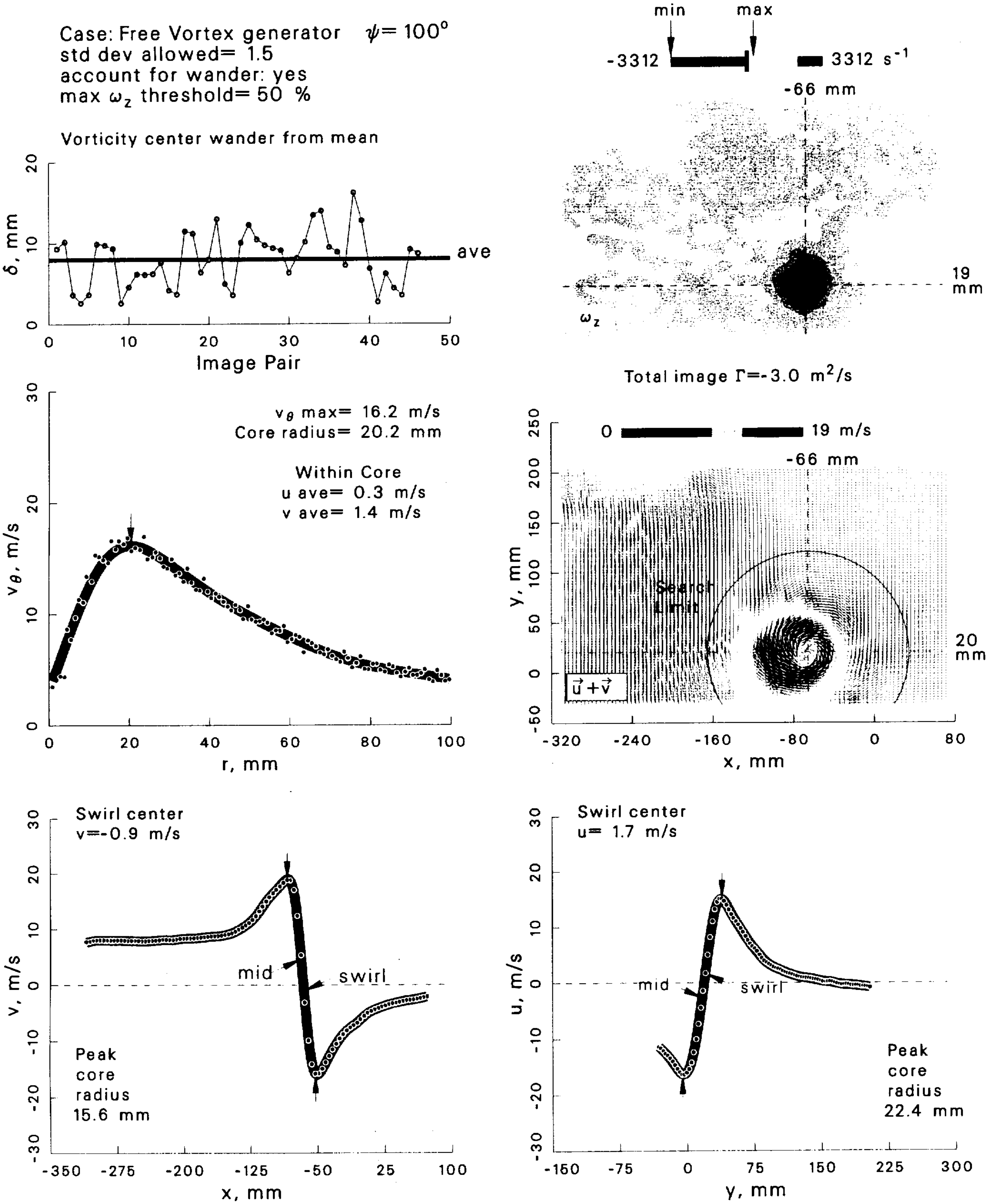

Figure 166: Vortex statistics at $\psi = 100°$ for the free vortex generator case.

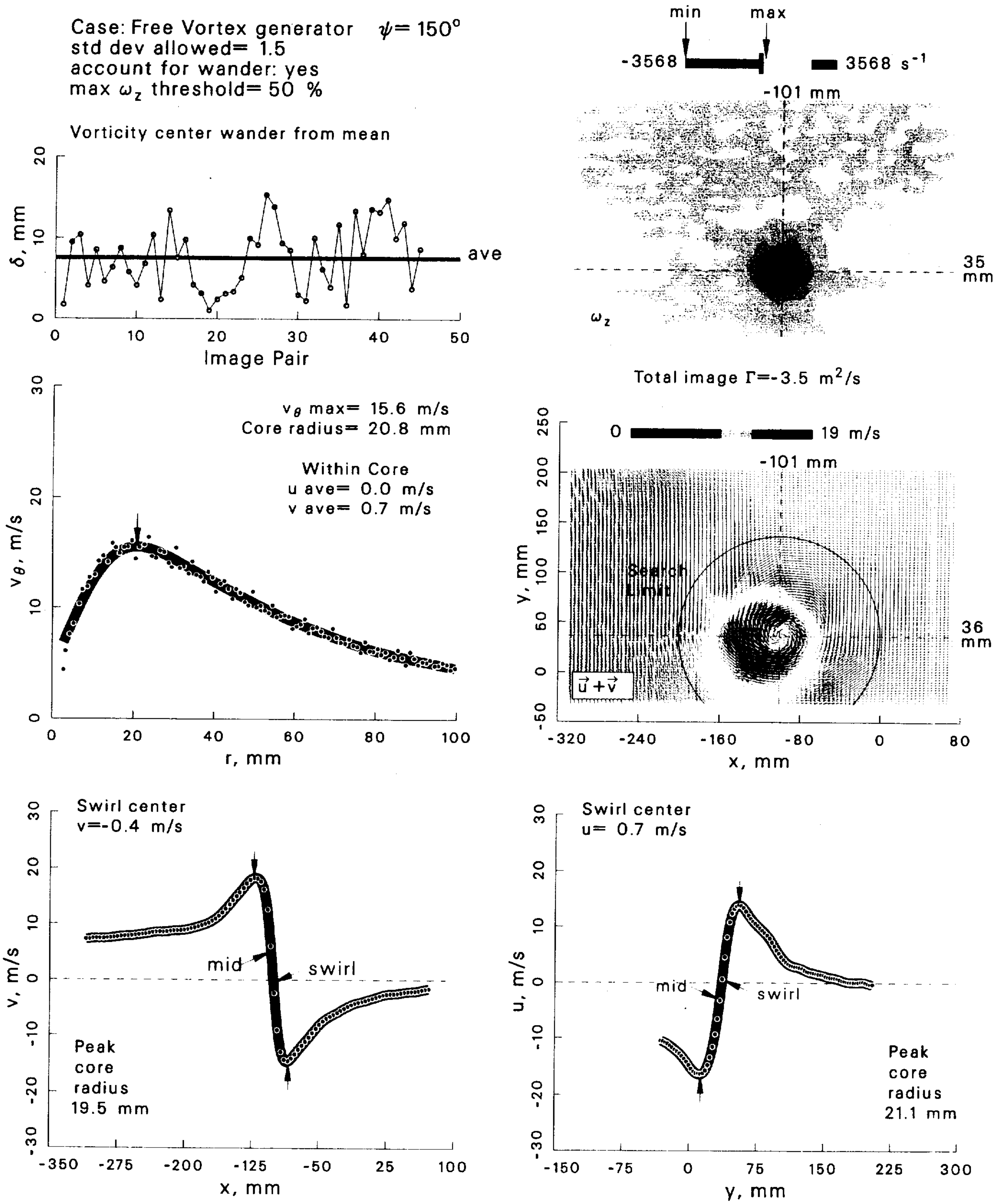

Figure 167: Vortex statistics at $\psi = 150°$ for the free vortex generator case.

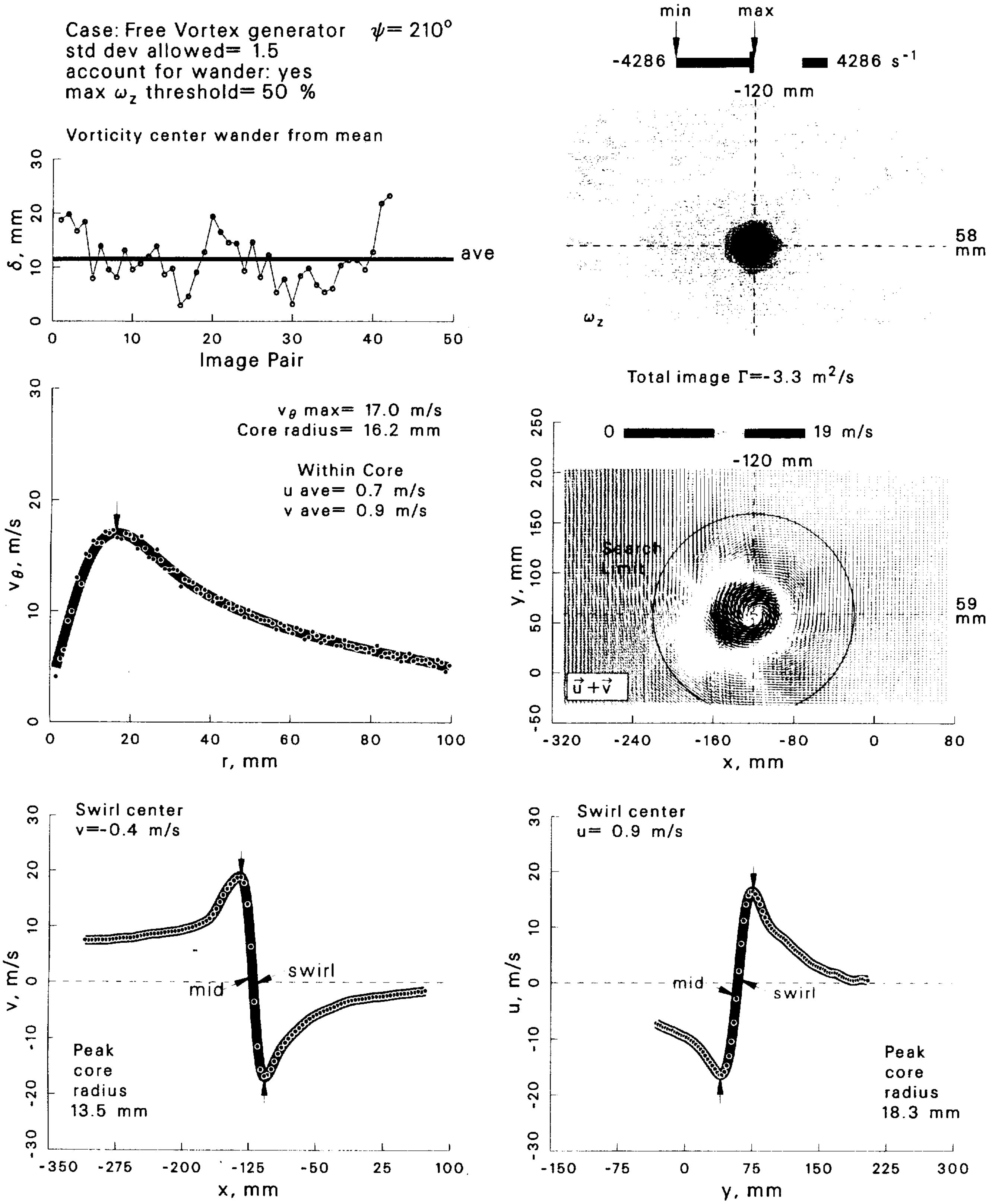

Figure 168: Vortex statistics at $\psi = 210°$ for the free vortex generator case.

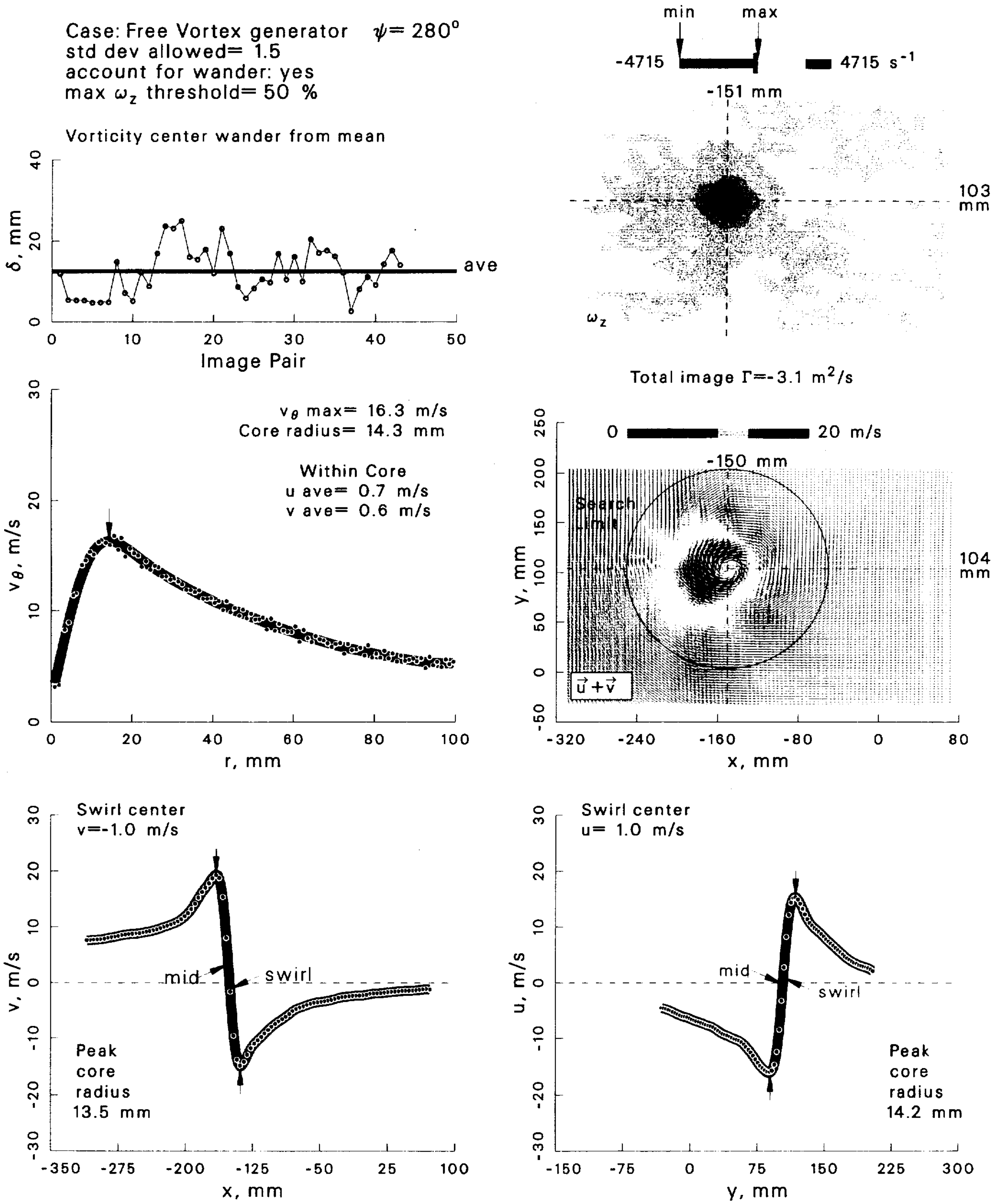

Figure 169: Vortex statistics at $\psi = 280°$ for the free vortex generator case.

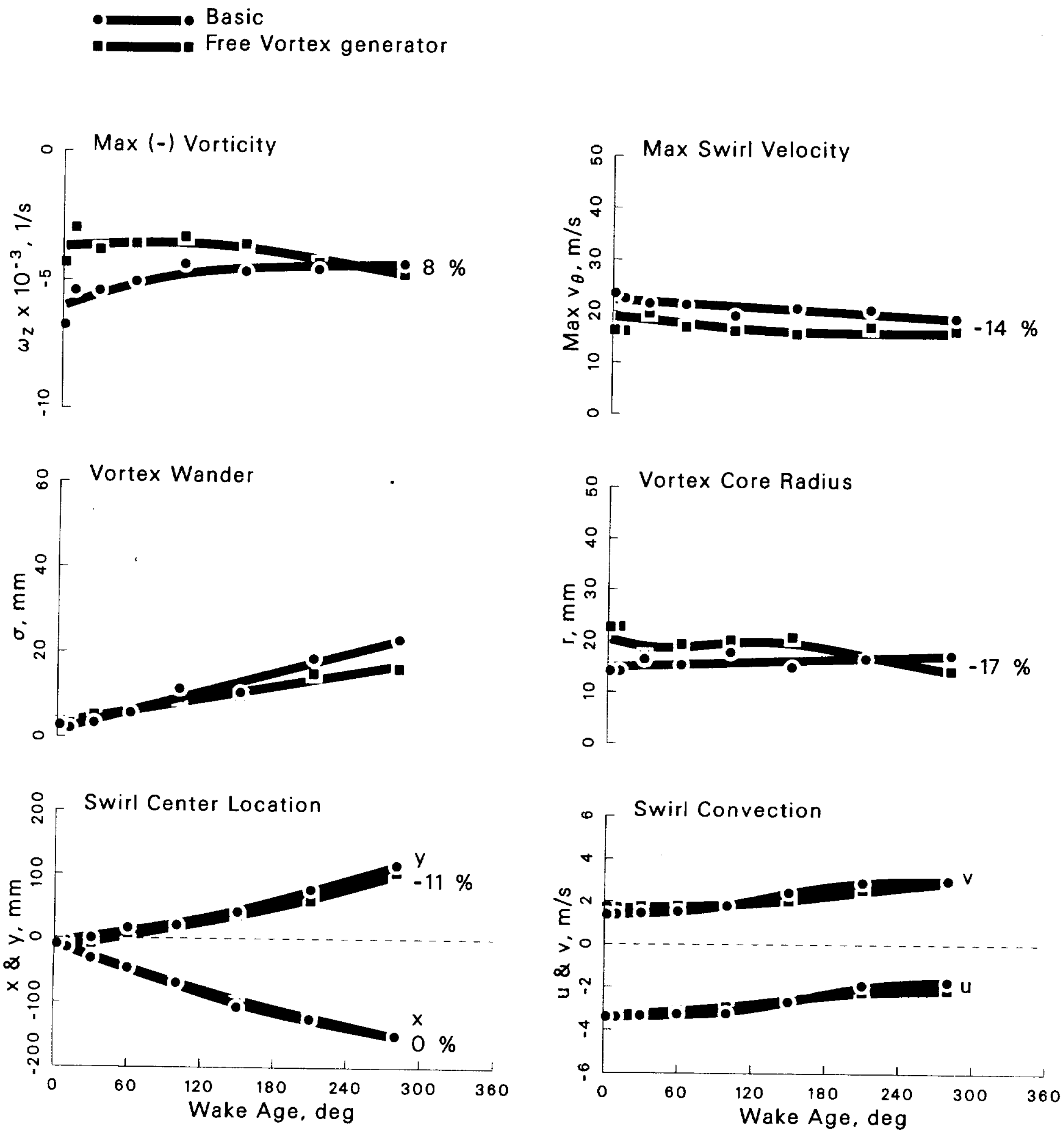

Figure 170: Summary of vortex development from $\psi = 2° \rightarrow 280°$ for the free vortex generator case.

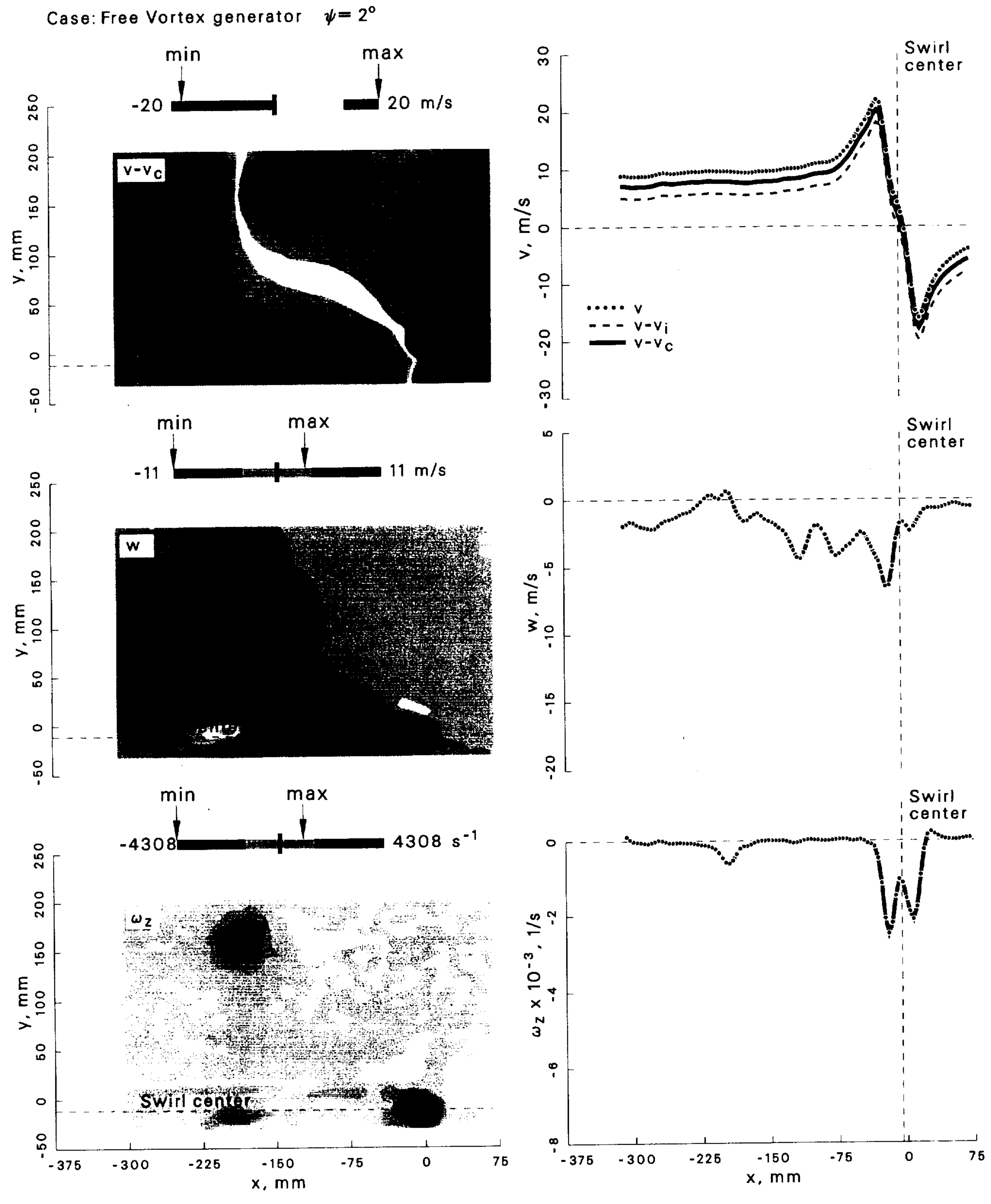

Figure 171: Velocity and vorticity components at $\psi = 2^\circ$ for the free vortex generator case.

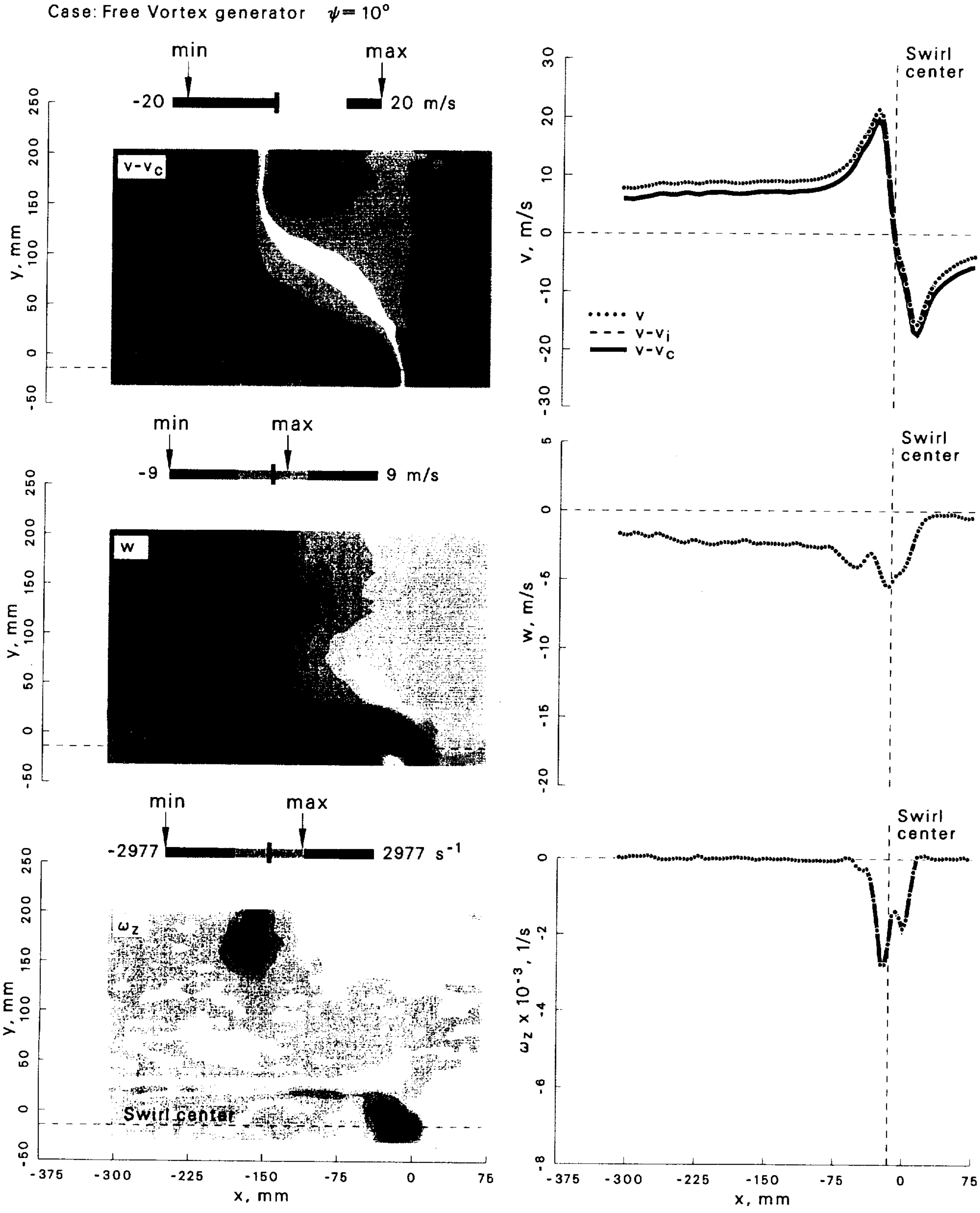

Figure 172: Velocity and vorticity components at $\psi = 10°$ for the free vortex generator case.

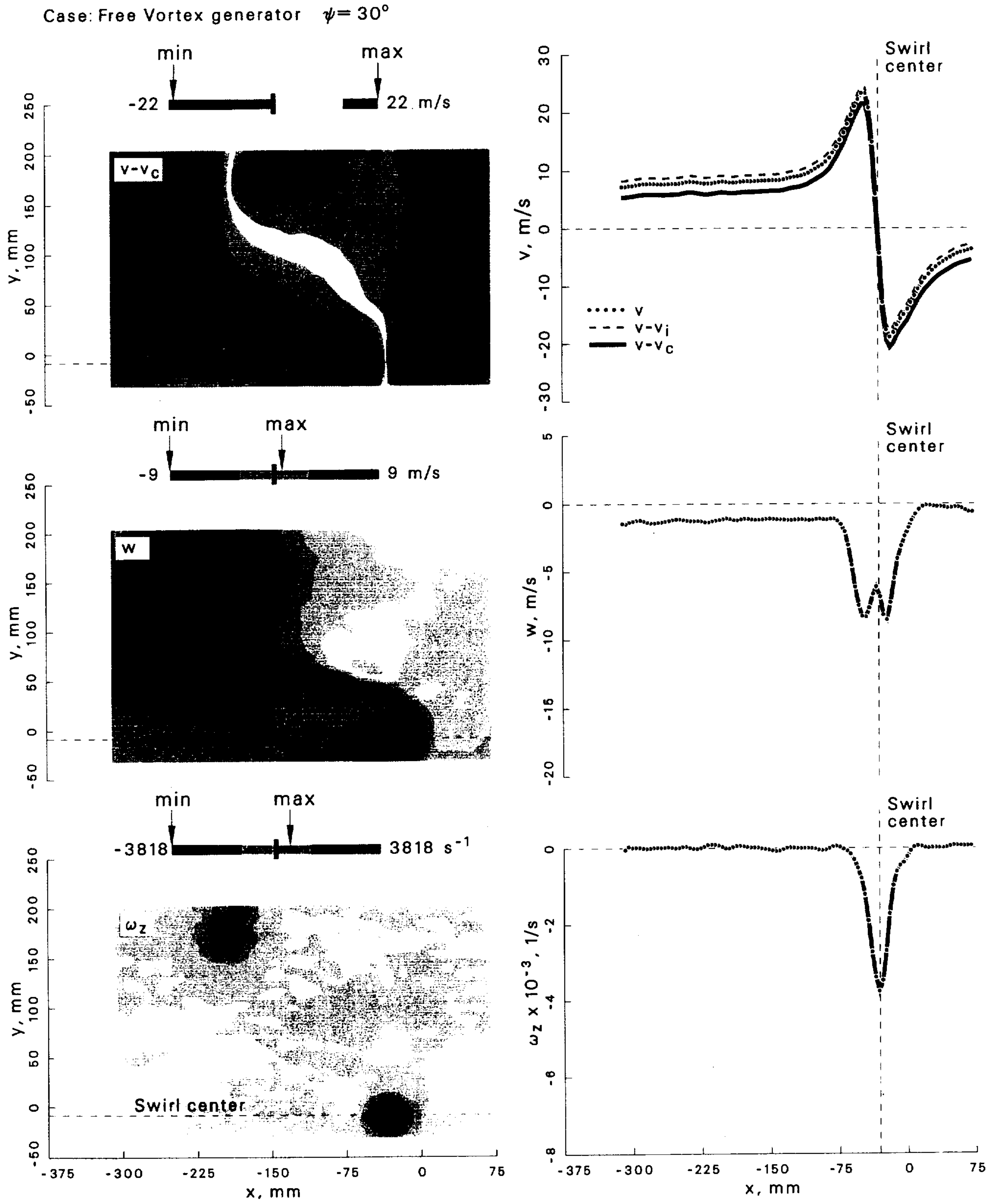

Figure 173: Velocity and vorticity components at $\psi = 30°$ for the free vortex generator case.

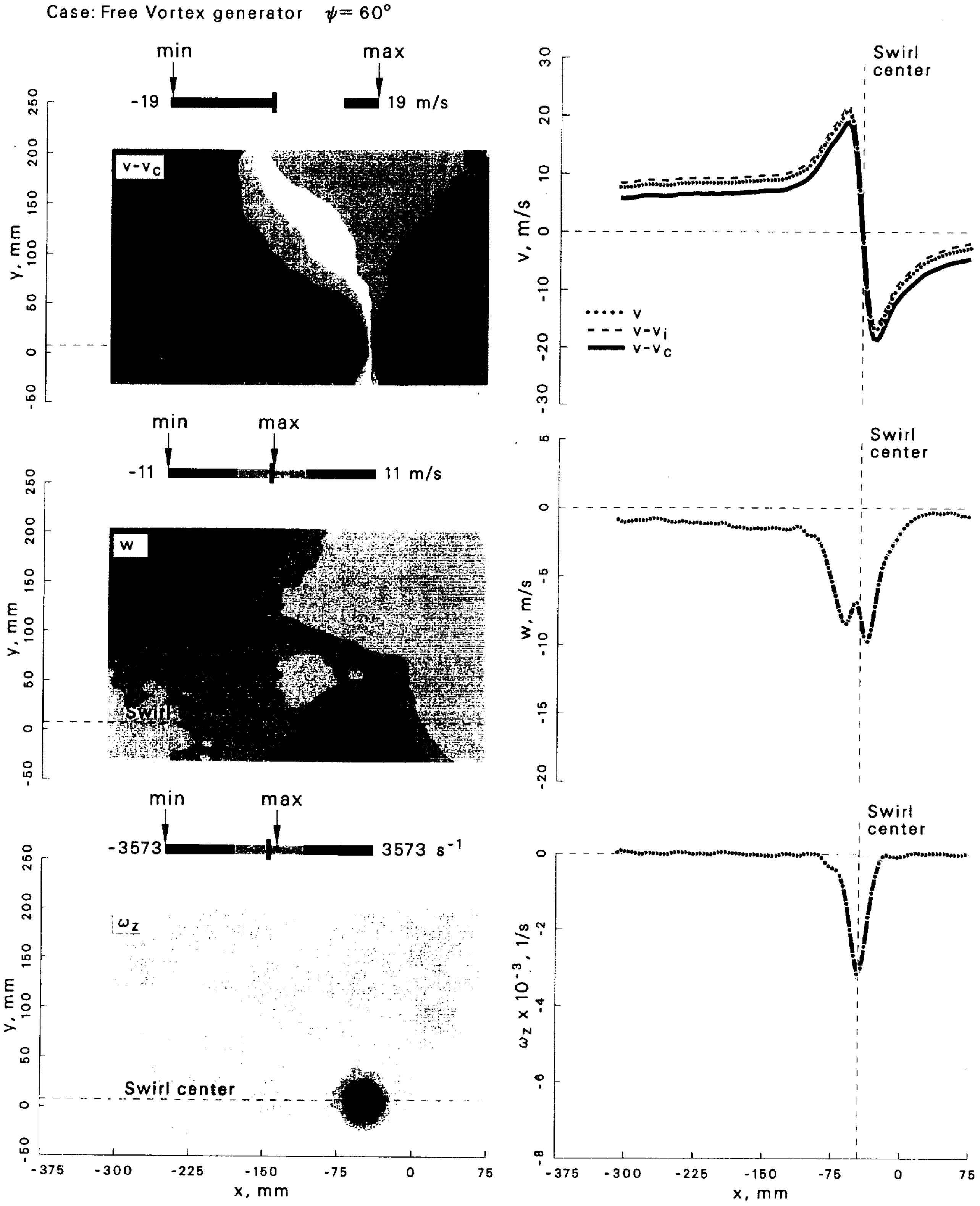

Figure 174: Velocity and vorticity components at $\psi = 60°$ for the free vortex generator case.

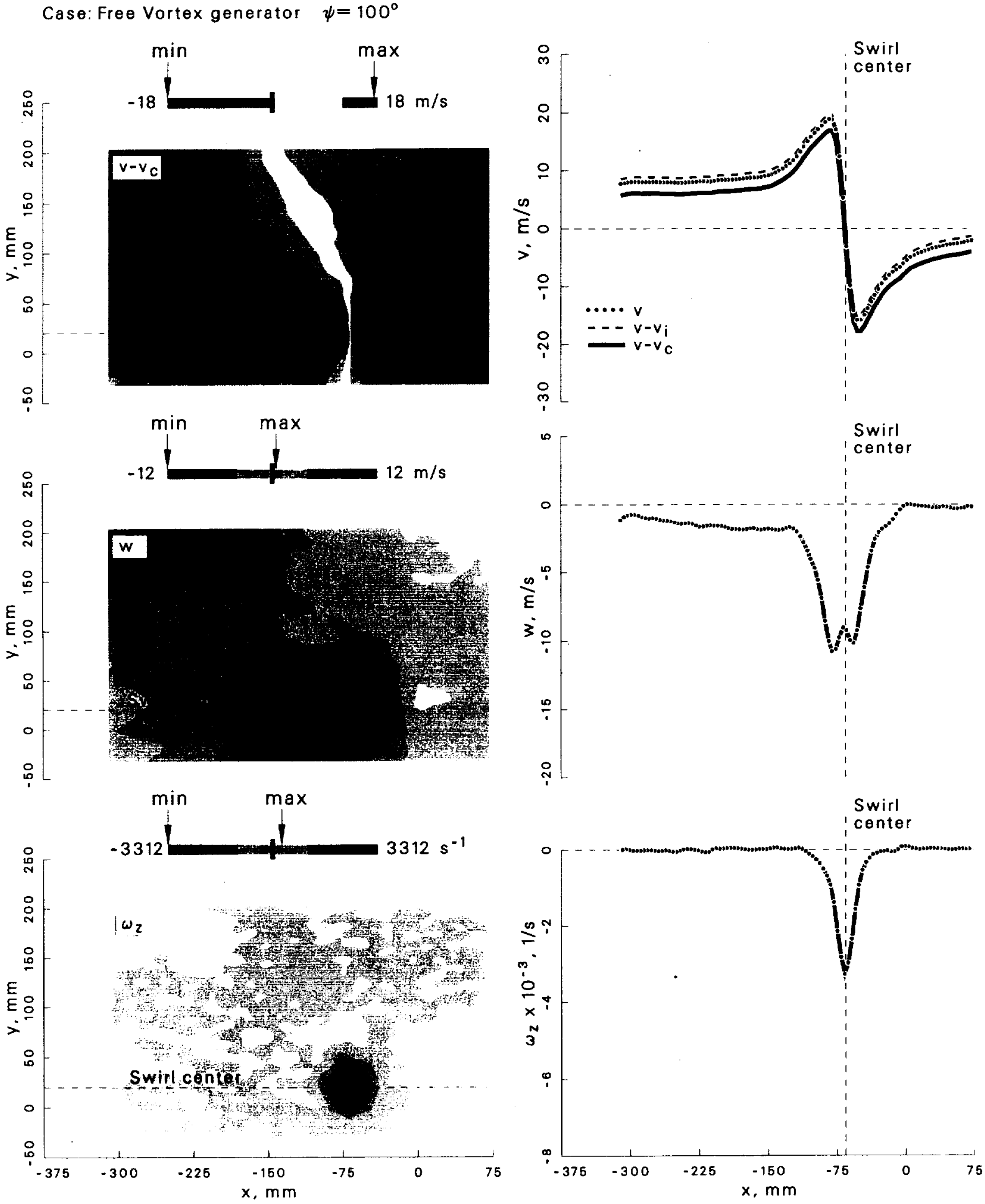

Figure 175: Velocity and vorticity components at $\psi = 100°$ for the free vortex generator case.

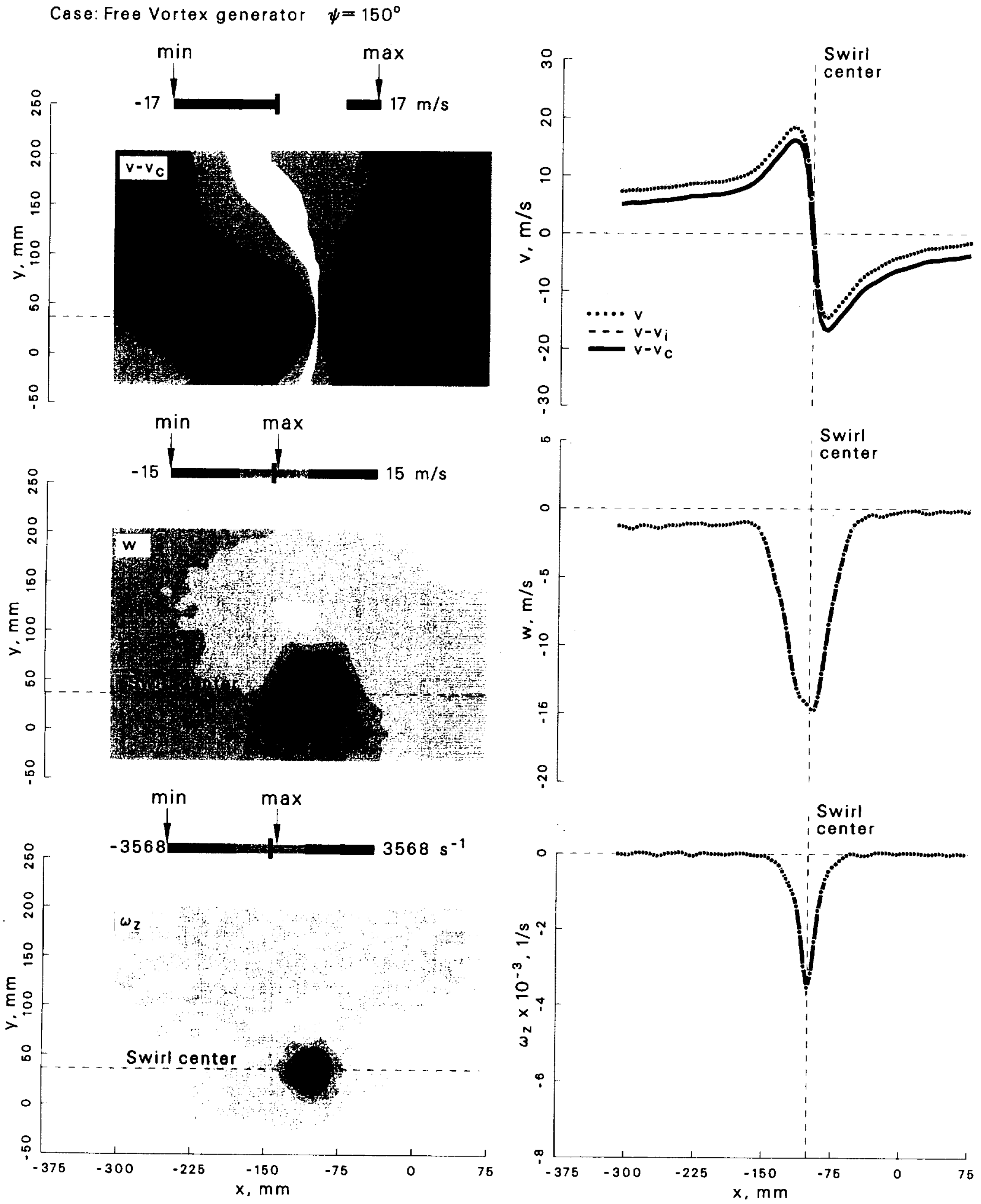

Figure 176: Velocity and vorticity components at $\psi = 150°$ for the free vortex generator case.

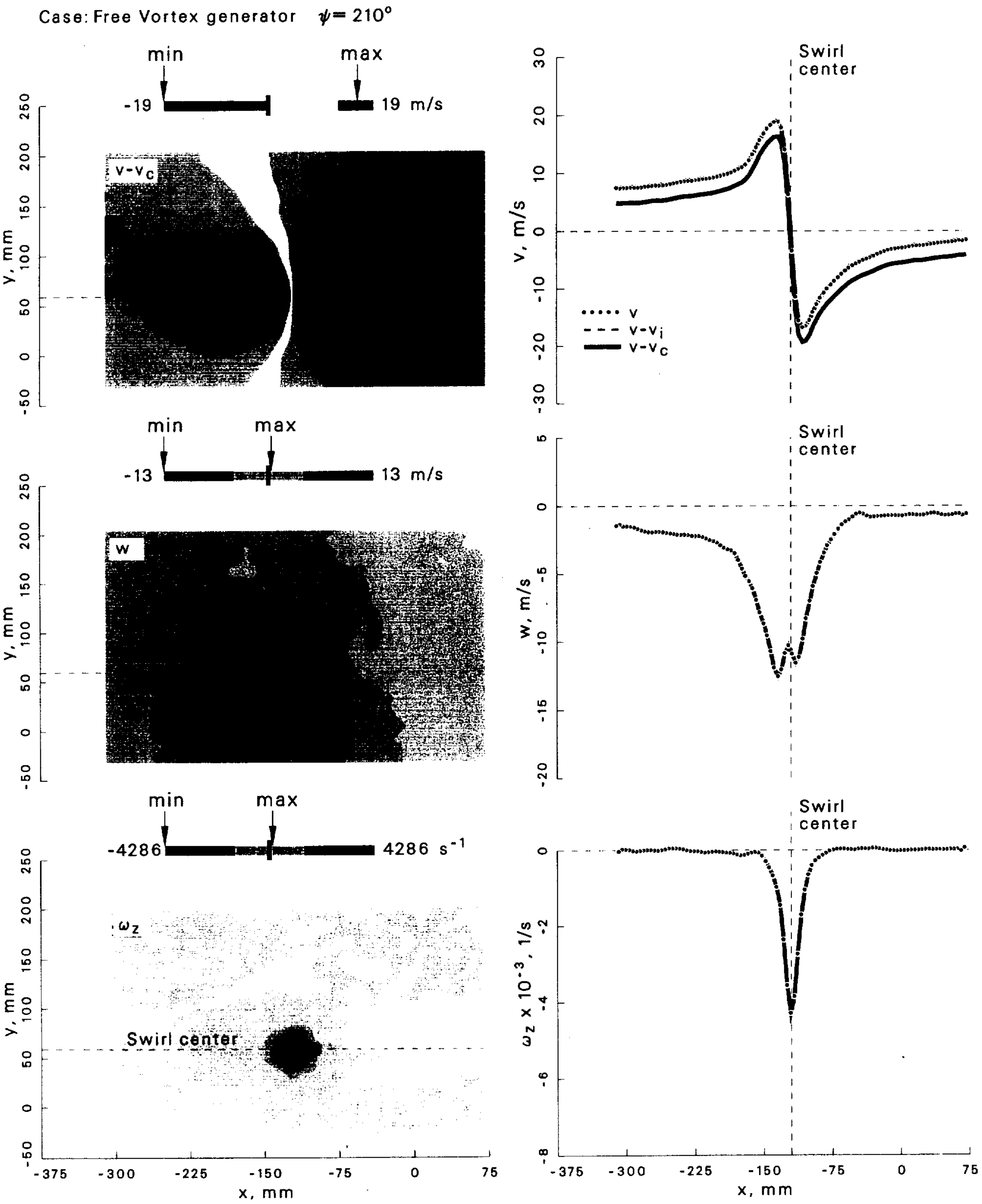

Figure 177: Velocity and vorticity components at $\psi = 210°$ for the free vortex generator case.

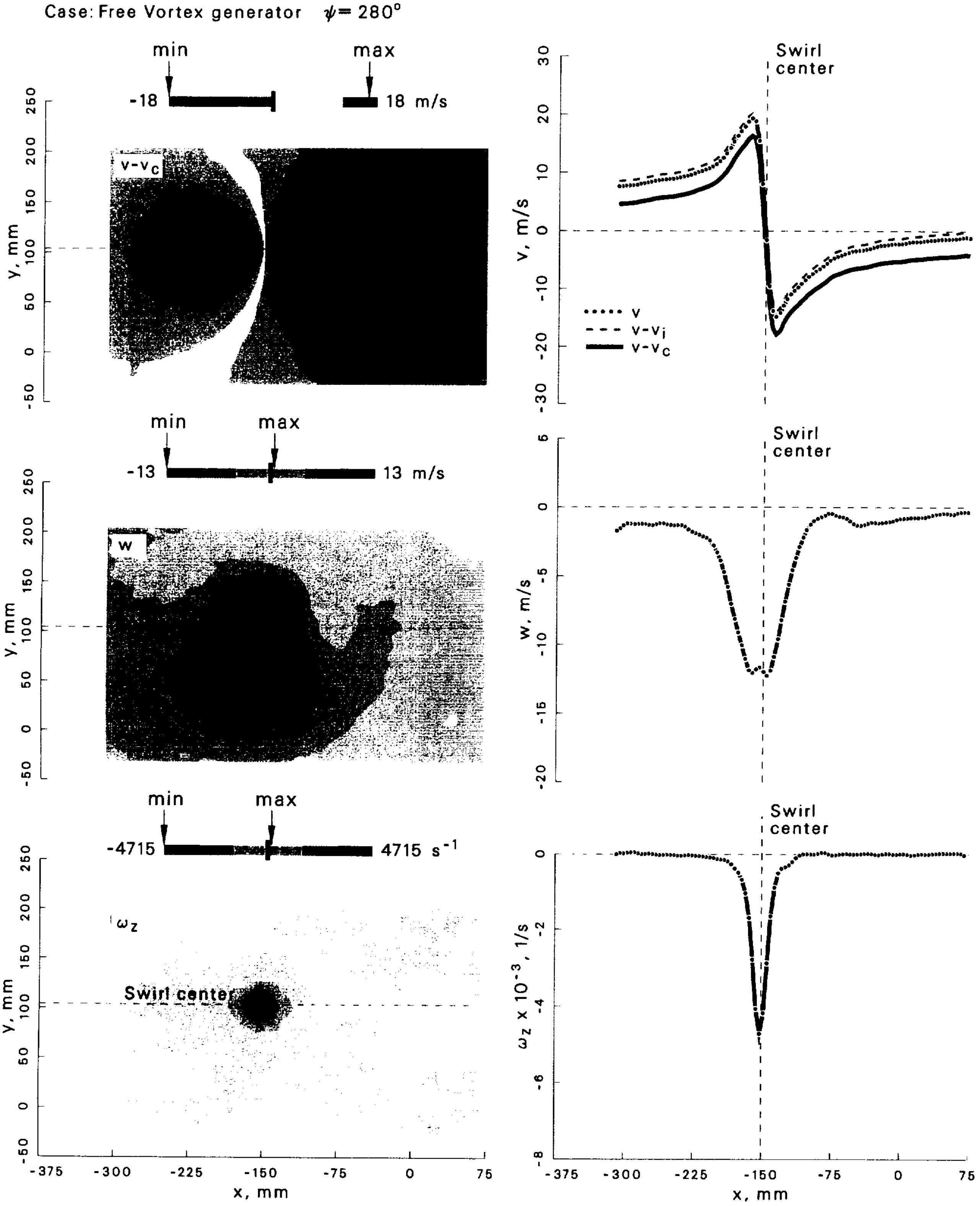

Figure 178: Velocity and vorticity components at $\psi = 280°$ for the free vortex generator case.

Case: Turbulence generator

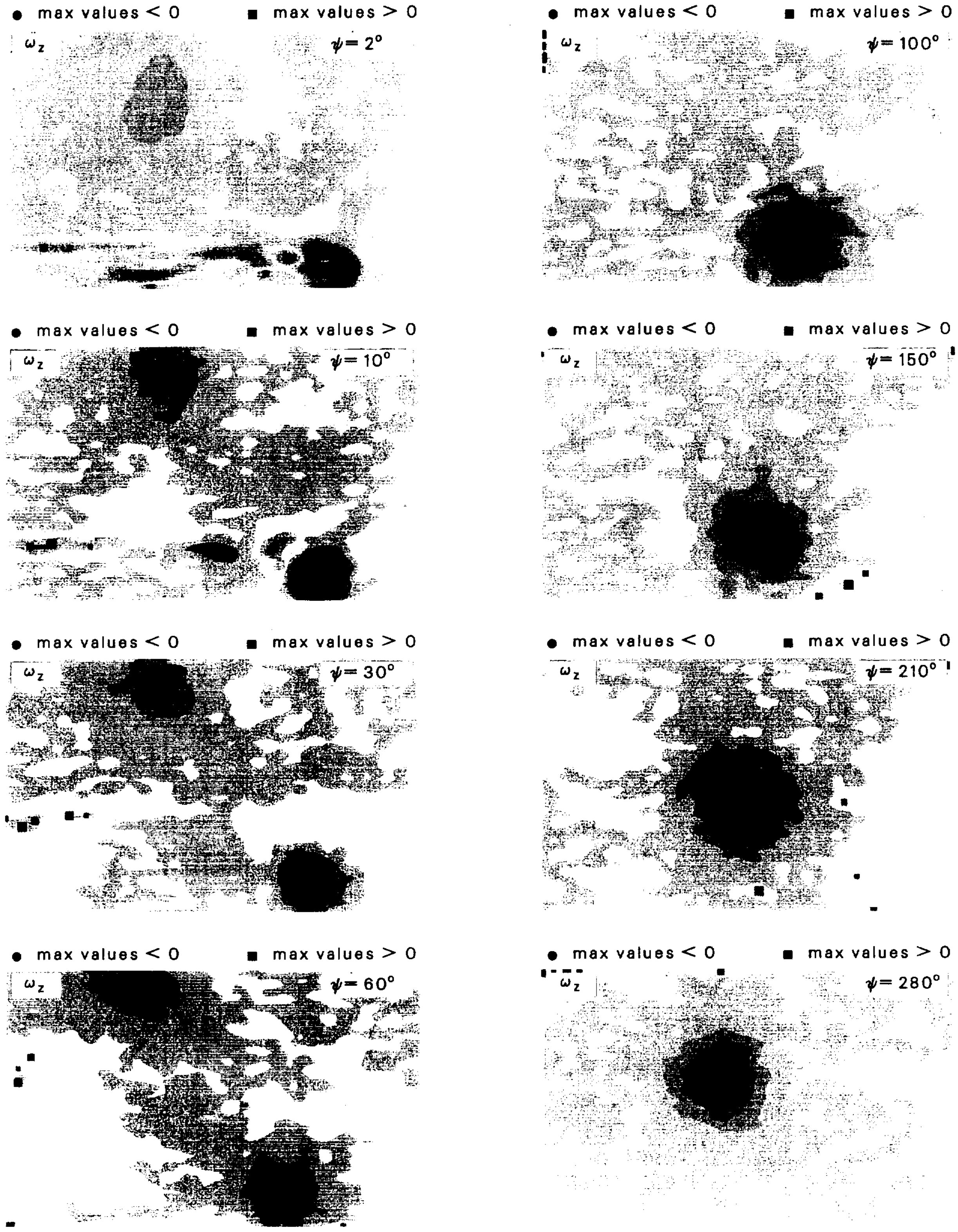

Figure 179: Locations of ω_z extrema at $\psi = 2^\circ \rightarrow 280^\circ$ for the turbulence generator case.

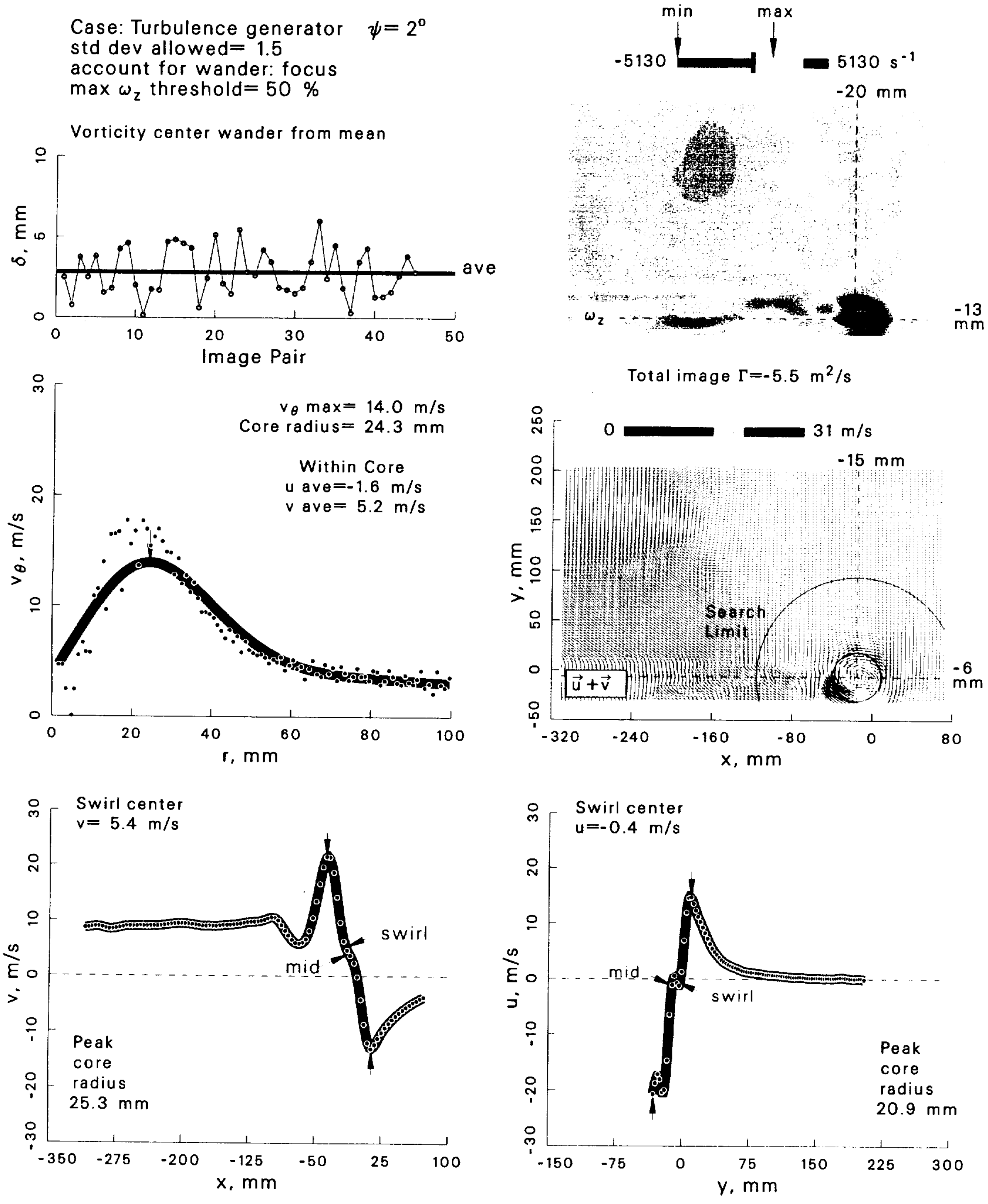

Figure 180: Vortex statistics at $\psi = 2°$ for the turbulence generator case.

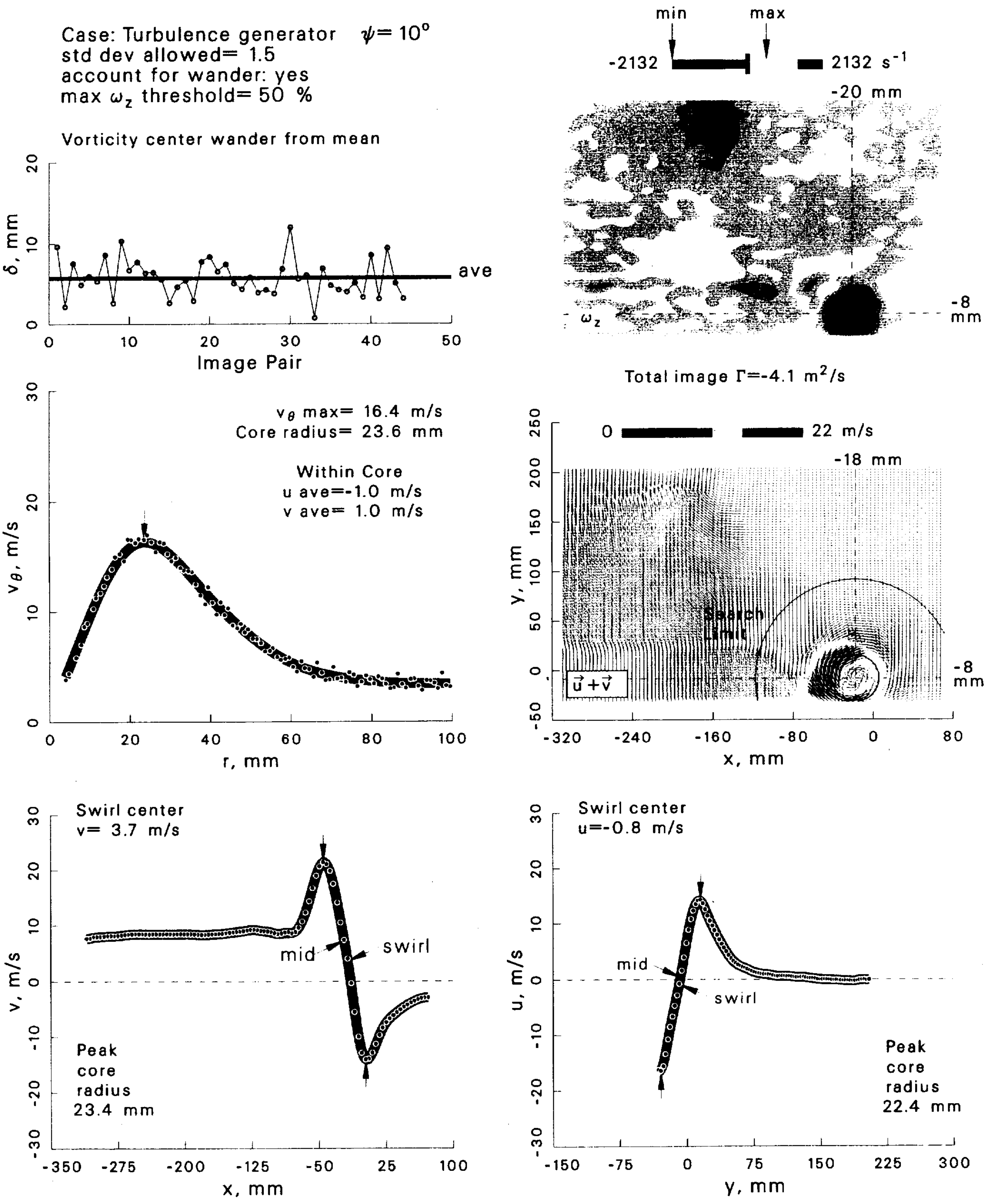

Figure 181: Vortex statistics at $\psi = 10°$ for the turbulence generator case.

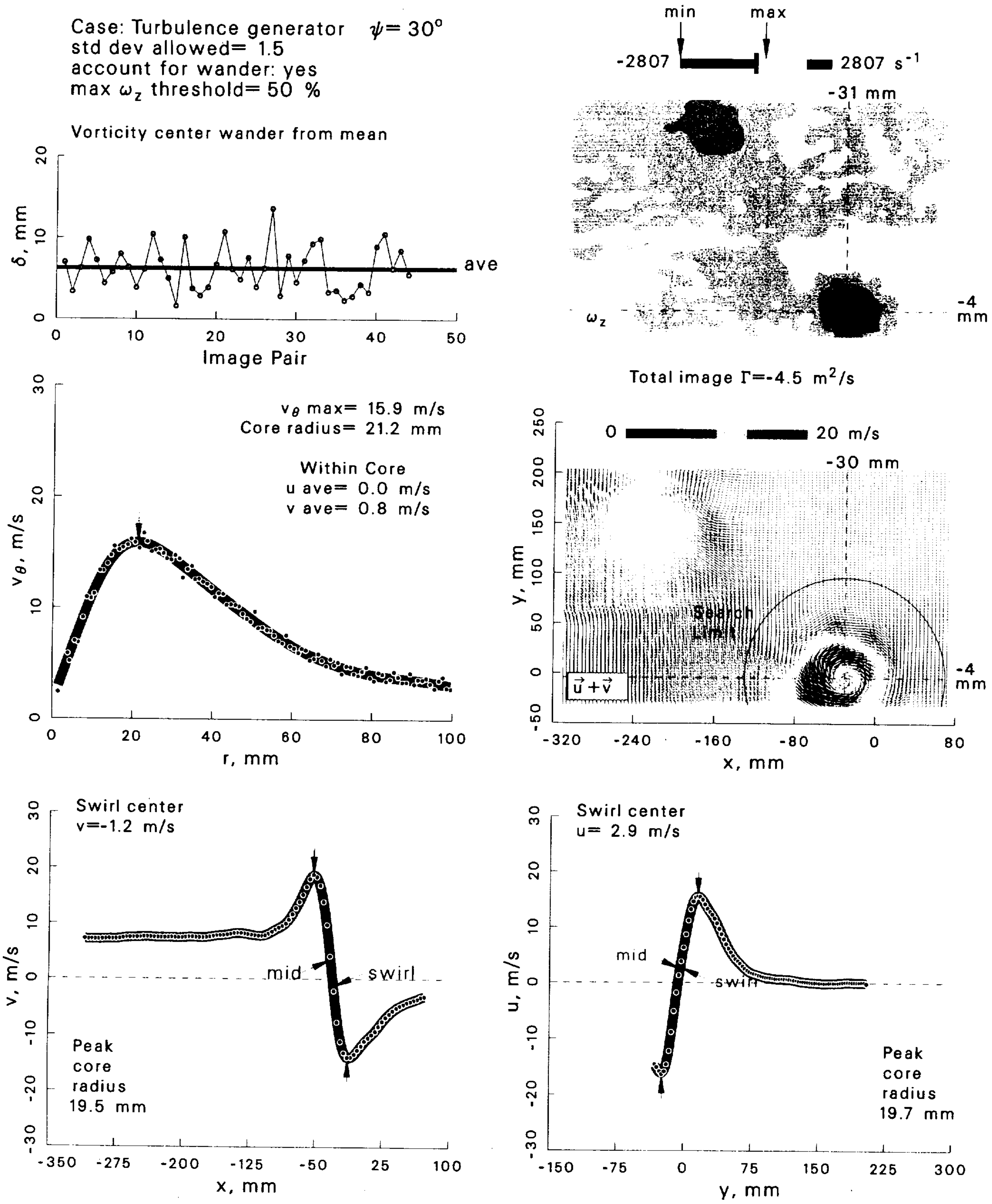

Figure 182: Vortex statistics at $\psi = 30°$ for the turbulence generator case.

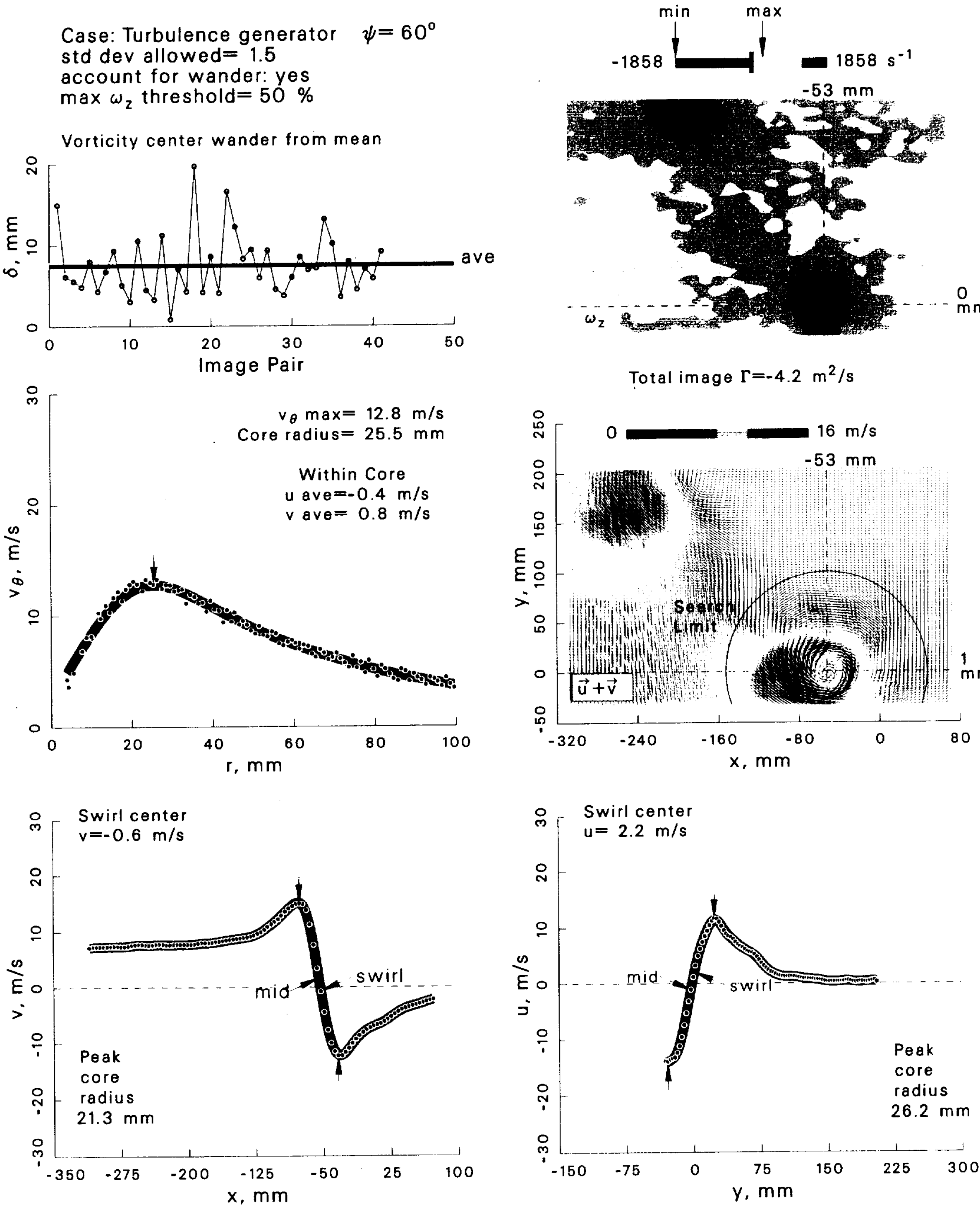

Figure 183: Vortex statistics at $\psi = 60°$ for the turbulence generator case.

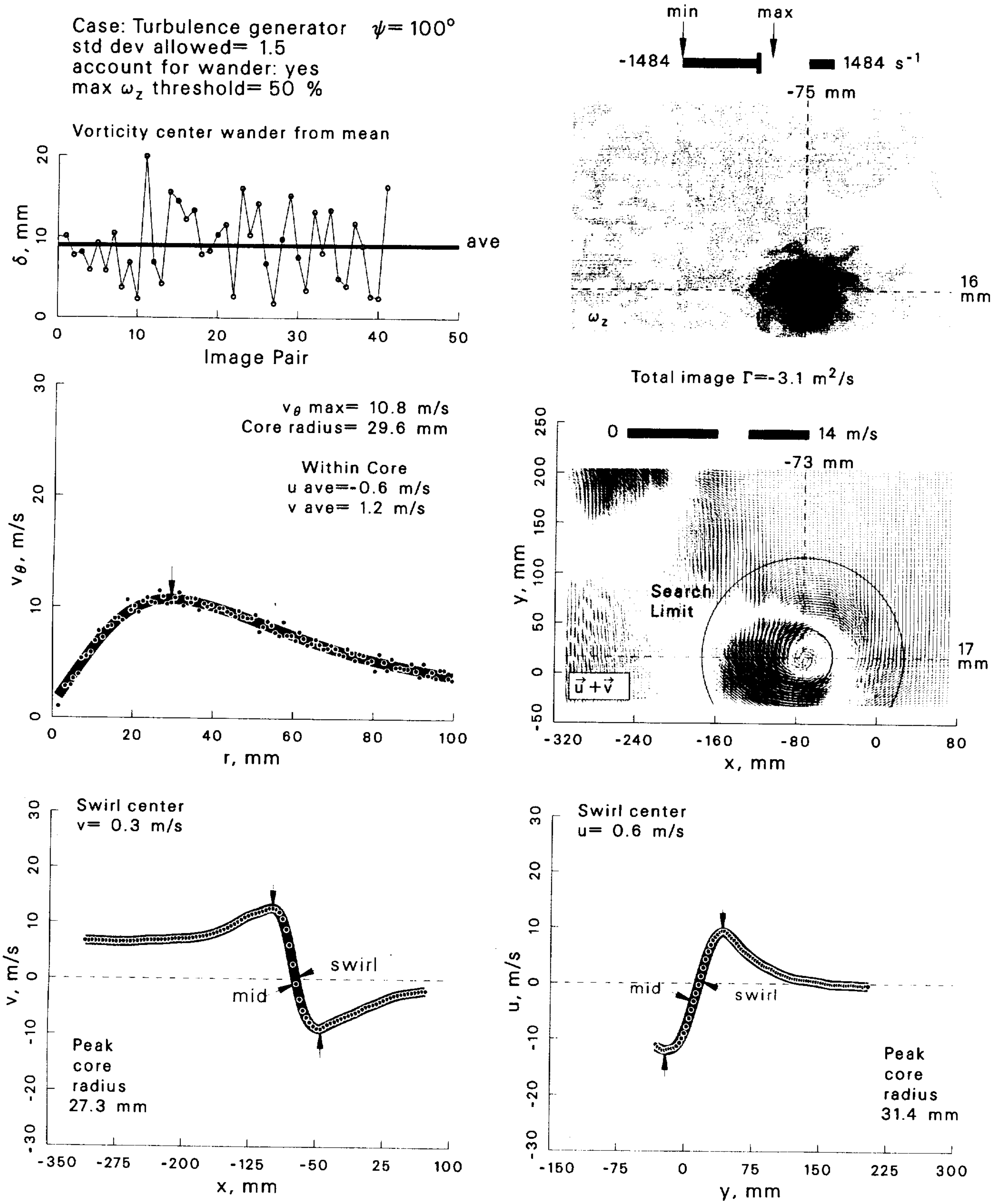

Figure 184: Vortex statistics at $\psi = 100°$ for the turbulence generator case.

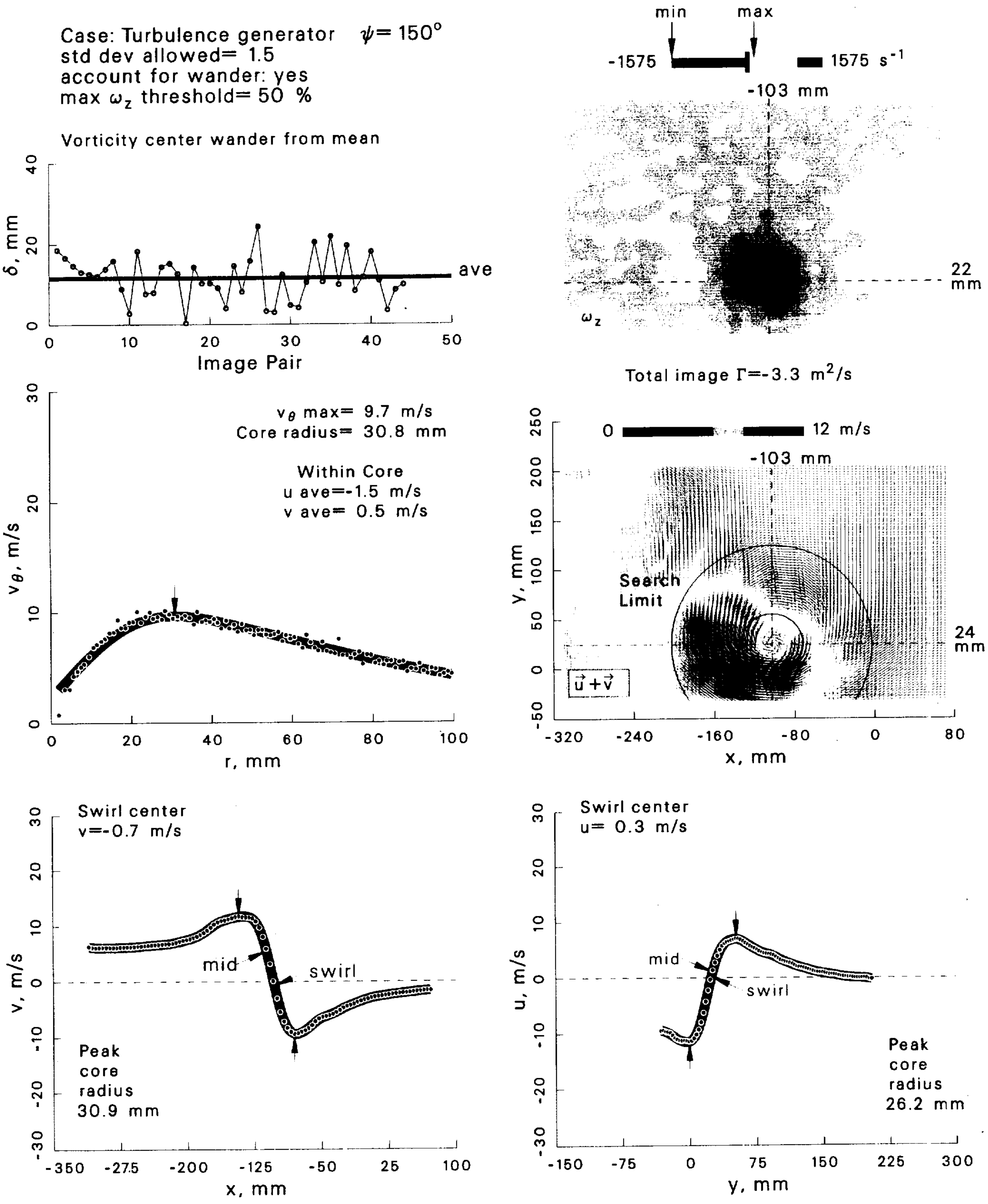

Figure 185: Vortex statistics at $\psi = 150°$ for the turbulence generator case.

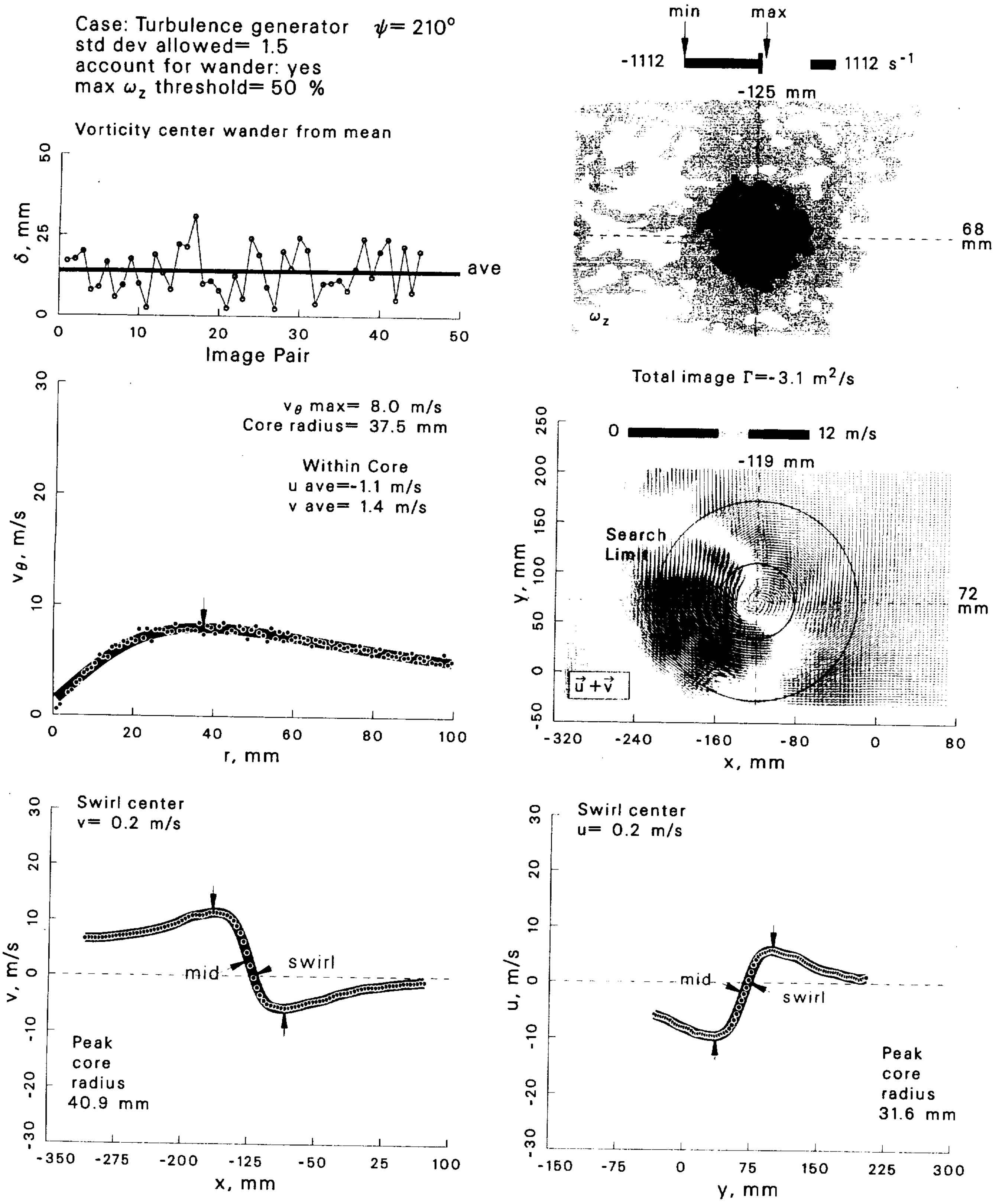

Figure 186: Vortex statistics at $\psi = 210°$ for the turbulence generator case.

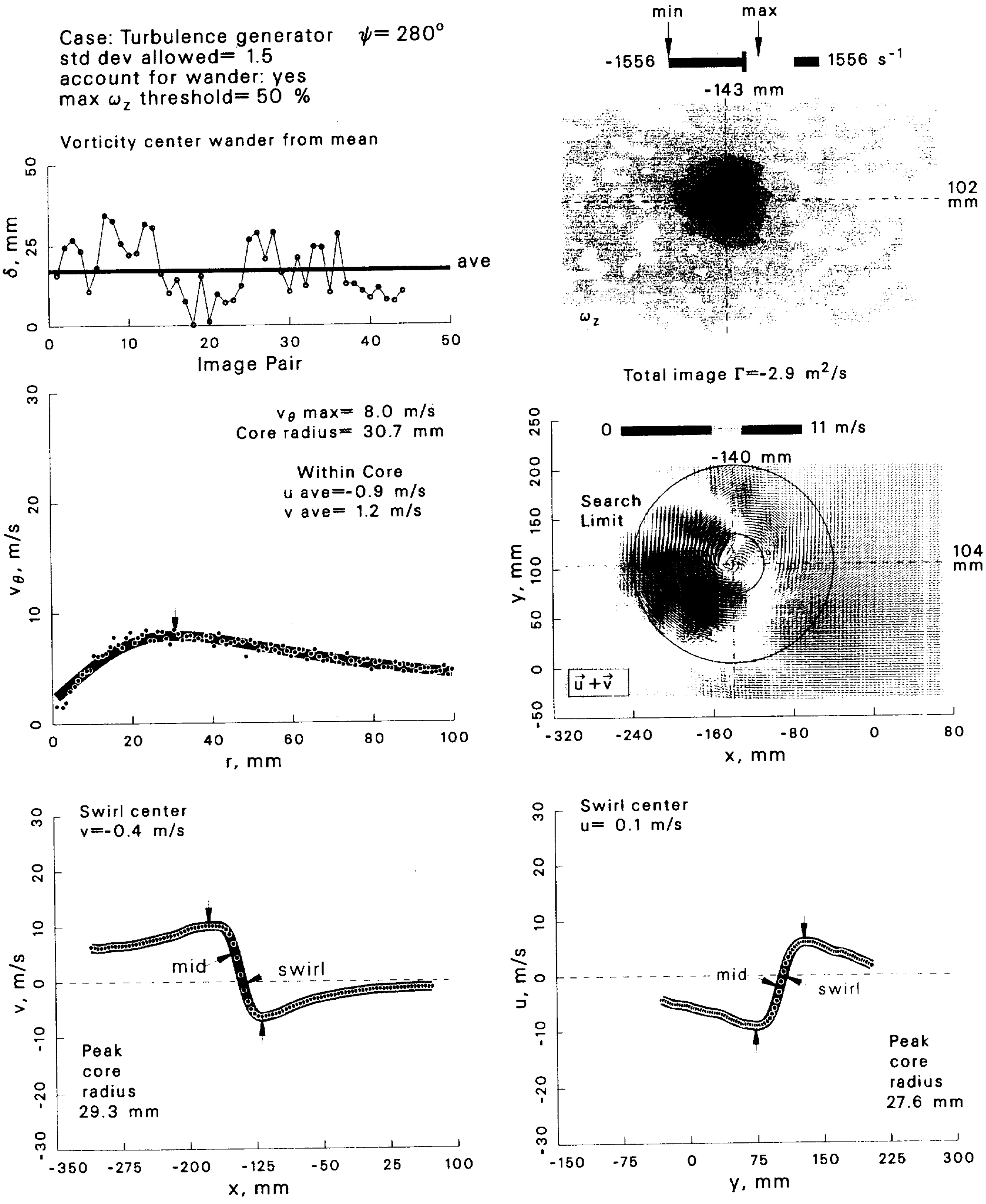

Figure 187: Vortex statistics at $\psi = 280°$ for the turbulence generator case.

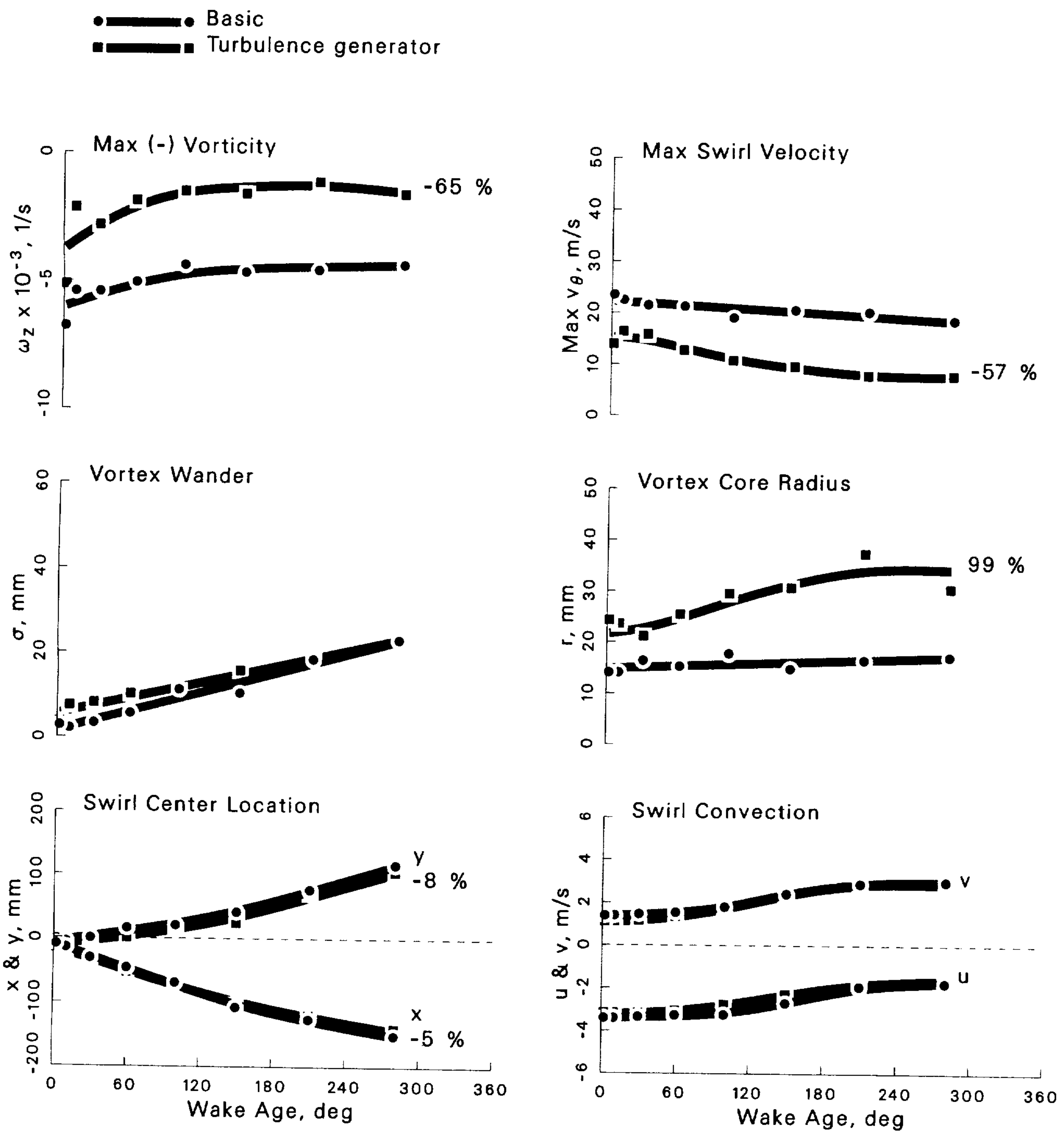

Figure 188: Summary of vortex development from $\psi = 2° \rightarrow 280°$ for the turbulence generator case.

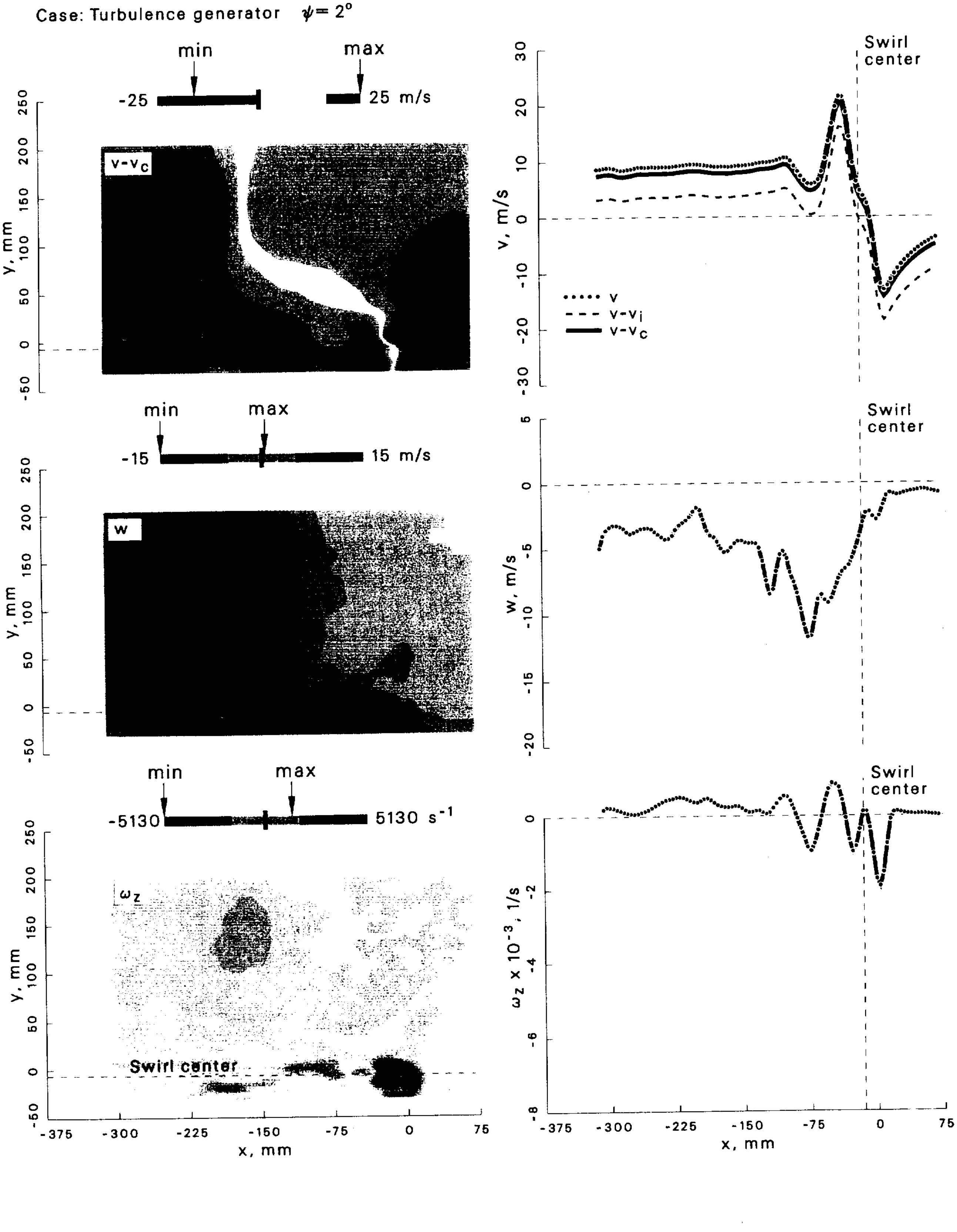

Figure 189: Velocity and vorticity components at $\psi = 2°$ for the turbulence generator case.

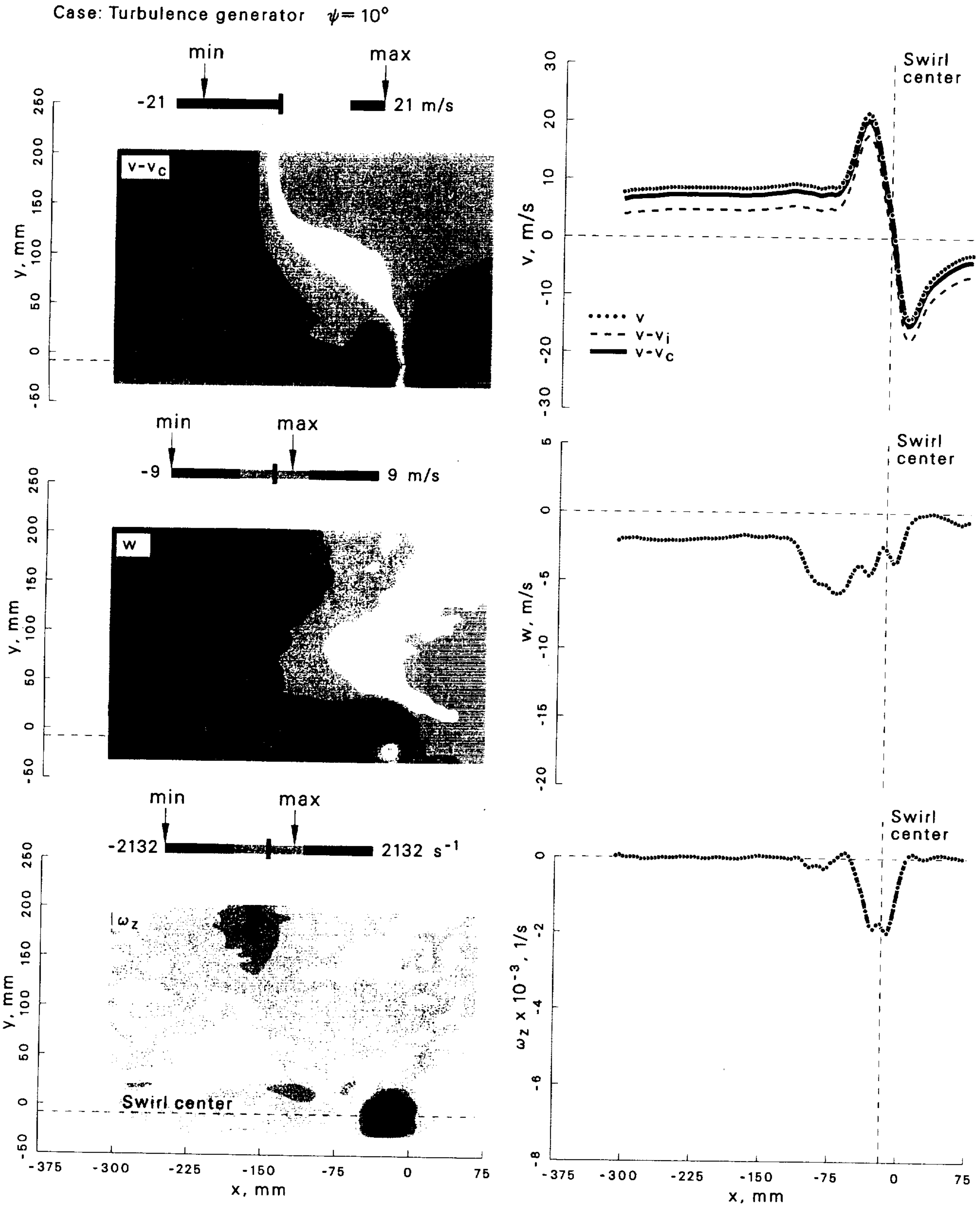

Figure 190: Velocity and vorticity components at $\psi = 10°$ for the turbulence generator case.

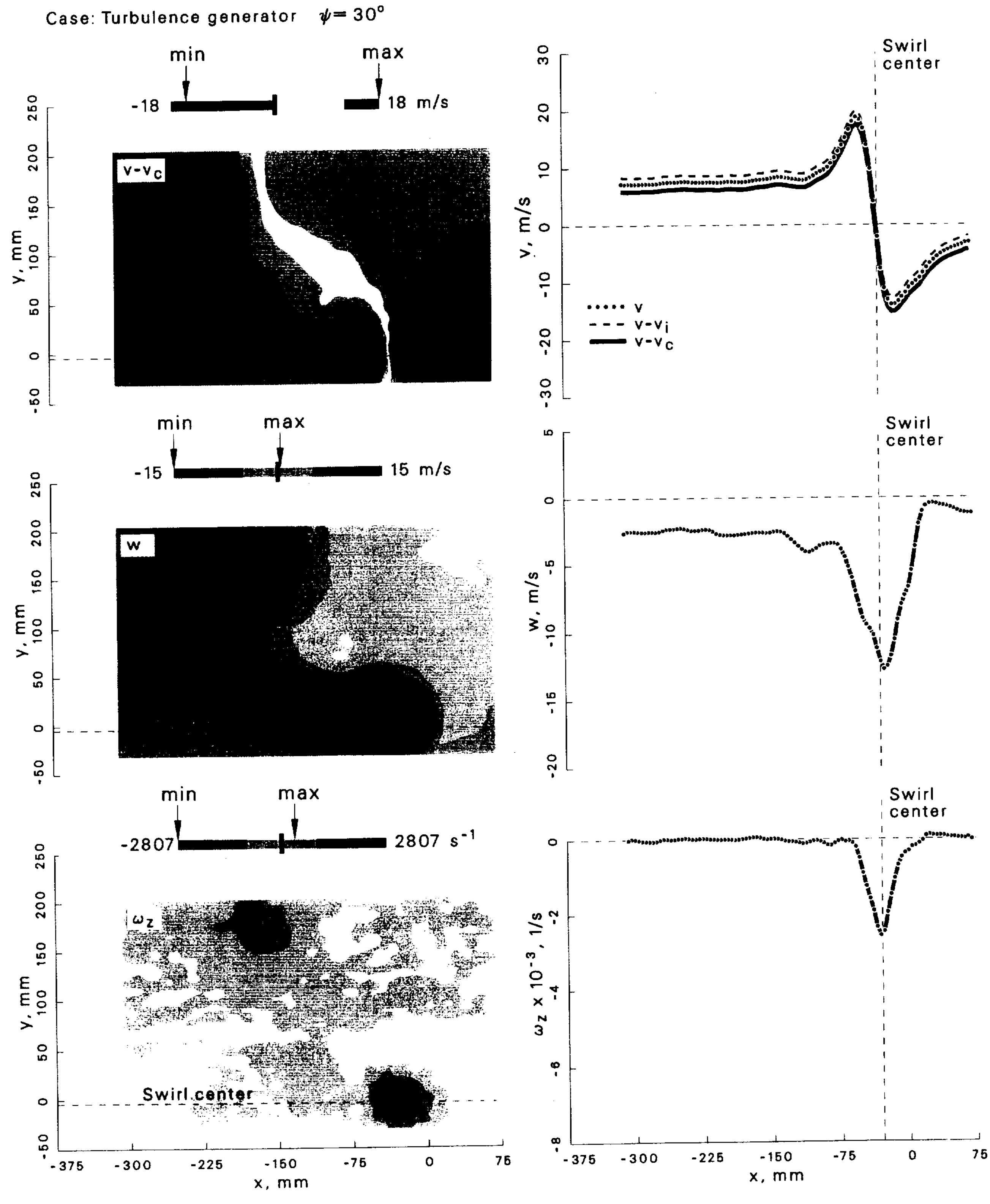

Figure 191: Velocity and vorticity components at $\psi = 30°$ for the turbulence generator case.

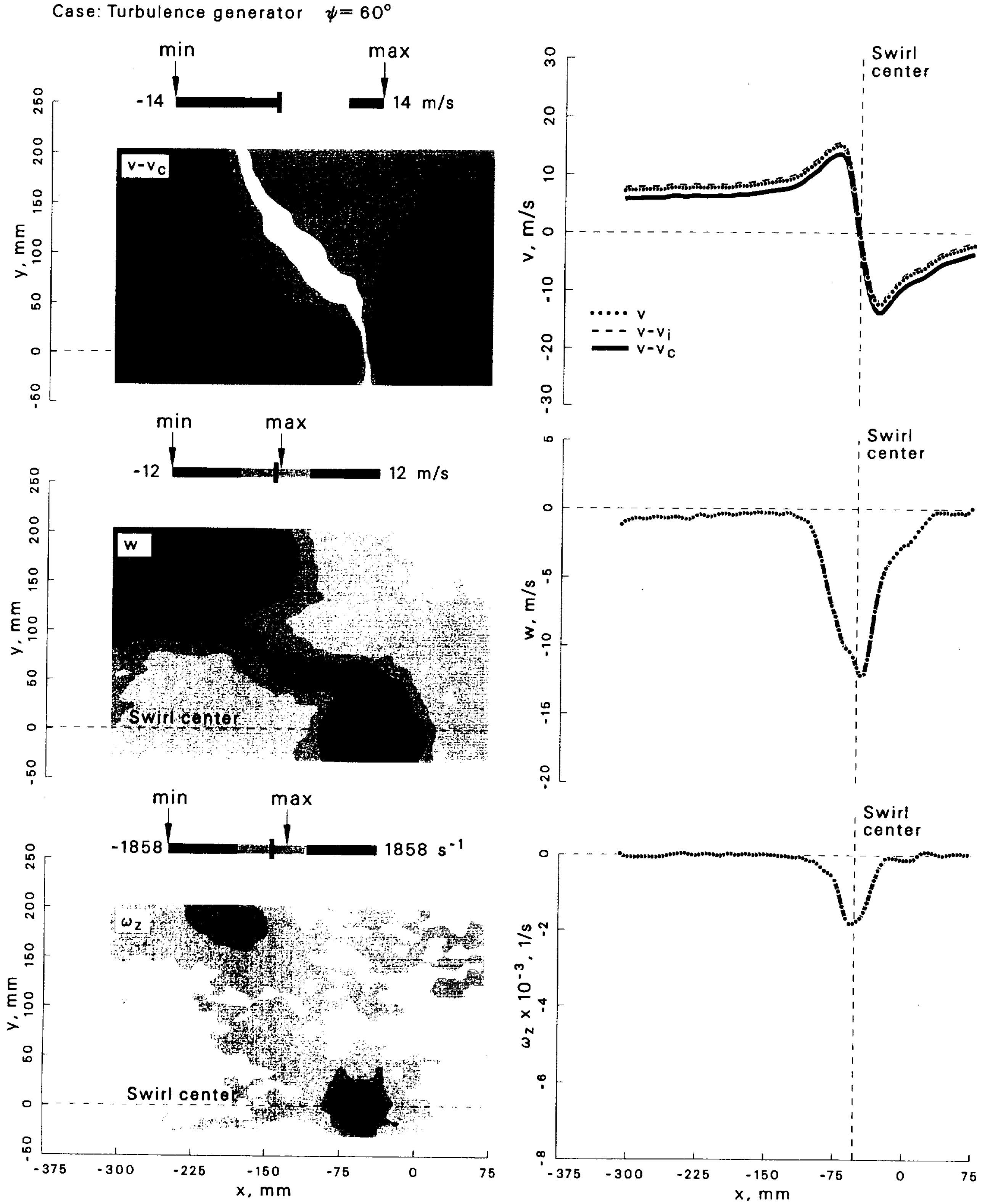

Figure 192: Velocity and vorticity components at $\psi = 60°$ for the turbulence generator case.

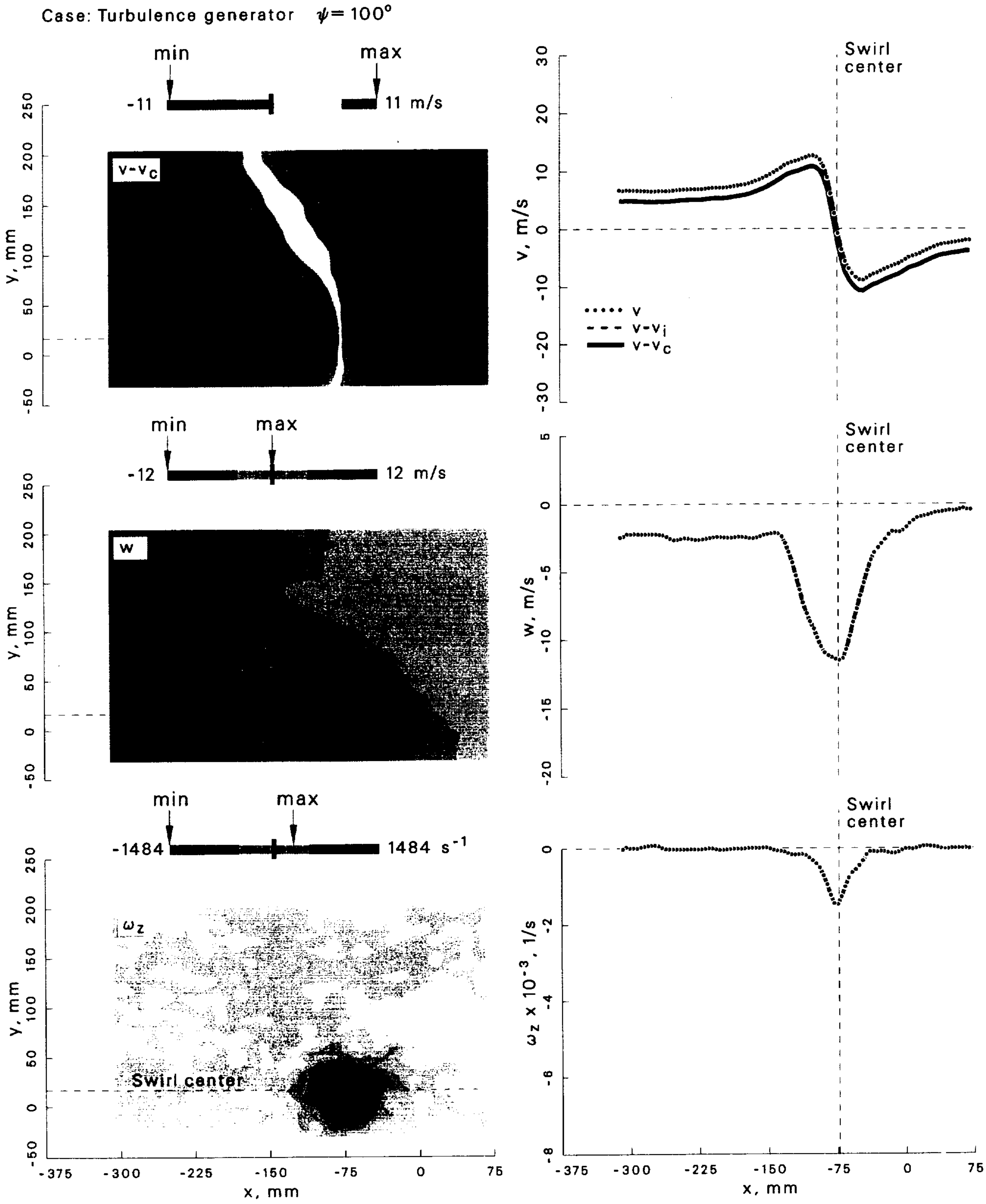

Figure 193: Velocity and vorticity components at $\psi = 100°$ for the turbulence generator case.

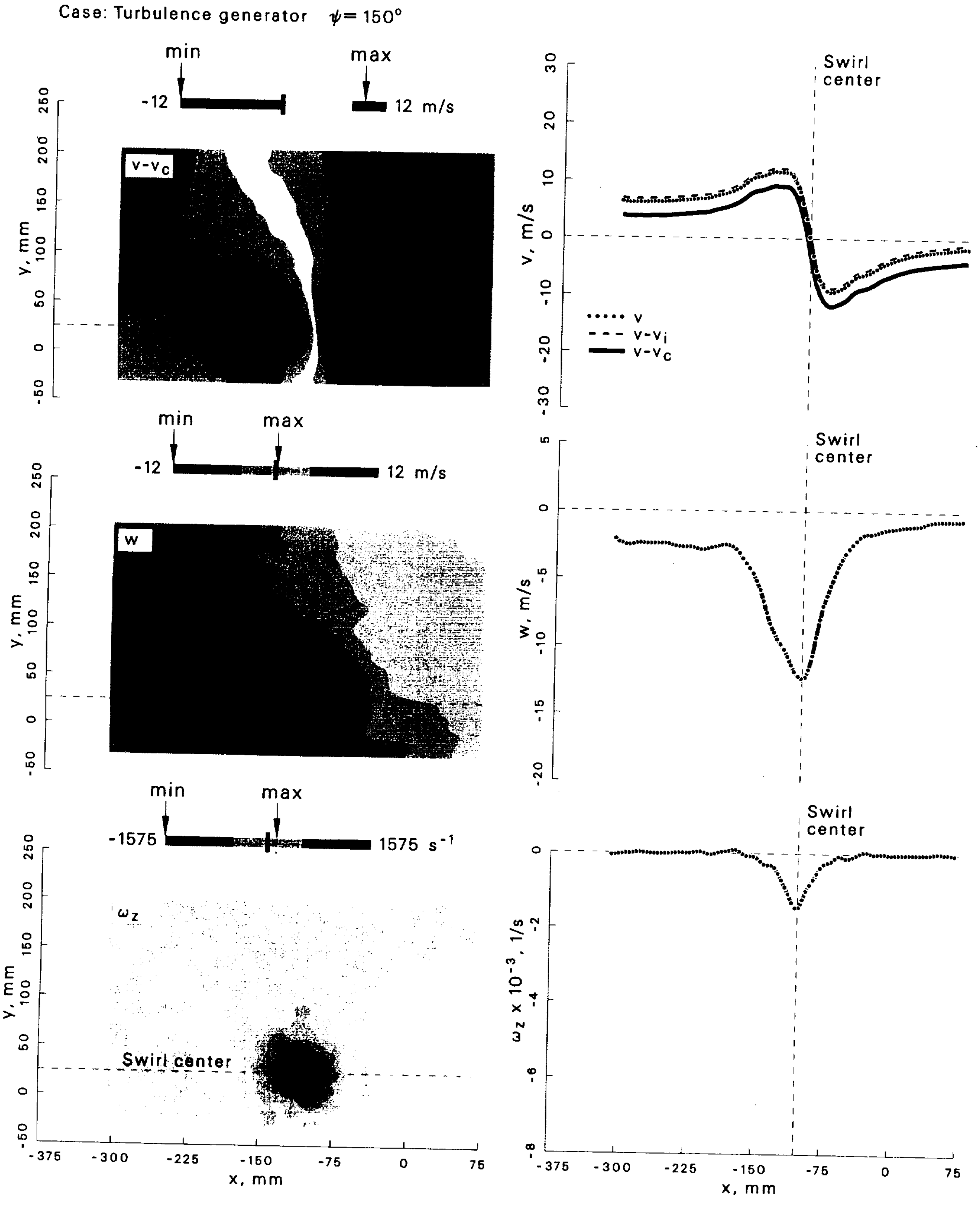

Figure 194: Velocity and vorticity components at $\psi = 150°$ for the turbulence generator case.

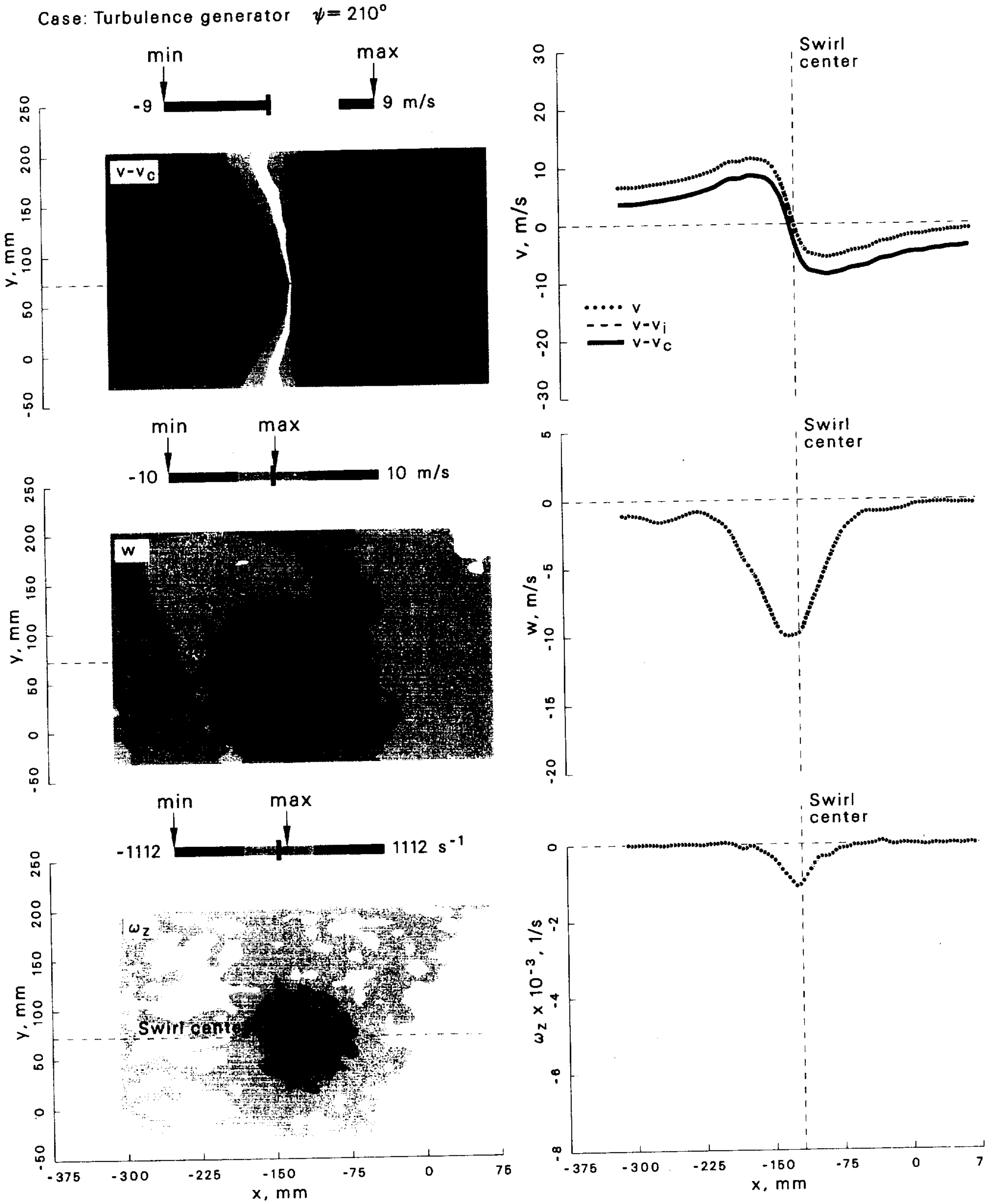

Figure 195: Velocity and vorticity components at $\psi = 210°$ for the turbulence generator case.

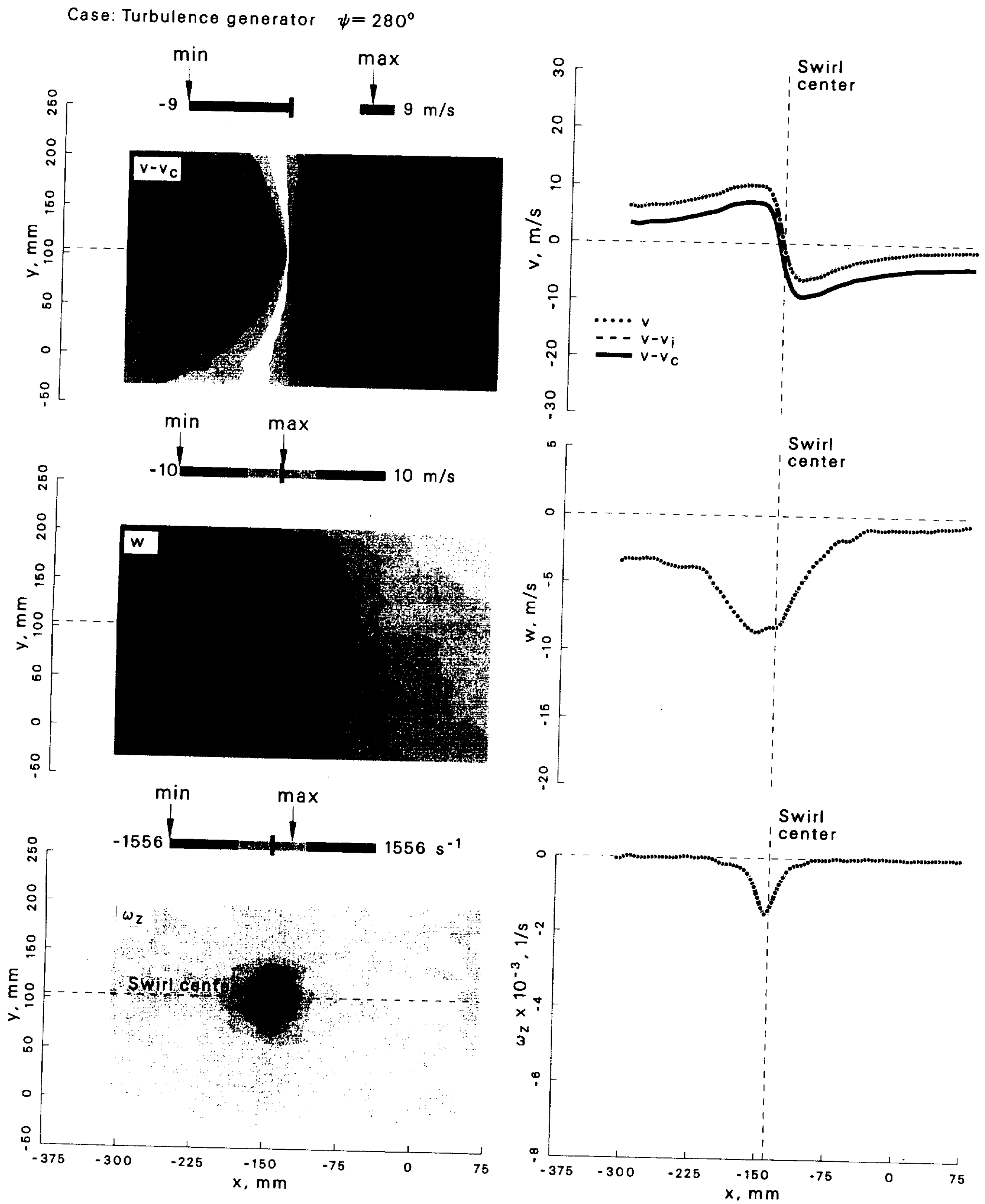

Figure 196: Velocity and vorticity components at $\psi = 280°$ for the turbulence generator case.

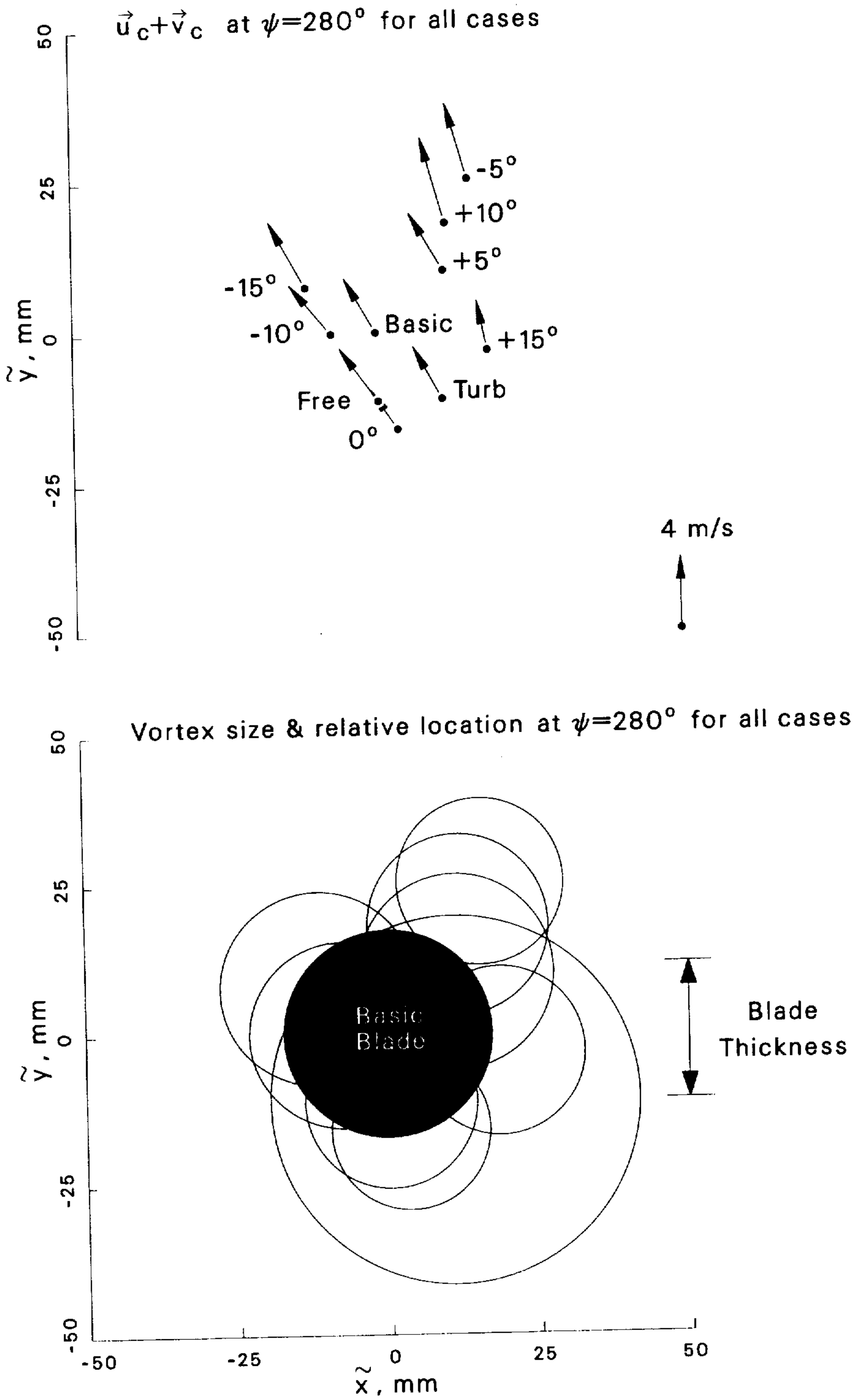

$\vec{u}_c+\vec{v}_c$ at ψ=280° for all cases

Vortex size & relative location at ψ=280° for all cases

Figure 197: Summary of convection velocity, size, and location of vortex when $\psi = 280°$.

REPORT DOCUMENTION PAGE

Form Approved
OMB No. 0704-0188

1. AGENCY USE ONLY

2. REPORT DATE
February 2001

3. REPORT TYPE AND DATES COVERED
Technical Memorandum

4. TITLE AND SUBTITLE
Devices that Alter the Tip Vortex of a Rotor

5. FUNDING NUMBERS
712-10-12

6. AUTHOR(S)
K.W. McAlister, C. Tung, J.T. Heineck

7. PERFORMING ORGANIZATION NAME(S) AND ADDRESS(ES)
Army/NASA Rotorcraft Division, Aeroflightdynamics Directorate
(AMRDEC), U.S. Army Aviation and Missile Command,
Ames Research Center, Moffett Field, CA 94035

8. PERFORMING ORGANIZATION REPORT NUMBER
A-00V0036

9. SPONSORING/MONITORING AGENCY NAME(S) AND ADDRESS(ES)
National Aeronautics and Space Administration
Washington, DC 20546-0001 and U.S. Army Aviation and Missile
Command, Redstone Arsenal, AL 35898-5000

10. SPONSORING/MONITORING AGENCY REPORT NUMBER
NASA/TM-2001-209625
AFDD/TR-01-A-003

11. SUPPLEMENTARY NOTES
Point of Contact: K.W. McAlister, Ames Research Center, MS 215-1, Moffett Field, CA 94035-1000

12a. DISTRIBUTION/AVAILABILITY STATEMENT
Unclassified - Unlimited
Subject Category 02
Distribution: Standard
Availability: NASA CASI (301) 621-0390

12b. DISTRIBUTION CODE

13. ABSTRACT ***(Maximum 200 words)***

Small devices were attached near the tip of a hovering rotor blade in order to alter the structure and trajectory of the trailing vortex. Stereo particle image velocimetry (PIV) images were used to quantify the wake behind the rotor blade during the first revolution. A procedure for analyzing the 3D-velocity field is presented that includes a method for accounting for vortex wander. The results show that a vortex generator can alter the trajectory of the trailing vortex and that a major change in the size and intensity of the trailing vortex can be achieved by introducing a high level of turbulence into the core of the vortex.

14. SUBJECT TERMS
Rotor wake, Trailing vortex, Vortex diffusion, Model rotor

15. NUMBER OF PAGES
210

16. PRICE CODE
A10

17. SECURITY CLASSIFICATION OF REPORT
Unclassified

18. SECURITY CLASSIFICATION OF THIS PAGE
Unclassified

19. SECURITY CLASSIFICATION OF ABSTRACT

20. LIMITATION OF ABSTRACT

NSN 7540-01-280-5500

Standard Form 298 (Rev . 2-89)
Prescribed by ANSI Std. 239-18
298-102